National Research Council Canada
Conseil national de recherches Canada

NRC CNRC

Canadian Journal of Physics

Revue canadienne de physique

Volume 69, Number 2, February 1991

Volume 69, numéro 2, février 1991

ISSN 0008-4204 CJPHAD 69(2) 75–163 (1991)

Canadian Journal of Physics

Published by
THE NATIONAL RESEARCH COUNCIL OF CANADA

Revue canadienne de physique

Publié par
LE CONSEIL NATIONAL DE RECHERCHES DU CANADA

Manuscripts for publication should be submitted to the appropriate editor as indicated on page i.

Correspondence concerning accepted manuscripts and corrected proofs should be sent to Research Journals, National Research Council of Canada, Ottawa, Ont., Canada K1A 0R6. **Telephone enquiries** should be directed to Frances Flavelle (613-993-5780). **FAX:** 613-952-7656. **Telex No.:** 053-3145.

Reprints may be purchased at the time of publication (an order form is sent out with the galley proof). All orders should be sent back with the galley proof to Research Journals, National Research Council of Canada, Ottawa, Ont., Canada K1A 0R6. **Telephone enquiries:** Eileen Fink at 613-993-0151.

Instructions to Authors are published at the back of each issue. Copies may be obtained from the Publishing Department.

Advertisement rates and information may be obtained from Hoda Jabbour at 613-993-9085.

The publisher grants permission to individuals who wish to quote short excerpts and reproduce figures, tables, or photographs from articles in this journal, provided that the source of such material is fully acknowledged. As a courtesy the consent of authors of such material should be obtained.

Les auteurs doivent adresser leurs manuscrits aux directeurs scientifiques appropriés, tel qu'indiqué en page iii.

La **correspondance ayant trait aux manuscrits acceptés** et les **épreuves corrigées** doivent être envoyées à Revues scientifiques, Conseil national de recherches du Canada, Ottawa (Ontario), Canada K1A 0R6. **On peut obtenir des renseignements en téléphonant à** Frances Flavelle (613-993-5780). **Télécopieur :** 613-952-7656. **Télex :** 053-3145.

Les **tirés à part** peuvent être achetés au moment de la publication. Un bon de commande à cet effet accompagne l'épreuve en placard et doit être retourné avec celle-ci à Revues scientifiques, Conseil national de recherches du Canada, Ottawa (Ontario), Canada K1A 0R6. **Renseignements supplémentaires :** Eileen Fink au 613-993-0151.

Les **Recommandations aux auteurs** sont publiées à la fin du chaque numéro. On peut s'en procurer une copie, sur demande, au Service de publication.

Pour toute information concernant les **annonces publicitaires** ou leur coût, s'adresser à Hoda Jabbour au 613-993-9085.

L'éditeur accorde aux particuliers la **permission de citer** de brefs extraits et de reproduire des figures, des tableaux ou des photographies d'articles de la revue, à la condition que la source soit indiquée explicitement. Dans ce cas, il convient, par courtoisie, d'obtenir le consentement des auteurs.

This journal is indexed or abstracted in / Cette revue est signalée ou résumée dans
Bulletin signalétique; Current Contents; Physics Abstracts; Science Citation Index; Vacuum

NOTICE TO AUTHORS

CANADIAN JOURNAL OF PHYSICS

REVUE CANADIENNE DE PHYSIQUE

NOTE AUX AUTEURS

Manuscripts for publication (**the original copy and three duplicates**) should be sent to the appropriate associate editors depending on their subject area. Each article should carry an **index number** according to the current Physics Abstracts indexing scheme (see the December 1988 issue of Can. J. Phys.). The associate editors responsible for receiving manuscripts in the following subject areas are:

10.00–14.80 series (Physics of Elementary Particles and Fields)/Série 10.00–14.80 (Physique des particules élémentaires et des champs)

Dr. Bernard Margolis
Department of Physics
McGill University
845 Sherbrooke Street West
Montréal, Que., Canada H3A 2T5

20.00–29.90 series (Nuclear Physics)/Série 20.00–29.90 (Physique nucléaire) Experimental papers/articles portant sur des travaux expérimentaux

Dr. W. P. Alford
Department of Physics
University of Western Ontario
London, Ont., Canada N6A 3K7

Theoretical papers/articles théoriques

Dr. P. G. Blunden
Department of Physics
University of Manitoba
Winnipeg, Man., Canada R3T 2N2

30.00–31.90 and 33.00–33.90 series (Atomic and Molecular Physics)/Séries 30.00–31.90 et 33.00–33.90 (Physique atomique et moléculaire)

Dr. J. A. Coxon
Department of Chemistry
Dalhousie University
Halifax, N.S., Canada B3H 4J3

32.00–32.90 and 34.00–36.90 series (Atomic and Molecular Physics)/Séries 32.00–32.90 et 34.00–36.90 (Physique atomique et moléculaire)

Dr. G. W. F. Drake
Department of Physics
University of Windsor
Windsor, Ont., Canada N9B 3P4

41.00–41.90 series (Electricity and Magnetism)/Série 41.00–41.90 (Électricité et magnétisme)

Dr. R. H. MacPhie
Department of Electrical Engineering
University of Waterloo
Waterloo, Ont., Canada N2L 3G1

42.00–42.90 series (Optics)/Série 42.00–42.90 (Optique)

Michel Piché
Laboratoire de recherches en optique et laser (LROL)
Université Laval
Cité universitaire
Québec (Québec), Canada G1K 7P4

Les manuscrits destinés à la publication (**l'original et trois copies**) doivent être envoyés aux directeurs scientifiques appropriés, selon leur domaine d'intérêt. Chaque article doit porter le **numéro de l'index** adopté par les Physics Abstracts (voir le numéro de décembre 1988 du Can. J. Phys.). Les directeurs scientifiques associés dans les domaines d'intérêt sont les suivants :

47.00–47.90 (Fluid Dynamics)/Série 47.00–47.90 (Dynamique des fluides)

Dr. J. J. Gottlieb
Institute for Aerospace Studies
University of Toronto
4925 Dufferin Street
Downsview, Ont., Canada M3H 5T6

50.00–52.90 series (Fluids, Plasmas, and Electric Discharges)/Série 50.00–52.90 (Fluides, plasmas et décharges électriques)

T. W. Johnston
Centre de recherche de l'énergie
Institut national de la recherche scientifique
Université du Québec, C. P. 1020
Varennes (Québec), Canada J0L 2P0

60.00–68.90 series (Condensed Matter: Structure, Thermal and Mechanical Properties)/Série 60.00–68.90 (État condensé : structure, propriétés thermiques et mécaniques)

Dr. B. Joos
Department of Physics
University of Ottawa
Ottawa, Ont., Canada K1N 6N5

70.00–79.90 series (Condensed Matter: Electronic Structure, Electrical, Magnetic, and Optical Properties)/Série 70.00–79.90 (État condensé : structure électronique, propriétés électriques, magnétiques et optiques)

Dr. W. R. Datars
Department of Physics
McMaster University
Hamilton, Ont., Canada L8S 4M1

94.00–94.90 series (Aeronomy and Space Physics)/Série 94.00–94.90 (Aéronomie et physique de l'espace)

Dr. A. Vallance Jones
Herzberg Institute of Astrophysics
National Research Council of Canada
Ottawa, Ont., Canada K1A 0R6

00.00–07.90 series (General); 43.00–46.90 (Acoustics); 80.00–87.90 (Cross-disciplinary Physics and Related Areas of Science and Technology); 90–93.85 and 95.00–98.90 (Geophysics, Astronomy, and Astrophysics)/Série 00.00–07.90 (Domaine général); 43.00–46.90 (Acoustique); 80.00–87.90 (Physique interdisciplinaire et domaines connexes en sciences et technologie) 90.00–93.85 et 95.00–98.90 (Geophysique, astronomie et astrophysique)

Dr. R. W. Nicholls
Department of Physics
York University
4700 Keele Street
North York, Ont., Canada M3J 1P3

General correspondence may be addressed to the Editor/La correspondance générale peut être adressée au directeur scientifique : Dr. R. W. Nicholls, Department of Physics, York University, 4700 Keele Street, North York, Ont., Canada M3J 1P3. Telephone: 416-736-5385. Fax: 416-736-5386; E-mail (Bitnet): CJP @ YUSOL.

Non-Newtonian-flow formation in Couette motion in magnetohydrodynamics with time-varying suction

NABIL T. ELDABE AND AHMED A. A. HASSAN
Department of Mathematics, Faculty of Education, Ain Shams University, Heliopolis, Cairo, Arab Republic of Egypt

Received March 20, 1990

This paper is an analysis of an incompressible flow of electrically conducting non-Newtonian fluid between two infinite parallel walls one of them moving with a uniform velocity under the action of a transverse magnetic field. The moving wall is subjected to a suction whose magnitude oscillates with respect to time over a constant mean. In our analysis we are taking into account the induced magnetic field; a matter that is neglected by the majority of the previous work. The main results show that the effect of the viscoelasticity of the fluid is to decrease both the flow and the induced magnetic field.

Cet article est une analyse de l'écoulement incompressible d'un fluide non newtonien électriquement conducteur entre deux parois parallèles infinies dont l'une se déplace à vitesse uniforme sous l'action d'un champ magnétique transversal. Cette paroi mobile est soumise à une succion dont la grandeur oscille en fonction du temps autour d'une moyenne constante. Dans notre analyse, nous prenons en compte le champ magnétique induit, qui a été négligé dans la majorité des travaux antérieurs. Les résultats principaux montrent que l'effet de la viscoélasticité du fluide est de diminuer à la fois l'écoulement et le champ magnétique induit.

[Traduit par la rédaction]

Can. J. Phys. 69, 75 (1991)

Introduction

Because of their extensive use in industry, non-Newtonian fluids have gained considerable importance (1–4). The Oldroyd model has been modified by Walters (5). This modified model, known as liquid B', is generally accepted as valid for elastico-viscous fluids such as oils, polymers, etc., which have short memories. Beard and Walters (6) solved the boundary-layer equations for liquid B' for the case of two-dimensional flow near a stagnation point when the elastico-viscous parameter is very small.

The steady and unsteady Couette-type flows in Newtonian hydrodynamics and hydromagnetics that are subject to wall suction have been discussed by several authors (7–11). Katagiri (12) has studied the Couette-flow formation in magnetohydrodynamics (MHD). Neglecting the induced field, he solved the momentum equation by the method of Laplace transformation. Muhuri (13) considered the more general case wherein the velocity of the moving wall varies as (time)^n and where the walls are subjected to uniform suction or injection. Balarm and Govindarajulu (14) have obtained exact solutions for the same problem by taking the induced field into account and the magnitude of the Prandtl number equal to one.

This report treats analytically the flow of an elastico-viscous, incompressible, and electrically conducting fluid between two infinite parallel walls one of them moving with a uniform velocity. The system is stressed by a magnetic field of constant strength acting perpendicular to the walls.

Basic equations

The constitutive equation for incompressible elastico-viscous fluids suggested by ref. 5 is

$$[1] \quad \tau_{ij} = 2\mu d_{ij} - 2k_o E_{ij} + 4\phi d_i^{\alpha} d_{\alpha j}$$

where

$$d_{ij} = \left(\frac{1}{2}\right)(v_{i,j} + v_{j,i})$$

$$E_{ij} = \left(\frac{1}{2}\right)(a_{i,j} + a_{j,i} + 2v_{,i}^{m} v_{m,j})$$

$$a_i \text{ (acceleration vector)} = \frac{\partial v_i}{\partial t} + v^m v_{i,m}$$

v_i is the velocity vector. A comma followed by an index implies covariant differentiation. μ, k_o, and ϕ are material constants representing, respectively, viscosity, elastico-viscosity, and cross-viscosity coefficients of the fluid.

The basic equation of MHD neglecting the displacement currents and free charges are (15)

$$[2] \quad \nabla \cdot \boldsymbol{H} = 0$$

$$[3] \quad \nabla \wedge \boldsymbol{H} = \boldsymbol{J}$$

$$[4] \quad \nabla \wedge \boldsymbol{E} = -\mu_e \frac{\partial \boldsymbol{H}}{\partial t}$$

Ohm's law

$$[5] \quad \boldsymbol{J} = \sigma(\boldsymbol{E} + \mu_e v \wedge \boldsymbol{H})$$

the equation of continuity

$$[6] \quad \nabla \cdot v = 0$$

and the momentum equation

$$[7] \quad \frac{\partial v}{\partial t} + (v \cdot \nabla)v = -\frac{1}{\rho}\nabla P + \frac{1}{\rho}\nabla \cdot \tau + \frac{\mu_e}{\rho} \boldsymbol{J} \wedge \boldsymbol{H}$$

Here $\boldsymbol{H}$ is the magnetic field, $\boldsymbol{E}$ the electric field, $\boldsymbol{J}$ the current density, and τ is defined by [1]. ρ, μ_e, σ, and P denote, respec-

tively, the density. magnetic permeability, conductivity, and fluid pressure. Eliminating E and J from [3]–[5] we get

$$[8] \quad \frac{\partial H}{\partial t} = \nabla \wedge (v \wedge H) + \eta \nabla^2 H$$

where $\eta = (\mu_e \sigma)^{-1}$ is the magnetic diffusivity.

Analysis

We consider the shear flow between two infinite parallel walls at a distance h apart. The lower wall moves with a uniform velocity U while the other is at rest. A suction whose magnitude oscillates in time over a constant mean is applied to the moving wall. A uniform magnetic field H_0 is imposed normal to the walls. The fluid is assumed to be elastico-viscous obeying Walter's see ref. 5, incompressible, and electrically conducting whereas the walls are taken to be nonconducting.

We take the x axis along the lower wall and the y axis normal to it. Since the plates are infinite in extent all quantities are functions of y and t only. We have $v = (u, v, 0)$ and $H = (H_x, H_y, 0)$. From [2] we get $H_y = H_0$, the applied field. Equation [6] gives

$$[9] \quad v(t) = -U(1 + \epsilon e^{iwt}), \qquad \epsilon << 1$$

which is the velocity of the suction that consists of a basic steady value U with a weak time-varying component. Let us introduce the nondimensional quantities as follows:

$$y = \frac{\nu}{U} y_1, \qquad t = \frac{4\nu}{U^2} t_1, \qquad w = \frac{U^2}{4\nu} w_1$$

$$u = U u_1, \qquad H = H_0 H_1, \qquad P = \rho U^2 P_1$$

Using [9], [7] and [8] may now be written in the nondimensional form after dropping the suffix 1

$$[10] \quad \frac{1}{4}\frac{\partial u}{\partial t} - (1+\epsilon e^{iwt})\frac{\partial u}{\partial y} = \frac{\partial^2 u}{\partial y^2} - k\left[\frac{1}{4}\frac{\partial^3 u}{\partial y^2 \partial t} - (1+\epsilon e^{iwt})\frac{\partial^3 u}{\partial y^3}\right] + s^2 \frac{\partial H}{\partial y}$$

$$[11] \quad \frac{\partial P^*}{\partial y} = \frac{iw\epsilon e^{iwt}}{4}$$

where P^* is the modified pressure given by

$$P^* = P - (2k + \lambda^*)\left(\frac{\partial u}{\partial y}\right)^2 - \frac{s^2}{2} H^2$$

$$[12] \quad \frac{1}{4}\frac{\partial H}{\partial t} - (1+\epsilon e^{iwt})\frac{\partial H}{\partial y} - \frac{\partial u}{\partial y} = \frac{1}{R_m}\frac{\partial^2 H}{\partial Y^2}$$

where

$$s = \left(\frac{\mu_e H_0^2}{\rho U^2}\right)^{1/2}$$

is the magnetic-pressure number, $R_m = \nu/\eta$ is the magnetic Reynolds number, $\nu = \mu/\rho$ is the kinematic viscosity,

$$k = k_0 U^2/\rho\nu^2$$

is the elasticity parameter, and $\lambda^* = \emptyset\, U^2/\rho\nu^2$ is the cross-viscosity parameter.

The boundary conditions are

$$[13] \quad \begin{aligned} y = 0, &: u = 1, \quad H = 0 \\ y = 1, &: u = 0, \quad H = 0 \end{aligned}$$

For small values of ϵ, we write

$$[14] \quad \begin{aligned} u(y,t) &= u_1(y) + \epsilon u_2(y)\, e^{iwt} \\ H(y,t) &= H_1(y) + \epsilon H_2(y)\, e^{iwt} \end{aligned}$$

The functions u_1, u_2, H_1, and H_2 then satisfy the set of equations

$$ku_1''' + u_1'' + u_1' + s^2 H_1' = 0$$

$$[15] \quad ku_2''' - \frac{iwku_2''}{4} + u_2'' + u_2' - \frac{iwu_2}{4} + s^2 H_2' = -ku_1''' - u_1'$$

$$H_1'' + R_m u_1' + R_m H_1' = 0$$

$$H_2'' + R_m H_2' - \frac{iwR_m H_2}{4} + R_m u_2' = -R_m H_1'$$

with the boundary conditions

$$[16] \quad \begin{aligned} y = 0 &: u_1 = 1, \quad u_2 = 0, \quad H_1 = H_2 = 0 \\ y = 1 &: u_1 = u_2 = 0, \quad H_1 = H_2 = 0 \end{aligned}$$

Equations [15] reduce to those governing the flow of a Newtonian fluid if $k = 0$.

Also we find that the order of the governing equations increases from two to three owing to the presence of the elastic property of the fluid. To have an unique solution of [15] satisfying the boundary conditions in [16], we follow Beard and Walters (6) and assume the solution in the form

$$[17] \quad \begin{aligned} u_1 &= u_{10} + k u_{11}, \quad H_1 = H_{10} + k H_{11} \\ u_2 &= u_{20} + k u_{22}, \quad H_2 = H_{20} + k H_{22} \end{aligned}$$

This assumption is satisfied in the case of liquids with short memories, see Walters ref. 5.

Inserting [17] in [15] and equating the coefficients of k, we obtain for the particular case $R_m = 1$

$$[18] \quad u_{10}'' + u_{10}' + s^2 H_{10}' = 0$$

$$[19] \quad H_{10}'' + H_{10}' + u_{10}' = 0$$

$$[20] \quad u_{11}'' + u_{11}' + s^2 H_{11}' = -u_{10}'''$$

[21] $H''_{11} + H'_{11} + u''_{11} = 0$

[22] $u''_{20} + u'_{20} - \frac{iwu_{20}}{4} + s^2 H'_{20} = -u'_{10}$

[23] $H''_{20} + H'_{20} - \frac{iwH_{20}}{4} + u'_{20} = -H'_{10}$

[24] $u''_{22} + u'_{22} - \frac{iwu_{22}}{4} + s^2 H'_{22}$

$$= -u''_{10} - u'_{11} - u''_{20} + \frac{iwu''_{20}}{4}$$

[25] $H''_{22} + H'_{22} - \frac{iwH_{22}}{4} + u'_{22} = -H'_{11}$

where a prime denotes differentiation with respect to y. The boundary conditions now reduce to

[26] $u_{10} = 1, \quad u_{11} = 0, \quad u_{20} = u_{22} = 0$

$H_{10} = H_{20} = H_{11} = H_{22} = 0$ at $y = 0$

[27] $u_{10} = u_{20} = u_{11} = u_{22} = 0$

$H_{10} = H_{20} = H_{11} = H_{22} = 0$ at $y = 1$

The solution of the system of equations [18]–[25] subject to the boundary conditions [26] and [27] is obtained analytically as

---

[28] $$u_{10} = \left[\frac{(e^{\lambda_2} - 1)(1 - e^{\lambda_3 y}) + (e^{\lambda_3} - 1)(1 - e^{\lambda_2 y}) + 2(e^{\lambda_2} - 1)(e^{\lambda_3} - 1)}{2(e^{\lambda_2} - 1)(e^{\lambda_3} - 1)}\right]$$

[29] $$u^{11} = \{[s\lambda_2^2 + (s^3 - 3s^2 + s - 1)(e^{\lambda_2} - 1)](1 - e^{\lambda_2 y})(e^{\lambda_3} - 1)^2 + s\lambda_2^2 (e^{\lambda_2} - 1)(e^{\lambda_3} - 1)^2 y e^{\lambda_2 y}$$

$$+ [s\lambda_3^2 + (s^3 + 3s^2 + s + 1)(e^{\lambda_3} - 1)](e^{\lambda_2} - 1)^2 (1 - e^{\lambda_3 y}) + s\lambda_3^2 (e^{\lambda_2} - 1)^2 (e^{\lambda_3} - 1) y e^{\lambda_3 y}\} / 4s(e^{\lambda_2} - 1)^2 (e^{\lambda_3} - 1)^2$$

[30] $$u_{20} = \frac{2i}{w}\left[\frac{2\lambda_2 e^{\lambda_2 y}}{(e^{\lambda_2} - 1)} + \frac{2\lambda_3 e^{\lambda_3 y}}{(e^{\lambda_3} - 1)} + \frac{\lambda_2 (e^{\lambda_4} - e^{\lambda_2}) e^{\lambda_3^* y}}{(e^{\lambda_2} - 1)(e^{\lambda_3^*} - e^{\lambda_4}} + \frac{\lambda_2 (e^{\lambda_3^*} - e^{\lambda_2}) e^{\lambda_4 y}}{(e^{\lambda_2} - 1)(e^{\lambda_3^*} - e^{\lambda_4})}\right.$$

$$\left. - \frac{\lambda_3 (e^{\lambda_6} - e^{\lambda_3}) e^{\lambda_5 y}}{(e^{\lambda_3} - 1)(e^{\lambda_6} - e^{\lambda_5})} - \frac{\lambda_3 (e^{\lambda_3} - e^{\lambda_5}) e^{\lambda_6 y}}{(e^{\lambda_3} - 1)(e^{\lambda_6} - e^{\lambda_5})}\right]$$

[31] $$u_{22} = (b_1^* e_1 + e_2 + r_6 y) e^{\lambda_3^* y} + (b_2^* e_3 + e_4 + r_8 y) e^{\lambda_4 y} + (b_3^* e_5 + e_6 + r_{10} y) e^{\lambda_5 y}$$

$$+ (b_4^* e_1 + e_8 + r_{12} y) e^{\lambda_5 y} + (r_1 + r_3 y) e^{\lambda_2 y} + (r_1 + r_4 y) e^{\lambda_3 y}$$

[32] $$H_{10} = \left[\frac{(e^{\lambda_2} - 1)(1 - e^{\lambda_3 y}) - (e^{\lambda_3} - 1)(1 - e^{\lambda_2 y})}{2s(e^{\lambda_2} - 1)(e^{\lambda_3} - 1)}\right]$$

[33] $$H_{11} = \{(e^{\lambda_2} - 1)^2 (1 - e^{\lambda_3 y})[-2(e^{\lambda_3} - 1) + \lambda_3^2 e^{\lambda_3}] + \lambda_3^2 (e^{\lambda_2} - 1)^2 (e^{\lambda_3} - 1) y e^{\lambda_3 y}$$

$$+ (e^{\lambda_3} - 1)^2 (1 - e^{\lambda_2 y})[2(e^{\lambda_2} - 1) + \lambda_2^2 e^{\lambda_2}] - \lambda_2^2 (e^{\lambda_2} - 1)(e^{\lambda_3} - 1) y e^{\lambda_2 y}\}$$

[34] $$H_{20} = \left(\frac{2i}{ws}\right)\left\{\frac{\lambda_2 e^{\lambda_2 y}}{(e^{\lambda_2} - 1)} + \frac{\lambda_3 e^{\lambda_3 y}}{(e^{\lambda_3} - 1)} + \frac{\lambda_2 (e^{\lambda_4} - e^{\lambda_2}) e^{\lambda_3^* y}}{(e^{\lambda_2} - 1)(e^{\lambda_4} - e^{\lambda_3^*})} - \frac{\lambda_2 (e^{\lambda_3^*} - e^{\lambda_2}) e^{\lambda_4 y}}{(e^{\lambda_2} - 1)(e^{\lambda_3^*} - e^{\lambda_4})}\right.$$

$$\left. - \frac{\lambda_3 (e^{\lambda_6} - e^{\lambda_3}) e^{\lambda_5 y}}{(e^{\lambda_3} - 1)(e^{\lambda_6} - e^{\lambda_5})} + \frac{\lambda_3 (e^{\lambda_3} - e^{\lambda_5}) e^{\lambda_6 y}}{(e^{\lambda_3} - 1)(e^{\lambda_6} - e^{\lambda_5})}\right\}$$

[35] $$H_{22} = (b_1^* + p_3 y) e^{\lambda_3^* y} + (b_2^* + P_4 y) e^{\lambda_4 y} + (b_3^* + p_5 y) e^{\lambda_5 y} + (b_4^* + p_6 y) e^{\lambda_6 y}$$

$$+ (p_1 + p_9 + p_7 y) e^{\lambda_2 y} + (p_2 + p_{10} + p_8 y) e^{\lambda_3 y}$$

where

$$\lambda_2 = s - 1, \quad \lambda_3 = -(s+1, \quad \lambda^*_{3,4} = \left[\frac{\lambda_2 \pm (\lambda_2^2 + iw)^{1/2}}{2}\right], \quad \lambda_{5,6} = \left[\frac{\lambda_3 \pm (\lambda_3^2 + iw)^{1/2}}{2}\right]$$

$$p_1 = \left\{\frac{N_9\left[s(s-1) - \frac{iw}{4}\right] + N_{11}\left[(2s-1) - \frac{iw}{4}\right] - (s-1)N_1 - N_3}{\frac{iw}{4}\left[\frac{iw}{4} - 2s(s-1)\right]}\right\}$$

$$p_2 = \left\{\frac{N_{\cdot\cdot}\left[s(s+1) - \frac{iw}{4}\right] - N_{12}\left[(2s+1) + \frac{iw}{4}\right] + (s+1)N_2 - N_4}{\frac{iw}{4}\left[\frac{iw}{4} - 2s(s+1)\right]}\right\}$$

$$P_3 = \frac{-N_5}{2s\,[(s-1)^2 + iw]^{1/2}}, \quad P_4 = \frac{N_6}{2s\,[(s-1)^2 + iw]^{1/2}}, \quad P_5 = \frac{N_7}{2s\,[(s+1)^2 + iw]^{1/2}}, \quad P_6 = \frac{-N_8}{2s\,[(s+1)^2 + iw]^{1/2}}$$

$$P_7 = \frac{[s(s-1)N_{11} - (s-1)N_3]}{\left(\frac{iw}{4}\right)\left[\frac{iw}{4} - 2s(s-1)\right]}, \quad P_8 = \frac{[s(s+1)N_{12} + (s+1)N_4]}{\left(\frac{iw}{4}\right)\left[\frac{iw}{4} - 2s(s+1)\right]}$$

$$P_9 = [s(s-1)N_{11} - (s-1)N_5]\left(\frac{iw}{4}\right)^2 \frac{\left[\frac{iw}{4} - 2s(s-1)\right]}{\left[\frac{iw(2s-1)}{2} - 2s(s-1)^2\right]},$$

$$P_{10} = \frac{[s(s+1)N_{12} + (s+1)N_4]\left(\frac{iw}{4}\right)^2\left[\frac{iw}{4} - 2s(s+1)\right]^2}{\left[2s(s+1)^2 - \frac{iw(2s+1)}{2}\right]}$$

$$e_1 = \frac{4s\lambda^*_3(\lambda_2 - \lambda^*_3)}{iw}, \quad e_2 = \left(\frac{4}{iw}\right)\{p_3[s^2 - \lambda^*_3 s - (2\lambda^*_3 + 1)(\lambda^*_3 + 1)] - N_3\}, \quad e_3 = \frac{4s\lambda_4(\lambda_4 - \lambda_2)}{iw}$$

$$e_4 = \left(\frac{4}{iw}\right)\{p_4[s^2 - \lambda_4 s - (2\lambda_4 + 1)(\lambda_4 + 1)] - N_6\}, \quad e_5 = \frac{4s\lambda_5(\lambda_5 - \lambda_3)}{iw}$$

$$e_6 = \left(\frac{4}{iw}\right)\{p_5[s^2 + \lambda_5 s - (2\lambda_5 + 1)(\lambda_5 + 1)] - N_7\}, \quad e_7 = \frac{4s\lambda_6(\lambda_6 - \lambda_3)}{iw}$$

$$e_8 = \left(\frac{4}{iw}\right)\{p_6[s^2 + \lambda_6 s - (2\lambda_6 + 1)(\lambda_6 + 1)] - N_8\}$$

$$r_1 = \left(\frac{4}{iw}\right)\left\{sN_9 + N_{11} - N_1 + \frac{iws(p_1 + p_9)}{4} - \left[2s(s-1) - \frac{iw}{4}\right]p_7\right\}$$

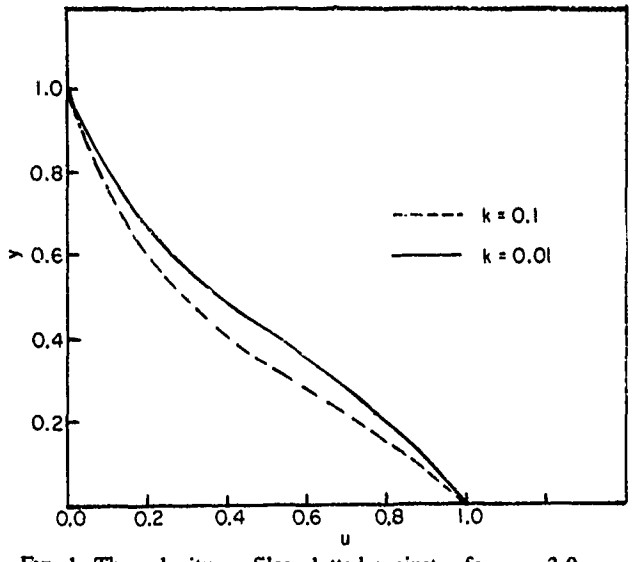

FIG. 1. The velocity profiles plotted against y for $s = 3.0$, $w = 2.0$, and $t = \pi$.

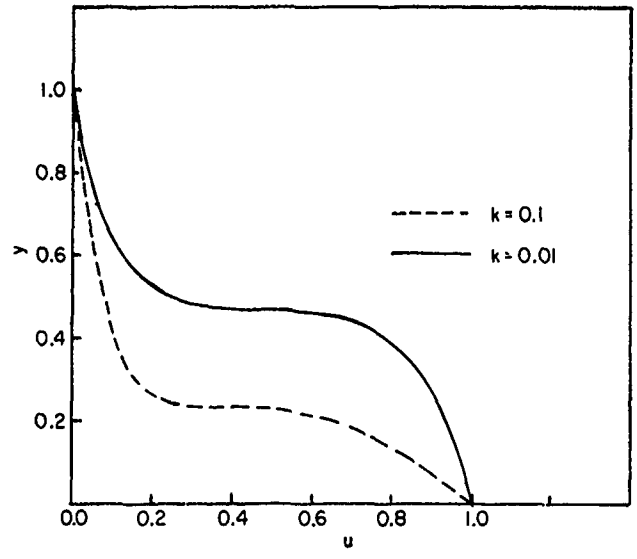

FIG. 2. The velocity profiles plotted against y for $s = 10.0$, $w = 2.0$, and $t = \pi$.

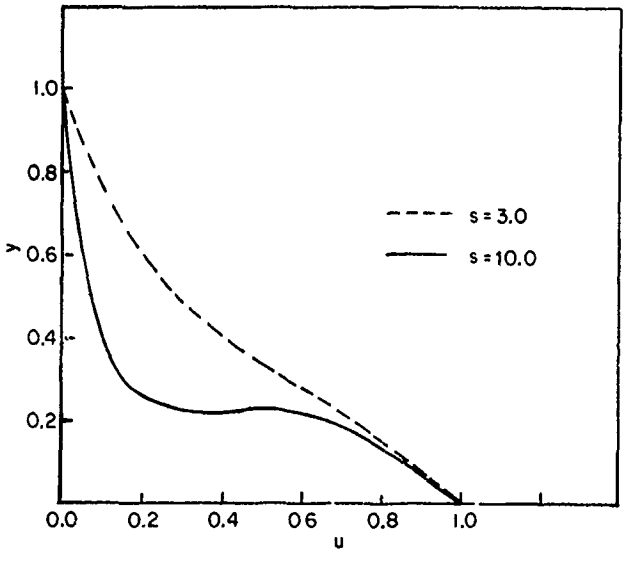

FIG. 3. The velocity profiles plotted against y for $k = 0.1$, $w = 2.0$, and $t = \pi$.

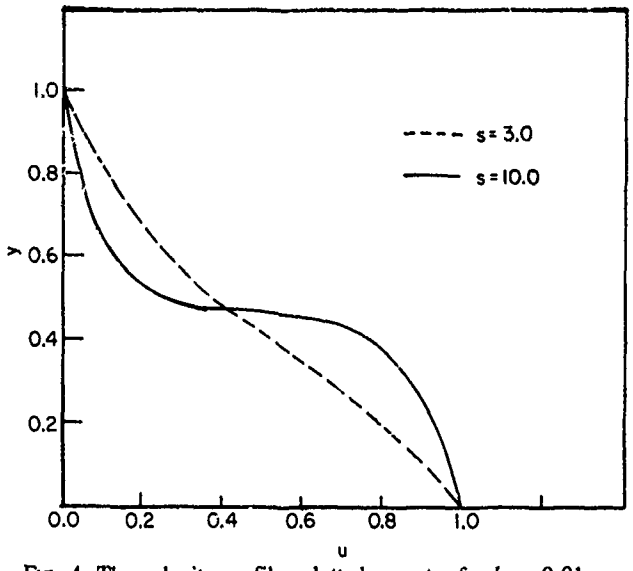

FIG. 4. The velocity profiles plotted aganst y for $k = 0.01$, $w = 2.0$, and $t = \pi$.

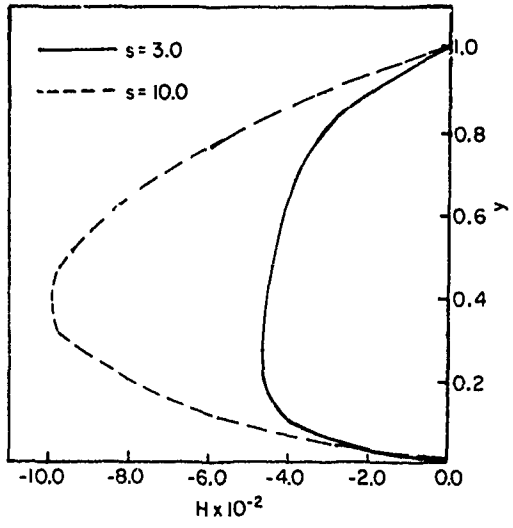

FIG. 5.The induced magnetic field plotted against y for $k = 0.1$, $w = 2.0$, and $t = \pi$.

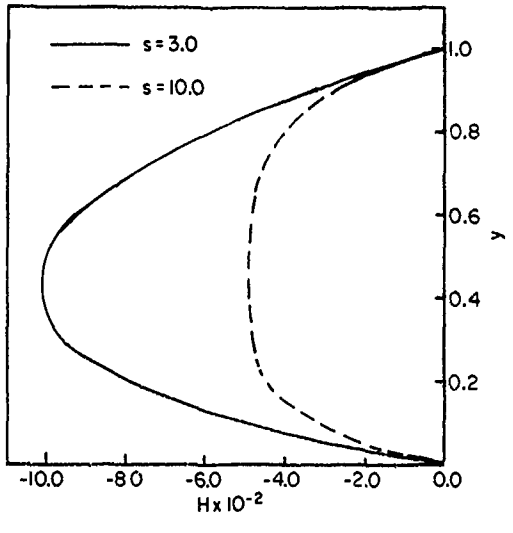

FIG. 6. The induced magnetic field plotted against y for $k = 0.01$, $w = 2.0$, and $t = \pi$.

$$r_2 = \left(\frac{4}{iw}\right)\left\{-sN_{10} + N_{12} - N_2 - \frac{iws(p_2+p_{10})}{4} - \left[2s(s+1) - \frac{iw}{4}\right]p_8\right\}$$

$$r_3 = \left(\frac{4}{iw}\right)\left\{sN_{11} - N_3 - \frac{iwsp_7}{4}\right\}, \quad r_4 = \left(\frac{4}{iw}\right)\left\{-sN_{12} - N_4 + \frac{iwsp_8}{4}\right\}, \quad r_6 = \frac{4s\lambda_3^* p_3(\lambda_2 - \lambda_3^*)}{iw}$$

$$r_8 = \frac{4s\lambda_4 p_4(\lambda_2 - \lambda_4)}{iw}, \quad r_{10} = \frac{4s\lambda_5 p_5(\lambda_5 - \lambda_3)}{iw}, \quad r_{12} = \frac{4s\lambda_6 p_6(\lambda_6 - \lambda_3)}{iw}$$

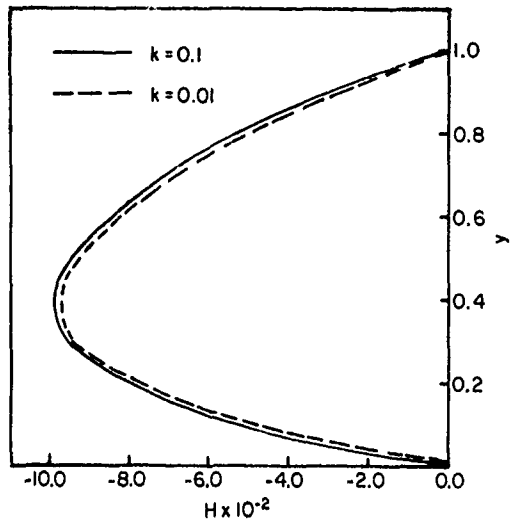

FIG. 7. The induced magnetic field is plotted against y for $s = 3.0$, $w = 2.0$, and $t = \pi$.

The values of N_i, $i = 1, 2, \ldots, 12$; $b_j^* = \Delta_j/\Delta$, $j = 1,2,3,4$; Δ_j, and Δ are given in the Appendix.

Numerical discussion

The velocity distribution is shown graphically in Figs. 1–4 for $w = 2.0$, $t = \pi$, and $\epsilon = 0.01$. For different values of the non-Newtonian parameter k, we find that the velocity increases when k decreases (see Figs. 1 and 2). That is, the effect of viscoelasticity of the fluid is to decrease the flow. Figure 3 shows that for $k = 0.1$, the velocity increases when the magnetic pressure number s decreases, while Fig. 4 shows that for $k = 0.01$ in the range $\{y : 0 \leq y \leq 0.46\}$, the velocity decreases when s increases. But in the range $\{y : 0.46 < y \leq 1\}$, the velocity increases when s decreases.

In the next step we discuss the effect of the viscoelasticity of the fluid and the magnetic-pressure number, on the induced magnetic field H taken in this research.

Figures 5–7 show that the induced magnetic field H increases when the non-Newtonian parameter k decreases, while H increases with s.

1. J. G. OLDROYD. Proc. R. Soc. London A, **200**, 523 (1950).
2. B. D. COLEMAN, W. NOLL. Arch. Rat. Mech. Anal. **6**, 355 (1960).
3. K. WALTERS. J. Mec. **1**, 479 (1962).
4. K. WALTERS. Non-Newtonian Fluid Mech. **5**, 113 (1979).
5. K. WALTERS. Second-order effect in elasticity, plasticity and fluid dynamics. Pergamon Press Ltd., Oxford. 1964. p. 507.
6. D. W. BEARD and K. WALTERS. Proc. Cambridge Phil. Soc. **60**, 667 (1964).
7. K. R. CRAMER. J. Aerospace Sci. **26**, 121 (1959).
8. P. D. VERMA and J. L. BANSAL. Proc. Indian Acad. Sci. **64**, 385 (1966).
9. P. RAMAMOORTY. J. Aerospace Sci. **29**, 111 (1962).
10. R. K. RATHY. Z. Angew. Math. Mech. **43**, 370 (1963).
11. J. B. SHUKLA. J. Phys. Soc. Jpn. **18**, 1214 (1963).
12. M. KATAGIRI. J. Phys. Soc. Jpn. **17**, 393 (1962).
13. P. K. MUHURI. J. Phys. Soc. Jpn. **18**, 1671 (1963).
14. M. BALARAM and T. GOVINDARAJULU. J. Appl. Mech. **40**, 620 (1973).
15. R. KANT. Indian J. Pure Appl. Math. **11**(4), 468 (1980).

Appendix

$$N_1 = \frac{\lambda_2^3}{2(e^{\lambda_2}-1)} - \frac{2\lambda_2^3\left(\frac{iw}{4} - \lambda_2\right)}{iw(e^{\lambda_2}-1)} + \frac{\lambda_2\lambda_3^3}{8s(e^{\lambda_2}-1)} - \frac{\lambda_2^2(2s^2e^{\lambda_2} - 5se^{\lambda_2} + e^{\lambda_2} + 3s - 1)}{8s(e^{\lambda_2}-1)^2}$$

$$N_2 = \frac{\lambda_3^3}{2(e^{\lambda_3}-1)} - \frac{2\lambda_3^3\left(\frac{iw}{4} - \lambda_3\right)}{iw(e^{\lambda_3}-1)} + \frac{\lambda_3\lambda_2^3}{8s(e^{\lambda_3}-1)} + \frac{\lambda_3^2(-2s^2e^{\lambda_3} - 5e^{\lambda_3} - se^{\lambda_3} + 1)}{8s(e^{\lambda_3}-1)^2}$$

$$N_3 = \frac{(s-1)^3}{4(e^{\lambda_2} - 1)}$$

$$N_4 = \frac{(s+1)^3}{4(e^{\lambda_3}-1)}$$

$$N_5 = \frac{-2(s-1)(e^{\lambda_4}-e^{\lambda_2})\,\lambda_3^*\left(\lambda_3^* - \frac{iw}{4}\right)}{iw(e^{\lambda_2}-1)(e^{\lambda_4}-e^{\lambda_3^*})}$$

$$N_6 = \frac{-2(s-1)(e^{\lambda_3^*}-e^{\lambda_2})\,\lambda_4^2\left(\lambda_4 - \frac{iw}{4}\right)}{iw(e^{\lambda_2}-1)(e^{\lambda_3^*}-e^{\lambda_4})}$$

$$N_7 = \frac{2(s+1)(e^{\lambda_6}-e^{\lambda_3})\,\lambda_5^2\left(\lambda_5 - \frac{iw}{4}\right)}{iw(e^{\lambda_3}-1)(e^{\lambda_6}-e^{\lambda_5})}$$

$$N_8 = \frac{2(s+1)(e^{\lambda_3}-e^{\lambda_5})\,\lambda_6^2\left(\lambda_6 - \frac{iw}{4}\right)}{iw(e^{\lambda_3}-1)(e^{\lambda_6}-e^{\lambda_5})}$$

$$N_9 = \frac{(s-1)\,[(s^3 - 2s^2 + 2s + 1)\,e^{\lambda_2} - (s+1)]}{4s^2(e^{\lambda_2}-1)^2}$$

$$N_{10} = \frac{-(s+1)\,[(s^3 + 2s^2 + 2s - 1)\,e^{\lambda_3} - (s+1)]}{4s^2(e^{\lambda_3}-1)^2}$$

$$N_{11} = \frac{-(s-1)^3}{4s(e^{\lambda_2}-1)}$$

$$N_{12} = \frac{(s+1)^3}{4s(e^{\lambda_3}-1)}$$

$$\Delta = (e_5-e_1)(e_3-e_7)(e^{\lambda_4}-e^{\lambda_5})(e^{\lambda_6}-e^{\lambda_3^*}) + (e_7-e_1)(e_3-e_7)(e^{\lambda_4}-e^{\lambda_6})(e^{\lambda_3^*}-e^{\lambda_5})$$

$$\Delta_1 = \frac{1}{Q_1-e_7Q_2}\{[e_3\,e^{\lambda_4}(Q_1-e_7Q_2) - e_7\,e^{\lambda_6}(Q_1-e_3Q_2) + Q_3(e_7-e_3)]$$

$$\times [e^{\lambda_5}(Q_1-e_7Q_2) - e^{\lambda_6}(Q_1-e_5Q_2) + Q_4(e_7-e_5)] - [e^{\lambda_4}(Q_1-e_7Q_2) - e^{\lambda_6}(Q_1-e_3Q_2)\,Q_4(e_7-e_3)]$$

$$\times [e_5\,e^{\lambda_5}(Q_1-e_7Q_2) - e_7\,e^{\lambda_6}(Q_1-e_5Q_2) + Q_3(e_7-e_5)]\}$$

$$\Delta_2 = \frac{-1}{(Q_1-e_1Q_2)}\{[e_5\,e^{\lambda_5}(Q_1-e_1Q_2) - e_1\,e^{\lambda_3^*}(Q_1-e_5Q_2) + Q_3(e_1-e_5)]$$

$$\times [(Q_1-e_1Q_2)\,e^{\lambda_6} - (Q_1-e_7Q_2)\,e^{\lambda_3} + Q_3(e_1-e_7)] - [(Q_1-e_1Q_2)\,e^{\lambda_5}$$

$$- (Q_1-e_5Q_2)\,e^{\lambda_3^*} + (e_1-e_5)Q_4]\,[Q_1-e_1Q_2)e_7\,e^{\lambda_6} - (Q_1-e_7Q_2)\,e^{\lambda_3^*} + (e_1-e_7)Q_3]\}$$

$$\Delta_3 = \frac{-1}{(e_3-e_1)}\{[-(Q_1-e_1Q_2)e_3\,e^{\lambda_4} + (Q_1-e_3Q_2)e_1\,e^{\lambda_3^*} + (e_3-e_1)Q_3]$$

$$+ [(e_3-e_1)\,e^{\lambda_6} - (e_7-e_1)\,e^{\lambda_4} + (e_7-e_3)\,e^{\lambda_3^*}] - [-(Q_1-e_1Q_2)\,e^{\lambda_4}$$

$$+ (Q_1-e_3Q_2)\,e^{\lambda_3^*} + (e_3-e_1)Q_4]\,[(e_3-e_1)e_7\,e^{\lambda_6} - (e_7-e_1)e_3\,e^{\lambda_4} + (e_7-e_3)e_1\,e^{\lambda_3^*}]\}$$

$$\Delta_4 = \frac{-1}{(e_3-e_1)}\{[(e_3-e_1)e_5\,e^{\lambda_5} - (e_5-e_1)e_3\,e^{\lambda_4} + (e_5-e_3)e_1\,e^{\lambda_3^*}]$$

$$\times [-(Q_1-e_1Q_2)\,e^{\lambda_4} + (Q_1-e_3Q_2)\,e^{\lambda_3^*} + (e_3-e_1)Q_4]\,[(e_3-e_1)\,e^{\lambda_5} - (e_5-e_1)\,e^{\lambda_4} + (e_5-e_3)\,e^{\lambda_3^*}]$$

$$\times [-(Q_1-e_1Q_2)e_3\,e^{\lambda_4} + (Q_1-e_3Q_2)e_1\,e^{\lambda_3^*} + (e_3-e_1)Q_3]\}$$

where

$$Q_1 = -(r_1+r_2+e_2+e_4+e_6+e_8)$$

$$Q_2 = -(p_1+p_2+p_9+p_{10})$$

$$Q_3 = -[(r_1+r_3)\,e^{\lambda_2} + (r_2+r_4)\,e^{\lambda_3} + (r_6+e_2)\,e^{\lambda_3^*} + (r_8+e_4)\,e^{\lambda_4} + (r_{10}+e_6)\,e^{\lambda_5} + (r_{12}+e_8)\,e^{\lambda_6}]$$

and

$$Q_4 = -[(p_1+p_7+p_9)\,e^{\lambda_2} + (p_2+p_8+p_{10})\,e^{\lambda_3} + p_3\,e^{\lambda_3^*} + p_4\,e^{\lambda_4} + p_5\,e^{\lambda_5} + p_6\,e^{\lambda_6}]$$

An integral approach to the calculation of skin friction and heat transfer in the laminar flow of a high-Prandtl-number power-law non-Newtonian fluid past a wedge

G. RAMAMURTY AND K. NARASIMHA RAO
Department of Mechanical Engineering, Osmania University, Hyderabad 500007, India
AND
K. N. SEETHARAMU
Department of Mechanical Engineering, Indian Institute of Technology, Madras 600036, India

Received November 2, 1989

An integral approach to the theoretical analysis for the skin friction of a non-Newtonian, power-law-fluid flow over a wedge is presented, when the inertia terms in the boundary-layer equations are small but need consideration. The method adopted for the solution of the equations considers an integrated average value of the inertia terms in the momentum equation. The values of the velocities and the boundary-layer thickness obtained from the hydrodynamic analysis are used for the calculation of the thermal-boundary-layer thickness. A linear velocity profile is assumed for the flow field within the thermal boundary layer as the fluids chosen for the analysis are high-Prandtl-number fluids. The results of the skin friction and the rates of the heat transfer are tabulated for a number of values of the flow behaviour index, n, varying from 0.05 to 5.0. This analysis is applicable to viscous polymer solutions having high Prandtl numbers.

On présente une approche intégrale à l'analyse du frottement de surface dans l'écoulement autour d'un coin, pour un fluide non newtonien à loi de puissance, lorsque les termes d'inertie dans les équations de la couche limite sont petits mais doivent être considérés. La méthode adoptée pour la résolution des équations considère une valeur moyenne intégrée des termes d'inertie dans l'équation de l'impulsion. Les valeurs des vitesses et de l'épaisseur de la couche limite obtenues à partir de l'analyse hydrodynamique sont utilisées pour le calcul de l'épaisseur de la couche limite thermique. On suppose un profil de vitesse linéaire pour le champ d'écoulement à l'intérieur de la couche limite thermique, étant donné que les fluides considérés dans cette analyse sont des fluides à nombre de Prandtl élevé. Les résultats concernant le frottement de surface et les vitesses de transfert de chaleur sont mis en tables pour un certain nombre de valeurs de l'indice de comportement de l'écoulement, n, variant de 0,05 à 5,0. Cette analyse est applicable aux solutions de polymères visqueux ayant des nombres de Prandtl élevés.

[Traduit par la rédaction]

Can. J. Phys. 69, 83 (1991)

1. Introduction

Non-Newtonian fluids have gained importance with the increased use of plastics, emulsions, slurries, pulp etc., which do not obey a linear relationship between the stress tensor and the deformation tensor. The behaviour of the fluids can be better described by the power-law relation

$$\tau = m\left(\frac{\partial u}{\partial y}\right)^n$$

where m stands for the consistency index, $n > 1$ for dilatant fluids, and $n < 1$ for pseudoplastic fluids. Most of the fluids, nevertheless, are non-Newtonian in behaviour.

Kubair and Pei (1) studied the theoretical combined laminar-free and forced-convection heat transfer to non-Newtonian fluids in external flows. Chen and Radulovic (2) presented an analysis of steady forced-convection heat transfer in the incompressible, laminar-boundary-layer flow of power-law fluids past wedges having a step change in the wall temperature.

Gorla (3) carried out an analysis of the transient thermal response of a power-law non-Newtonian fluid over a wedge with a step change in the surface temperature.

Acrivos and Shah (4) presented a theoretical analysis of the laminar flow past arbitrary surfaces for non-Newtonian fluids of power-law variation. The problem, of predicting the drag and rate of heat transfer from an isothermal surface was considered. Inspectional analysis of the modified boundary-layer equations yield a general relationship for both the drag coefficient and for the Nusselt numbers as functions of the generalized Reynolds and Prandtl numbers. The numerical study of the flow past a horizontal plate is included. The shear stress coefficients $c(n)^*$ and $c(n)^{**}$, obtained from the exact analysis and the Acrivos analysis, respectively, were tabulated and compared. This paper has improved upon the values of $c(n)^{**}$ and used the improved values for the calculation of the hydrodynamic boundary-layer thickness, which ultimately leads to the calculation of heat-transfer rates.

Chen (5) suggested a new approach, based on the two-region model, to analyse the heat-transfer problems of a laminar flow of a Newtonian fluid passing a wedge at small Prandtl numbers.

2. Analysis

Boundary-layer equations are usually applied to the flow problems where the Reynolds number is large. The local Reynolds number can be written as

$$(Re)_x = \left[\frac{\rho U_\infty^{2-n} x^n}{m}\right]$$

On perusal of the above equation, the following inferences can be drawn (4):

(*i*) If $n < 2$, the Reynolds number is large provided U_∞ is sufficiently large.
(*ii*) If $n > 2$, the Reynolds number is large only when U_∞ is sufficiently small.

Hence the boundary layer equations can be applied to non-Newtonian fluid-flow problems provided the above conditions

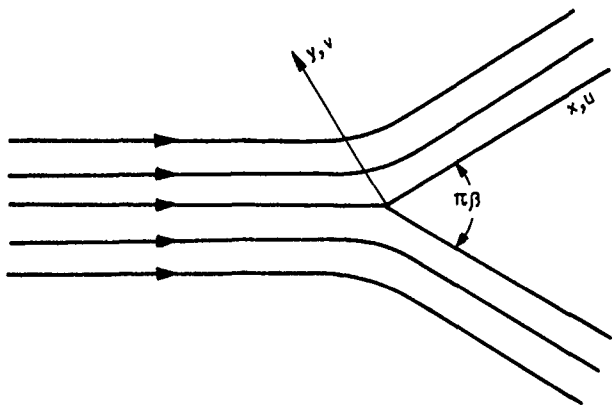

FIG. 1. Configuration of wedge flow.

are satisfied. For moderate values of U_∞, the inertial terms, though small in the boundary layer equations, require inclusion in the analysis. In this situation where the inertial terms are small but warrant consideration in the boundary-layer equations, the present analysis is carried out to obtain the solution for the skin friction and the heat-transfer rate.

For a constant-property fluid, with the steady-state laminar flow over a wedge with body forces neglected, Fig. 1, the governing equations are as follows:

Continuity equation

$$[1] \quad \frac{\partial u}{\partial x} + \frac{\partial v}{\partial y} = 0$$

Momentum equation

$$[2] \quad u\frac{\partial u}{\partial x} + v\frac{\partial u}{\partial y} = U_\infty \frac{dU_\infty}{dx} + \frac{m}{\rho}\frac{\partial}{\partial y}\left[\left(\frac{\partial u}{\partial y}\right)^n\right]$$

Boundary conditions

$$[3] \quad \begin{aligned} &y = 0, \qquad u = v = 0 \\ &y = \delta, \qquad u = U_\infty = Cx^M, \qquad \frac{\partial u}{\partial y} = 0 \end{aligned}$$

Assuming the inertial forces to be small, the momentum equation can be modified by including the integrated average value of the inertial term over the boundary-layer thickness.

$$[4] \quad \left[\frac{\rho}{m\delta}\int_0^\delta \left(u\frac{\partial u}{\partial x} + v\frac{\partial u}{\partial y}\right) dy\right] - \frac{\rho}{m}U_\infty\frac{dU_\infty}{dx} = \frac{\partial}{\partial y}\left[\left(\frac{\partial u}{\partial y}\right)^n\right]$$

To facilitate the mathematical analysis, we define the new independent variable as $Y = \delta - y$ and dependent variable as $V = -v$

We get

$$dy = -dY, \qquad \frac{\partial u}{\partial Y} = -\frac{\partial u}{\partial Y}, \qquad \frac{\partial v}{\partial y} = \frac{\partial V}{\partial Y}$$

In terms of the new variables, [1] and [4] can be transformed to

$$[5] \quad \frac{\partial u}{\partial x} + \frac{\partial V}{\partial Y} = 0$$

$$[6] \quad \left[-\frac{\rho}{m\delta}\int_0^\delta \left(u\frac{\partial u}{\partial x} + V\frac{\partial u}{\partial Y}\right) dY\right] + \frac{\rho}{m}U_\infty\frac{dU_\infty}{dx} = \frac{\partial}{\partial Y}\left[\left(-\frac{\partial u}{\partial y}\right)^n\right]$$

along with boundary conditions:

$$\begin{aligned} &\text{At } Y = 0, \qquad u = U_\infty, \qquad \frac{\partial u}{\partial Y} = 0 \\ &\text{At } Y = \delta, \qquad u = V = 0 \end{aligned}$$

The integral expression on the left-hand side of [6] is a function of x on integration with respect to Y. The second term is also a function of x since $U_\infty = Cx^M$. Therefore, the left-hand side of [6] is a function of x only.

Let

$$[7] \quad \left[-\frac{\rho}{m\delta}\int_0^\delta \left(u\frac{\partial u}{\partial x} + V\frac{\partial u}{\partial Y}\right) dY\right] + \frac{\rho}{m}U_\infty\frac{dU_\infty}{dx} = \psi_1(x)$$

and hence

$$[8] \quad \frac{\partial}{\partial Y}\left[\left(-\frac{\partial u}{\partial Y}\right)^n\right] = \psi_1(x)$$

Integrating [8] with respect to Y and using transformed boundary conditions, it can be shown that

$$\left(-\frac{\partial u}{\partial y}\right)^n = [\psi_1(x)]\,Y$$

$$u = -[\psi_1(x)]^{1/n} \cdot \frac{n}{1+n}(Y)^{(1+n)/n} + U_\infty$$

and

$$\psi_1(x) = \left[\frac{1+n}{n}\frac{U_\infty}{\delta^{(1+n)/n}}\right]^n$$

hence

$$[9] \quad u = U_\infty\left[1 - \left(\frac{Y}{\delta}\right)^{(1+n/n}\right]$$

and from the continuity equation [5]

TABLE 1. A comparison of the values of $c(n)$ for different n using three different methods

n	This work $c(n)$	Acrivos results $c(n)$**	Exact solutions $c(n)$*	Deviation of present results from exact solution (%)	Deviation of Acrivos results from exact solution (%)
0.05	0.9621	0.926	1.107	5.39	8.9
0.1	0.9198	0.860	0.969	0.507	11.2
0.2	0.8312	0.75	0.8725	4.74	14.0
0.3	0.7456	0.655	0.7325	1.78	7.75
0.5	0.5954	0.5180	0.5755	3.97	9.99
1.0	0.3631	0.323	0.332 06	9.34	2.7
1.5	0.2453	0.238	0.2189	12.06	8.7
2.0	0.1778	0.169	0.1612	10.30	4.8
2.5	0.1363	0.133	0.1266	11.17	8.4
3.0	0.1088	0.109	0.097 06	12.09	12.3
4.0	0.0757	0.079	0.067 77	11.70	16.69
5.0	0.0569	0.061	0.051 11	11.32	19.3

$$[10]\quad V = -U_\infty \frac{d\delta}{dx} \times \left[\frac{n}{(1+2n)} + \frac{(Y)^{(1+2n)/n}}{\delta^{(1+2n)/n}} \cdot \frac{(1+n)}{(1+2n)} - \frac{(Y)^{(1+n)/n}}{\delta^{(1+n)/n}} \right] - \frac{dU_\infty}{dx} \left[-\delta \frac{(1+n)}{1+2n} + Y - \frac{n}{(1+2n)} \frac{(Y)^{(1+2n)/n}}{\delta^{(1+n)/n}} \right]$$

Transforming the above equations into the original variables u, v and x, y

$$[11]\quad u = U_\infty \left[1 - \left(\frac{\delta - y}{\delta} \right)^{(1+n)/n} \right]$$

$$[12]\quad v = U_\infty \frac{d\delta}{dx} \times \left[\frac{n}{1+2n} + \frac{(\delta - y)^{(1+2n)/n}}{\delta^{(1+2n)/n}} \frac{(1+n)}{(1+2n)} - \frac{(\delta - y)^{(1+n)/n}}{\delta^{(1+n)/n}} \right] + \frac{dU_\infty}{dx} \left[\delta \frac{n}{1+2n} - y - \frac{n}{(1+2n)} \frac{(\delta - y)^{(1+2n)/n}}{\delta^{(1+n)/n}} \right]$$

Hydrodynamic boundary-layer thickness can be calculated from [4], [11], and [12] as

$$[13]\quad \delta = A^{1/(1+n)} (Re)_x^{-1/(1+n)} \cdot x$$

where

$$[14]\quad (Re)_x = \left[\frac{\rho U_\infty^{2-n} x^n}{m} \right]$$

$$[15]\quad A = \frac{(1+n)^n (1+2n) (2+3n)}{n^{1+n} [2M (1+3n) + 1]}$$

The skin-friction coefficient is given by

$$c_f = \frac{\tau_w}{\rho U_\infty^2} = m \left(\frac{\partial u}{\partial y} \right)^n \Big|_{y=0}$$

$$[16]\quad c_f = c(n) \cdot (Re)_x^{-1/(1+n)}$$

$$[17]\quad c(n) = \left[\frac{(1+n) [2M (1+3n) + 1]}{(1+2n) (2+3n)} \right]^{n/(1+n)}$$

3. Comparison

3.1. Hydrodynamic boundary-layer thickness

For a Newtonian fluid ($n = 1$) flowing over a flat plate with zero angle of incidence ($M = 0$), from [13], [14], and [15] we find that $\delta = \dfrac{5.47\,x}{\sqrt{(Re)_x}}$ compared with a value of $\delta = \dfrac{4.96\,x}{\sqrt{(Re)_x}}$ from the Blasius–Howarth solution (6).

Skin friction

$$\frac{c_f}{(Re)_x^{1/(1+n)}} = c(n)$$

The value of $c(n)$ for different values of n are tabulated and compared with:

$c(n)$*: Values from a similar analysis (exact analysis) (4) for a flat plate ($M = 0$)

$c(n)$**: Values from the Pohlhausen method as tabulated by Acrivos (4).

The method followed by Acrivos (4) is the integral method using a third-order velocity profile for the calculation of the $c(n)$** values, which give the shear-stress coefficients.

The comparison shown in Table 1 indicates that the present analysis gives values very close to the exact analysis except for

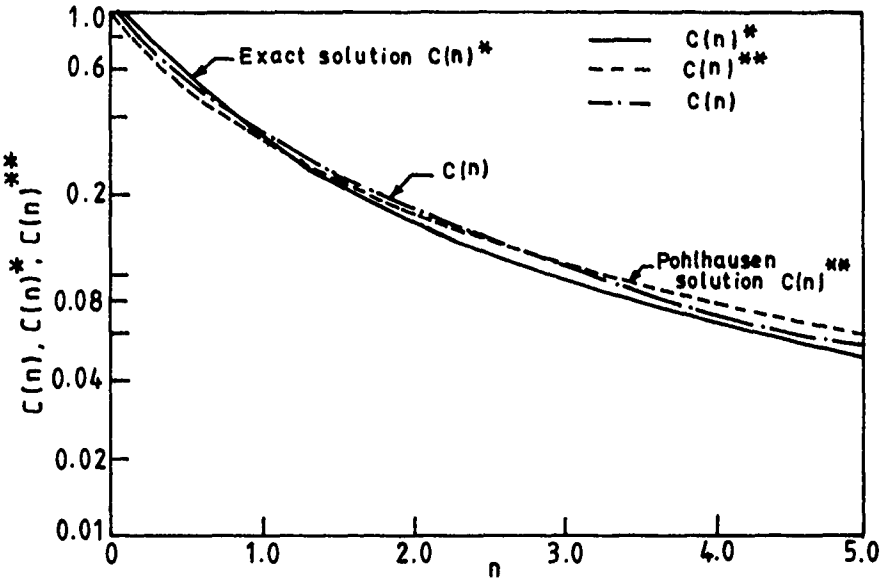

FIG. 2. Comparison of different methods.

TABLE 2. Values of $c(n)$ for different values of the wedge-angle parameter M

	$c(n)$		
n	$M = 0.1892$	$M = 0.3333$	$M = 1.0000$
0.05	0.9788	0.9885	1.0184
0.1	0.9538	0.9735	1.0334
0.3	0.5448	0.9005	1.0708
0.5	0.7471	0.8298	1.0874
1.0	0.5789	0.6992	1.0954
2.0	0.4215	0.5652	1.0817
3.0	0.3520	0.5013	1.0674
5.0	0.2899	0.4409	1.0488

four values near $n = 1.0$. The method is better than the Pohlhausen integral method carried out by Acrivos. The comparison is graphically represented in Fig. 2.

Values of $c(n)$ for different values of the wedge-angle parameter M are also tabulated (Table 2).

4. Heat-transfer analysis

Since high-Prandtl-number fluids are chosen for this analysis, the velocity profile within the thermal boundary layer can be approximated by a linear velocity profile for u, which is justified by the fact that the thermal boundary-layer thickness Δ is small compared with the hydrodynamic boundary-layer thickness δ.

Hence by linearizing the velocity equation [11]

$$[18] \quad u = U_\infty \left(\frac{1+n}{n}\right)\left(\frac{y}{\delta}\right), \qquad \because \Delta \ll \delta$$

From the continuity equation [1] and [18]

$$[19] \quad v = \left[U_\infty \frac{1+n}{n}\frac{1}{\delta^2}\frac{d\delta}{dx} - \frac{1+n}{n}\frac{1}{\delta}\frac{dU_\infty}{dx} \right]\frac{y^2}{2}$$

For a constant-property fluid and in the absence of viscous dissipation, the energy equation is

$$[20] \quad u\frac{\partial t}{\partial x} + v\frac{\partial t}{\partial y} = \alpha\frac{\partial^2 t}{\partial y^2}$$

Following a similar method adopted in the momentum equation [4], [20] can be modified by including the integrated average value of the convective term over the thermal boundary-layer thickness Δ.

$$[21] \quad \frac{1}{\alpha\Delta}\int_o^\Delta \left(u\frac{\partial t}{\partial x} + v\frac{\partial t}{\partial y}\right) dy = \frac{\partial^2 t}{\partial y^2}$$

On integration with respect to y, the left-hand side of the above equation is a function of only x.

Let

$$[20] \quad \frac{1}{\alpha\Delta}\int_o^\Delta \left(u\frac{\partial t}{\partial x} + v\frac{\partial t}{\partial y}\right) dy = \psi_2(x)$$

hence

$$[23] \quad \frac{\partial^2 t}{\partial y^2} = \psi_2(x)$$

The boundary conditions are

$$[24] \quad \begin{aligned} &\text{At } y = 0, && t = t_w \\ &\text{At } y = \Delta, && t = t_\infty, \quad \frac{\partial t}{\partial y} = 0 \end{aligned}$$

Integrating [23] with respect to y and using the boundary conditions

$$[25] \quad \frac{t - t_w}{t_\infty - t_w} = \left[\frac{2y}{\Delta} - \frac{y^2}{\Delta^2}\right]$$

gives the temperature distribution.

Using [25] in [21] and solving for thermal boundary-layer thickness

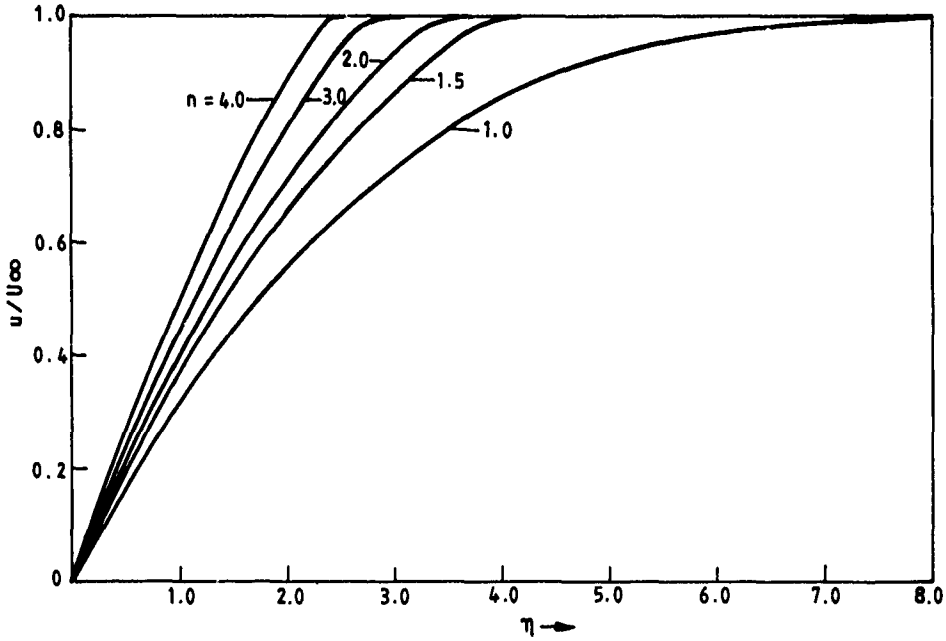

FIG. 3. Velocity profile for flat plate for dilatant fluids.

TABLE 3. Values of $(CT)_x$ and $(CT)_L$ for different values of the wedge-angle parameter M and n

	$(CT)_x$				$(CT)_L$			
n	$M=0.0$	$M=0.1892$	$M=0.3333$	$M=1.0$	$M=0.0$	$M=0.1892$	$M=0.3333$	$M=1.0$
0.05	0.3773	0.4861	0.5607	0.8546	0.5798	0.7470	0.8616	1.3132
0.1	0.3745	0.4810	0.5538	0.8383	0.5885	0.7559	0.8702	1.3713
0.3	0.3718	0.4727	0.5391	0.7904	0.6304	0.8015	0.9142	1.3402
0.5	0.3757	0.4735	0.5349	0.7594	0.6763	0.8523	0.9628	1.3669
1.0	0.3933	0.4859	0.5376	0.7148	0.7867	0.9719	1.0752	1.4295
2.0	0.4274	0.5116	0.5508	0.6754	0.9617	1.1510	1.2392	1.5198
3.0	0.4528	0.5295	0.5610	0.6572	1.0867	1.2707	1.3463	1.5773
5.0	0.4861	0.5509	0.5735	0.6397	1.2499	1.4167	1.4748	1.6449

$$[26]\quad \Delta = \delta \left[\frac{72\,n}{(2n + 3M + 1)\,A^{2/(1+n)}} \right]^{1/3} \cdot \left[\frac{1}{Pr} \right]^{1/3}$$

Where

$$[27]\quad Pr = \left[\frac{\rho\, c_p\, U_\infty\, x}{K} \right] \left[\frac{m}{\rho\, U_\infty^{2-n} \cdot x^n} \right]^{2/(1+n)}$$

Heat transfer

$$[28]\quad q_w = -K A_n \left. \frac{\partial t}{\partial y} \right|_{y=0} = h A_n (t_w - t_\infty)$$

$$[29]\quad \frac{(NU)_x}{(Pr)^{1/3}\,(Re)_x^{1/(1+n)}} = (CT)_x = 2 \left[\frac{(2n + 3M + 1)}{72 \cdot n \cdot A^{1/(1+n)}} \right]^{1/3}$$

The average Nusselt number is

$$[30]\quad (NU)_L = (CT)_L\,(Pr)_L^{1/3}\,(Re)_L^{1/(1+n)}$$

$$[31]\quad (CT)_L = \frac{3\,(1+n)}{2+n}\,(CT)_x$$

5. Comparison with a Newtonian fluid flowing over a flat plate

For a Newtonian fluid ($n = 1$) flowing over a flat plate ($M = 0$) from [26] we find $\Delta/\delta = 0.929\ (Pr)^{-1/3}$ as compared with the value obtained by using the Pohlhausen method $\Delta/\delta = 0.976(Pr)^{-1/3}$, which is close even though the analysis is based on a high-Prandtl-number assumption (linear-velocity profile in the thermal boundary layer) and $(CT)_x = 0.393$ as compared with a value of 0.332 when the Pohlhausen method is used. The error is 18% owing to a high-Prandtl-number assumption in the analysis. As the Prandtl number increases the error reduces. The value of $(CT)_x$ and $(CT)_L$ for different values of M and n are tabulated in Table 3.

6. Discussion

From the tabulated values and graphical representation the following are noted:

The trend of velocity profiles (Figs. 3,4) is similar to the one observed by Acrivos [4]. For dilatant fluids (Fig. 3), the hydrodynamic boundary-layer thickness decreases with increase in the flow behaviour index, n and the reverse trend is observed in the velocity gradient at the surface. For pseudoplastic fluids with $n = 0.1$, the hydrodynamic boundary-layer thickness is

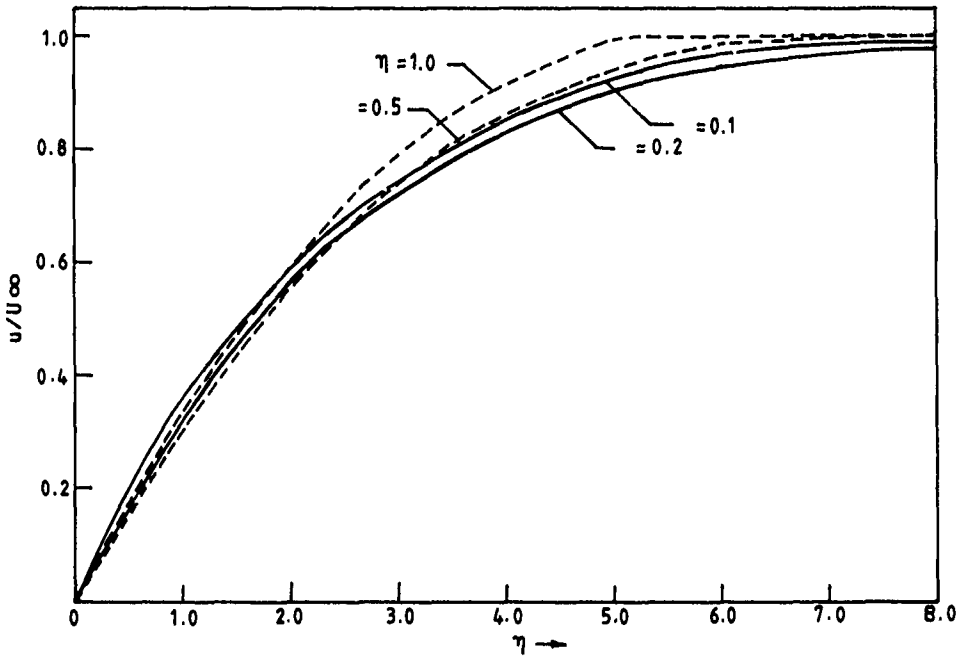

FIG. 4. Velocity profile for flat plate for pseudoplastic fluids.

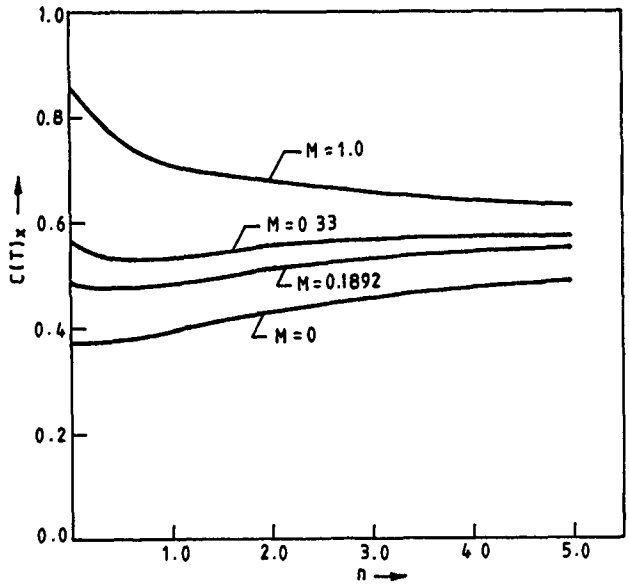

FIG. 5. Heat-transfer results.

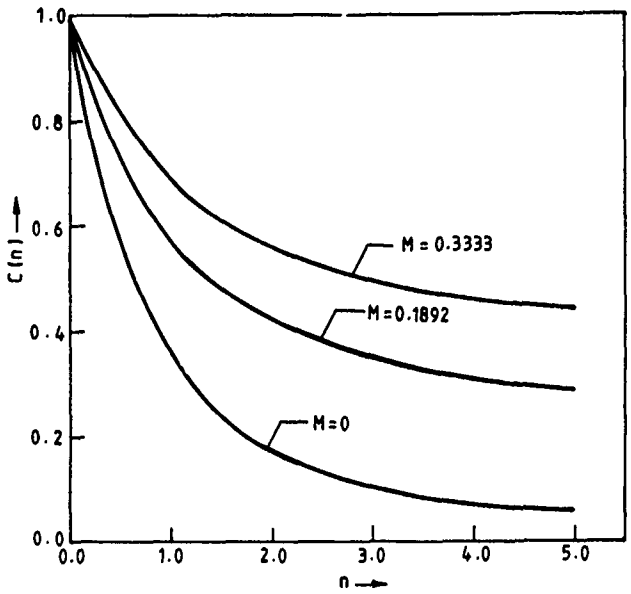

FIG. 6. Skin-friction results.

found to be larger than the boundary-layer thickness for a fluid with $n = 0.5$, even though the velocity gradient at the plate for a fluid with $n = 0.1$ is greater than the velocity gradient of a fluid with $n = 0.5$. The thermal boundary layer is proportional to $(Pr)^{-1/3}$. This is in conformity with earlier work; see pages 480–483 of ref. 6. The heat-transfer rate increases with the increase in the value of M for a given value of n, Pr, and Re (Fig. 5). For a given value of M, Pr, and $(Re)_x$ the change of the heat-transfer rate is greater in the pseudoplastic-fluid range than in the dilatant-fluid range (Fig. 5).

Skin friction increases with increase in wedge-angle parameter M for a given value of n and Re (Fig. 6).

The results obtained for skin friction (Fig. 2) give accurate values except at four points near $n = 1.0$, the maximum percentage of error is 12.1% as against the error of 19% when the Pohlhausen method is used for the flow over a flat plate. For $n = 0.3$ the highest accuracy obtained is within 1.7% of the exact value (Table 1).

The results of thermal boundary-layer thickness are of sufficient accuracy and hence the heat-transfer rates are sufficiently accurate for engineering applications. The thermal boundary-layer thickness is proportional to $(Pr)^{-1/3}$. As the Prandtl number increases, the error in heat-transfer values will reduce. Hence the results are valid for Prandtl numbers greater than 5.

7. Conclusions

(*i*) Rapid calculation of the skin friction and heat transfer are possible with the help of tabulated values of $c(n)$ and $(CT)_L$ for

different configurations of a wedge with non-Newtonian fluids, more so for Newtonian fluids.

(*ii*) The calculation of the skin friction and the Nusselt number can be done on a desk calculator and the large amount of computer time necessary for the computation of values in the exact analysis can be avoided.

(*iii*) The results obtained for the shear-stress coefficient $c(n)$ by the present method are in the acceptable range. These values are closer to the values obtained from the exact analysis than those reported by Acrivos (4) for the range of fluid behaviour index, n, below 1 and above 3.

(*iv*) The method presented here is observed to be valid for the calculation of heat-transfer rates in the range of Prandtl numbers from 10 to 300. The percentage error in the heat-transfer-rate values decreases with the increase in the Prandtl numbers owing to the fact that the hydrodynamic boundary thickness is much larger compared with the thermal boundary-layer thickness in the high-Prandtl-number range. This leads to the justification of the assumption of the linear velocity profile adopted in the thermal boundary-layer region. Hence, the results obtained recommend the present method to calculate the heat-transfer rates in the higher range of Prandtl numbers, i.e., above 300.

1. V. G. Kubair and D. C. T. Pei. Int. J. Heat Mass Transfer, **11**, 855 (1968)
2. J. L. S. Chen and P. T. Radulovic. J. Heat. Transfer, **95**, 498 (1973).
3. R. S. R. Gorla. J.A.I. Chem. Eng. **28**, 56 (1982).
4. A. Acrivos and M. J. Shah. J.A.I. Chem. Eng. **6**, 312 (1960).
5. Ye-Mon-Chen. Int. J. Heat Mass Transfer, **28**, 1517 (1985).
6. J. G. Knudsen and L. K. Donald. Fluid dynamics and heat transfer. McGraw-Hill Book Company, Inc., New York. 1958.

List of symbols

A $\dfrac{(1+n)^n\,(1+2n)\,(2+3n)}{n^{1+n}\,[2M\,(1+3n)\,+\,1]}$

A_n Area normal to the direction of heat flow

C Constant

$(CT)_x$ $\dfrac{(NU)_x}{[(Pr)^{1/3}\,(Re)_x^{1/(1+n)}]}$, coefficient for the calculation of the local Nusselt number

$(CT)_L$ $\dfrac{3\,(1+n)\,(CT)_x}{(2+n)}$, coefficient for the calculation of the average Nusselt number

K Thermal conductivity

L Length of the plate

M Wedge-angle parameter, $\dfrac{\beta}{2-\beta}$

$(NU)_x$ Local Nusselt number

Pr Modified Prandtl number, $\dfrac{U_\infty x}{\alpha}\left[\dfrac{1}{(Re)_x}\right]^{2/(1+n)}$

$(Re)_x$ Local Reynolds number, $\left[\dfrac{\rho\,C^{2-n}\,x^{M(2-n)\,+\,n}}{m}\right]$

U_∞ Free stream velocity, Cx^M

c_f Skin friction coefficient

c_p Specific heat at constant pressure

$c(n)$ $\dfrac{c_f}{(Re)_x^{1/(1+n)}}$, shear stress coefficient

$c(n)^*$ Values of $c(n)$ from exact analysis

$c(n)^{**}$ Values of $c(n)$ from Acrivos

h Heat transfer coefficient

m Consistency index

n Flow behaviour index

q_w Rate of heat transfer at the wall

q_w'' Heat flux at the wall

t Temperature of the fluid

t_w Surface temperature

t_∞ Free stream temperature

u Velocity of fluid in the x direction

v Velocity of fluid in the y direction

x x coordinate

y y coordiante

Greek symbols

α Thermal diffusivity, $k/\rho c_p$

$\pi\beta$ Included angle of the wedge

Δ Thermal boundary-layer thickness

δ Hydrodynamic boundary-layer thickness

η A function of x and y, $\left[\dfrac{y}{x^{1/(1+n)}}\right](Re)_L^{1/(1+n)}$

ρ Density of the fluid

τ Shear stress

τ_w Wall shear stress

$\psi_1(x)$ A function of x used in momentum equation

$\psi_2(x)$ A function of x used in energy equation

Study of the radioactive decays of ^{140}Ba and ^{140}La

BAKHSHISH CHAND, JATINDER GOSWAMY, DEVINDER MEHTA, NIRMAL SINGH, AND P. N. TREHAN[1]
Department of Physics, Panjab University, Chandigarh 160014, India

Received June 20, 1990

The intensities of X rays and γ rays from the decays of ^{140}Ba and ^{140}La were measured precisely using Si(Li) and HPGe detectors. The *L* X-ray intensities in ^{140}Ba decay are reported for the first time. The conversion electrons from these decays are investigated using a mini-orange electron spectrometer. The electron intensities for the (*M* + *N*.) conversion of 329, 487, 1596, and 1903 keV transitions in ^{140}Ce were measured for the first time. From the present conversion-electron and γ-ray intensities, the conversion coefficients for various transitions in ^{140}La and ^{140}Ce were determined. Also, the γ–γ directional correlations for 15 cascades in ^{140}Ce were studied using a HPGe–HPGe detector coincidence setup (time resolution = 7 ns). The 109–(329)– 487, 131–242, and 131–266 keV cascades in ^{140}Ce were studied for the first time. The multipole mixing ratios for the 109, 131, 242, 266, 329, 432, 487, 751, 816, 868, 919, 925, and 951 keV transitions in ^{140}Ce are deduced from the present directional correlation and conversion-coefficient measurements.

On a mesuré avec précision, en utilisant des détecteurs Si(Li) et HPGe, les intensités des rayons X et des rayons γ provenant des désintégrations de ^{140}Ba et ^{140}La. Les intensités des rayons X *L* dans la désintégration de ^{140}Ba sont rapportées pour la première fois. Les électrons de conversion provenant de ces désintégrations ont été étudiés en utilisant un spectromètre à électrons mini-orange. Les intensités électroniques pour la conversion (*M* + *N*) des transitions de 329, 487, 1596 et 1903 keV dans ^{140}Ce ont été mesurées pour la première fois. A partir de ces mesures des intensités d'électrons de conversion et de rayons γ, on a déterminé les coefficients de conversion pour diverses transitions dans ^{140}La et ^{140}Ce. On a aussi étudié les corrélations directionnelles γ–γ pour 15 cascades dans ^{140}Ce, en utilisant un arrangement de détecteurs HPGe–HPGe en coïncidence (résolution temporelle = 7 ns). Les cascades 109–(329)–487, 131–242 et 131–266 keV dans ^{140}Ce ont été étudiées pour la première fois. Les rapports de mélange multipolaire pour les transitions de 109, 131, 242, 266, 329, 432, 487, 751, 816, 866, 919, 925 et 951 keV dans ^{140}Ce ont été déduits des mesures de corrélation directionnelle et de coefficients de conversion.
[Traduit par la rédaction]

Can. J. Phys. 69, 90 (1991)

1. Introduction

The radionuclides ^{140}Ba ($T_{1/2}$ = 12.7 d) and ^{140}La ($T_{1/2}$ = 1.68 d) undergo β^- decay to the excited states of ^{140}La and ^{140}Ce, respectively. These excited states de-excite through the competing γ emission and internal conversion process. The study of the precise energy and intensity of the emitted γ rays and conversion electrons provides information on the nuclear levels. For a better understanding of subsequent atomic processes, there is a need for the measurement of the intensities of the X rays emitted following these decays. The level structure of ^{140}La and ^{140}Ce from the above mentioned decays has been extensively investigated by many research workers (1–18). These studies include the measurements of energies and intensities of γ rays (1–10), conversion electrons (5, 10), and multipole-mixing ratios (9–14) for the various transitions involved in these decays. Some conclusions about the excited states of ^{140}La and ^{140}Ce have also been drawn from reaction work (15, 16) and model calculations (17, 18). In spite of these investigations, uncertainties regarding the following features in these decays still prevail.

In ^{140}Ba decay, the earlier-measured intensities (2–4) for weak and low-energy γ rays are either available sparsely or found to be inconsistent. Recently, Adam *et al.* (10) measured the intensities of *K* X rays, γ rays, and conversion electrons from this decay and reported a new γ transition of 551.2 keV, which de-excites the 581 keV level and still needs to be confirmed. Kalinnikov *et al.* (4) measured the *K* X-ray and γ-ray intensities from ^{140}Ba decay using a poor energy-resolution Ge(Li) detector (resolution = 3.2 keV at 537.3 keV). The *K* X-ray intensities measured by them are found to be significantly higher than the evaluated results (19). To the best of our knowledge, no report of measured *L* X-ray intensities from the ^{140}Ba decay is available in the literature.

In the ^{140}La decay, γ-ray intensities have been reported by many workers (5–10). The available intensities for a few weak γ rays have been found to be inconsistent. Kaur *et al* (9) observed a new γ ray at 1303.5 keV and also proposed a new level at 3000.7 keV in ^{140}Ce. Adam *et al.* (10) reported new γ rays of energy 992.9 and 1877.3 keV and proposed three levels at 3394.9, 3473.6, and 3520.8 keV to fit the newly observed γ rays. The existence and placement of these γ rays and energy levels still needs to be confirmed. Also, the *K* X-ray intensities measured by Kalinnikov *et al.* (7) are significantly higher than the evaluated results (19).

Karlsson *et al.* (5) measured the intensities of conversion electrons from the ^{140}La decay using a double-focusing electron spectrometer, and the directional correlation measurements for different cascades in ^{140}Ce have been reported by many workers (9–14) using NaI (Tl) and Ge(Li) detector coincidence setups. The multipole mixing ratios of some of the transitions and the spin of the 2516 keV level in ^{140}Ce, determined on the basis of directional correlation and conversion-coefficient measurements by earlier workers, are found to be controversial.

In view of the above, it was thought worthwhile to reinvestigate the level structure of ^{140}La and ^{140}Ce precisely. The present work includes the intensity measurements of X rays and γ rays using well-calibrated high-resolution Si(Li) and HPGe detectors. We had a particular interest in investigating weak and low-energy γ rays. The conversion-electron spectra were studied using a mini-orange electron spectrometer. Also, γ–γ directional correlation measurements for various cascades in ^{140}Ce were carried out using a HPGe–HPGe detectors coincidence setup that had better energy and time resolution than those

[1]Author to whom correspondence should be addressed.

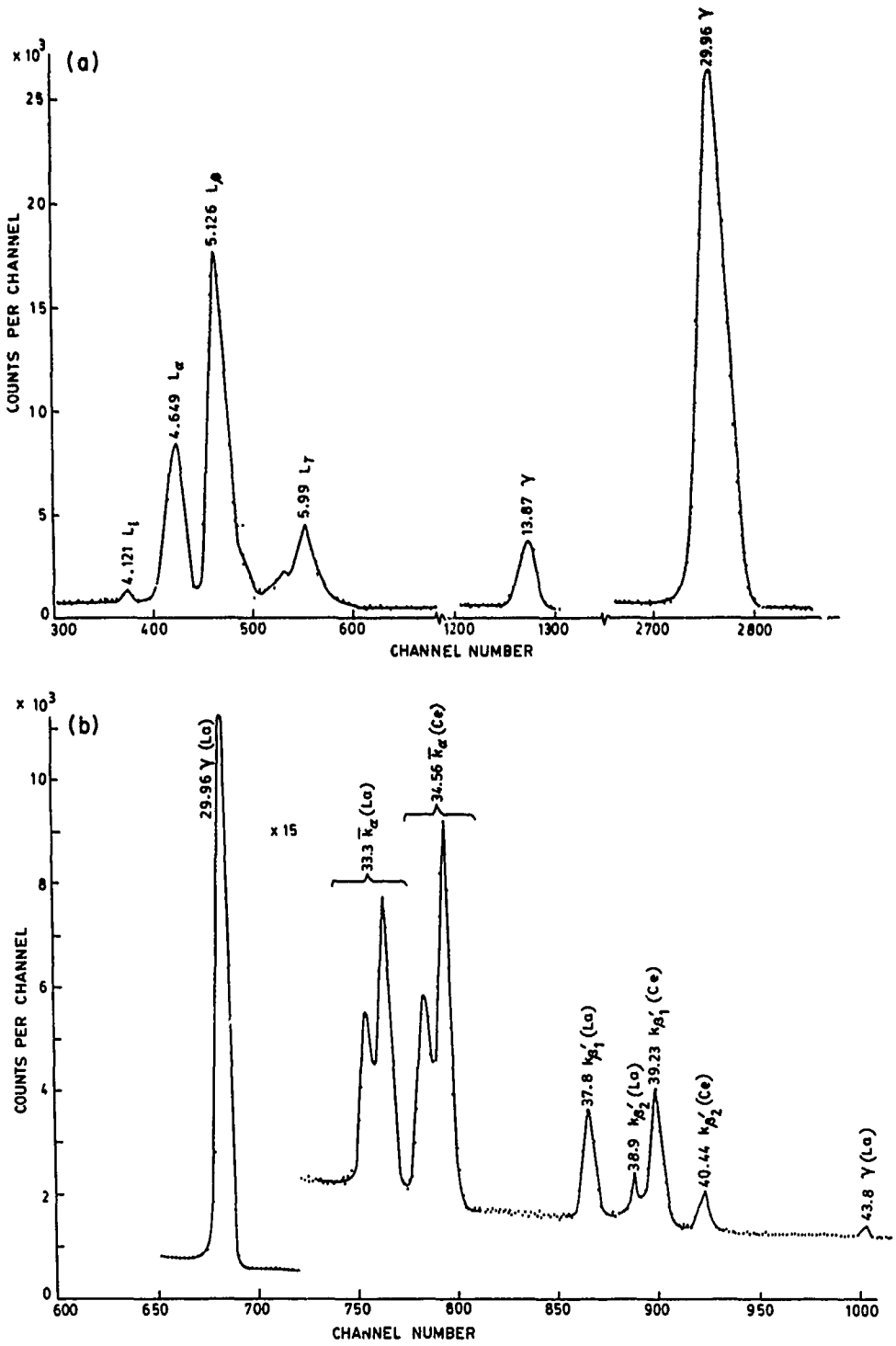

FIG. 1. Typical spectrum of ^{140}Ba decay: (*a*) The *L* X-ray part taken with the Si(Li) detector and (*b*) The *K* X-ray part taken with vertical HPGe detector.

used by previous workers (9–14). From these measurements, it has been possible to determine the multipole-mixing ratios of 13 transitions in ^{140}Ce.

2. Experimental methods and results

2.1. X-ray and γ-ray intensity measurements

The radioactive liquid sources of ^{140}Ba and ^{140}La in dilute HCl were obtained from Bhabha Atomic Research Centre, Bombay, India. Thin uncovered sources were prepared by drying the respective source solutions on Mylar backing for the measurements of X rays and low-energy γ rays. The count rates for these sources were kept at about 250 counts s^{-1} with the vertical HPGe and Si(Li) detectors. For intensity measurements of γ rays above 80 keV, the strength of the sources were so adjusted that they provided about 1200 counts s^{-1} when placed at a distance of 25 cm from the coaxial HPGe detectors.

The present X-ray and γ-ray intensity measurements were

performed using a set of four semiconductor detectors; a horizontal planar Si(Li) detector (active volume = 28.27 mm^2 × 5.5 mm; FWHM = 165 eV at 5.9 keV), a vertical planar HPGe detector (active volume = 28.27 mm^2 × 5.0 mm; FWHM = 459 eV at 122 keV) and two coaxial HPGe detectors (active volumes = 57.1 cm^3 and 96.0 cm^3; FWHM = 1.7 keV at 1332 keV). These detectors were coupled to an 8K-channel analyser (ND 66B) through a spectroscopy amplifier (ORTEC 572).

The efficiency calibration curves for the coaxial HPGe detectors in the energy region 80–4000 keV, for the vertical planar HPGe detector in the energy region 20–600 keV, and for the Si(Li) detector in the energy region 4–90 keV were generated using standard radioactive sources as described in our earlier papers (20, 21).

Ten spectra were taken with each source and detector combination, for the time duration 25 000–150 000 s, which depended upon the counting statistics. The spectra in the X-ray regions were analyzed by adding the counts under the peaks, and background counts were subtracted by extrapolating the background counts above and below the peak region. The X-ray spectrum from the successive decay of $^{140}Ba \rightarrow {}^{140}La \rightarrow {}^{140}Ce$ obtained with Si(Li) and vertical HPGe detectors is shown in Fig. 1. It is clear from Fig. 1*b* that the *K* X rays from two decays are well separated except that the K_{β_2} peak of ^{140}La overlaps the K_{β_1} peak of ^{140}Ce. The area of K_{β_2} peak of ^{140}La was obtained by subtracting the area of the K_{β_1} peak of ^{140}Ce (measured from the ^{140}La decay separately) from the total area of the [K_{β_2} (La) + K_{β_1} (Ce)] peak. The contributions to the different *L* X rays from the ^{140}Ba decay due to *L* X rays from the ^{140}La decay were subtracted by using the intensity results from ref. 19 and were found to be less than 2%.

The γ-ray spectra were analyzed to obtain the area of different γ-ray peaks using the computer program SAMPO (22).

TABLE 1. Summing corrections for certain weak cross-over γ rays from ^{140}Ba and ^{140}La decays with a 96.0 cm^3 HPGe detector

γ ray (keV)	Summing γ rays ($\gamma_1 + \gamma_2$)	Estimated summing area ($\gamma_1 + \gamma_2$)	Observed area γ_3	%Summing correction
		^{140}Ba		
467.6	304.9+162.7	0.041	0.081(12)	−50.6%
		^{140}La		
1924.6	328.7+1596.2	0.018	0.031(2)	−58.1%
2083.2	487.0+1596.2	0.034	0.070(4)	−48.6%
2464.9	868.7+1596.2	0.0019	0.0089(9)	−21.3%

The areas of various cascading and cross-over γ rays were corrected for summing, using the formulation suggested by Gehrke *et al.* (8). The total efficiency curves for the coaxial HPGe detectors, required for an estimation of summing corrections, were obtained from the knowledge of the absorption coefficients for γ rays in germanium and the size of the detectors (23). The summing corrections in the case of measurements done using a 96.0 cm^3 coaxial HPGe detector, for example, are found to be 0.14 and 0.22% for the 162.7 and 304.9 keV γ rays in the ^{140}Ba decay and the 0.2, −1.7, 0.3, 0.3, 0.2, −0.3, and −0.3% for the 328.8, 397.5, 432.5, 487.0, 925.2, 2347.9, and 2547.3 keV γ rays in the ^{140}La decay. The estimated areas due to the summing of cascading γ rays for certain weak cross-over transitions, where summing corrections are found to be significantly large, are compared with the observed areas in Table 1.

The present measured X-ray and γ-ray intensities from ^{140}Ba and ^{140}La decays are shown in Tables 2 and 3. The intensity values for different γ rays as well as *K* X rays, measured with

TABLE 2. Relative intensities of X rays and γ rays in a ^{140}Ba decay

Energy (keV)	Relative intensities				
	This work	Ref. 8	Ref. 4	Ref. 10	Ref. 19
4.121 L_1	0.40(4)	—	—	—	0.49(9)
4.649 L_α	13.9(8)	—	—	—	13.8(25)
5.126 L_β	33.2(20)	—	—	—	31.6(57)
5.99 L_γ	6.6(5)	—	—	—	6.1(6)
13.87 γ	4.69(12)	—	7.2(25)	4.9(6)	4.9(6)
29.96 γ	58.4(10)	—	72(12)	60(3)	55.8(5)
33.3 $\bar{K}_\alpha$	6.10(18)	—	10.0(20)	6.5(5)	7.01(3)
37.8 K_{β_1}	1.15(5)	—	<2.3	1.60(5)	1.27(7)
38.9 K_{β_2}	0.32(5)	—			0.33(2)
43.8	0.054(7)	—	—	<0.007	0.062(4)
113.6	0.072(6)	—	—	0.077(16)	0.074
118.9	0.25(1)	—	0.21(2)	0.27(3)	0.21(2)
132.7	0.81(2)	—	0.83(7)	0.90(8)	0.83(7)
162.7	25.3(3)	26.4(3)	28.4(9)	28.0(8)	25.5(5)
304.9	17.54(15)	17.67(18)	17.30(70)	17.8(5)	17.63(37)
423.7	12.65(12)	12.73(14)	12.80(60)	12.80(30)	12.79(62)
437.6	7.91(8)	7.82(9)	7.80(40)	7.80(25)	7.91(16)
467.7	0.029(3) 0.028(5)[a] 0.030(4)[b]	—	0.60(5)	<0.01	0.60(5)
537.3	100(1)	100(1)	100	100(1)	100
551.2	0.028(4)	—	—	0.027(9)	—

[a]Values measured using 96.0 cm^3 HPGe detector.
[b]Values measured using 57.1 cm^3 HPGe detector.

TABLE 3. Relative intensities of X rays and γ rays in a ^{140}La decay

Energy (keV)	Relative intensities					
	This work	Ref. 7	Ref. 9	Ref. 8	Ref. 10	Ref. 19
34.56 $\overline{K}_\alpha$	1.72(4)	2.35(70)	--	—	1.77(6)	1.67(6)
39.23 K_{β_1}	0.31(1)	0.36(8)	—	—	0.36(2)	0.31(2)
40.44 K_{β_2}	0.085(4)		—	—	0.089(4)	0.082(5)
64.14 γ	0.015(2)	0.01	—	—	0.011(4)	0.011
68.91	0.079(2)	0.064(16)	0.070(16)	—	0.080(6)	0.070(16)
109.4	0.230(4)	0.210(15)	0.170(10)	—	0.220(10)	0.209(15)
131.1	0.49(1)	0.50(3)	0.44(1)	—	0.48(1)	0.46(1)
173.5	0.133(4)	0.130(20)	0.120(10)	—	0.120(10)	0.135(21)
241.9	0.434(8)	0.410(30)	0.450(10)	—	0.460(30)	0.493(10)
266.5	0.488(8)	0.490(30)	0.520(10)	—	0.510(30)	0.474(26)
306.9	0.026(7)	0.035(17)	0.022(6)	—	0.020(5)	0.022(7)
328.7	21.1(3)	19.4(6)	21.5(4)	21.5(2)	21.7(4)	21.7(4)
397.5	0.077(5)	0.110(35)	0.078(3)	—	0.070(5)	0.105(31)
432.5	3.04(3)	2.85(15)	3.05(3)	3.08(3)	2.97(15)	3.13(6)
438.5	0.041(10)					
	0.046(18)[a]	0.021(10)	0.006(3)	—	<0.0014	0.021(11)
	0.038(12)[b]					
445.5	0.003(1)	≈0.025	0.005(3)	—	0.004(1)	0.025
487.0	47.7(6)	45.0(15)	46.6(9)	47.7(5)	46.4(9)	48.1(10)
618.1	0.039(4)	≈0.045	0.049(6)	—	0.014(3)	0.063(31)
751.6	4.54(4)	4.40(20)	4.45(5)	4.65(5)	4.36(16)	4.51(31)
815.8	24.4(2)	23.5(7)	24.0(4)	24.8(2)	23.5(7)	24.7(5)
867.7	5.77(7)	5.60(30)	5.69(6)	5.90(6)	5.56(19)	5.86(12)
919.5	2.79(3)	2.64(16)	2.83(4)	2.91(4)	2.80(9)	2.81(5)
925.2	7.23(7)	7.10(30)	7.26(8)	7.42(8)	7.10(21)	7.37(4)
950.9	0.544(7)	0.550(30)	0.553(7)	—	0.56(3)	0.567(20)
992.9	0.014(5)	—	—	—	0.009(3)	—
1045.0	0.026(15)	—	0.024(4)	—	0.016(4)	—
1097.2	0.024(5)	—	0.024(5)	—	0.022(5)	—
1303.5	0.044(7)	—	0.046(6)	—	0.050(7)	—
1405.2	0.062(7)	—	0.066(9)	—	0.068(8)	—
1596.2	100.0(15)	100.0	100.0	100(1)	100	100
1877.3	0.043(4)	—	--	—	0.042(6)	—
1924.6	0.014(2)					
	0.014(2)[a]	—	0.014(3)	—	0.006(2)	—
	0.013(3)[b]					
2083.2	0.031(2)					
	0.033(4)[a]	—	0.045(3)	—	0.007(2)	0.012(7)
	0.029(3)[b]					
2347.9	0.89(3)	0.90(6)	0.89(2)	0.89(2)	0.89(3)	0.89(2)
2464.1	0.012(2)	0.002(1)	0.012(1)	—	0.008(1)	0.018(6)
2521.4	3.63(4)	3.60(18)	3.58(15)	3.62(7)	3.61(9)	3.58(5)
2547.3	0.106(3)	0.110(7)	0.105(2)	0.109(3)	0.109(5)	0.109(3)
2899.6	0.070(2)	0.065(6)	0.070(1)	0.069(1)	0.069(3)	0.069(2)
3118.5	0.026(1)	0.027(4)	0.027(1)	0.027(1)	0.028(2)	0.027(1)
3320.4	0.0040(3)	0.0047(15)	0.0040(3)	—	0.0045(4)	0.0047(15)

[a]Values measured using 96.0 cm^3 HPGe detector.
[b]Values measured using 57.1 cm^3 HPGe detector.

different detectors in the coinciding regions, were found to be consistent with each other and the weighted averages of these results are given in Tables 2 and 3. The overall uncertainty in the intensity measurements includes the uncertainties due to statistics and peak-area evaluation (less than 0.5% for intense peaks), the efficiency-calibration error (1.5–2.5% over the energy region 4–100 keV and 0.5–2.0% over the energy region 100–4000 keV) and other systematic errors (0.3%). All of these uncertainties are added in quadrature to give the final uncertainties in the intensity results. The results of the earlier measurements are also included in the Tables 2 and 3 for comparison.

2.1.1. ^{140}Ba decay

The present measured γ-ray-intensity values in the ^{140}Ba decay agree well with the values reported by Gehrke *et al.* (8) and Adam *et al.* (10) (Table 2). The 551.2 keV γ ray reported only by Adam *et al.* (10) was seen clearly in our measurements and the intensity values are found to be consistent. The intensity

of the 467.7 keV γ ray is found to differ remarkably from the earlier reported value (4). This may be due to a large summing of cascading γ rays falling under this peak (Table 1). The intensity values of K X rays and low-energy γ rays measured by us are found to be significantly lower than the earlier measured values of Kalinnikov *et al.* (4). However, the present intensity values of K X rays are more precise and show good agreement with the values measured by Adam *et al.* (10) as well as those calculated by using the physical parameters from internal-conversion and sequential atomic processes (19). The intensities of the different components of L X rays in the ^{140}Ba decay were measured by us for the first time and are found to be in good agreement with the evaluated results (19).

2.1.2. ^{140}La decay

In the case of the ^{140}La decay, the γ-ray intensities were measured separately from both the ^{140}La decay and from the successive decay of ^{140}Ba. The intensity values obtained from both of these measurements were found to be consistent and their weighted average is shown in Table 3. The present measured intensity values for most of the γ rays are in general agreement with the earlier measured values (5–10). The intensities of 438.5, 1924.6, and 2083.2 keV γ rays are found to differ significantly from the earlier reported values for these transitions (Table 3). The existence of 992.9 and 1877.2 keV γ rays in the ^{140}La decay, reported only by Adam *et al.* (10), was confirmed in the present measurements, and results are found to be in good agreement (Table 3). The present K X-ray intensities are about 20% lower than those measured by Kalinnikov *et al.* (7), but are in good agreement with those of Adam *et al.* (10) and the evaluated results (19). It is worth mentioning that the intensities of the L X rays in the ^{140}La decay are very small and could not be measured in our measurements.

In conclusion, we believe that the present results are more reliable and determined with better precision when compared with previous results because of the very good statistics collected under the weak peaks and the use of four well-calibrated semiconductor detectors.

3. Internal conversion-electron measurements

The mini-orange electron spectrometer used for the conversion-electron measurements comprises (*i*) a windowless Si(Li) detector (surface area = 200 mm^2, depletion depth = 3 mm, FWHM = 1.7 keV for 624.5 keV conversion electrons from ^{137}Cs decay); (*ii*) a mini-orange filter composed of five thin square (side = 1.5 cm) $SmCo_5$ permanent magnets fixed in an orange array in an aluminium circular frame (diameter = 6.0 cm). The filter has a lead absorber (diameter = 0.8 cm, thickness = 1.8 cm) at the centre to avoid direct exposure of the Si(Li) detector to the photons emitted from the source. A clean vacuum of 3×10^{-7} Torr (1 Torr = 133.3 Pa) was maintained in the spectrometer using a triode vacion pump. The detector was coupled to an 8K-channel analyser (ND 66B) through a spectroscopy amplifier (ORTEC 572, shaping time = 2 μs).

Thin and uncovered sources of ^{140}Ba and ^{140}La were prepared by drying the source solution on aluminized Mylar backing supported on a brass ring (diameter = 1.0 cm). The count rate for the different sources was kept between 500–1000 counts s^{-1} for all the measurements. The efficiency calibration curve for this spectrometer at source-to-filter and filter-to-detector distances = 2.8 cm (optimized for maximum efficiency in the energy range 200–1800 keV) was generated as described in our earlier paper (24). An overall uncertainty due to efficiency calibration was estimated to be 3.5% in the entire energy region 200–1800 keV.

Ten spectra were taken with each ^{140}Ba and ^{140}La source for time durations ranging from 30 000 to 300 000 s. A typical conversion-electron spectrum obtained with the ^{140}Ba source is shown in Fig. 2. The electron intensities were obtained by measuring the area under the conversion peaks and dividing it by the corresponding efficiency value at that energy.

The conversion-electron intensities for various transitions in ^{140}La and ^{140}Ce are presented in Tables 4 and 5, respectively. In the case of the ^{140}La decay, the conversion-electron intensities were measured from both ^{140}La and ^{140}Ba→ ^{140}La→ ^{140}Ce decays, and the results obtained were consistent with each other. A weighted average of two intensity results is shown in Table 5. The uncertainties shown in intensity values correspond to one standard deviation (1σ) and include uncertainties due to statistics and peak-area evaluation (less than 1.0% for intense peaks), efficiency-calibration error (3.5%), and other systematic errors (1.0%). All these uncertainties are added in quadrature to calculate the final uncertainties in the conversion-electron intensities.

3.1. ^{140}Ba decay

The conversion-electron intensities for various transitions from the ^{140}Ba decay are found to be in general agreement with the only available results of Adam *et al.* (10) as shown in Table 4. The present results show better precision when compared with the earlier measurements. The electron intensity for the (M + N.) conversion line of the 537.3 keV transition is reported for the first time.

The internal conversion coefficients for various transitions in ^{140}La were deduced using present-measured conversion-electron and γ-ray intensities. The γ-ray and conversion-electron intensities were normalized to yield the theoretically predicted α_K value (25) for the 537.3 keV ($1^- - 0^-$) pure $M1$ transition. The internal-conversion coefficients given by Adam *et al.* (10) are found to be, in general, higher than our values except for the 304.8 keV transition. The results quoted by Adam *et al.* (10) were normalized to yield the 162.3 keV ($2^- - 3^-$) transition to be pure $M1$, while present results were normalized to yield 537.3 keV ($1^- - 0^-$) transition to be pure $M1$. However, if we renormalize the results of Adam *et al.* (10) according to our values, the agreement with the present results is found to be reasonably good for all the transitions. The present measured conversion coefficients along with the theoretical values of Hager and Seltzer (25) are shown in Table 4. The multipolarities assigned to the different transitions in ^{140}La are shown in the last column of Table 4.

3.2. ^{140}La decay

In the case of ^{140}La decay, the present results for conversion-electron intensities agree well with the earlier measured results (5) (Table 5). The electron intensities for the (M + N) conversion of 328.8, 487.0, 1596.2, and 1903.5 keV transitions in ^{140}Ce are reported for the first time. The conversion coefficients for the various transitions in ^{140}Ce were calculated using the present conversion-electron and γ-ray intensity values and are presented in Table 5. The γ-ray and conversion-electron intensities were normalized to yield the theoretical α_K value (25) for the 1596.2 keV ($2^+ - 0^+$) pure $E2$ transition.

A comparison of measured values of K-conversion coefficients was made with those of the theoretical values of Hager

TABLE 4. Conversion-electron intensities, conversion coefficients, and multipolarities of various transitions in the decay of ^{140}Ba to ^{140}La

Energy of transitions (keV)	Shell	Internal conversion-electron intensities		Internal conversion coefficients (α)			Multipolarity
		This work[a]	Ref. 10[b]	Expt. this work ($\times 10^{-2}$)	Theoretical $M1$ ($\times 10^{-2}$)	Theoretical $E2$ ($\times 10^{-2}$)	
304.8	K	0.71(3)	0.62(3)	4.1(2)	4.4	3.6	$E2+M1$
423.7	K	0.23(2)	0.26(4)	1.8(2)	1.9	1.4	$M1$
437.6	K	0.12(1)	0.15(2)	1.5(1)	1.7	1.3	$M1$
537.3	K	1.04(4)	1.04(4)	1.04(4)	1.04	—	$M1$
	L	0.13(1)	0.15(2)	0.13(1)	0.14	—	
	$M+N$	0.057(8)	—	0.06(1)	—	—	

[a]Normalized to theoretical α_K value (25) for 537.3 keV ($0^- \rightarrow 1^-$) pure $M1$ transition α_K (537) = 1.04×10^{-2}
[b]Renormalized to theoretical α_K value (25) for 537.3 keV pure $M1$ transition.

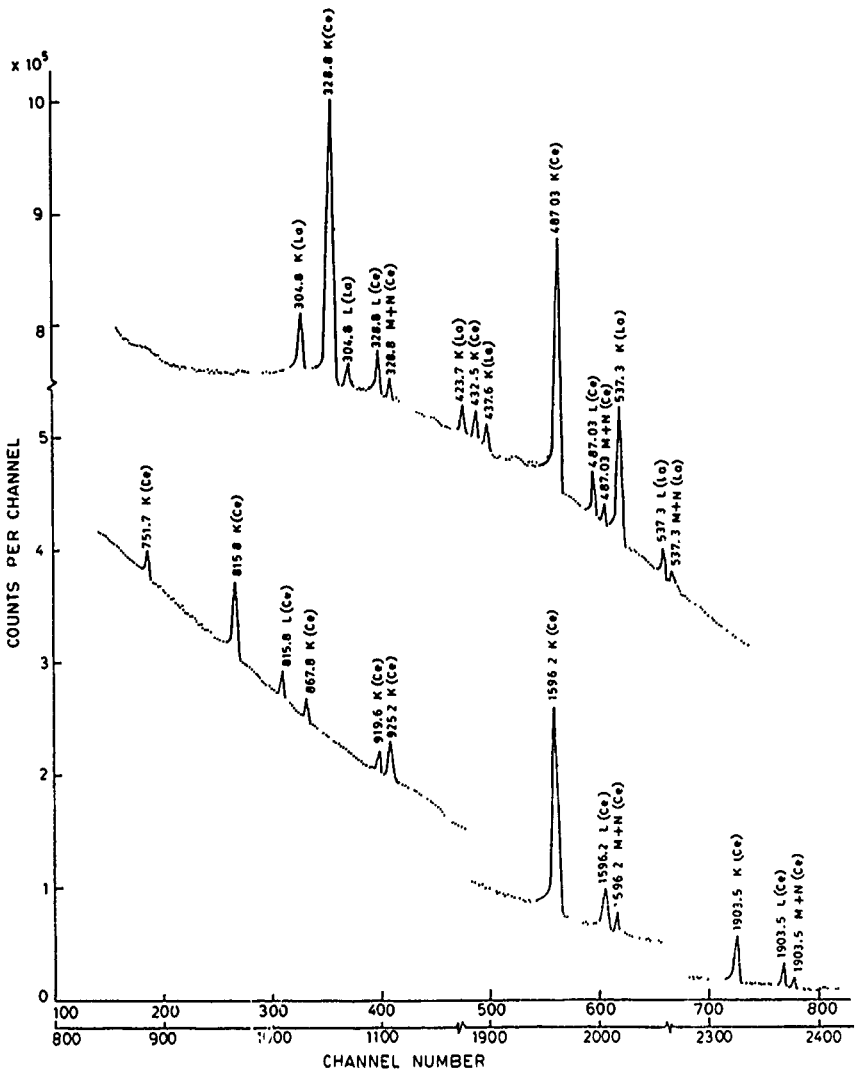

FIG. 2. Internal conversion-electron spectrum from ^{140}Ba decay taken with mini-orange electron spectrometer.

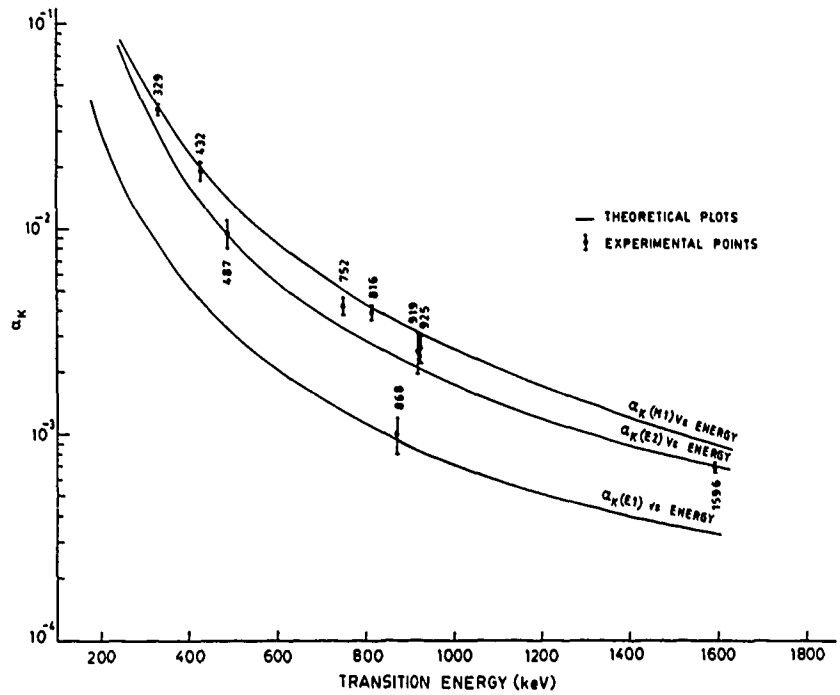

FIG. 3. Experimental K-conversion coefficients compared with the theoretical coefficients for $Z = 58$ given by Hager and Seltzer (25).

TABLE 5. Conversion-electron intensities, conversion coefficients, and multipolarities of transitions in decay of ^{140}La to ^{140}Ce

Energy of transitions (keV)	Shell	Internal conversion-electron intensities		Internal conversion coefficients (α)			Multipolarity
				Expt.	Theoretical		
		This work	Ref. 5	This work[a] ($\times 10^{-2}$)	$M1$	$E2$ ($\times 10^{-2}$)	
328.8	K	0.08(3)	0.76(1)	3.8(2)	3.92	2.98	$M1+E2$
	L	0.097(9)	0.102(5)	0.46(5)	0.52	0.55	
	$M+N$	0.021(3)	—	0.10(2)	0.11	0.12	
432.5	K	0.057(4)	0.058(3)	1.9(2)	1.94	1.34	$M1$
487.0	K	0.455(19)	0.440(23)	0.95(5)	$M3$; 12.9	0.92	$E2$
	L	0.062(5)	0.073(4)	0.13(1)	($M3$); 2.3	0.15	
	$M+N$	0.019(2)	—	0.040(4)	$M3$; 0.5	0.033	
751.7	K	0.019(2)	0.020(3)	0.42(4)	0.50	0.33	$M1+E2$
815.8	K	0.094(4)	0.095(6)	0.39(2)	0.41	0.27	$M1+E2$
	L	0.014(3)	0.014(1)	0.06(1)	0.05	0.04	
867.8	K	0.0058(9)	0.0061(15)	0.10(2)	$E1$; 0.11	$M2$; 0.92	$E1$
919.6	K	0.0070(15)	0.0061(15)	0.25(6)	0.31	0.21	$M1+E2$
925.2	K	0.019(2)	0.023(2)	0.26(3)	0.31	0.21	$M1+E2$
1596.2	K	0.069(3)	0.069(4)	0.069(3)	—	0.069	$E2$
	L	0.0071(10)	0.0084(10)	0.0071(11)	—	—	
	$M+N$	0.0012(3)	—	0.0012(3)	—	—	
1903.2	K	0.013(1)	0.015(2)	—	—	—	$E0$
	L	0.0013(2)	0.0018(3)	—	—	—	
	$M+N$	0.000 35(6)	—	—	—	—	

[a]Values normalized to α_K ($E2$) = 0.069 × 10^{-2} for the 1596.2 keV ($4^+ - 2^+$) pure $E2$ transition.

and Seltzer (25) for various possible multipolarities in Fig. 3. From this comparison multipolarities to various transitions in ^{140}Ce were assigned as shown in Table 5.

4. γ–γ directional correlation measurements in ^{140}Ce

For the directional correlation measurements, the sources were prepared in perspex holders that had a vertical cavity of 2 mm diameter and 3 mm depth. The count rates for these sources were kept at about 7000 counts s^{-1}. A 90 cm^3 HPGe – 96 cm^3 HPGe detector coincidence setup having a time resolution (2τ) = 7 ns for the 1173–1332 keV cascade following the ^{60}Co decay was used for these measurements. The energy resolution of both the detectors (1.7 keV at 1332 keV) was sufficient to completely separate the various γ rays from the ^{140}La

TABLE 6. γ–γ directional correlation coefficients for various cascade in ^{140}Ce

Cascade (keV)	Spin sequence	Directional correlation coefficients A_{22}	A_{44}	Ref.
131–242	$4^+-5^+-6^+$	−0.28(13)	0.12(16)	This work
131–266	$4^+-5^+-4^+$	0.31(15)	−0.16(21)	This work
109–(329)–487	$2^+-(3^+-4^+)-2^+$	−0.31(2)	−0.14(2)	This work
266–487	$5^+-4^+-2^+$	−0.16(8)	0.14(11)	This work
		−0.10(3)	−0.05(4)	14
329–487	$3^+-4^+-2^+$	−0.102(9)	−0.012(11)	This work
		−0.105(9)	0.005(9)	14
		−0.092(12)	−0.037(23)	12
432–487	$(4^+)-4^+-2^+$	0.178(33)	0.073(45)	This work
	$(3^+)-4^+-2^+$	0.239(37)	−0.058(54)	14
		0.215(18)	−0.048(33)	12
329–(487)–1596	$3^+-(4^+-2^+)-0^+$	−0.081(9)	−0.029(11)	This work
		−0.096(6)	0.004(6)	14
		−0.124(21)	0.018(29)	9
		−0.110(5)	−0.041(8)	12
432–(487)–1596	$(4^+)-(4^+-2^+)-0^+$	0.15(6)	0.06(8)	This work
		0.16(3)	0.09(5)	9
		0.26(1)	0.03(2)	13
		0.15(1)	−0.01(2)	11
	$(3^+)-(4^+-2^+)-0^+$	0.26(3)	−0.04(4)	14
487–1596	$4^+-2^+-0^+$	0.100(10)	0.021(15)	This work
		0.102(5)	0.018(7)	14
		0.097(8)	0.020(11)	9
		0.099(3)	0.002(8)	13
751–1596	$2^+-2^+-0^+$	−0.035(25)	0.072(33)	This work
		−0.022(18)	0.041(25)	14
		−0.024(33)	0.026(47)	9
		−0.030(36)	0.029(67)	13
815–1596	$3^+-2^+-0^+$	−0.097(8)	0.009(10)	This work
		−0.066(7)	0.001(9)	14
		−0.084(6)	−0.006(8)	9
		−0.097(6)	0.009(11)	12
868–1596	$3^--2^+-0^+$	−0.106(17)	−0.043(22)	This work
		−0.037(15)	−0.017(20)	14
		−0.084(16)	−0.048(22)	9
		−0.099(8)	0.007(10)	13
919–1596	$(4^+)-2^+-0^+$	0.145(52)	−0.114(69)	This work
		0.140(23)	0.009(34)	9
		0.130(80)	−0.02(12)	12
	$(3^+)-2^+-0^+$	0.077(35)	−0.035(53)	14
925–1596	$2^+-2^+-0^+$	0.386(21)	0.030(30)	This work
		0.322(23)	0.017(35)	14
		0.350(43)	−0.022(64)	9
		0.340(50)	0.010(70)	12
951–1596	$1^+-2^+-0^+$	−0.32(7)	0.009(9)	This work
		−0.27(7)	−0.07(11)	14
		−0.35(4)	0.21(5)	9
		−0.36(3)	0.008(51)	13

decay. The source to detector distance was kept at 15 cm for both the detectors. The γ rays of the 131, 487, and 1596 keV transitions observed by a movable 90 cm^3 HPGe detector were used for gating. The coincidence spectra were recorded at seven angles from 90 to 180° in intervals of 15°. The data were corrected for the miscentering of the source (<1.0%), the chance coincidences, and the Compton contributions. Also, the correlation coefficients were corrected for the finite resolution of the HPGe detectors by the method developed by Krane (26). The details of the experimental setup and method of analysis are described elsewhere (27, 28).

The results of directional correlation measurements for 15 cascades in ^{140}Ce along with the results reported by earlier workers are presented in Table 6. The directional correlation coefficients for 131–242, 131–266, and 109–(329)–487 keV cascades in ^{140}Ce were measured for the first time. The present measured values of the directional correlation coefficients for the 432–487, 816–1596, 868–1596, and 919–1596 keV cascades differ from the values reported by Michelkakis and Hamilton (14), but, are in agreement with the available results of Kaur *et al.* (9) and Saxena and Sharma (12).

The directional correlation coefficients from the present

TABLE 7. Multipole mixing ratio (δ) for various transitions in ^{140}Ce

Cascade (keV)	Transition (keV)		Mixing ratio (δ) This work	Ref. 14	Ref. 9	Ref. 12	Multipole admixture (This work)
266–131	131		0.15 ± 0.18	$-0.13^{+0.02}_{-0.05}$	—	—	$M1+(2.2^{+8}_{-2})\%E2$
242–131	242		$-0.60^{+0.35}_{-0.30}$	—	—	—	$M1+(26.5^{+19.0}_{-17.7})\%E2$
266–487	266		-0.14 ± 0.12	20.2^{+43}_{-8}	—	—	$M1+(1.9^{+5.4}_{-1.9})\%E2$
109–(329)–487	109		0.26 ± 0.02	—	—	—	$M1+(6.5^{+1.0}_{-1.2})\%E2$
329–487	329		-0.04 ± 0.01	-0.049 ± 0.006	—	-0.04 ± 0.02	$M1+(0.2\pm0.1)\%E2$
329–(487)–1596	329		-0.07 ± 0.01	—	$0.0^{+0.05}_{-0.0}$	-0.02 ± 0.01	$M1+(0.5\pm0.14)\%E2$
432–487	432*	(*i*)	0.05 ± 0.01		—	$0.5^{+0.07}_{-0.03}$	$M1+(0.25^{+0.17}_{-1.8})\%E2$
		(*ii*)	-0.41 ± 0.06	-0.54 ± 0.05		-0.8 ± 0.01	$M1+(14.6^{+3.7}_{-3.0})\%E2$
432–(487)–1596	432*	(*i*)	$0.13^{+0.18}_{-0.15}$		-0.14 ± 0.06	$-0.5^{+0.1}_{-0.07}$	$M1+(1.7^{+1.5}_{-5.6})\%E2$
		(*ii*)	-0.37 ± 0.08			-0.55 ± 0.10	$M1+(12.0^{+6.0}_{-4.4})\%E2$
487–1596	487		-0.005 ± 0.02	—	$0.0^{+0.05}_{-0.0}$	0.0 ± 0.01	$E2+(0.003^{+0.02}_{-0.03})\%M3$
751–1596	751		0.38 ± 0.04	0.36 ± 0.03	0.37 ± 0.06	$0.30^{+0.07}_{-0.02}$	$M1+(13^{+2.3}_{-2.1})\%E2$
815–1596	815		-0.03 ± 0.01	0.01 ± 0.01	-0.0	-0.04 ± 0.01	$M1+(0.11\pm0.01)\%E2$
868–1596	868		-0.044 ± 0.02	0.04 ± 0.02	-0.0 ± 0.05	0.25 ± 0.02	$E1+(0.2^{+0.2}_{-0.15})\%M2$
919–1596	919*	(*i*)	0.07 ± 0.1	—	$0.07^{+0.05}_{-0.07}$	0.06 ± 0.09	$E2+(0.6^{+2.7}_{-0.5})\%M3$
		(*ii*)	$1.9^{+0.5}_{-0.4}$	2.6 ± 0.4	—	$-0.08^{+0.06}_{-0.02}$	$M1+(80\pm1)\%E2$
925–1596	925		-0.22 ± 0.04	-0.10 ± 0.04	$-0.16^{+0.07}_{-0.06}$	-0.15 ± 0.07	$M1+(4.4^{+1.9}_{-1.4})\%E2$
951–1596	951		0.06 ± 0.07	0.01 ± 0.07	$0.06^{+0.03}_{-0.01}$	—	$M1+(0.4^{+1.3}_{-0.4})\%E2$

*Values evaluated using the 2516 keV level spin (*i*) $I^{\pi}=4^+$ and (*ii*) $I^{\pi}=3^+$.

TABLE 8. Summary of multipole mixing ratios and *K*-conversion coefficients for 432 and 919 keV transitions in ^{140}Ce

Cascade (keV)	Spin sequence	Transition	Mixing ratio (δ)	Multipole admixture	α_K (calc.) Ref. 25	α_K (expt.)
432–487	$4^+-4^+-2^+$	432	$\delta_1=0.05\pm0.01$	$M1+(0.25^{+0.17}_{-1.8})\%E2$	0.019	0.019(1)[a]
			$\delta_2=-1.06\pm0.22$*	$M1+(52^{+10}_{-12})\%E2$	0.016*	0.019(2)[b]
	$3^+-4^+-2^+$	432	$\delta_1=-0.41\pm0.06$	$M1+(14.6^{+3.7}_{-3.0})\%E2$	0.018	
			$\delta_2=-4.84^{+0.97*}_{-1.42}$	$M1+(96\pm2)\%E2$	0.013*	
432–(487)–1596	$4^+-(4^+-2^+)-0^+$	432	$\delta_1=0.13^{+0.15}_{-0.18}$	$M1+(1.7^{+1.5}_{-5.6})\%E2$	0.019	
			$\delta_2=-1.24^{+0.37*}_{-0.45}$	$M1+(60^{+14}_{-17})\%E2$	0.015*	
	$3^+-(4^+-2^+)-0^+$	432	$\delta_1=-6.0^{+1.9*}_{-4.9}$	$M1+(97^{+2}_{-3})\%E2$	0.013*	
			$\delta_2=-0.37\pm0.08$	$M1+(12^{+6.0}_{-4.4})\%E2$	0.018	
919–1596	$4^+-2^+-0^+$	919	$\delta_1=0.07\pm0.10$	$E2+(0.6^{+2.7}_{-0.5})\%M3$	0.0022	0.0025(6)[a]
			$\delta_2=1.38\pm0.30$*	$E2+(66^{+8}_{-12})\%M3$	0.011*	0.0023(7)[b]
	$3^+-2^+-0^+$	919	$\delta_1=0.32^{+0.12*}_{-0.09}$	$M1+(9.5^{+7}_{-4})\%E2$	0.0030*	
			$\delta_2=1.9^{+0.5}_{-0.4}$	$M1+(80\pm1)\%E2$	0.0023	

*δ values rejected on the basis of ICC measurements.
[a]Values taken from present measurements.
[b]Values taken from Karlsson *et al.* (5).

measurements were further used to deduce the mixing ratios for various transitions in ^{140}Ce using the method described by Krane and Steffen (29), whose notations and sign conventions are followed throughout. For the present analysis the 487 (4^+-2^+) and 1596 keV (2^+-0^+) γ transitions in ^{140}Ce were assumed to be pure *E*2 in character (30). The deduced multipole mixing ratios for the various transitions in ^{140}Ce are given in Table 7, along with the results reported by earlier workers (9, 12, 14).

The mixing ratio of the 266 keV transition is found to differ from that of Michelkakis and Hamilton (14), but is in agreement with the value reported by Garcia Bermudez *et al.* (13) from polarization-correlation measurements. The present value of mixing ratio for the 816 keV transition is somewhat higher than the value measured by Michelkakis and Hamilton (14) whereas, it is comparable with the value reported by Saxena and Sharma (12). The important aspects of the results from present γ–γ directional correlation measurements are discussed in the following sections.

4.1. The 109–(329)–487 keV cascade

The cascade was attempted for the first time. The measured correlation coefficients after solid-angle corrections are shown

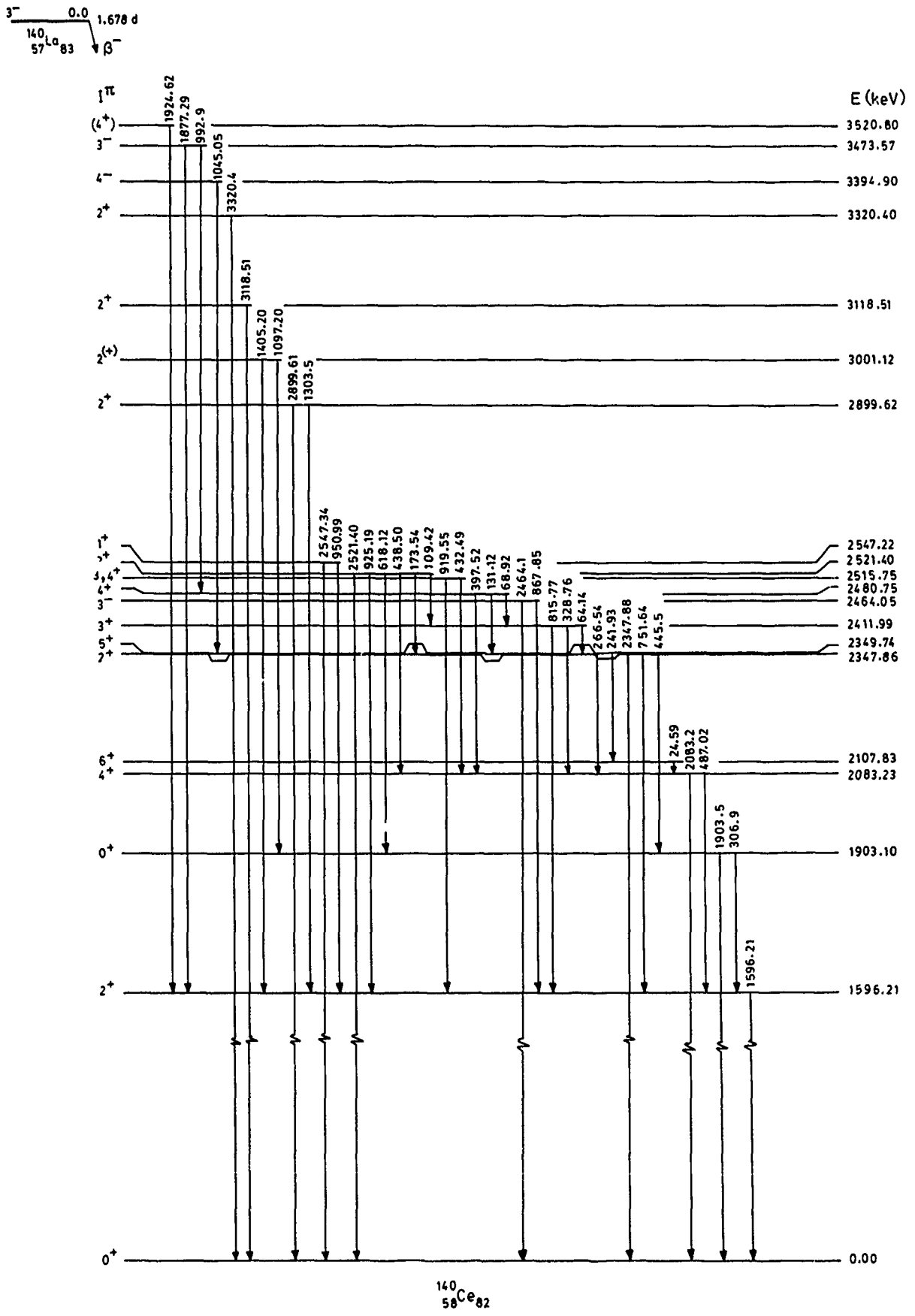

FIG. 4. Level scheme of ^{140}Ce from ^{140}La decay.

in Table 6. This cascade follows a spin sequence $2^+-(3^+-4^+)-2^+$ having 3^+-4^+ spins for the unobserved 329 keV intermediate transition. Taking the 329 keV transition as $M1$ + 0.2% $E2$, from the present measurements, the U_k (329) coefficients were calculated using the tabulated values of Rose and Brink (30). Assuming the 487 keV transition to be pure $E2$ (31), the mixing ratio analysis for the 109 keV transition yields two values of the mixing ratio, δ(109),

$$\delta(109) = 0.26 \pm 0.02 \text{ and } \delta(109) = 1.85 \pm 0.10$$

Out of these two values, the value compatible with the measured internal-conversion coefficients (5) is $\delta(109) = 0.26 \pm 0.02$, which gives an admixture of $M1 + (6.5^{+1\,0}_{-1\,2})\%E2$ for the 109 keV transition.

4.2. Multipole admixture of the 266 keV transition

The measured A_{22} coefficient for the 266–487 keV cascade (spin sequence, $5^+-4^+-2^+$) in ^{140}Ce yields two possible values of mixing ratio for the 266 keV transition, i.e.,

$$\delta(266) = -0.14 \pm 0.12 \text{ and } \delta(266) = -17.5 \pm 5.5$$

The δ values and the measured K-conversion coefficients (5) indicate that the possible multipole components in the 266 keV transition are $M1$ and $E2$. However, it is not possible to select a unique δ value for the 266 keV transition on the basis of the measured α_K value (5) as shown below;

Mixing ratio	Multipole admixture	α_K calc. (ref. 25)	α_K expt. (ref. 5)
-0.14 ± 0.12	$M1 + (1.9^{+5\,4}_{-1.9})\%\ E2$	0.068	0.063(10)
-17.5 ± 5.5	$E2$	0.057	—

On the other hand, the comparison of the measured K/L ratio = 6.5(10), see ref. 5, with the theoretical K/L values ($K/L(M1)$ = 7.5, $K/L(E2)$ = 4.5), see ref. 25, supports the multipolarity of the 266 keV transition as being of the predominantly $M1$ type. This is in contradiction to the 99%$E2$ component of this transition as reported by Michelkakis and Hamilton (14).

Also, if we use the above δ values of the 266 keV transition in the analysis of the 131–266 keV cascade, the $\delta(266) = -17.5 \pm 5.5$ gives the imaginary values of the mixing ratios for the 131 keV transition and is, therefore, ruled out. The value of $\delta(266) = -0.14 \pm 0.12$ gives two values of δ(131) viz.

$$\delta(131) = 0.15 \pm 0.18 \text{ and } \delta(131) = 3.1 \pm 1.2$$

Out of these two values, $\delta(131) = 0.15 \pm 0.18$, i.e., $M1 + (2.2^{+8.0}_{-2.0})\%E2$ admixture for the 131 keV is found to be compatible with the ICC measurements (5).

Thus, we can conclude from the measured K/L ratio for the 266 keV transition and from the directional correlation measurements of the 131–266 keV cascade that the multipolarity of the 266 keV transition is $M1 + (1.9^{+5.4}_{-1.9})\%E2$.

4.3. Spin of the 2516 keV level

The directional correlation measurements were made for three cascades, 432–487, 432–(487)–1596, and 919–1596 keV to assign a definite spin to the 2516 keV level. The mixing ratio analysis for the 432 and 919 keV transitions were done by taking the spin of the 2516 keV level to be 3^+ and 4^+; the values obtained are shown in Table 8. Also, in Table 8, K-conversion coefficients calculated using these mixing-ratio values and theoretical conversion coefficients from the Tables of ref. 25 by Hager and Seltzer are compared with the measured α_K values (5). Certain δ values were accepted on this basis. It is clear from this comparison that it is not possible to distinguish clearly between the 3^+ and 4^+ spin assignment to the 2516 keV level.

The spin assignment to this level by the previous workers was done on the basis of weak arguments. Garcia Bermudez *et al.* (13) assigned a spin of 4^+ to this level from the γγ(θ) measurements of the 432–(487)–1596 keV cascade. More recently, Michelkakis and Hamilton (14) assigned a spin of 3^+ from the γγ(θ) measurements of the 432–487 and 432–(487)–1596 keV cascades. The value of A_{22} coefficients for the 432–(487)–1596 keV cascade measured by Garcia Bermudez *et al.* (13) and Michelkakis and Hamilton (14) are the same (Table 6), but these workers distinguished between two spin assignments on the basis of small A_{44} = 0.03(2) and −0.04(4) values measured by them. Further, no systematic trend was noticed in the A_{44} values measured by earlier workers (Table 6). The spin assignment of 4^+ by Kaur *et al.* (9) on the basis of comparison of ICC measurements is also found to be not very reliable.

TABLE 9. Transition probabilities of various γ transitions in ^{140}Ce

Transition energy (keV)	Type	Transition probabilities: Single Particle	Transition probabilities: Experimental: This work	Transition probabilities: Experimental: Ref. 9
109	$M1$	3.76×10^{10}	1.49×10^{11}	—
109	$E2$	8.28×10^{5}	1.01×10^{10}	—
242	$M1$	4.11×10^{11}	2.18×10^{7}	—
242	$E2$	4.46×10^{7}	7.80×10^{6}	—
266	$M1$	5.46×10^{11}	3.37×10^{7}	—
266	$E2$	7.16×10^{7}	6.50×10^{5}	—
329	$M1$	1.03×10^{12}	5.60×10^{9}	5.7×10^{9}
329	$E2$	2.06×10^{8}	1.7×10^{7}	1.4×10^{7}
487	$E2$	1.47×10^{9}	4.96×10^{3}	5.0×10^{5}
816	$M1$	1.57×10^{13}	6.74×10^{9}	6.6×10^{9}
816	$E2$	1.94×10^{10}	7.35×10^{6}	—
868	$E1$	1.76×10^{15}	6.90×10^{12}	—
868	$M2$	1.10×10^{9}	1.33×10^{10}	—
925	$M1$	2.30×10^{13}	1.01×10^{13}	1.0×10^{10}
925	$E2$	3.65×10^{10}	4.87×10^{11}	2.6×10^{8}

5. Decay scheme and conclusions

The decay scheme of ^{140}La ($T_{1/2}$ = 1.68 d) based on the present and earlier measurements is shown in Fig. 4. The energies indicated in this figure are taken from ref. 31. The presence of the 1045.0 and 1924.6 keV transitions confirms the existence of the 3399.4 and 3520.8 keV levels, respectively. The level at 3000.7 keV is confirmed by the presence of γ rays of energy 1097.2 and 1404.9 keV. The presence of γ rays at 1877.3 and 992.9 keV confirm the existence of the level at 3473.6 keV in ^{140}Ce. The relative intensities of X rays and γ rays from the ^{140}Ba and ^{140}La decays were measured precisely and in some cases, these have been measured for the first time, using a set of well-calibrated, high-resolution Si(Li) and HPGe detectors. This work provides the conversion-electron intensities that have been determined with better precision.

The mixing ratios for the 109 and 242 keV transitions in ^{140}Ce have been determined for the first time from the directional correction measurements. These transitions are found to be almost $M1$ in character with a small admixture of $E2$. The

266 keV transition in ^{140}Ce is found to be dominantly $M1$, which is contrary to the accepted 99% $E2$ multipole admixture for this transition as given in ref. 31. The deduced multipole admixtures for the 329, 432, 487, 751, 816, 868, 919, 925, and 951 keV transitions, on the basis of γ–γ directional correlation measurements, are in good agreement with the values deduced from conversion-coefficient measurements as well as earlier reported values from reaction work (16).

The experimental transition probabilities for the 109, 242, 266, 329, 487, 816, 868, and 925 keV γ transitions in ^{140}Ce have been calculated using the present multipole mixing ratios and γ-ray-branching ratios. The values so obtained are compared with the earlier reported values (9) and with the single particles estimates in Table 9. The present values of transition probabilities for the 329 and 816 keV transitions show good agreement with the earlier reported values (9), whereas, significant differences are observed for the 487 and 925 keV transitions.

Acknowledgements

Three of us BC (SRF, CSIR) DM (Scientist's Pool Officer, CSIR), and JG (SRF, DAE) acknowledge the financial assistance given by the Council of Scientific and Industrial Research and the Department of Atomic Energy, Government of India, India.

1. J. Brude, M. Rakavy and G. Adam. Nucl. Phys. **68**, 561 (1965).
2. Y. K. Aggarwal, C. V. K. Baba and S. K. Bhattacherjee. Nucl. Phys. **58**, 641 (1964).
3. P. Boskma and D. Dewaard. Nucl. Phys. **14**, 145 (1959/60).
4. V. G. Kalinnikov and K. L. Ravn. Izv. Akad. Nauk. SSSR. Ser. Fiz. **33**, 1389 (1969).
5. S. E. Karlsson, B. Svahn, H. Petterson, and G. Malmsten. Nucl. Phys. **A100**, 113 (1965).
6. H. W. Bear, J. J. Reidy, and M. L. Wiedenbeck. Nucl. Phys. **A113**, 33 (1968).
7. V. G. Kalinnikov, K. L. Ravn, H. G. Hansen, and N. A. Lebedev. Izv. Akad. Nauk. SSSR. Ser. Fiz. **34**, 916 (1970).
8. R. J. Gehrke, R. G. Helmer, and R. C. Greenwood. Nucl. Instrum. Methods, **147**, 405 (1977).
9. R. Kaur, A. K. Sharma, S. S. Sooch, and P. N. Trehan. J. Phys. Soc. Jpn. **49**, 2122 (1980).
10. I. Adam *et al.* Izv. Akad. Nauk. SSSR. Ser. Fiz. **46**, 2 (1982).
11. M. E. Wiedenbeck, and D. E. Raeside. Nucl. Phys. **A176**, 381 (1971).
12. R. N. Saxena and H. D. Sharma. Phys. Rev. C: Nucl. Phys. **7**, 395 (1973).
13. G. Garcia Bermudez, A. Filevich, and M. Behar. Phys. Rev. C: Nucl. Phys. **13**, 2461 (1976).
14. E. Michelkakis and W. D. Hamilton. J. Phys. G: Nucl. Phys. **8**, 581 (1982).
15. F. T. Baker and R. Tickle. Phys. Rev. C: Nucl. Phys. 5, 182 (1972).
16. I. Dioszegi, A. Veres, W. Enghardt, and H. Prade. J. Phys. G: Nucl. Phys. **11**, 853 (1985).
17. M. Rho. Nucl. Phys. **65**, 497 (1965).
18. B. H. Wildenthal. Phys. Rev. Lett. **22**, 1118 (1969).
19. E. Browne and R. B. Firestone. Table of radioactive isotopes. Wiley & Sons, New York. 1986.
20. D. Mehta, M. L. Garg, J. Singh, N. Singh and P. N. Trehan. Nucl. Instrum. Methods Sect. A, **245**, 447 (1986).
21. B. Chand, J. Goswamy, D. Mehta, N. Singh, and P. N. Trehan. Nucl. Instrum. Methods Sect. A, **284**, 393 (1989).
22. J. T. Routti and S. G. Prussin. Nucl. Instrum. Methods, **72**, 125 (1969).
23. R. Griffiths. Nucl. Instrum. Methods, **91**, 377 (1971).
24. B. Chand, J. Goswamy, D. Mehta, N. Singh, and P. N. Trehan. Can. J. Phys. **68**, 1479 (1990).
25. R. S. Hager and E. C. Seltzer. Nucl. Data, **4**, 95 (1968).
26. K. S. Krane. Nucl. Instrum. Methods, **98**, 205 (1972).
27. A. K. Sharma, R. Kaur, H. R. Verma, K. K. Suri, and P. N. Trehan. J. Phys. Soc. Jpn. **46**, 1057 (1979).
28. S. S. Sooch, R. Kaur, N. Singh, and P. N. Trehan. J. Phys. Soc. Jpn. **52**, 61 (1983).
29. K. S. Krane and R. M. Steffen. Phys. Rev. C: Nucl. Phys. **4**, 1419 (1971).
30. H. J. Rose and D. M. Brink. Rev. Mod. Phys. **39**, 306 (1967).
31. L. K. Peker. Nucl. Data Sheets, **51**, 395 (1987).

Local kinetic analysis of low-frequency electrostatic modes in tokamaks

A. HIROSE

Plasma Physics Laboratory, Department of Physics, University of Saskatchewan, Saskatoon, Sask., Canada S7N 0W0

Received September 6, 1990

Analysis, based on a local kinetic dispersion relation in the tokamak magnetic geometry incorporating the ion transit frequency and trapped electrons, indicates that modes with positive frequencies are predominant. Unstable "drift"-type modes can have frequencies well above the diamagnetic frequency. They have been identified as the destabilized ion acoustic mode suffering little ion Landau damping even when $T_e \simeq T_i$.

Une analyse, basée sur une relation de dispersion cinétique locale dans la géométrie magnétique du tokamak et incorporant la fréquence de transit des ions ainsi que les électrons piégés, indique que les modes à fréquences positives sont prédominants. Les modes instables de type «dérive» peuvent avoir des fréquences bien au-dessus de la fréquence diamagnétique. Ils ont été identifiés comme le mode ionique acoustique déstabilisé subissant peu d'amortissement ionique de Landau même lorsque $T_e \simeq T_i$.

[Traduit par la rédaction]

Can. J. Phys. 69, 102 (1991)

Identifying the key instabilities responsible for the anomalous thermal and particle (often radially inward) transport in tokamaks has been a challenging problem. Several candidate instabilities have been investigated extensively. Among them, the hydrodynamic ion-temperature-gradient (ITG) mode and the trapped-electron mode (either collissionless or dissipative) have received particular attention because of their large growth rates. However, the effects of kinetic resonances on these modes have not been fully revealed. Regarding the ITG mode, the ion-magnetic-drift resonance has been incorporated in some studies (1, 2), but parallel ion dynamics (ion Landau resonance) has not been considered in refs. 1 and 2. As recently shown, ion Landau damping has a significant stabilizing influence on the ITG mode (3) and for a relatively flat density profile, a steep temperature gradient, $L_T/R < 0.1$, is required, where L_T is the temperature-gradient scale length and R is the major radius. The parallel ion dynamics has been implemented in the integro-differential formulation by Romanelli (4). Unfortunately, no details of eigenfunctions are given, and the results presented are remarked as "preliminary." Recently, the ion thermal diffusivities in TFTR (tokamak fusion test reactor) (5) and JET (joint European torus) (6) have been compared specifically with those predicted from the ITG theories. A general conclusion is that the tokamak anomalous transport is not consistent with what is expected from the ITG mode, which appears to support the carlier prediction (3, 7) that the ITG mode is unlikely to be a strong candidate for anomalous transport in tokamaks.

The previous analyses of the trapped-electron mode are based on a rather crude ion response either without ion magnetic drift effects (8, 9) or with the assumption that the ion transit frequency is small (10). However, in the long-wavelength regime, the mode frequency becomes small, and the ion transit frequency is not necessarily a small quantity and often exceeds the diamagnetic frequency. The customary expansion in powers of $k_\parallel v_\parallel$ should therefore be avoided in order to assess the growth rate in a more satisfactory manner.

Another important electrostatic mode, which has not received much attention presumably because of its relatively small growth rate, is the toroidal drift mode. After the original discovery (11), a rigorous analysis was made of this mode by Schep and Venema (12) based on an integro-differential equation. Unfortunately, the magnetic drift resonance of trapped electrons has been omitted in ref. 12. As will be shown, the growth rate is significantly enhanced if this effect is retained. Perhaps more important, the dispersion relation of the toroidal drift mode has little resemblance to that in slab geometry, and is well described by

$$\omega \simeq k_\parallel c_s$$

(the ion acoustic frequency), where c_s is the ion acoustic speed.

In this study, the three modes described above will be analyzed in terms of a single local kinetic electrostatic-dispersion relation incorporating all possible kinetic resonances of ions and trapped electrons. Evidently, the disadvantage of local analysis is that the norms of all differential operators ($k_\perp$, $k_\parallel$, and ω_D, the magnetic drift frequency) have to be assumed, rather than reduced. However, as shown in ref. 12, the eigenfunctions in the ballooning space θ are confined in the region $|\theta| < \pi$, and the assumption of strong ballooning should not cause qualitative errors. The main findings made in this study are:

(*i*) The unstable "drift"-type modes in tokamaks can have frequencies well above the electron diamagnetic frequency ($\omega \simeq 3\omega_{*e}$),

(*ii*) the dispersion relation of long-wavelength modes can be well approximated by that of the ion acoustic mode,

(*iii*) ion Landau damping of the acoustic mode is prohibited by the ion magnetic drift even when $T_e \simeq T_i$, and

(*iv*) the ITG mode is unlikely to exist in tokamaks.

We assume a low-β tokamak discharge with axisymmetry. Circulating electrons are assumed to be adiabatic with $|\omega| \ll k_\parallel v_{Te}$ (the electron transit frequency). This assumption allows us to ignore the rather minor electron inverse Landau damping. The frequency regime of interest is

$$\omega_{bi} \ll |\omega| \ll \omega_{be}$$

where ω_{bj} is the bounce frequency of ions or electrons. Low-frequency, trapped-ion modes will therefore be ignored. With

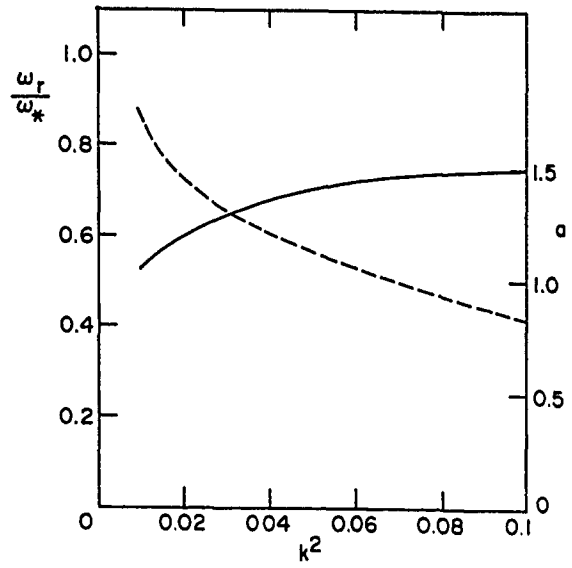

FIG. 1. The dispersion relation found in ref. 12 (– – –) and the parameter a in $k_\parallel = as/qR\kappa_0$ to reproduce it (—). $\varepsilon_n = 0.1$, $T_i = T_e$, $\eta_i = 0$, $\kappa_0 = \pi/2$, $s/q = 1$, no trapped electrons.

these assumptions, the local kinetic dispersion relation for Maxwellian ions and electrons is

$$[1] \quad 1 + \tau = \tau \int \frac{\omega + \bar{\omega}_{*_i}(v^2)}{\omega + \bar{\omega}_{Di}(v) - k_\parallel v_\parallel} J_0^2(\Lambda) f_{Mi}(v^2)\, d^3v + \int_{Tr} \frac{\omega - \bar{\omega}_{*e}(v^2)}{\omega - \bar{\omega}_{De}(v)} f_{Me}(v^2)\, d^3v$$

where $\tau = T_e T_i$ is the temperature ratio,

$$[2] \quad \bar{\omega}_{*j}(v^2) = \omega_{*j}\left[1 + \eta_j\left(\frac{\mathscr{E}_j}{T_j} - \frac{3}{2}\right)\right]$$

$$\mathscr{E}_j = \frac{1}{2} m_j v^2, \qquad j = i \text{ or } e$$

is the energy-dependent diamagnetic drift frequency with

$$[3] \quad \omega_{*j} = \frac{cT_j}{eB^2}(\nabla \ln n_0 \times \boldsymbol{B}) \cdot \boldsymbol{k}_\perp$$

being the diamagnetic drift frequency,

$$\Lambda = \frac{k_\perp v_\perp}{\Omega_i}$$

is the argument of the Bessel function J_0,

$$[4] \quad \bar{\omega}_{Dj}(v) = 2\varepsilon_n \omega_{*j} \frac{m}{2T}\left(\frac{v_\perp^2}{2} + v_\parallel^2\right) \times \left[\cos\left(\frac{\kappa}{s}\right) + \kappa \sin\left(\frac{\kappa}{s}\right)\right]$$

is the velocity-dependent magnetic drift frequency with $\varepsilon_n = L_n/R$ the density gradient inverse aspect ratio, $\kappa = k_r/k_\theta$ the ballooning variable, $k_\perp^2 = k_\theta^2 + k_r^2$, and finally Tr indicates the trapped region in the electron velocity space that may be approximated by $|v_\parallel| < \sqrt{\varepsilon}\, v_\perp$. Solutions for ω can be found through numerical integration of [1] over the velocity. The parallel wave number $k_\parallel$ may be approximated by

$$[5] \quad k_\parallel \simeq \frac{s}{qR}\left|\frac{d}{d\kappa}\right| \simeq \frac{s}{qR}\frac{1}{\kappa_0}$$

where κ_0 is the mode width of the eigenfunction in the Fourier (or ballooning) space κ. In several ballooning analyses devoted to drift-type modes in tokamaks, it has been established that $\kappa_0 \simeq \mathcal{O}(1)$ remains constant over a wide range of the poloidal wave number κ_θ. For example, in the work by Schep and Venema (12) $(k_\theta\rho)^2$ is varied from 0.01 to 0.1, but the mode width κ_0 remains essentially constant. To determine the value of $k_\parallel$ that satisfactorily recovers the dispersion relation worked out in ref. 12 in terms of a rigorous integro-differential formulation, we consider the parameters identical to those in ref. 12, $T_e = T_i$, $\eta_c = \eta_i = 0$, $\varepsilon_n = 0.1$, $s = q = 1$ and we ignore trapped electrons in [1]. Figure 1 shows the parameter a (—) when $k_\parallel$ in [1] is written as

$$k_\parallel = a\frac{s}{qR}\frac{1}{\kappa_0}$$

in order to recover the (marginally stable) dispersion relation in Fig. 1 of ref. 12. Here κ_0 is chosen as $\kappa_0 = \pi/2$ since, when $s = 1$, the eigenfunction tends to peak at this value. As can be seen, a is rather insensitive to $k = k_\theta\rho$. We therefore assume

$$[6] \quad k_\parallel \simeq \frac{s}{qR}$$

throughout this study. (The finiteness of effective $k_\parallel$ even for modes localized at a mode rational surface is evidently due to the toroidicity, namely, the coupling between modes localized on neighboring rational surfaces. In the past, $k_\parallel \simeq s/qR$ has been assumed in numerous qualitative studies of electrostatic and electromagnetic ballooning modes.) In the long-wavelength region $(k_\theta\rho)^2 \simeq 0.01$ where the drift frequency ω_* is very small, the ion acoustic transit frequency thus becomes predominant, and the appearance of modes with $\omega > \omega_{*_e}$ is due to the coupling with the ion acoustic mode. Throughout this study, we also assume $T_i = T_e$, thus $\eta = \eta_i = \eta e$.

If $k_\parallel$ is *artificially suppressed*, the dispersion relation yields the familiar η_i mode with negative frequencies, and also the trapped-electron mode with positive frequencies. (When $k_\parallel = 0$, the toroidal drift mode is evidently suppressed because of a lack of coupling to the ion acoustic mode.) The dispersion relations of these modes are shown in Figs. 2 and 3, respectively, for the case $\eta = 2$, $\varepsilon_n = 0.2$, and $\sqrt{\varepsilon} = 0.5$. The mode frequency $\omega = \omega_r + i\gamma$ is normalized by the density gradient diamagnetic frequency ω_* $(= \omega_{*_i} = \omega_{*_e})$. Compared with the local kinetic result in Fig. 4 of ref. 4, it can be seen that the η_i mode is further destabilized by trapped electrons. However, if the parallel wave number given in [6] is assumed, the ion temperature-gradient mode is suppressed even with trapped electrons.

Figure 4 shows the results when $k_\parallel$ in [6] is assumed. (Other parameters are unchanged from those in Figs. 2 and 3.) Note

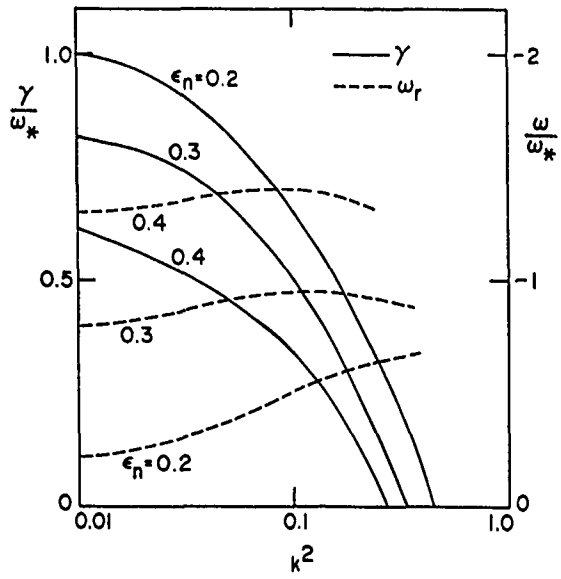

FIG. 2. Dispersion relation ($\omega - k_\theta$ diagram) of the η_i mode with trapped electrons when $k_\parallel = 0$. $k = k_\theta\rho$, $T_i = T_e$, $\eta = \eta_e = \eta_i = 2$, $\varepsilon_n = 0.2$, $\varepsilon = 0.25$.

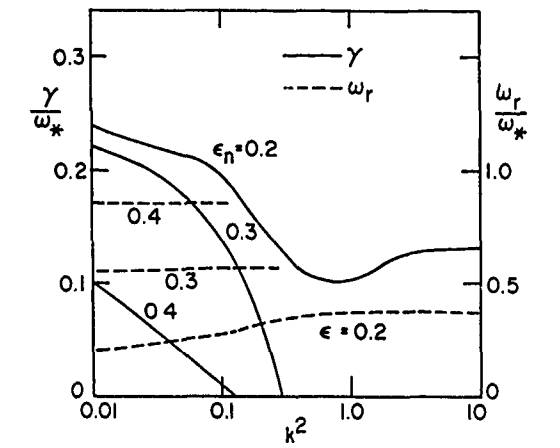

FIG. 3. Dispersion relation of the trapped-electron mode when $k_\parallel = 0$ with the same parameters as in Fig. 2.

that both modes have positive frequencies. No unstable modes with negative frequencies have been found. Mode I in Fig. 4 is the toroidicity-induced drift mode destabilized by temperature gradients and trapped electrons. (The contribution from the inverse Landau damping on untrapped electrons is negligibly small; see ref. 12.) It has a threshold in k, $k^2 \gtrsim 0.01$ for instability. The long-wavelength regime ($k^2 \lesssim 0.04$) is the trapped-electron mode. However, in this regime, the trapped-ion contribution should also be considered, and Mode II shown in Fig. 4 requires more detailed analysis incorporating collisions.

The frequency of Mode I can exceed the electron diamagnetic frequency by a factor as large as 3 to 4. Therefore, it is inappropriate to call it a drift mode. In fact, if the mode frequency ω_r is normalized by the ion acoustic frequency $\omega_s = k_\parallel c_s$, ω_r/ω_s remains of order unity over a wide range of k. (For example, at $k = 0.1$, $\omega_r/\omega_s \simeq 1.7$, at $k = 1$, the ratio is 1.5.) Since $T_e = T_i$ by assumption, one would expect such an

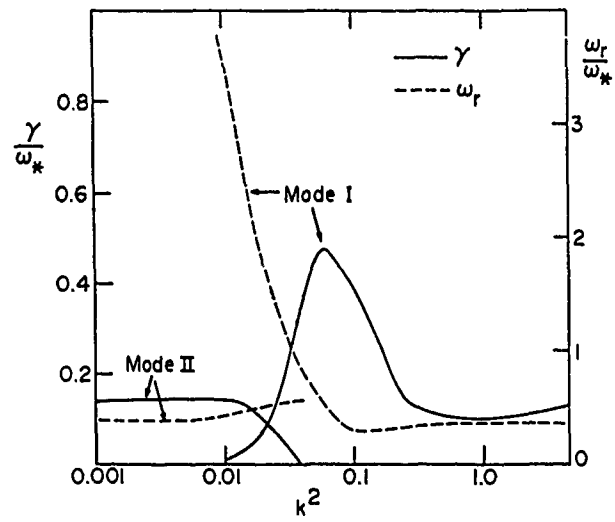

FIG. 4. Dispersion relation when $k_\parallel$ in [6] is assumed. $s/q = 1$, $\varepsilon_n = 0.2$. Other parameters unchanged from Fig. 2. No unstable modes with negative frequencies have been found.

"acoustic" mode should be strongly ion Landau damped. However, the ion kinetic resonance

$$[7] \quad \omega + \bar{\omega}_{Di}(v) - k_\parallel v_\parallel = 0$$

requires

$$[8] \quad (k_\parallel v_{Ti})^2 > 8\varepsilon_n \omega_* \omega$$

where $v_{Ti} = \sqrt{2T_i/M}$. Since $\omega \simeq \omega_s \simeq k_\parallel v_{Ti}$ ($T_e = T_i$), the above condition becomes

$$(k_\perp\rho)^2 < \frac{1}{64}\left(\frac{s}{q}\right)^2 \simeq \mathcal{O}(0.01)$$

which approximately corresponds to the lower unstable boundary of Mode I shown in Fig. 4. Therefore, the acoustic mode prevails in the region $k^2 > 0.01$ without suffering ion Landau damping even when $T_e = T_i$. (The acoustic mode persists for relatively flat density profiles as will be shown in Figs. 6 and 7.) This observation indicates that unstable low-frequency modes in tokamaks are largely determined by the magnetic curvature rather than by the pressure gradient. In fact, the instability prevails even with a flat density profile ($L_n > R$). (Note that the frequency is dictated by the ion acoustic transit effect ($\omega_s \propto 1/R$) and the growth rate by trapped electrons whose fraction is proportional to $1/\sqrt{R}$.) The familiar dispersion relation of drift mode in slab geometry

$$\omega \simeq \frac{1 - (k_\perp\rho_i)^2}{1 + (k_\perp\rho_s)^2}\omega_{*e}$$

is irrelevant for tokamaks, and failure of experimental attempts (14) to identify the slab-mode dispersion relation in tokamaks is not really surprising.

The absence of the η_i mode with negative frequencies in Fig. 4 is owing to its disappearance when a finite $k_\parallel$ given in [6] is assumed, that is, when parallel ion dynamics is fully implemented. Figure 5 shows the transition of three modes, the η_i mode in Fig. 2 with $k^2 = 0.1$, and the two electron modes

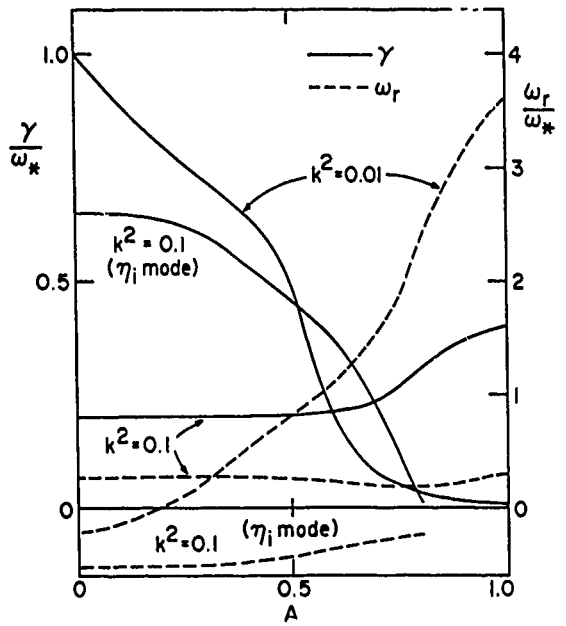

FIG. 5. Effects of $k_\parallel$ on three modes: the τ_i mode ($k^2 = 0.1$), and two electron modes with $k^2 = 0.01$ and 0.1 The parameter A is the suppression coefficient for $Ak_\parallel$. $T_e = T_i$, $\varepsilon = 0.2$, $\varepsilon = 0.25$, $\eta = 2$.

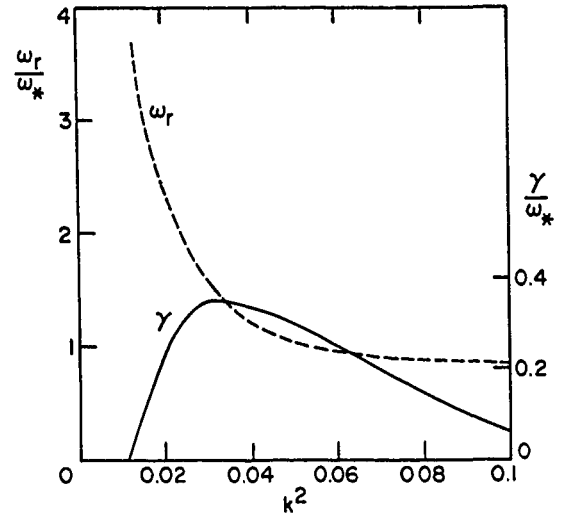

FIG. 6. Dispersion relation when $T_i = T_e$, $\eta = 2$, $\varepsilon_n = 0.4$, $\varepsilon = 0.25$, $s/q = 1$. Note the disappearance of pure electron trapped-electron mode in the region $k^2 \lesssim 0.01$ and $k^2 > 1$ in Fig. 4.

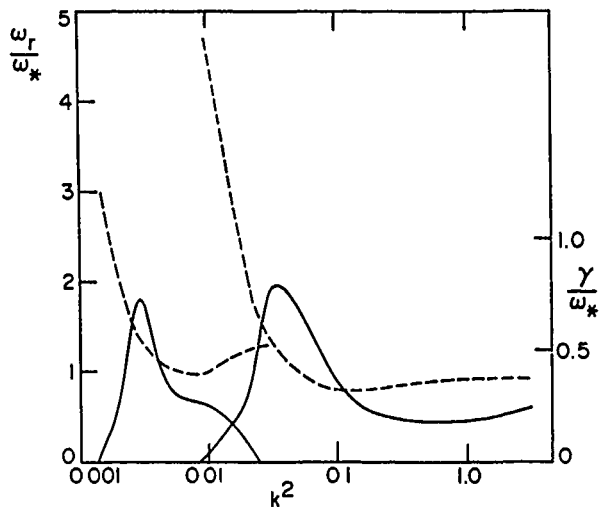

FIG. 7. Dispersion relation when $T_i = T_e$, $\eta = 4$, $\varepsilon_n = 0.4$, $\varepsilon = 0.25$, $s/q = 1$.

with $k^2 = 0.01$ and 0.1 as $Ak_\parallel$ is gradually increased from zero. (The parameter A is the suppression coefficient for $k_\parallel$.) The η_i mode becomes damped before the full value of $k_\parallel$ ($A = 1$) is reached. The trapped-electron mode with $k^2 = 0.01$ is also strongly damped as $k_\parallel$ increases, but not completely. The shorter wavelength trapped-electron mode ($k^2 = 0.1$) is further destabilized by $k_\parallel$. The disappearance of the η_i mode is not inconsistent with the finding in ref. 7 in which a search for hydrodynamic unstable eigenfunctions was not successful. (Romanelli (4) has claimed that the η_i mode is insensitive to the value of $k_\parallel$ (see Fig. 1 of ref. 6), based on a hydrodynamic analysis, which, however, evidently lacks kinetic ion damping.)

We now return to Fig. 4. In extremely long-($k^2 < 0.01$) and short-($k^2 > 0.5$) wavelength regimes, both Mode I and Mode II become similar. This is due to the fact that in both limits, the ion response tends to be adiabatic. In the long-wavelength limit, the ion transit frequency is dominant, while in the short-wavelength limit, the finite (or large) ion Larmor radius makes ion dynamics adiabatic. Of course, Mode II is subject to the condition that the ion bounce frequency be smaller than the mode frequency, and in the region of extremely long wavelength ($k^2 \simeq 0.001$), effects of trapped ions should be incorporated. When the ion term in [1] is suppressed, and the velocity dispersion of the trapped-electron magnetic drift is also ignored, we obtain the following hydrodynamic dispersion relation,

$$[9] \quad 1 + \tau = \frac{\sqrt{\varepsilon}}{\omega - \omega_{De}}\left(\omega - \omega_{*e} - \frac{\eta_e \omega_{*e}\omega_{De}}{\omega - \omega_{De}}\right)$$

which describes the short-wavelength ubiquitos mode (15) with an electron temperature gradient. When $\tau = 1$, $\varepsilon_n = 0.2$, $\sqrt{\varepsilon} = 0.5$, and $\eta_e = 2$ (as in Fig. 4), [9] predicts $\omega \simeq (0.3 + i\,0.51)\omega_{*e}$. In Fig. 4, the frequency is in a reasonable agreement with $\omega_r \simeq 0.35\omega_{*e}$ at $k^2 \gtrsim 0.5$. However, the growth rate from the hydrodynamic approximation is a significant overestimate ($\gamma/\omega_{*e} = 0.51$ vs. 0.1 at $k^2 = 3$ in Fig. 4). It is evident that the velocity dispersion of the magnetic drift resonance of trapped electrons has a significant stabilizing influence.

The absence of negative frequency modes (the η_i mode) persists over a wide variation of ε_n and η. Figure 6 depicts the dispersion relation for the case $\eta = 2$, $\varepsilon_n = 0.4$ with other parameters unchanged. For $\eta = 2$, the pure electron modes with extremely long and short wavelengths seen in Fig. 4 disappear at about $\varepsilon_n \simeq 0.25$. However, it reappears when the temperature gradient is increased. Figure 7 shows the dispersion relation for the case $\eta = 4$, $\varepsilon_n = 0.4$. The apparent large growth rate is due to the normalization by the density-gradient diamagnetic frequency. When $\eta > 1$, normalization by the temperature-gradient diamagnetic frequency, $\gamma/\eta\omega_*$, is more appropriate. In terms of such normalization, the maximum

growth rate decreases to $\gamma/\eta\omega_* \simeq 0.18$. The high-frequency modes ($\omega > \omega_*$) seen in Figs. 6 and 7 are essentially the acoustic mode described earlier.

Finally, the underlying electrostatic approximation will be commented on. It is generally accepted that the electrostatic approximation should be valid if the β factor is small. However, its upper limit has not been well established. When circulating electrons are adiabatic, $|\omega - \omega_{De}| \ll k_\parallel v_{Te}$, their density and parallel current perturbations are given by

$$[10] \quad n_e = \left(\phi - \frac{\omega - \omega_{*e}}{k_\parallel c} A_\parallel\right) \frac{en_o}{T_e}$$

$$[11] \quad J_{\parallel e} = \frac{n_o e^2}{k_\parallel T_e} (\omega_{*e} - \omega) \left(\phi - \frac{\omega - \omega_{De}}{k_\parallel c} A_\parallel\right)$$

where $A_\parallel$ is the parallel vector potential, and for simplicity the electron temperature gradient is ignored. The electrostatic approximation obviously requires

$$|ck_\parallel \phi| \gg |(\omega - \omega_{*e}) A_\parallel|$$

If the contributions from ions and trapped electrons to the parallel current are ignored, which is the case when $\beta \ll 1$, Ampere's law yields

$$\left[k_\parallel^2 k_\perp^2 - \left(\frac{k_{De}}{c}\right)^2 (\omega - \omega_{*e})(\omega - \omega_{De})\right] A_\parallel = ck_\parallel \left(\frac{k_{De}}{c}\right)^2 (\omega_{*e} - \omega)\phi$$

where

$$k_{De}^2 = \frac{4\pi n_o e^2}{T_e}$$

Then, the inequality reduces to

$$(k_\parallel k_\perp)^2 \gg \left(\frac{k_{De}}{c}\right)^2 |\omega - \omega_{*e}|^2$$

provided $\omega_{*e} > \omega_{De}$. Since $k_\parallel \simeq s/qR$, $|\gamma| \simeq \omega_{*e}$, we find

$$[12] \quad \beta \ll \left(\frac{sL_p}{qR}\right)^2$$

as the condition for the electrostatic approximation. Here L_p is the pressure-gradient scale length. In the core region of a tokamak discharge, the shear parameter s is small, while near the edge, the pressure-gradient scale length L_p is small, and the safety factor $q(r)$ is large. Therefore, the condition derived above is rather stringent. (For a flat temperature profile, L_p is large, but the shear is expected to be small if the classical plasma resistivity prevails.) It has recently been observed in several tokamaks that the density and magnetic fluctuations are closely correlated even in low-β ($\simeq \mathcal{O}(10^{-3})$) ohmic discharges (16). The traditional electrostatic approximation may not be adequate even in low-β tokamaks, and should be generalized to electromagnetic analysis. For example, it has been found recently that a low-β tokamak should be unstable in the wavelength regime $k_\perp \simeq \omega_{pe}/c$ (17), which may have important implications to the anomalous electron thermal diffusivity in tokamaks.

One of the main findings in this study is that the popular hydrodynamic ITG mode is unlikely to exist in tokamaks. This supports the theoretical (3, 7) and experimental (5, 6) indications that the ITG mode may not be playing a major role in the tokamak anomalous transport. Furthermore, a modest β (of order 1%) can stabilize the ITG mode, as recently shown (18).

In summary, it has been shown in terms of local kinetic analysis that low-frequency electrostatic instabilities in tokamaks are dominated by positive frequency modes provided the ion kinetic effects (the ion magnetic drift and parallel Landau resonances) are properly taken into account. The dispersion relation of the trapped-electron-induced toroidal drift mode is well described by that of the ion acoustic mode, which is shown to be free from ion Landau damping even when $T_e = T_i$ because of the ion magnetic drift.

Acknowledgements

Helpful comments by Professor J. Weiland on the local kinetic approximation are gratefully acknowledged. This research has been sponsored by the Natural Sciences and Engineering Research Council of Canada.

1. P. Terry, W. Anderson, and W. Horton. Nucl. Fusion, **22**, 487 (1982).
2. H. Biglari, P. H. Diamond, and M. N. Rosenbluth. Phys. Fluids B, **1**, 109 (1989).
3. A. Hirose. Phys. Fluids, B, **2**, 1087 (1990).
4. F. Romanelli. Phys. Fluids B, **1**, 1018 (1989).
5. M. C. Zahnstorff *et al.* Proceedings of the 17th European Conference on Controlled Fusion and Plasma Heating. Part 1. European Physical Society, 1990; p. 42; *In* Proceedings of the 13th IAEA Int. Conf. on Plasma Physics and Controlled Nuclear Fusion Research. Washington, D.C. 1990. IAEA, Vienna. In press.
6. F. Tibone *et al.* Proceedings of the 17th European Conference on Controlled Fusion and Plasma Heating. Part 2. European Physical Society. p. 805; *In* Proc. 13th IAEA Int. Conf. on Plasma Physics and Controlled Nuclear Fusion Research. Washington, D.C. 1990. In press.
7. A. Hirose and O. Ishihara. Nucl. Fusion, **27**, 1439 (1987).
8. J. C. Adam, W. M. Tang, and P. H. Rutherford. Phys. Fluids, **19**, 561 (1976).
9. J. F. Santarius and F. L. Hinton. Phys. Fluids, **23**, 537 (1980).
10. G. Rewoldt, W. M. Tang, and E. A. Freeman. Phys. Fluids, **21**, 1513 (1978).
11. C. Z. Cheng and L. Chen. Phys. Fluids, **23**, 1770 (1980).
12. T. J. Schep and M. Venema. Plasma Phys. Controlled Fusion, **27**, 653 (1985).
13. A. Hirose and S. G. Tsotsonis. Nucl. Fusion. **30**, 2063 (1990).
14. R. L. Hickok *et al.* *In* Proc. 13th IAEA Int. Conf. on Plasma Physics and Controlled Nuclear Fusion Research. Washington, D.C. 1990. IAEA, Vienna. In press.
15. B. Coppi and G. Rewoldt. Phys. Rev. Lett. **33**, 1329 (1974).
16. V. V. Bulanin *et al.* Sov. J. Plasma. Phys. **15**, 147 (1989); E. J. Hains *et al.* Bull. Am. Phys. Soc. **34**, 1923 (1989).
17. A. Hirose *et al.* *In* Proc. 13th IAEA Int. Conf. on Plasma Physics and Controlled Nuclear Fusion Research. Washington, D.C. 1990. IAEA, Vienna. In press.
18. B. G. Hong, W. Horton, and D. I. Choi. Plasma Phys. Controlled Fusion, **31**. 1291 (1989).

Optical absorption in gold caused by a granular dielectric overlayer

VO-VAN TRUONG, P. V. ASHRIT, G. BADER, P. COURTEAU, AND F. E. GIROUARD
Department of Physics, Université de Moncton, Moncton, N.B., Canada E1A 3E9
AND
TOMUO YAMAGUCHI
Research Institute of Electronics, Shizuoka University, Hamamatsu 432, Japan

Received August 21, 1990

Light can be used to excite surface plasmons if there are proper mechanisms for coupling with those surface plasmons. This coupling can usually be achieved via surface roughness or evanescent waves in attenuated total-reflection experiments. In the present work, we report evidence of the possibility of having a resonant optical absorption when a granular dielectric layer is deposited on a metallic surface. Very thin films of MgF_2 of mass thickness up to 8 nm have been used as a discontinuous overcoat on Au films of 100 nm thickness. Reflectivity measurements with p-polarized light incident at 40° show a resonant-type absorption near 520 nm when the dielectric layer is added to the Au surface. As the MgF_2 film grows thicker and becomes continuous this absorption feature is no longer prominent. To account for this phenomenon, an effective-medium theory is used to describe the optical behavior of the coated Au surface. By including mirror-image effects in the dipole approximation, basic features of experimental measurements can be reproduced.

La lumière peut être utilisée pour exciter des plasmons de surface, s'il existe des mécanismes appropriés pour le couplage avec ces plasmons de surface. Ce couplage peut habituellement être réalisé via les rugosités de la surface ou les ondes évanescentes dans les expériences de réflexion totale atténuée. Dans le présent travail, nous apportons une preuve de la possibilité d'avoir une absorption optique résonante lorsqu'une couche diélectrique granulaire est déposée sur une surface métallique. Des couches très minces de MgF_2, d'épaisseur de masse allant jusqu'à 8 nm, ont été utilisés comme recouvrement discontinu sur des films d'or de 100 nm d'épaisseur. Des mesures de réflectivité en lumière polarisée p à 40° d'incidence montrent qu'il y a absorption de type résonant près de 510 nm lorsque la couche diélectrique est placée sur la surface Au. Lorsque la couche de MgH_2 s'épaissit et devient continue, cet effet d'absorption n'est plus aussi prononcé. Afin de rendre compte de ce phénomène, on utilise une théorie de milieu effectif pour décrire le comportement optique de la surface Au recouverte. En incluant des effets d'images de miroir dans l'approximation dipolaire, les caractéristiques principales des données expérimentales peuvent être reproduites.

[Traduit par la rédaction]

Can. J. Phys. 69, 107 (1991)

Introduction

Surface-plasmon studies have attracted a great deal of interest from various workers (1). Collective electron resonances in bulk metals can be excited by energetic charged particles or by light under some conditions. They are also observed in metallic particles and the resonance frequencies depend on the particular geometry of those particles. The most studied particle shapes are spherical and ellipsoidal ones (2).

In the case of a solid smooth surface, light cannot be used to excite surface plasmons unless there are some mechanisms for photon–surface-plasmon coupling. It is well known that this coupling can be achieved through surface roughness (3), a grating (4) or evanescent waves in attenuated total-reflection methods (5). In this paper, we report evidence of the possibility of having a resonant absorption when a granular dielectric layer is deposited on a metallic surface. For that matter, ultrathin MgF_2 was used as the dielectric material and Au was the metallic substrate. The main features of the absorption can be accounted for by an effective-medium theory considering mirror-image effects. Some of the important results found by this approach are given together with suggestions for future work.

Theoretical considerations

The model used for describing the optical properties of a superficial granular overlayer has been described in previous works (6, 7). Basically, the particles constituting the overlayer are assumed to be of spheroidal shape and very small compared with the wavelength of light so that the dipole approximation can be justified. Dipole–dipole interactions can be taken into account and include two parts, one giving the interaction between the induced dipole in the particle and its mirror image in the substrate, and the other the interaction with surrounding particles located on the substrate. If the particles are sufficiently well separated, the interaction with surrounding particles can be neglected and one may only consider the interaction with mirror images in the substrate. It is precisely this interaction that allows the optical resonance to take place. The consideration of this interaction leads to the determination of an effective dielectric constant for the granular layer, which shows strong anisotropy characteristics. The effective depolarization factors $F_\parallel$ and $F_\perp$ for the spheroidal particle are found to be (6).

$$[1] \quad F_\parallel = f_\parallel - \left(\frac{\gamma^2}{24\eta^3}\right)\left[\frac{(\epsilon_b - 1)}{(\epsilon_s + 1)}\right]$$

and

$$[2] \quad F_\perp = f_\perp - \left(\frac{\gamma^2}{12\eta^3}\right)\left[\frac{(\epsilon_s - 1)}{(\epsilon_s + 1)}\right]$$

where the subscripts $\parallel$ and $\perp$ refer to directions parallel and perpendicular to the film plan, respectively, γ is the axial ratio of the particle, η is the distance separating the induced dipole and its mirror image divided by the rotational axis of the ellipsoid, and ϵ_s represents the dielectric constant of the substrate,

i.e., Au in the present study. The real depolarization factors $f_{\|}$ and $f_{\perp}$ are functions of the axial ratio of the particle. Their values increase with decreasing dimensions of the particle along the direction of the applied field. In particular, when the spherical shape is considered, $f_{\|}$ and $f_{\perp}$ are both equal to 1/3.

The expressions for the anisotropic dielectric granular overlayer are then given by:

$$[3] \quad \epsilon_{\|} = 1 + \frac{Q}{(F_{\|} + G)}$$

and

$$[4] \quad \epsilon_{\perp} = \left[1 - \frac{Q}{(F_{\perp} + G)}\right]^{-1}$$

where Q is the filling factor of the dielectric particles, and

$$[5] \quad G = \frac{1}{(\epsilon_i - 1)}$$

with ϵ_i representing the dielectric constant of the particles, i.e., of MgF_2 in the present work.

If $N_{\|} = (\epsilon_{\|})^{1/2}$, $N_{\perp} = (\epsilon_{\perp})^{1/2}$, and $N_s = (\epsilon_s)^{1/2}$, the reflectivity coefficients for p- and s-polarized light at the incident angle θ_o, are given by (8)

$$[6] \quad R_p = \frac{r_{1p} + r_{2p}\, e^{-j2\beta_p}}{1 + r_{1p}\, r_{2p}\, e^{-j2\beta_p}}$$

$$[7] \quad R_s = \frac{r_{1s} + r_{2s}\, e^{-j2\beta_s}}{1 + r_{1s}\, r_{2s}\, e^{-j2\beta_s}}$$

respectively, with

$$[8] \quad r_{1p} = \frac{N_{\|} N_{\perp} \cos\theta_o - (N_{\perp}^2 - \sin^2\theta_o)^{1/2}}{N_{\|} N_{\perp} \cos\theta_o + (N_{\perp}^2 - \sin^2\theta_o)^{1/2}}$$

$$[9] \quad r_{2p} = \frac{-N_{\|} N_{\perp} \cos\theta_o + N_s (N_{\perp}^2 - N_s^2 \sin^2\theta_s)^{1/2}}{N_{\|} N_{\perp} \cos\theta_o + N_s (N_{\perp}^2 - N_s^2 \sin^2\theta_s)^{1/2}}$$

$$[10] \quad \beta_p = 2\pi \frac{d}{\lambda} \frac{N_{\|}}{N_{\perp}} (N_{\perp}^2 - \sin^2\theta_o)^{1/2}$$

$$[11] \quad r_{1s} = \frac{\cos\theta_o - (N_{\|}^2 - \sin^2\theta_o)^{1/2}}{\cos\theta_o + (N_{\|}^2 - \sin^2\theta_o)^{1/2}}$$

$$[12] \quad r_{2s} = \frac{-N_s \cos\theta_s + (N_{\|}^2 - N_s^2 \sin^2\theta_s)^{1/2}}{N_s \cos\theta_s + (N_{\|}^2 - N_s^2 \sin^2\theta_s)^{1/2}}$$

$$[13] \quad \beta_s = 2\pi \frac{d}{\lambda} (N_{\|}^2 - \sin^2\theta_o)^{1/2}$$

It is noted that in the above formulas, the convention defining the imaginary part of the dielectric constant as negative is adopted. The dielectric film thickness is d and λ is the light wavelength. The angles θ_o and θ_s are related through $N_s \sin\theta_s = \sin\theta_o$.

Consequences of the model

With the above effective-medium model and tabulated data for material optical constants (9), the reflectivity of a gold substrate overcoated by a granular MgF_2 layer can be calculated. The granular film parameters can be chosen in such a way as to reflect realistic situations (6). Both the s- and p-polarizations of the incident light are considered and examples are shown in Figs. 1 and 2 for three different incidence angles, namely 0, 40, and 50. In Figs. 1 and 2 the magnitude of the drop in reflectivity of the gold surface when it is overcoated with MgF_2 is shown. At normal incidence the drop is of course identical for s- and p-polarizations, but as the incident angle is increased, a well-defined peak can be seen in the case of p-polarization while the maximum observed with s-polarization is rather broad. By contrast with the p-polarization case, the peak at normal incidence for s-polarized light is better defined than for higher angles of incidence. In general, it would be preferable to make experimental measurements with p-polarized light at oblique incidence to locate the absorption feature.

Comparison can also be made between gold surfaces overcoated, respectively, with a continuous MgF_2 layer and a granular MgF_2, having an equivalent mass thickness. Figure 3 shows such a comparison, and clearly in the case of a continuous overlayer no resonant structure can be found. One should however note the smallness of the drop in reflectivity.

If the coverage of the gold surface by the dielectric particles is increased, the drop in reflectivity can increase noticeably (Fig. 4). The same trend is also observed with the film thickness and the axial ratio of the particles.

Experimental results and discussion

Gold films of 100 nm thickness were first deposited in high vacuum on a glass slide and served as the metallic substrates. The purity of Au as quoted by the manufacturer was 99.999%. Very thin films of MgF_2 were formed on Au at room temperature by thermal evaporation. The thickness of the deposits was monitored by a quartz oscillator and varied from 2 to 8 nm. At such thicknesses, MgF_2 films would be discontinuous. Thicker and thus continuous films have also been prepared for comparison with theory. The drop in reflectivity with respect to bare Au films was then measured with incident p-polarized light and denoted by ΔR_p representing $R_p(\text{Au}) - R_p(\text{Au} + MgF_2)$. The incident angle was 40° in all cases. The optical measurements were made with a reflectometer (10) using a lock-in detection system and a Glan–Taylor prism as a polarizer. The reflectivity of each surface was stored in a computer and the difference in reflectivity between surfaces found directly. The general shape of the experimental curves for this difference can be easily reproduced with a precision of the order of 0.002.

In the case of very thin discontinuous MgF_2 overlayers, measurements clearly showed a peak in the reflectivity difference near the 520 nm wavelength. This is consistent with predictions of the theoretical model. To obtain more quantitative agreement between theory and experiment, a log–normal distribution function was introduced to account for the variety of particle shapes. A similar approach also can be found in previous studies on aggregated films (11). Such distributions

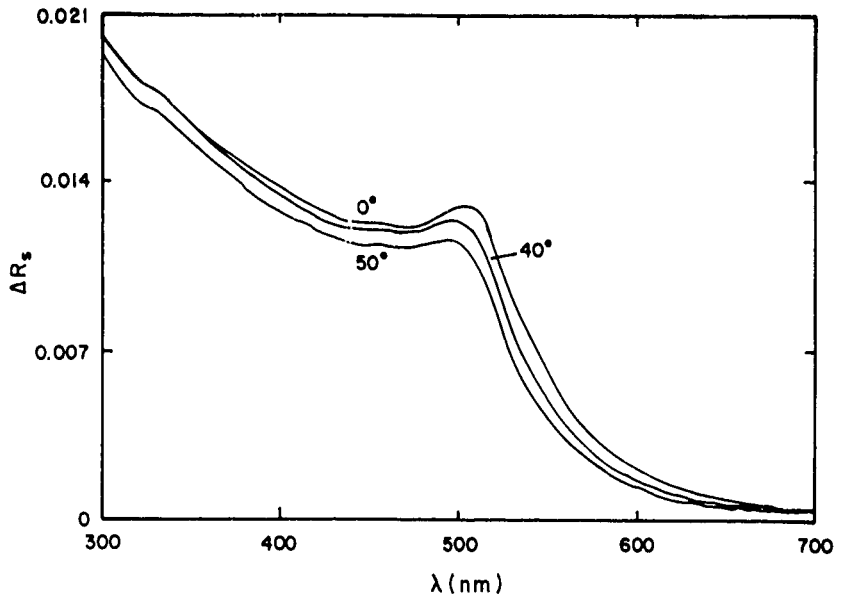

FIG. 1. The difference in s-polarized light between the bare Au substrate and the Au substrate overcoated with a MgF_2 film characterized by $\gamma = 2.0$, $Q = 0.3$, $\eta = 0.85$, and $d = 10$ nm. This difference, denoted by ΔR_s, is shown for three different angles of incidence: 0, 40, and 50°.

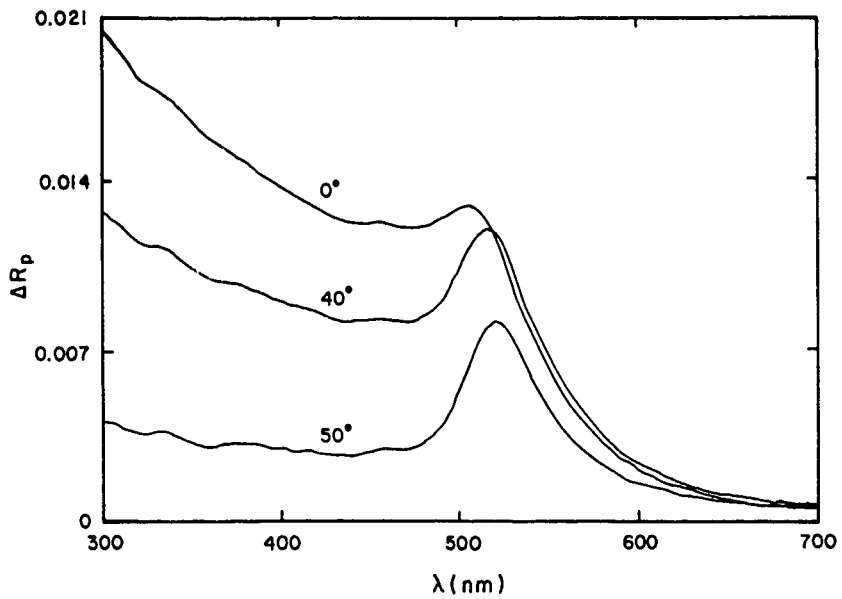

FIG. 2. Same as in Fig. 1, but with p-polarized light. The difference is now denoted as ΔR_p.

should be normalized to the filling factor for the granular layer and thus expressions [3] and [4] become:

$$[14] \quad \epsilon_{\parallel} = 1 + \int_1^{\infty} \frac{g(\gamma)}{F(\gamma) + G} \, d\gamma$$

$$[15] \quad \epsilon_{\perp} = \left[1 - \int_1^{\infty} \frac{g(\gamma)}{F_{\perp}(\gamma) + G} \, d\gamma \right]^{-1}$$

where $g(\gamma)$ represents the log–normal-distribution function.

Figures 5–7 show the experimental and calculated curves representing the magnitude of the reflectivity drop for three films of experimental mass thicknesses 2, 3, and 7.7 nm, respectively. The figure captions list the parameters used for obtaining the calculated curves. The mean axial ratio is found to vary between 2.1 and 2.5, suggesting that there is not much change in particle shape, and the filling factors for the three films are 0.23, 0.23, and 0.32, respectively. When thicker overlayers were deposited, the resonant feature in the reflectivity difference curve was less obvious. For those films, the granular nature may no longer be true and no satisfactory comparison with theory could be obtained. Good agreement

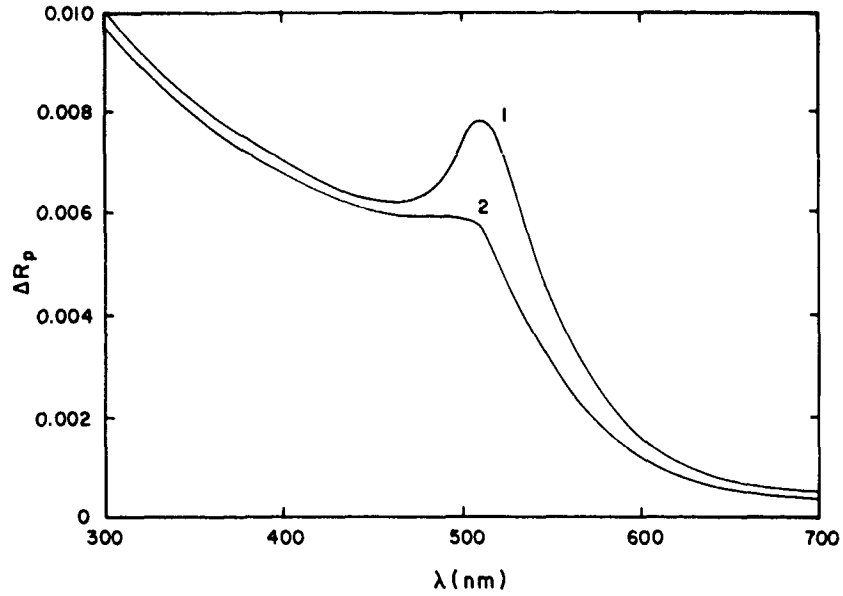

FIG. 3. ΔR_p at 40° calculated for a granular MgF_2 characterized by $\gamma = 2.0$, $Q = 0.2$, $\eta = 0.95$, and $d = 15$ nm (curve 1) and for a continuous MgF_2 film with an optical thickness of 3 nm.

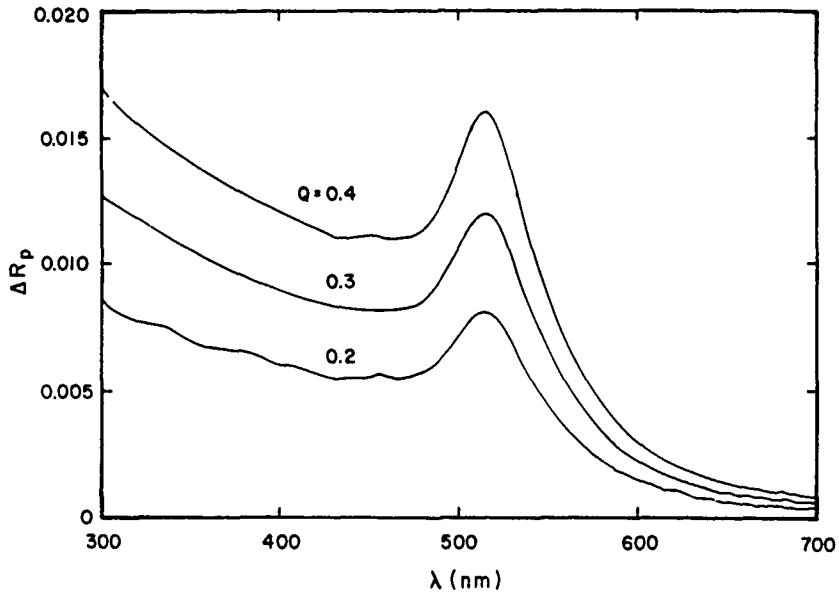

FIG. 4. ΔR_p at 40° calculated for a MgF_2 film characterized by $\gamma = 2.0$, $\eta = 0.85$, and $d = 10$ nm. The three curves are for respective Q values of 0.2, 0.3, and 0.4.

between measured values and calculated curves was however easily obtained with thick films such as a 50 nm MgF_2. In that case, calculations were performed with the overlayer considered as continuous. In a sense, a thickness of about 8 nm constituted an upper limit for the applicability of the model. Below the thickness of 2 nm, observation of the resonant feature was difficult owing to experimental limitation. These facts explain the relative narrow range of values for the thicknesses studied. It should be noted that the thickness parameter used in the calculations represents the optical thickness, which, in principle, would be given by the mass thickness divided by the filling factor Q. If such a relation is assumed, the parameters used would give 2.3, 2.6, and 8.5 nm, respectively, as mass thicknesses for the three films studied. Such values are not very far off the experimental ones which are 2, 3, and 7.7 nm, respectively.

Jasperson and Schnatterly (12), in a study of coupling between photon and surface plasmons in Ag foils, have used polarization modulation techniques to observe a resonance shift with increasing MgF_2 overcoat thickness. No attempt however

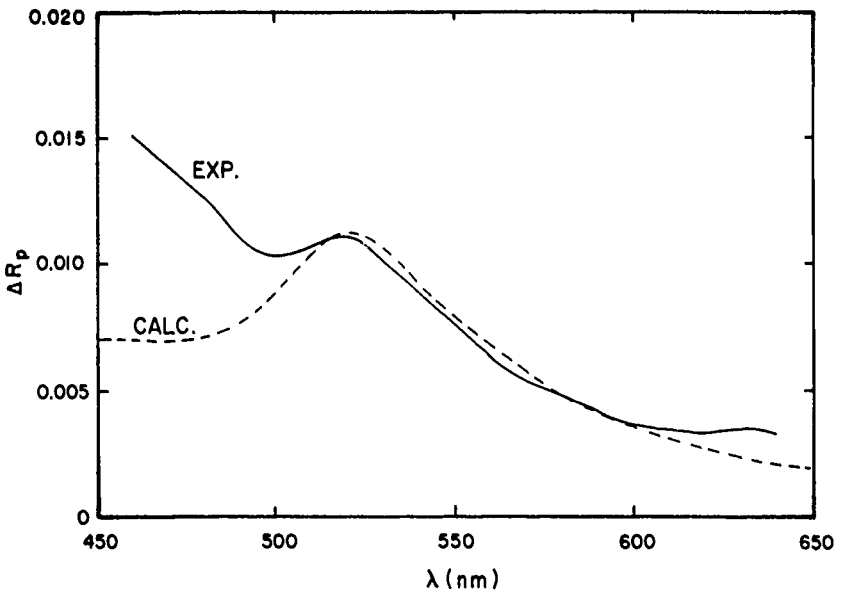

FIG. 5. ΔR_p at 40° as a function of wavelength. The continuous line curve is the experimental data, with a MgF_2 film having a mass thickness of 2 nm. The broken line curve is the calculated data, with the following parameters: $Q = 0.23$, $\eta = 0.97$, $d = 10$ nm, and a mean axial ratio of 2.2 with a standard deviation of 1.22.

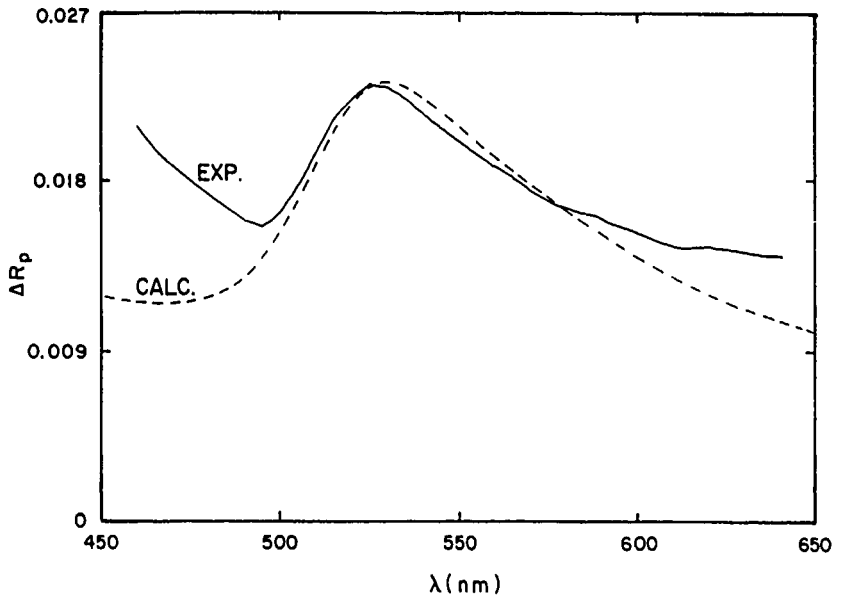

FIG. 6. ΔR_p at 40° as a function of wavelength. The continuous line curve is the experimental data, with a MgF_2 film having a mass thickness of 3 nm. The broken line curve is the calculated data, with the following parameters: $Q = 1.26$, $\eta = 0.99$, $d = 11.5$ nm, and a mean axial ratio of 2.5 with a standard deviation of 1.26.

was made to distinguish the granular and discontinuous nature of the overcoat and the authors suggested that such phenomenon may be attributed to impurities or surface roughness. Mirror-image effects have not been considered.

Concluding remarks

In this paper, we show that mirror-image effects may provide the necessary mechanism for coupling between the incident light and surface plasmons in metals. A resonant-type absorption can be observed when a granular MgF_2 is deposited on a smooth Au surface. As this overlayer thickens and becomes continuous, the structure in ΔR_p, found by calculations based on an effective-medium approach, is no longer observed. Instead, the experimental data are consistent with calculations performed assuming a continuous MgF_2 overlayer.

Attempts at using electron microscopy to characterize the very thin MgF_2 overcoat were not successful because of the smallness of the particles and the lack of good contrast in the micrographs. Based however on studies of dielectric film growth on metal substrates, it is not unreasonable to assume

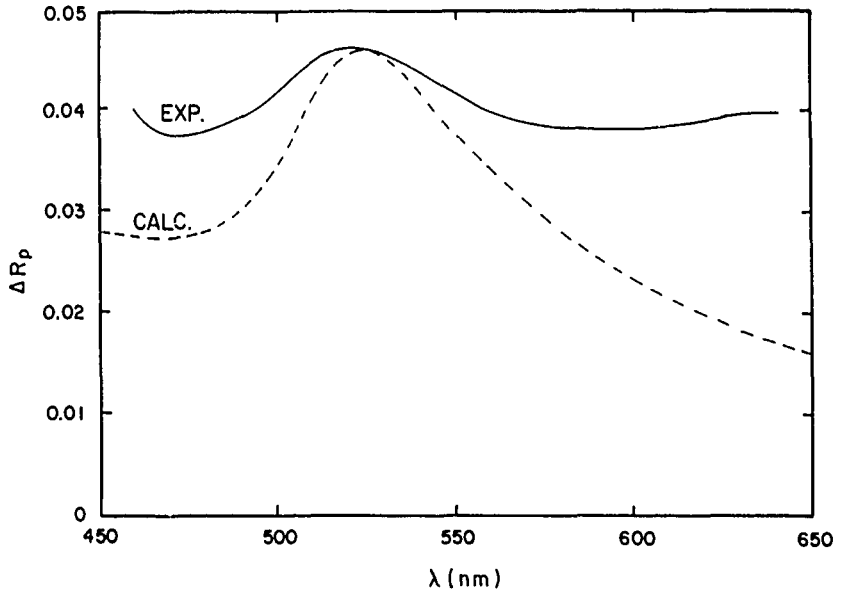

FIG. 7. ΔR_p at 40° as a function of wavelength. The continuous line curve is the experimental data, with a MgF_2 film having a mass thickness of 7.7 nm. The broken line curve is the calculated data, with the following parameters: $Q = 0.30$, $\eta = 0.98$, $d = 26.5$ nm, and a mean axial ratio of 2.1 with a standard deviation of 1.3.

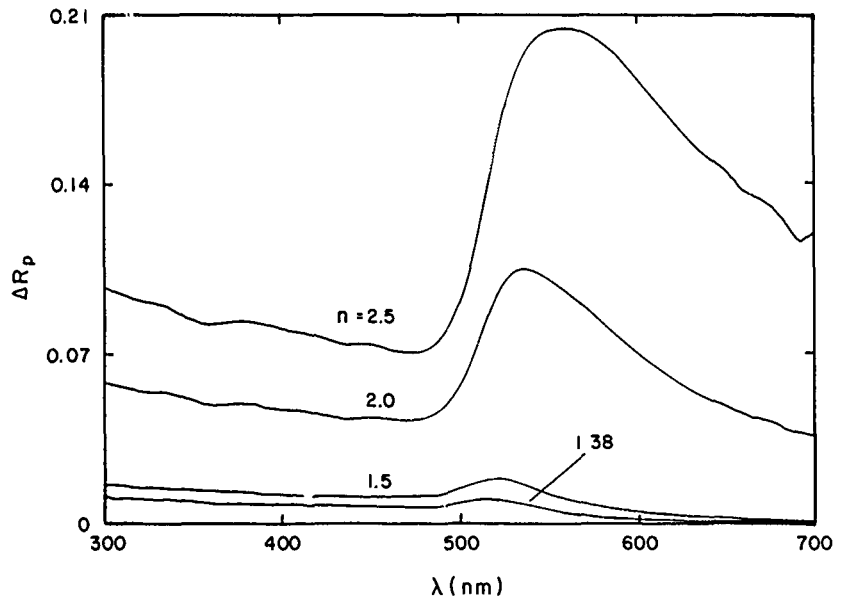

FIG. 8. ΔR_p at 40° calculated for films characterized by $\gamma = 2.0$, $\eta = 0.95$, and $d = 15$ nm with different values for the index of refraction.

the discontinuous nature of the very thin MgF_2 overcoats (13). Moreover, the washing out of the peak found in ΔR_p, with increasing overcoat thickness, seems to confirm this assumption.

More experiments are underway to confirm the observations made in the present work. Calculations, performed with the effective-medium approach presented above, give in particular a strong dependence on the optical constant of the dielectric material. Such a dependence can be seen in Fig. 8 where ΔR_p is calculated with realistic film parameters and size distribution. The peak found with MgF_2 is indeed minimal when compared with other materials of higher optical constant values. Preliminary results with tin oxide whose refractive index is near 2 have confirmed such behavior. Those results will be the subject of a subsequent paper.

In conclusion, experimental evidence and analysis based on an effective-medium theory may form the basis for further work on coupling between photon and surface plasmons via mirror-image effects provided by a granular dielectric overcoat. Thus, in addition to roughness and evanescent waves, this coupling mechanism may provide a new tool for studies of surface plasmons. Because of the reversibility of some adsorption processes on metallic surfaces, the above phenomenon may also be exploited for applications such as humidity or vapor sensors.

1. V. M. AGRANOVICH and D. L. MILLS (*Editors*). Surface polaritons, electromagnetic waves at surfaces and interfaces. North-Holland Publishing Co., Amsterdam. 1982.
2. L. WARD. The optical constants of bulk materials and films. The Adam Hilger Series on Optics and Optoelectronics. Adam Hilger, Bristol and Philadelphia. 1983. pp. 214–238; R. H. RITCHIE, J. C. ASHLEY, and T. L. FERRELL. *In* Electromagnetic surface modes. *Edited by* A. D. Boardman. John Wiley & Sons Ltd., Chicester. 1982. pp. 119–142.
3. J. M. ELSON and R. H. RITCHIE. Phys. Rev. B: Solid State, **4**, 4129 (1971).
4. U. FANO. J. Opt. Soc. Am. **31**, 213 (1941).
5. A. OTTO. Z. Phys. **216**, 398 (1968); E. KRETSCHMANN. Z. Phys. **241**, 313 (1971).
6. T. YAMAGUCHI, S. YOSHIDA, and A. KINBARA. Thin Solid Films, **21**, 173 (1974).
7. V. V. TRUONG and G. D. SCOTT. J. Opt. Soc. Am. **67**, 502 (1977).
8. R. M. A. AZZAM and N. M. BASHARA. Ellipsometry and polarized light. North-Holland Publishing Co., Amsterdam. 1977.
9. T. YAMAGUCHI, M. SAKAI, and N. SAITO. Phys. Rev. B: Condens. Matter, **32**, 2126 (1985); P. B. JOHNSON and R. W. CHRISTY. Phys. Rev. B: Solid State, **6**, 4370 (1972).
10. S. ELOUATIK. M. Sc. Thesis, Université de Moncton, Moncton. 1990.
11. S. YOSHIDA, T. YAMAGUCHI, and A. KINBARA. J. Opt. Soc. Am. **61**, 62 (1971); S. NORMAN, T. ANDERSSON, C. G. GRANQVIST, and O. HUNDERI. Phys. Rev. B: Condens. Matter. 18, 674 (1978).
12. S. N. JASPERSON and S. E. SCHNATTERLY. Phys. Rev. **188**, 758 (1969).
13. B. DREVILLON. Thin Solid Films, **163**, 157 (1988).

Semiclassical approximation for the isotopic shift of charge radii in Ca isotopes

GERASSIMOS S. ANAGNOSTATOS[1]

Center for Theoretical Physics, Laboratory for Nuclear Science and Department of Physics, Massachusetts Institute of Technology, Cambridge, MA 02139, U.S.A.

and

Institute of Nuclear Physics, National Center for Scientific Research "Demokritos," 153 10 Ag. Paraskevi, Attiki, Greece

AND

THEOHARIS S. KOSMAS,[2] ERNST F. HEFTER,[3] AND CONSTANTINE N. PANOS[4]

Institute of Nuclear Physics, National Center for Scientific Research "Demokritos," 153 10 Ag. Paraskevi, Attiki, Greece

Received February 27, 1990

The peculiar behavior of the rms-charge and mass radii of the Ca isotopes is explained by current approaches. Here these approaches are supplemented by microscopic calculations within the isomorphic shell model. The model verifies the trend of the data correctly, as a result of shell structure (particle–hole) and deformation effects. These results involve *two numerical* (not adjustable) parameters and are quantitatively at least equally as good as those of the best available theoretical calculations. In the case of ^{41}Ca, however, a further investigation is required.

Le comportement particulier des rayons (charge rms et masse) des isotopes de Ca est expliqué suivant les approches courantes. Ces approches ont été complétées ici par des calculs microscopiques dans le cadre du modèle en couches isomorphes. Ce modèle vérifie correctement la tendance des données, comme résultat de la structure des couches (particules–trous) et des effets de déformation. Nos résultats font intervenir *deux* paramètres *numériques* (non ajustables) et sont, du moins quantitativement, également en bon accord avec ceux des meilleurs calculs théoriques disponibles. Dans le cas de ^{41}Ca cependant, l'investigation devra être poussée plus loin.

[Traduit par la rédaction]

Can. J. Phys. 69, 114 (1991)

1. Introduction

The extent to which we can understand charge and matter distributions within nuclei describes the state of understanding of much more fundamental concepts, such as the particle's interactions and their importance in scattering and reaction phenomena.

The Ca isotopic series, with its large number of stable isotopes including two double-magic nuclei, constitutes a particularly excellent case of an isotopic chain for testing nuclear theories and exploring various methods of analysing nuclear-size experimental data (1–22).

In their recent paper Andl *et al.* (23) presented new experimental data for the relative (rms-charge) radii of the Ca isotopes together with a thorough discussion of the available theoretical interpretations. The emerging conclusion is that there are quite a few nice and interesting attempts to provide a theoretical description of these data. The one that comes closest to the data is a simple formula (23, 24) containing the number of particles in the $f_{7/2}$ shell and (depending on its usage), one to three adjustable parameters to fit nine data points. The recent paper by Talmi (25) gives a more detailed discussion of this formula and shows that it yields a rather nice correspondence to the experimental data with three fit parameters. In principle, however, these parameters can be calculated, if an effective interaction is given. Further references to this formula and to other approaches can be taken from the careful considerations presented in refs. 23–25, so there is no need to repeat them here.

Recently, some new experimental data (26, 27) and theoretical interpretations (28) of Ca isotopes have appeared. Barranco and Broglia (28) support the idea that it is likely that the presence of low-lying vibrations in the nuclear spectrum can influence some of the average nuclear properties, such as the mean square radius, through the associated zero-point fluctuations. This latest theoretical work deals with charge and matter rms radii, while Talmi's work (25) refers only to charge radii. However, ref. 25 includes odd and even Ca isotopes, while ref. 28 work deals only with even isotopes.

Hartree–Fock calculations (29, 30) predict a mean-square radius that is essentially constant. Thus, although they can reproduce the ^{48}Ca–^{40}Ca isotope shift (cf. refs. 31 and 32), they are unable to predict (28) the parabolic behaviour displayed by the charge mean-square radius between ^{40}Ca and ^{48}Ca.

Recently, there has been a further development, which might help to shed additional light on this problem. Calculations within the isomorphic shell model (33) have been pursued to such a stage that it is possible to evaluate the radii of these nuclei on a microscopic basis. Both charge and matter radii for even and odd Ca isotopes are examined, and in addition the binding energies of all these nuclei are consistently included. Thus, this work besides being microscopic deals with more nuclear properties than any other previous theory.

The main concepts used in the isomorphic shell model, which are that (*i*) nucleons are not dealt with as point particles, but as extended objects presented by their bags, and (*ii*) the average sizes of shells are determined by the close-packing of these bags

[1]Author to whom correspondence may be addressed.

[2]Permanent address: Theoretical Physics Division, University of Ioannina, Ioannina, Greece.

[3]Permanent address: The Institut fur Theoretische Physik, University Hannover, Appelstrasse 2, D-3000, Hannover 1, Germany.

[4]Permanent address: Department of Physics, Technological Educational Institutes, Thivon 250, 12244 Aegaleo, Greece.

(33), are almost identical to the concepts used in a recent paper. This paper deals with the charge symmetry violation in the structure of the ^3H–^3H sysem (34), with three-body forces.

Both of these papers and this paper are in the spirit of a review paper by Thomas (35) describing how a system of finite-size bags might behave. In this review, for the size of bags considered here, chains of bags touching one another are reasonably expected, like the instantaneous successive contact of bags from the inner shell to the outer shell of a nucleus in the isomorphic shell model (33).

The purpose of this paper is to show that the isomorphic shell model, catering in a microscopic way for shell (particle–hole) effects and deformations, and based on *two numerical* parameters, yields results for the isotopic shifts of charge and matter radii that are close to experiment and at least as equally good as the best theoretical results available (25, 28).

2. The isomorphic shell model

A comprehensive and exhaustive development of the semiclassical part of the model and a brief development of the quantum mechanical part of the model can be found in refs. 33 and 36. Here, only a short outline of the semiclassical part of the model follows, to assist in the comprehension of the present paper.

2.1. *Assumptions and their justifications*

The model employs the following two assumptions:

(*i*) The neutrons (protons) of a closed neutron (proton) shell, considered at their *average* positions, are in *dynamic equilibrium* on the sphere presenting the average size of that shell.

(*ii*) The average sizes of the shells are determined by the *close-packing* of the *the shells* themselves, provided that a neutron and proton are represented by *hard spheres* of definite sizes (i.e., $r_n = 0.974$ fm and $r_p = 0.860$ fm).

It is apparent that assumption (*i*) is along the lines of the shell model, while assumption (*ii*) is along the lines of the liquid-drop model. Thus, the isomorphic shell model is a microscopic nuclear-structure model that incorporates into a hybrid model the prominent features of single-particle and collective approaches, in conjunction with the nucleon finite size.

The model employs a specific equilibrium of nucleons, considered at their average positions on concentric spherical cells, which is valid whatever the law of nuclear force may be: assumption (*i*). This equilibrium leads uniquely to Leech (37) (equilibrium) polyhedra as average forms of nuclear shells. All such nested polyhedra are close-packed thus taking their minimum size: assumption (*ii*). The cumulative number of vertices of these polyhedra, counted successively from the innermost to the outermost, reproduce the magic numbers each time a polyhedral shell is completed (33) (see the numbers in the brackets in Fig. 1).

For one to intuitively conceive the isomorphic shell model, one should first relate this model to the conventional shell model. Specifically, the main assumption of the simple shell model, that is, that each nucleon in a nucleus moves (in an average potential due to all nucleons) independently of the motion of the other nucleons may be understood here in terms of a *dynamic equilibrium* in the following sense (33). Each nucleon in a nucleus is *on average* in a *dynamic equilibrium* with the other nucleons and, as a *consequence*, its motion may be described independently of the motions of the other nucleons. From this one realizes that dynamic equilibrium and independent particle motion are *consistent* concepts in the framework of the isomorphic shell model.

In other words, the model implies that *at some instant in time* (reached *periodically*) all nucleons could be thought of as residing at their individual average positions, which coincide with the vertices of an equilibrium polyhedron for each shell. This system of particles evolves in time according to each independent particle motion. This is possible, since axes standing for the angular-momenta quantization of directions are *identically* described by the rotational symmetries of the polyhedra employed (38–41). For example, see ref. 40, where one can find a complete interpretation of the independent particle model in relation to the symmetries of these polyhedra. Such vectors are shown in Fig. 1 for all orbital angular-momentum quantization of directions involved in nuclei up to $N = 50$ and $Z = 40$. Thus, the polyhedra invoked by the isomorphic shell model possess some unique properties:

They are equilibrium polyhedra and thus consistent with the independent particle motion assumed by the conventional shell model.

Their vertices are identical, a property that is consistent with the fundamental requirement of indistinguishability of identical particles.

Degenerate energy levels are expected to have angular-momentum quantization of directions indistinguishable from each other, which implies that these directions should transform into each other through the symmetry operations of a rotation group. This requirement is fulfilled by the symmetry properties of these polyhedra as explained in ref. 41.

They permit periodic appearance of the average forms of nuclear shells, if their vertices are assumed to rotate round the orbital angular-momentum quantization of direction vectors as shown in Fig. 1. Thus, these polyhedra represent the *average motion patterns* of nucleons. The independent particle motion of nucleons could be imagined (harmonized) in such a way that the nucleons pass *periodically* through the equilibrium polyhedra vertices standing for their average positions.

The model for the shells 1*s*, 1*p*, 1*d*, and 2*s* for neutrons and protons, *f*, *g*, *h* 9/2 for neutrons, and 1*f* 7/2 for protons is presented in Fig. 1, where the shapes shown are concentric equilibrium polyhedra standing for average forms of the indicated nuclear shells. All the symbols included in Fig. 1 are explained in the figure caption.

As we will see shortly (Sect. 3), the nuclear properties in the model are derived as properties of the quantum cluster consisting of the average positions of nucleons for the specific nucleus, according to Fig. 1.

2.2. *Technical details of the model*

In the isomorphic shell model, while for closed-shell nuclei a specified polyhedron with a definite radius R stands for the average form of a specific neutron or proton shell (characterized by the letters N and Z, respectively; see Fig. 1), for open-shell nuclei the valent-nucleon average positions may occupy vertices of the next (either) neutron or proton polyhedral shell. This, together with the consideration of different neutron and proton bag sizes, is the reason that two values for the radius of the exscribed sphere for each polyhedron are given (and also two values of ρ; see the last two rows in each block of Fig. 1). Those values in the first row (R and ρ) correspond to the case

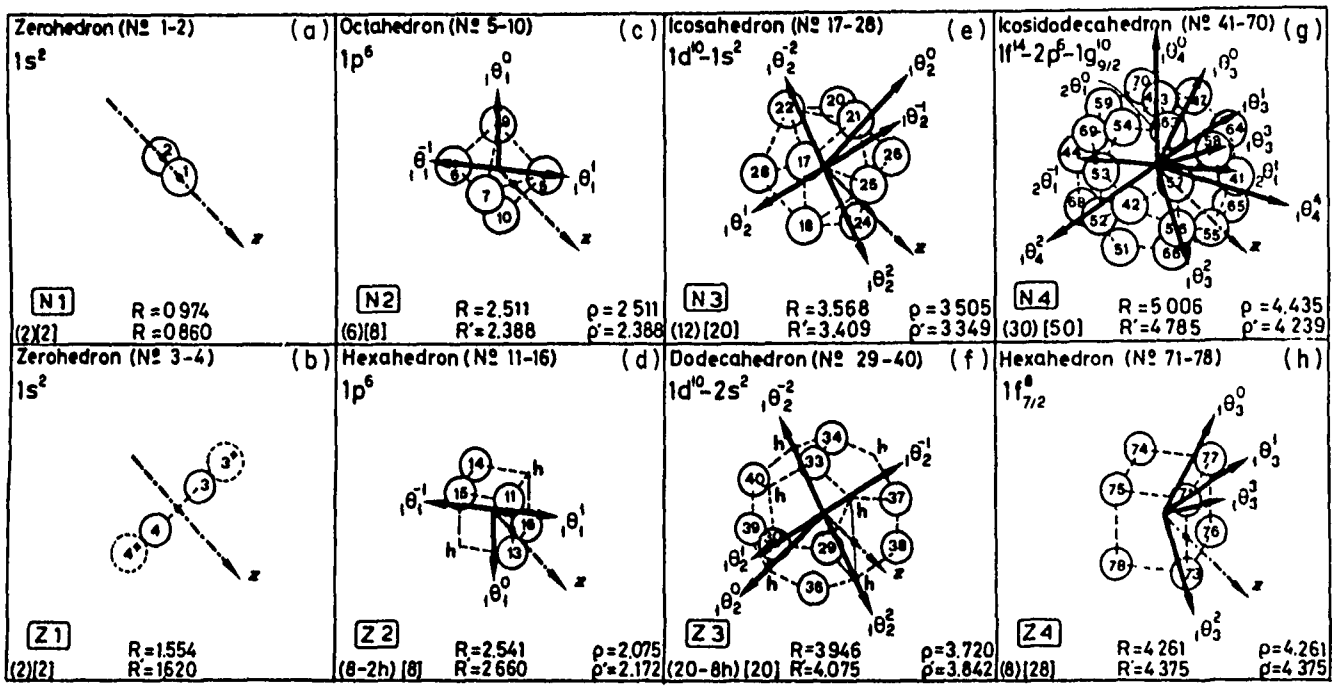

FIG. 1. The isomorphic shell model for the nuclei up to $N = 50$ and $Z = 28$. The high-symmetry polyhedra in row 1 stand for the average forms for neutrons of (*a*) the 1*s*, (*c*) the 1*p*, (*e*) the 1*d*–2*s*, and (*g*) the 1*f*–2*p*–1*g* 9/2 shells, while the polyhedra in row 2 stand for the average forms of (*b*) the 1*s*, (*d*) the 1*p*, (*f*) the 1*d*–2*s*, (*h*) the 1*f* 7/2 shells for protons. The vertices of polyhedra stand for the average positions of nucleons in definite quantum states (τ, n, l, m, s). The letters h stand for the empty vertices (holes). The z axis is common for all polyhedra when these are superimposed with a common centre and with relative orientations as shown. At the bottom of each block the number of succession of the neutron (N) or proton (Z) shell is shown inside a box. Underneath this box, the number of vertices of the specific polyhedron and the number of holes (where they exist) are given in parentheses, while inside square brackets the cumulative number of average nucleon positions is given. Values of R give the radii of the spheres exscribed to the polyhedra, while values of ρ give the maximum distances of the vertices states (τ, n, l, m, s) from the axes ${}_n\theta^m$ precisely representing orbital angular momentum axes with definite n, l, and m values. The difference between R and R', and ρ and ρ', is explained in the text. All polyhedral vertices are numbered, as shown. The numbers employed for each polyhedron are given inside parenthesis at the top of the relevant block. The backside (hidden) vertices of the polyhedra and related numbering are not shown in the figure. Specifically, 3^+ and 4^+ refer to neutron average positions (whose related bags are shown in broken line in Fig. 1*b*) which form a zerohedron in the same line with $Z1$ and in close-packing with it.

where neutrons(protons) have average positions at the vertices of the neutron(proton) polyhedron shell, i.e., $N1(Z1)$, $N2(Z2)$, $N2(Z3)$, and $N4(Z4)$, while those in the second row (R' and ρ') correspond to the case where protons(neutrons) have average positions at the vertices of the neutron(proton) polyhedral shell, i.e., $N1(Z1)$, $N2(Z2)$, $N3(Z3)$, and $N4(Z4)$, while those in the second row (R' and ρ') correspond to the case where protons(neutrons) have average positions at the vertices of the neutron(proton) polyhedral shell, i.e., on $N1'(Z1')$, $N2'(Z2')$, $N3'(Z3')$, and $N4'(Z4')$. Following the same reasoning, the vertices of the different polyhedra may be referred to, in the text or in the tables, by unprimed or primed numbers. In Appendix C of ref. 33 way of correlating R and bag size is explained in every detail. The ρ' values come by multiplying the ρ values by the ratio R'/R.

Since the radial and angular parts of the polyhedral shells in Fig. 1 are well defined, the coordinates of the polyhedral vertices (nucleon average positions) can be easily computed. These coordinates up to $N = Z = 20$ are already published in footnote 14 of ref 42 and in footnote 15 of ref. 43, while for $N = 21$–50 and $Z = 21$–28 they are given here.[5] These coordinates correspond to the R values of the exscribed polyhedral spheres,

[5]Coordinates (x, y, z, in units of femtometres) of 40 nucleon average positions (NAP), i.e., of NAP41–NAP78, and NAP3$^+$ and NAP4$^+$ according to the numbering of Fig. 1.

NAP41: (0.000, 5.006, 0.000);	51: (2.503, −1.547, −4.050);	61: (−4.050, −2.503, −1.547);	71: (2.460, 2.460, 2.460);
42: (5.006, 0.000, 0.000)	52: (4.050), −2.503, −1.547)	62: (−1.547, −4.050, −2.503)	72: (−2.460, −2.460, −2.460)
43: (0.000, 0.000, 5.006);	53: (4.050, −2.503, 1.547);	63: (2.503, 1.547, 4.050);	73: (2.460, 2.460, −2.460);
44: (0.000, −5.006, 0.000)	54: (2.503, −1.547, 4.050)	64: (−1.547, 4.050, 2.503)	74: (−2.460, −2.460, 2.460)
45: (−5.006, 0.000, 0.000);	55: (1.547, 4.050, −2.503);	65: (−1.547, 4.050, −2.503);	75: (2.460, −2.460, 2.460);
46: (0.000, 0.000, −5.006)	56: (4.050, 2.503, −1.547)	66: (2.503, 1.547, −4.050)	76: (−2.460, 2.460, −2.460)
47: (−2.503, 1.547, 4.050);	57: (4.050, 2.503, 1.547);	67: (−2.503, −1.547, −4.050);	77: (−2.460, 2.460, 2.460);
48: (−4.050, 2.503, 1.547)	58: (1.547, 4.050, 2.503)	68: (1.547, −4.050, −2.503	78: (2.460, −2.460, −2.460)
49: (−4.050, 2.503, −1.547);	59: (−1.547, −4.050, 2.503);	69: (1.547, −4.050, 2.503);	3+: (−1.956, 1.956, 1.956);
50: (−2.503, 1.547, −4.050)	60: (−4.050, −2.503, 1.547)	70: (−2.503, −1.547, 4.050)	4+: (1.956, −1.956, −1.956).

The numbering of the first nucleon average positions (NAP) given by Anagnostatos and Panos (43, 44) is related to that of Fig. 1 according to the following correspondence: $N1$-$N2$: 1-2; $Z1$-$Z2$: 3-4; $N3$-$N8$:5-10; $Z3$-$Z8$: 11-16; $N9$-$N20$: 17-28; and $Z9$-$Z20$: 29-40.

TABLE 1. Vertex configurations and calculated potential, Coulomb, kinetic, and binding energies of the ground states for Ca isotopes (A = 40–48), and experimental binding energies

Isotope	Vertex configuration		ΣV_{ij}^{c} (MeV)	ECoul.^{d} (MeV)	$A\langle T\rangle_{nlm}^{e}$ (MeV)	$E\delta^{f}$ (MeV)	BE (MeV)	
	Core[a]	Valent[b]					Model[f]	Expt.[g]
40	2h (21, 26)	$2p\,\overline{2\nu\,(41, 42)}$	747.0	64.8	339.5	0.0	342.7	342.063
41	2h (21, 34)	$3p\,\frac{1\pi\,(84')}{2\nu\,(41, 42)}$	784.5	65.2	366.4	3.3	349.6	350.427
42	3h (26, 29, 30)	$5p\,\frac{2\pi\,(72, 74)}{2\nu\,(59, 60, 70)}$	801.2	66.0	373.7	0.0	361.5	361.900
43	1h (34)	$4p\,\frac{1\pi\,(72)}{3\nu\,(61, 62, 67)}$	827.7	65.2	388.2	3.1	371.1	369.832
44	2h (30.36)	$6p\,\frac{2\pi\,(72, 74)}{4\nu\,(59, 60, 61, 70)}$	851.7	65.8	402.8	0.0	383.1	380.969
45	1h (34)	$6p\,\frac{1\pi\,(71)}{5\nu\,(57, 58, 63, 3^{+}, 75')}$	880.1	65.1	424.1	3.0	387.9	388.383
46	1h (34)	$7p\,\frac{1\pi\,(71)}{6\nu\,(57, 58, 63, 3^{+}, 73', 75')}$	900.3	65.1	437.7	0.0	397.5	398.787
47	0h	$7p\,\overline{7\nu\,(3^{+}, 4^{+}, 71'–75')}$	926.1	64.8	451.8	2.9	406.6	406.063
48	0h	$8p\,\overline{8\nu\,(3^{+}, 4^{+}, 71'–76')}$	946.1	64.8	465.5	0.0	415.8	416.014
41[h]	1h (34)	$2p\,\frac{1\pi\,(71)}{1\nu\,(57)}$	779.8	65.1	363.1	3.3	348.3	350.427

[a]h stands for hole, which refer to proton or neutron average positions as shown in the parenthesis following.
[b]p, π, and ν stand for particles, protons, and neutrons, respectively. Primed and unprimed numbers refer to the numbering of polyhedral vertices, as shown in Fig. 1 and explained in the text. Specifically, 3^{+} and 4^{+} refer to neutron average positions as shown by the broken line in Fig. 1b.
[c]Computed for all pairs of nucleons i and j, according to [1].
[d]Computed for all proton pairs, according to [2].
[e]Average kinetic energy per particle computed according to [3].
[f]Computed according to [4].
[g]From ref. 56.
[h]An alternative model consideration. See text.

while those corresponding to R' come from the previous by multiplying by R'/R.

According to the isomorphic shell model, the nucleon average positions of a nucleus are distributed at the vertices of the polyhedral shells, as shown, for example, in Fig. 1. The specific vertices occupied, for a given (closed- or open-shell) nucleus at the ground state, form a vertex configuration (corresponding to a state configuration) that possesses maximum binding energy (BE) in relation to any other possible vertex configuration. This maximum BE vertex configuration defines the average form and structure of the ground state of this nucleus. All bulk (static) ground-state properties of this nucleus (e.g., BE, rms radii, etc.) are derived as properties of this structure, as has been fully explained in ref. 33 and references cited therein.

The quantities estimated by the model in the framework of this paper (see the next section) are: potential energy, V_{ij}; Coulomb energy, $(E_C)_{ij}$; average kinetic energy, $\langle T\rangle_{nlm}$; odd–even energy, E_δ; binding energy, E_{BE}; and rms charge, and neutron and mass radii, $\langle r^2\rangle^{1/2}$ of the $^{40-48}$Ca isotopes, by using [1]–[7], respectively, (33, 42, 44).

$$[1]\quad V_{ij} = 1.7(\times 10^{17})\,\frac{e^{-(31.8538)r_{ij}}}{r_{ij}} - 187\,\frac{e^{-(1\,3538)r_{ij}}}{r_{ij}}$$

where the internucleon distance r_{ij} is estimated following Fig. 1 or (the same) the corresponding coordinates of polyhedral vertices (see footnote 3 here, and footnotes 14 and 15 in refs. 42 and 43, respectively).

$$[2]\quad (E_C)_{ij} = \frac{e^2}{r_{ij}}$$

where distances r_{ij} are computed as explained above.

$$[3]\quad \langle T\rangle_{nlm} = \frac{\hbar 2}{2M}\left(\frac{1}{R^2_{max}} + \frac{l\,(l+1)}{\rho^2_{nlm}}\right)$$

where R_{max} is the outermost polyhedral radius (R) plus the relevant nucleon raduis (r_n = 0.974 fm and r_p = 0.860 fm), i.e., the radius of the nuclear volume in which the nucleons are confined, M is the nucleon mass, ρ_{nlm} is the distance (44) of the vertex (n, l, m) from the axis ${}_n\theta^m 1$ (see Fig. 1).

TABLE 2. Calculated and experimental root-mean-square charge radii ($<r^2>^{1/2}_{ch}$ in fm) for Ca isotopes (A = 40–48)

Isotope	Isomorphic shell model[a]	Experiment (e, e)	Experiment μ atom	Experiment μ atom	2p3/2-1s1/2 transitions Ref. 58	2p3/2-1s1/2 transitions Ref. 16
40	3.471	3.474(3)[b]	3.479[b]	3.480[b]	3.4813	3.4800
41	3.464					
42	3.506	3.504[c]	3.510[b]	3.510[b]	3.5115	3.5101
43	3.487				3.4980	3.4966
44	3.504	3.502[c]	3.518[b]	3.520[b]	3.5214	3.5201
45	3.485					
46	3.484		3.497[b]	3.501[b]	3.5024	3.5011
47	3.465					
48	3.464	3.465(5)[b]	3.475[b]	3.481[b]	3.4823	3.4809
41[d]	3.488					

[a]Model predictions according to [5].
[b]From ref. 57.
[c]From ref. 15.
[d]An alternative model consideration. See text.

$$[4]\quad E_{BE} = -\sum_{\substack{\text{all nucleon}\\ \text{pairs}}} V_{ij} - \sum_{\substack{\text{all proton}\\ \text{pairs}}} \frac{e^2}{r_{ij}} - \sum_{\substack{\text{all}\\ \text{nucleons}}} A<T>_{nlm} - E_\delta$$

where distances r_{ij} are estimated as above and E_δ is a correction "odd–even" term familiar from the liquid drop model. Here its value is equal to zero for even-Z – even-N nuclei for which our potential in [1] is exclusively derived (42) and thus no correction is needed, while for odd-A nuclei its value is taken (45) equal to 135/A MeV.

$$[5]\quad <r^2>^{1/2}_{ch} = \left[\sum_{i=1}^{Z} \frac{R_i^2}{Z} + (0.8)^2 - (0.116)\frac{N}{Z}\right]^{1/2}$$

$$[6]\quad <r^2>^{1/2}_{n} = \left[\sum_{i=1}^{N} \frac{R_i^2}{N} + (0.91)^2\right]^{1/2}$$

and

$$[7]\quad <r^2>^{1/2}_{m} = \left[\sum_{i=1}^{N} \frac{R_i^2}{Z} + \sum_{i=1}^{N} \frac{R_i^2}{N} + \frac{Z(0.8)^2 + N(0.91)^2}{Z+N}\right]^{1/2}$$

where the subscripts ch, n, and m refer to charge, neutron, and mass and where R_i is the radius of the ith proton or neutron average position and from Fig. 1, Z and N are the proton and the neutron numbers of the nucleus, 0.8 and 0.91 fm are the rms radii of a proton and of a neutron, and -0.116 fm^2 is the *ms* charge radius of a neutron (46). The 0.91 fm value for a neutron is taken from the 0.8 fm value for a proton by considering proportionality according to the sizes of their bags 0.974 and 0.860 fm, respectively, i.e., 0.91 = 0.8 (0.974/0.860).

3. Results and discussion

Our computer program re-arranges, in all possible ways, the nucleons of the nucleus under examination at the vertices of the close-packed polyhedral shells, as shown in Fig. 1, or as specified by the relevant coordinates of the polyhedral vertices (42, 43). For each such arrangement (given that the ground-state spin and parity are satisfied), using [1]–[4], the potential, Coulomb, kinetic, and binding energies are determined. The vertex configuration whose binding energy is larger than that of any other configuration corresponds to the nuclear ground state, and its charge, neutron, and mass radii are estimated by using [5]–[7].

In Table 1, columns 2 and 3, the ground-state vertex configurations are given for all nine Ca isotopes examined. In columns 4–7, the total potential, Coulomb, kinetic, and odd–even energies (respectively) for each isotope, corresponding to the given vertex configuration, are listed. In columns 8 and 9, the calculated and experimental binding energies are shown. The agreement between these two last values is satisfactory. One can visualize the shell structure and deformation for each Ca isotope by using the configuration numbers of columns 2 and 3, and Fig. 1, where these numbers are used to identify the nucleon average positions.

In Table 2 for the same vertex configurations, as in Table 1, the isomorphic shell-model values for the charge rms radii are given (column 2). In columns 3–7 experimental radius values, where they exist, are given from different references. The agreement between these values and our calculated values is also satisfactory. The model and experimental values for $<r^2>^{1/2}_{ch}$ from Table 2 are shown in Fig. 2 together with the theoretical values from ref. 28. This reference examines only even isotopes, and its prediction for ^{44}Ca shows a rather large deviation from the experimental value and our value for this isotope.

In Table 3 the $\delta<r^2>$ values for the model, derived from Table 2, and for three references are given. The agreement is also good. The model values, based on two numerical parameters (i.e., the sizes of neutron and proton bags; see solid line and open circles) and the experimental values from ref. 23 (solid circles) are presented in Fig. 3 for a visualization of the comparison. The best available theoretical calculations for even and odd isotopes (25), based on three adjustable parameters, are also shown for a further comparison. Both calculations give good results and the difference between them refers mainly to

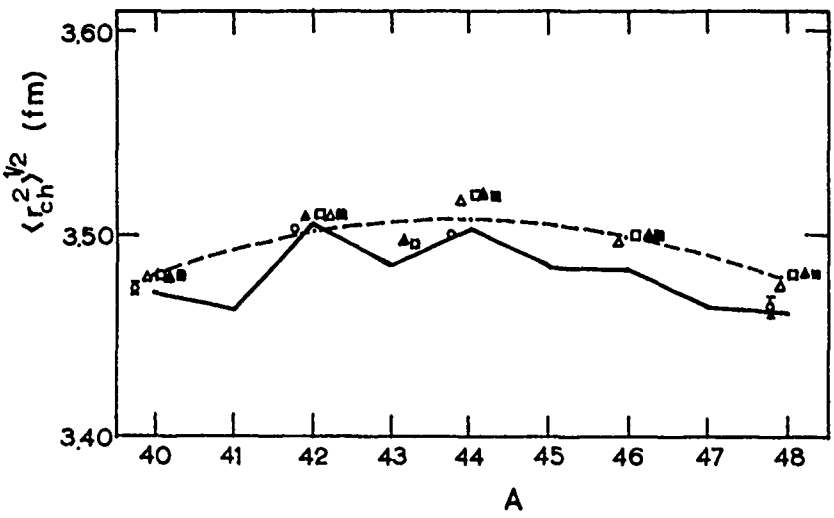

FIG. 2. Root-mean-square charge radii $\langle r^2_{ch} \rangle^{1/2}$, of $^{40-48}$Ca isotopes. Symbols ■, ▲, □, ○, and △ present experimental data from different methods as shown in Table 2, columns 1–5, respectively. The solid line stands for the present calculations, while the broken line presents calculations from ref. 28.

TABLE 3. Calculated and experimental mean-square charge radii ($\delta\langle r^2 \rangle_{ch}$ in fm^2) for Ca isotopes (A = 40–48)

40–A	Isomorphic shell model[a]	Optical isotope shifts[b]	Isotope shifts $4s^2{}^1S_0$–$4s4p{}^1P_1$ resonance[c]	Isotope shifts[d] $2p$ 3/2 – $1s$ 1/2
40–41	−0.049	0.0033(28)	−0.012(7)	
40–42	0.244	0.2198(71)	0.221(12)	0.215(11)
40–43	0.111	0.1286(70)	0.117(6)	0.116(24)
40–44	0.230	0.290(10)	0.293(12)	0.298(9)
40–45	0.097	0.127(10)	0.128(20)	
40–46	0.090	0.136(11)	0.128(8)	0.164(43)
40–47	−0.042	0.036(26)	0.007(10)	
40–48	−0.049	0.010(12)	0.000(9)	−0.001(6)
40–41[e]	0.118			

[a]From Table 2.
[b]From ref. 59.
[c]From ref. 23.
[d]From ref. 16.
[e]An alternative model consideration. See text.

the number (two versus three) and kind (numerical versus adjustable) of parameters employed by each of them Talmi's prediction (25), however, for ^{46}Ca shows a rather large deviation from the experimental and our values for this isotope.

The arrows in Fig. 3 show the directions that our isomorphic-model results will follow on the figure, if mixing of configurations are considered for the cases of ^{42}Ca and ^{44}Ca (0h and 2h, and 0h, 2h, and 4h, respectively). Indeed, such mixing leads to an improvement of our radii.

In the case of ^{41}Ca, the isomorphic shell model cannot distinguish between two values of the charge rms radius: the one leading to a small negative and the other to a rather large positive value of $\delta\langle r^2 \rangle$. Before additional properties, e.g., quadrupole moments, are evaluated, we consider both values for this isotope. Thus, both values are shown in Fig. 3 and discussed in Tables 1–3. In general, the study of ^{41}Ca here is not considered complete and a further investigation is required. It is interesting, however, that very recent experimental data (47) concerning this isotope specify the $f_{7/2}$ neutron radius as 3.99 ± 0.06 fm, which is in fair agreement with our value 4.375 fm (see Fig. 1h).

In Table 4 for the same vertex configurations, as in Table 1, the isomorphic shell-model values for the neutron and mass rms radii for all Ca isotopes are given together with experimental values from different references for comparison. The agreement is satisfactory as well. The best agreement between our results and the experimental data, as becomes obvious from this table, corresponds to the most recent data of 20–50 MeV proton scattering on Ca isotopes (26). For a visualization of the comparison all information from Table 4 is shown in Figs. 4 and 5, together with the theoretical prediction of Barranco and Broglia (28) for rms mass radii (Fig. 5). Finally in Table 5, calculated and experimental Δr_{np} values for ^{40}Ca–^{48}Ca are given for an overall comparison with the present work.

TABLE 4. Calculated and experimental root-mean-square neutron and mass radii ($\langle r^2\rangle^{1/2}_n$ and $\langle r^2\rangle^{1/2}_m$ in fm) for Ca isotopes (A = 40–48)

Isotope	Isomorphic shell mode		Proton scattering (26) (20–50 MeV)		α-particle scattering (6) (1.37 GeV)		Proton scattering (7)		α scattering (61) (166 MeV)	Proton electron scattering
A	$\langle r^2\rangle^{1/2}_n$	$\langle r^2\rangle^{1/2}_m$	$\langle r^2\rangle^{1/2}_n$	$\langle r^2\rangle^{1/2}_m$	$\langle r^2\rangle^{1/2}_n$	$\langle r^2\rangle^{1/2}_m$	$\langle r^2\rangle^{1/2}_n$	$\langle r^2\rangle^{1/2}_m$	$\langle r^2\rangle^{1/2}_n$	$\langle r^2\rangle^{1/2}_n$
40	3.42	3.45	3.42±0.06	3.41±0.03	3.46±0.05	3.47±0.025	3.50±0.03	3.49	3.43±0.12	3.45
42	3.52	3.52	3.48±0.13	3.45±0.07	3.54±0.05	3.53±0.025	3.58±0.03	3.54		3.50
43	3.53	3.52								
44	3.61	3.57	3.53±0.17	3.48±0.09	3.60±0.05	3.56±0.025	3.60±0.03	3.55	3.61±0.16	3.52
45	3.57	3.54								
46	3.61	3.57								
47	3.51	3.50								
48	3.55	3.53	3.60±0.11	3.51±0.06	3.67±0.05	3.59±0.025	3.66±0.003	3.58	3.80±0.12	3.58

Besides the numerical comparison of our results with those of other theories, one should notice the basic differences in a physical sense among these theories. Specifically, Talmi's (25) predictions are based on a simple formula containing the number of particles in the $f^{7/2}$ shell, the Barranco and Broglia (28) predictions are based on the assumption that the presence of low-lying vibrations in the nuclear spectrum can influence nuclear radii through the associated zero-point fluctuations, while our predictions are based on shell structure (particle–hole) and deformation effects. Moreover, it is interesting to notice that the number of holes predicted by our model (see Table 1) for ^{42}Ca (2 holes), ^{44}Ca (2 holes), and ^{46}Ca (1 hole) are in good agreement with the number of holes (i.e., 1.7, 1.8, and 1.05, respectively) predicted by Hodgson (48) using a completely different approach.

The credibility of the model's accuracy in evaluating charge radii and binding energies is discussed further below. While the radii come directly from the geometry of the model, by using, for example, [5], the binding-energy calculations, in addition to the geometry of the model, require a two-body potential, e.g., that of [1], which is used throughout the model, but it is not an unseparable part of the model. That is, instead of the potential in [1], other successful effective potentials could be used.

To start with, we coment on the potential of [1]. First, the constants of this two-Yukawa potential have been determined by Anagnostatos and Panos, see ref. 42, using the free nucleon-scattering cross sections, prior to and independent of the material in the present paper. Second, if another effective potential had been employed, the numerical value of the BE for each isotope could be different, but the largest binding energy (among the energies of the different possible occupied vertex configurations) would correspond to the same (as here) vertex configuration, and thus the ground-state charge radius would also be the same. This has been verified by using the effective potential[6] of [8]

$$[8]\qquad V_{ij} = 8018.5\,\frac{e^{-(1.9567)r_{ij}}}{r_{ij}} - 7903.3\,\frac{e^{-(1.9116)r_{ij}}}{r_{ij}}$$

That is, two different effective potentials (independent of both spin and isospin) like those of [1] and [8] with quite different core radii (i.e., 1.13 and 0.43 fm, respectively) and depths (i.e., −27.5 and −267.8 MeV, respectively) lead to the same ground-state vertex configurations and thus to the same charge radii for all $^{40-48}$Ca isotopes.

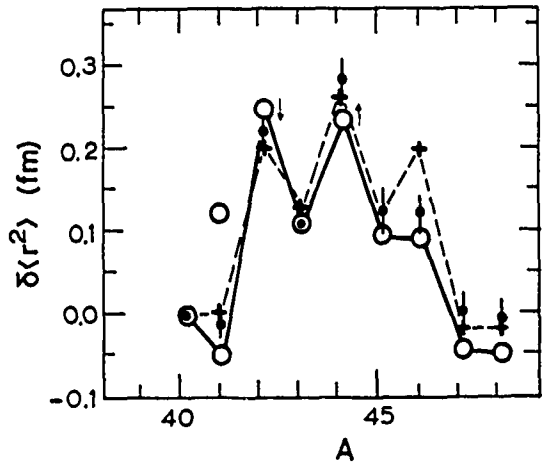

FIG. 3. Relative radii, $\delta\langle r^2\rangle$, of calcium isotopes, $^{40-80}$Ca, as function of mass number A. ● stand for the experimental values from ref. 23. For other experimental values see Fig. 4 of ref. 23, and explanation of that figure, and Table 3 here. The ○ and solid line represent the results from the present calculations, while the broken line stands for calculations by Talmi (25). For ^{41}Ca two predictions are given but for a final choice between them further research is required. The arrows represent trends of results for ^{42}Ca and ^{44}Ca when configuration mixing is considered.

In addition, I would like to compare the potential of [1] with the central effective nucleon–nucleon potentials in the $^3S_1$ and $^1S_0$ channels that arise from residual colour forces. These two potentials, comprising the latest efforts to derive nuclear physics from the quark model with chromodynamics (49), are very similar to each other and to our potential of [1]. (All three potentials have the form of two Yukawa-type components, core radius 1.0–1.1 fm, and depth 22–28 MeV). In conclusion we may say that there is sufficient credibility in the accuracy of the model's results, particularly on nuclear radii.

We continue the discussion on the credibility of the model by referring to the size of the neutron and proton bags. The sizes of the "hard spheres" representing a neutron and a proton appear here as arbitrary assumptions and thus one could think that they were chosen to optimize the model results in the isotopic shift of charge radii in Ca isotopes (see Tables 2 and 3).

[6]I. Lagaris and V. A. Vutsadakis, private communication 1985.

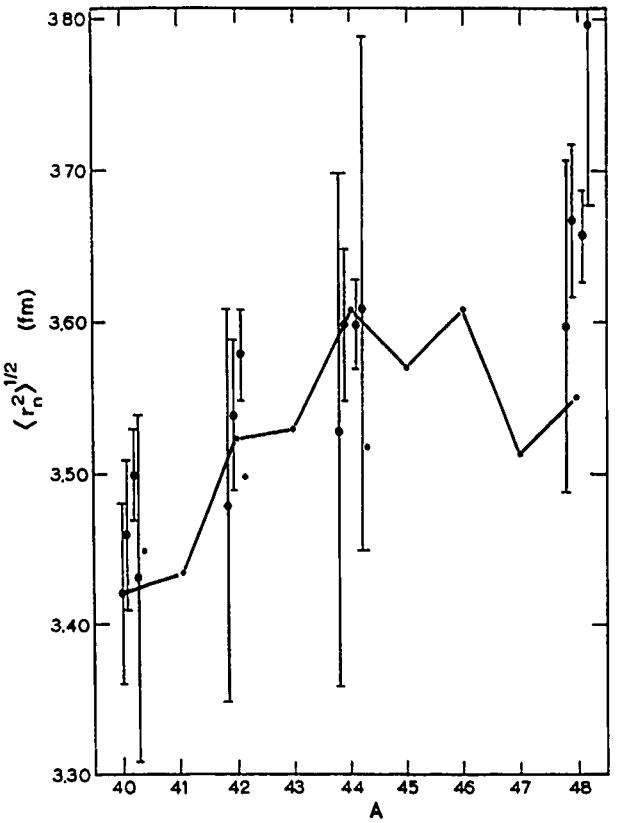

FIG. 4. Root-mean-square neutron radii, $\langle r^2 \rangle^{1/2}$, of $^{40-48}$Ca isotopes. Experimental data come from Table 4. The solid line stands for the present calculations.

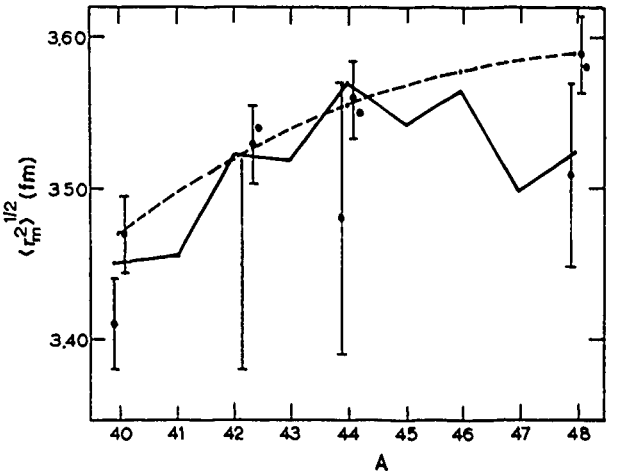

FIG. 5. Root-mean-square mass radii, $\langle r^2_m \rangle^{1/2}$, of $^{40-48}$Ca isotopes. Experimental data come from Table 4. The solid line stands for the present calculations, while the broken line presents calculations from ref. 28.

It should be made clear, however, that the value $r_n = 0.974$ fm for a neutron and $r_p = 0.860$ fm for a proton are numerical parameters of the model and as such remain constant for all nuclei and for all properties. These values were first published in ref. 44 and are also included by Anagnostatos in ref. 33, and by Anagnostatos and Panos in ref. 43, i.e., they were determined well prior and independently of the present article.

As explained in ref. 33, the average form of each shell is in close-packing with a prior neutron or proton shell in the sense that the hard spheres (nucleon bags) of that shell are in contact with the hard spheres of a previous shell. Thus (see Appendix E of ref. 33), the average sizes of proton shells (which are responsible for the charge radius; see [5]) depend on the size of both the hard sphere representing a neutron and that representing a proton. The importance of the absolute and relative present values of these parameters could be better understood by consulting Anagnostatos (50). There, it is apparent that with these values the majority of model charge radii for all elements are within the experimental error. If other values had been chosen (e.g., equal size for a neutron and a proton bag), no charge radii (50) or neutron–proton distribution radial differences (33) of such good accuracy would have resulted for the whole spectrum of elements. For example, let $r_n = r_p = 0.860$ fm. For these sizes of bags (using Appendix E of ref. 33), the resulting sizes of the average forms of the first four proton shells (see Fig. 1) are 1.490, 2.349, 3.598, and 4.069 fm, respectively. Using these values of R_i in [5], we get, for example, for ^{40,42,43}Ca rms charge radii 3.189, 3.243, and 3.214 fm, respectively. That is, we get values that are too small with respect to all corresponding experimental values listed in Table 2 and also with respect to the model values listed in the same table, when $r_n = 0.974$ fm and $r_p = 0.860$ fm, as is always taken in the isomorphic shell model. In addition, it is interesting for one to observe that while the above absolute radii are too small, the relative radii (with respect to ^{40}Ca) are too large, i.e., the isotopic shift is larger than before. Thus, the choice of different sizes for a neutron and a proton bag is well justified within the model and, moreover, is supported by the literature (51, 52).

Furthermore one may notice that the proton charge rms radius 0.8 fm, used throughout the paper (see [5] and [7]), and the size of the proton bag 0.860 fm appear inconsistent at first glance, if one considers that the relationship "rms radius = $\sqrt{3/5}$ *bag radius" is valid for a proton. However, the previous formula is valid only for a uniform charge distribution inside the proton, which is not the case here. A proton (and a neutron) is made up of quarks, which carry the positive and negative components of charge that are responsible for the spatial distribution of charge, which according to the core model (53) is far from uniform.

Finally, we comment on the presence of holes in the $2s$–$1d$ proton shell and the variation from isotope to isotope, as listed in Table 1. The core taking of the $2s$–$1d$ shell for nuclei in the mass region over $A = 40$ is verified by recent experiments (54). The fact that the dominant configuration in ^{41,43,45}Ca has one proton hole, while in ^{42,44}Ca the configuration has two proton holes in the $2s$–$1d$ shell is understood as a result of a pairing effect between the protons coming from the $2s1d$ shell and the valence neutrons in the $1f$ 7/2 subshell. For the number of proton holes in Ca isotopes calculated by others, see the previous discussion in this section and Hodgson (48). Here, the appearance of holes in ^{40}Ca (two neutron holes), while holes do not exist in ^{48}Ca (see Table 1), leads to the conclusion that, according to the present study, ^{48}Ca is a better core than ^{40}Ca for heavier nuclei.

4. Conclusions

We have shown that microscopic calculations within the isomorphic shell model *do* reproduce the experimental charge and matter radii for $^{40-48}$Ca isotopes well, as a consequence of shell (particle–hole) and deformation effects.

TABLE 5. Calculated and experimental Δr_{np} values in fm for Ca isotopes (A = 40–48)

Method	^{40}Ca	^{42}Ca	^{43}Ca	^{44}Ca	^{45}Ca	^{46}Ca	^{47}Ca	^{48}Ca	Reference
This work	−0.05	0.01	0.04	0.11	0.08	0.13	0.04	0.09	
(p,p) 1 GeV	−0.03	0.07		0.07				0.17	61
	−0.07							0.21	62
	−0.03	0.04		0.05				0.16 ± 0.05	5
	0.02	0.08		0.13				0.21 ± 0.03	Footnote *a* of 5.
	0.01	0.05		0.09				0.18 ± 0.03	6
20–50 MeV	0.03 ± 0.05	0.06 ± 0.13		0.11 ± 0.17				0.22 ± 0.11	26
20–50 MeV	0.03 ± 0.05	0.00 ± 0.22		0.11 ± 0.18				0.29 ± 0.17	26 (relativistic)
800 MeV	0.01	0.08		0.10				0.18 ± 0.08	5
LEP	0.01			−0.02				0.39 ± 0.12	14
(α, α)	−0.03	0.02		0.10				0.20 ± 0.05	7
	−0.07			0.09				0.33 ± 0.12	60
								0.03 ± 0.08	22
104 MeV	−0.016 ± 0.04	0.03 ± 0.04		0.02 ± 0.04				0.17 ± 0.05	63
CE		0.01		0.02				0.06	64
πA				0.35 ± 0.15					65
				0.49 ± 0.07					11
(π, π)				0.13				0.20 ± 0.08	12
								0.30	2
116 MeV	0.15 ± 0.07			0.21 ± 0.10				0.33 ± 0.09	1
180 MeV	−0.02 ± 0.04	−0.04 ± 0.03		0.11 ± 0.04				0.18 ± 0.04	1
292.5 MeV	−0.09 ± 0.02	−0.11 ± 0.05		0.05 ± 0.10				0.16 ± 0.04	1
HF	−0.05							0.18	66
	−0.06							0.18	67
	−0.05							0.18	68
	−0.04							0.14	69
	−0.04							0.14	31
	−0.05							0.21	70
	−0.05							0.18	30
DME	−0.05								71
	−0.05	0.03		0.09				0.19	Footnote 1 of 5
BHF	−0.04							0.25	72
HFB	−0.04							0.14	Footnote 2 of 5
	−0.04	0.01		0.06				0.14	73
SM	−0.04			0.19				0.34	74
	0.03			0.24				0.45	75
TF	0.01							0.07	67
	−0.05							0.12	76

The present calculations involve three properties, which are, binding energies, and proton and neutron (and consequently mass) radii for both even and odd Ca isotopes, while the best calculations available today involve either one property (charge radii) and deal with even and odd Ca isotopes (25) or two properties (charge and mass radii) and deal with only even Ca isotopes (26). Our results are at least of equal accuracy (with respect to the experimental data) when compared with those of the other calculations besides being microscopic and involving one additional property. Also, an important difference between our calculations and the previous calculations on nuclear radii is the kind of parameters used. Here, we use only two *numerical* parameters (the size of the neutron and proton bags) previously and independently published, constant for all properties and for all nuclei, while in other models adjustable parameters are employed. Finally, we mention that Hartree–Fock calculations badly miss the parabolic behaviour displayed by the charge *ms* radius from ^{40}Ca – ^{48}Ca (29, 30).

For ^{41}Ca, before a final conclusion, some additional investigation is needed (see Fig. 3). The proton 2*s*–1*d* core breaking involved in the present calculations is experimentally (54) and theoretically (48) verified.

Finally, it is interesting for one to associate the success of the isomorphic shell model for the Ca isotopes described here with the success of the model for another string of isotopes, the oxygen isotopes, as reported by Anagnostatos *et al.* in ref. 55.

Acknowledgement

This work was supported in part by funds provided by the U.S. Department of Energy under contract No. DE-AC02-76ER03069.

1. K. G. BOYER, W. J. BRAITHWAITE, W. B. GOTTINGAME *et al.* Phys. Rev. C: Nucl. Phys. **29**, 182 (1984).
2. J. P. EGGER, R. CORFU, P. GRETILLAT *et al.* Phys. Rev. Lett. **39**, 1608 (1977).
3. L. RAY, G. W. HOFFMANN, M. BARLETT *et al.* Phys. Rev. C: Nucl. Phys. **23**, 828 (1981).
4. M. L. BARLETT, W. R. COKER, G. W. HOFFMAN, and L. RAY. Phys. Rev. C: Nucl. Phys. **29**, 1407 (1984).
5. G. IGO, G. S. ADAMS, T. S. BAUER *et al.* Phys. Lett. **81B**, 151 (1979).
6. G. D. ALKHAZOV, T. BAUER, R. BEURTEY *et al.* Nucl. Phys. **A274**, 443 (1976).
7. G. D. ALKHAZOV, T. BAUER, R. BERTINI *et al.* Nucl. Phys. **A280**, 365 (1977).
8. E. FRIEDMAN, H. J. GILS, H. REBEL, and Z. MAJKA. Phys. Rev. Lett. **41**, 1220 (1978).
9. H. J. GILS, E. FRIEDMAN, Z. MAJKA, and H. REBEL. Phys. Rev. C: Nucl. Phys. **21**, 1245 (1980)

10. C. J. Batty, S. F. Biagi, E. Friedman *et al.* Phys. Lett. **81B**, 165 (1979).
11. L. Tauscher and S. Wycech. Phys. Lett. **62B**, 413 (1976); S. Theberge and A. W. Thomas. Nucl. Phys. **A393**, 252 (1983).
12. M. J. Jacobson, G. R. Burleson, J. R. Calarco *et al.* Phys. Rev. Lett. **38**, 1201 (1977).
13. H. Sakaguchi, M. Nakamura, K. Hatanaka *et al.* Phys. Rev. C: Nucl. Phys. **26**, 944 (1982).
14. J. C. Lombard, R. N. Boyd, R. Arking, and A. B. Robbins. Nucl. Phys. **A188**, 103 (1972).
15. R. F. Frosch, R. Hofstadter, J. S. McCarthy *et al.* Phys. Rev. **174**, 1380 (1968).
16. H. D. Wohlfahrt, E. B. Shera, M. V. Hoehn, Y. Yamazaki, and R. M. Steffen. Phys. Lett. **73B**, 131 (1978).
17. M. B. Johnson and H. Bethe. Comments. Nucl. Part. Phys. **8**, 75 (1978).
18. J. A. McNeil, J. Shepard, and S. J. Wallace. Phys. Rev. Lett. **50**, 1439 (1983): **50**, 1443 (1983).
19. B. C. Clark, S. Hama, R. L. Mercer, L. Ray, and B. D. Serot. Phys. Rev. Lett. **50**, 1644 (1983); B. C. Clark, S. Hama, R. L. Mercer, L. Ray, G. W. Hoffman, and B. D. Serot. Phys. Rev. C: Nucl. Phys. **28**, 1421 (1983).
20. M. V. Hynes, A. Picklesimer, P. C. Tandy, and R. M. Thaler. Phys. Rev. Lett. **52**, 978 (1984).
21. L. Ray. Phys. Rev. C: Nucl. Phys. **19**, 1855 (1979).
22. G. M. Lerner, J. C. Heibert, L. L. Rutlegee, Jr., C. Papanicolas, and A. M. Berstein. Phys. Rev. C: Nucl. Phys. **12**, 778 (1975).
23. A. Andl, K. Bekk, S. Goring, A. Hanser, G. Nowicki, H. Rebel, G. Schatz, and R. C. Thompson. Phys. Rev. C: Nucl. Phys. **26**, 2194 (1982).
24. K. Zamick. Ann. Phys. (N.Y.), **66**, 784 (1971).
25. I. Talmi. Nucl. Phys. **A423**, 189 (1984).
26. R. H. McCamis, T. N. Nasr, J. Birchall *et al.* Phys. Rev. **33**, 1624 (1986).
27. E. Bleszynski, M. Bleszynski, and R. J. Glauber. Phys. Rev. Lett. **60**, 15 (1988).
28. F. Barranco and R. A. Broglia. Phys. Lett. **151B**, 90 (1985).
29. M. Waroquier, K. Heyde, and G. Wenes. Nucl. Phys. **A404**, 269 (1983).
30. X. Campi and D. Sprung. Nucl. Phys. **A194**, 401 (1982); A. Chaumeaux, V. Layly, and R. Schaeffer. Phys. Lett. **72B**, 33 (1977).
31. H. S. Kohler. Nucl. Phys. **A258**, 301 (1976).
32. W. Bertozzi, J. Friar, J. Heisenberg, and J. W. Negele. Phys. Rev. A: Gen. Phys. **418**, 408 (1972).
33. G. S. Anagnostatos. Int. J. Theor. Phys. **24**, 579 (1985).
34. S. Barshay and L. M. Sehgal. Phys. Rev. C: Nucl. Phys. **31**, 2133 (1985).
35. A. W. Thomas. Cern preprint No. TH 3552-CERN. 1983; J. W. Negele and E. Vogt (*Editors*). Adv. Nucl. Phys. **13**, 1 (1984); G. S. Anagnostatos, C. N. Panos, T. S. Kosmas, and J. C. Varvitsiotis. Proceedings of the Int. Conf. Nucl. Physics, Florence, August 29–September 3, 1983. Tipografia Compositori, Bologna, **1**, A15 (1983).
36. G. S. Anagnostatos. Proceedings of the Int. Conf. Nucl. Structure through Static and Dynamic Moments, Melbourne, August 25–28, 1987. Vol. 2. Organizing Committee of the Conference, Melbourne. **1**, 71 (1987).
37. J. Leech. Math. Gaz. **41**, 81 (1987).
38. G. S. Anagnostatos. Lett. Nuovo Cimento Soc. Ital. Fis. **22**, 507 (1978).
39. G. S. Anagnostatos. Lett. Nuovo Cimento Soc. Ital. Fis. **28**, 573 (1980).
40. G. S. Anagnostatos. Lett. Nuovo Cimento Soc. Ital. Fis. **29**, 188 (1980).
41. G. S. Anagnostatos, J. Yapitzakis, and A. Kyritsis. Lett. Nuovo Cimento Soc. Ital. Fis. **32**, 332 (1981).
42. G. S. Anagnostatos and C. N. Panos. Phys. Rev. C: Nucl. Phys. **26**, 260 (1982).
43. G. S. Anagnostatos. Lett. Nuovo Cimento Soc. Ital. Fis. **41**, 409 (1984).
44. C. N. Panos and G. S. Anagnostatos. J. Phys. G: Nucl. Phys. **8**, 1651 (1982).
45. I. Kaplan. Nuclear physics. 2nd ed. Addison-Wesley Publishing Co. Inc., Reading, MA, 1964. p. 537.
46. C. W. de Jarer, H. de Vries, and C. de Vries. At. Data Nucl. Data Tables **14**, 479 (1974).
47. S. Platchkov, A. Amroun, P. Bricault *et al.* Phys. Rev. Lett. **61**, 1465 (1988).
48. P. E. Hodgson. Lect. Notes Phys. **168**, 70 (1982).
49. N. Isgur. Proc. Int. Nucl. Phys. Conf. Harrogate, August 25–30, 1986. *Edited by* J. L. Durell, J. M. Irvine and G. C. Morrison. Institute of Physics, Bristol. **2**, 345 (1986).
50. G. S. Anagnostatos. Proceedings of the PANIC Particles and Nuclei. 10th Int. Conf. Heidelberg, Germany. July 30–August 3, 1984. Vol. II. *Edited by* F. Guttner B. Povh, G. zu Putlitz. North-Holland Publishing Co., Amsterdam 1984. p. 156.
51. L. S. Celenza and C. M. Shakin. Phys. Rev. C: **27**, 1561 (1983).
52. E. F. Hefter. Lett. Nuovo Cimento Soc. Ital. Fis. **44**, 99 (1985).
53. R. M. Littauer, H. F. Schopper, and R. R. Wilson. Phys. Rev. Lett. **7**, 141 (1961): **7**, 144 (1961).
54. B. J. Cole and W. L. Gadinabokao. Proc. Int. Nucl. Phys. Conf. Harrogate U.K. August 25–30, 1986. *Edited by* J. L. Durell, J. M. Irvine, and G. C. Morrison. Institute of Physics, Bristol **1**, C96 (1986).
55. G. S. Anagnostatos, T. S. Kosmas, S. E. Massen, and C. N. Panos. Bull. Am. Phys. Soc. **29**, 1029 (1984).
56. A. H. Wapstra and G. Audi. Nucl. Phys. **A432**, 1 (1985).
57. B. A. Brown, S. E. Massen, and P. E. Hodgson. J. Phys. G: Nucl. Phys. **5**, 1655 (1979).
58. H. D. Wohlfahrt, E. B. Shera, M. V. Hoehn, Y. Yamazaki, G. Fricke, and R. M. Steffen. Phys. Rev. C: Nucl. Phys. **23**, 533 (1981).
59. F. Trager. Z. Phys. A: At. Nucl. **299**, 33 (1981).
60. I. Brissaux, Y. Le Bornec, B. Tatischeff, L. Bimbot, and G. Duhamel. Nucl. Phys. **A191**, 145 (1972).
61. L. Ray and W. R. Coker. University of Texas Technical Preprint No. UTNT-3 1977.
62. G. K. Varma and L. Zamick. Phys. Rev. C: Nucl. Phys. **16**, 308 (1977).
63. H. J. Gils, H. Rebek, and E. Friedman. Phys. Rev. C: Nucl. Phys. **29**, 1295 (1984).
64. J. A. Nolen and J. P. Schiffer. Ann. Rev. Nucl. Sci. **19**, 471 (1969).
65. R. Kunselman and G. Grin. Phys. Rev. Lett. **24**, 838 (1970).
66. J. W. Negele. Proc. 2nd European Physical Society Nucl. Phys. Conf. Radial Shape of Nuclei. Cracow, June 22–25, 1976. *Edited by* A. Budzanowski and A. Kapuscik. Jagellonian University, Institute of Nuclear Physics, Cracow. p. 79. 1976.
67. J. Nemeth. Nucl. Phys. **A156**, 183 (1970).
68. D. Wautherin and D. M. Brink. Phys. Rev. C: Nucl. Phys. **5**, 626 (1972).
69. M. Beiner, H. Flocard, N. Van Giai, and P. Quentin. Nucl. Phys. **A238**, 29 (1975).
70. D. Kolb, R. Y. Cusson, and M. Harvey. Nucl. Phys. **A215** 1, (1973).
71. J. W. Negele and D. Vautherin. Phys. Rev. C: Nucl. Phys. **5**, 1472 (1972).
72. K. T. R. Davis *et al.* Phys. Rev. C: Nucl. Phys. **4**, 81 (1971).
73. J. Decharge and D. Gogny. Phys. Rev. C: Nucl. Phys. **21**, 1568 (1980).
74. L. R. B. Elton. Phys. Rev. **158**, 970 (1967).
75. C. J. Batty and G. W. Greenlees. Nucl. Phys. **A133**, 673 (1969).
76. R. J. Lombard. Ann. Phys. (N.Y.), **77**, 380 (1973).

A study of high-purity Cd_xSe_{1-x} vacuum-deposited thin films

E. DUFRESNE[1] AND D. E. BRODIE

Guelph-Waterloo Program for Graduate Work in Physics, Waterloo Campus, University of Waterloo, Waterloo, Ont., Canada N2L 3G1

Received November 6, 1990

Pure CdSe films were vacuum deposited onto liquid-nitrogen-cooled substrates using a doubly baffled source in an attempt to prepare and study amorphous CdSe. The deposition of stable stoichiometric amorphous pure films was not verified since the films were always polycrystalline when analyzed at room temperature. CdSe appears to be different from some other II–VI compounds that can be prepared as pure stoichiometric amorphous materials and can be studied at a temperature up to 400 K. Pure nonstoichiometric films were also prepared using a second source to supply the excess component. Amorphous Se-rich films could only be produced for samples with at least 59 at.% Se. For Cd-rich films, the excess Cd agglomerates and the CdSe crystallite sizes are smaller than those observed in stoichiometric films. The electrical and optical properties scale as a function of the Cd content and the films become metallike as the Cd content increases through 60 at.%. The electrical transport properties are very different for polycrystalline films, depending on whether the CdSe is deposited on a hot substrate, or on a cold substrate and annealed to the same high temperature. We show that impure amorphous films of CdSe can be deposited if the system's background pressure is high.

Des couches minces de CdSe pur ont été déposées sous vide sur des substrats refroidis à l'axote liquide, en utilisant une source à double écran, dans le but de préparer et d'étudier du CdSe amorphe. Le dépôt de couches stoéchiométriques amorphes pures n'a pu être vérifié, étant donné que les couches déposées sont toujours polycristallines lorsqu'on les analyse à température ambiante. Il semble que CdSe soit différent de certains autres composés II–VI qu'on peut préparer sous forme de matériaux stoéchiométriques amorphes pure et qu'on peut étudier à des températures allant jusqu'à 400 K. On a aussi préparé des couches non stoéchiométriques pures en utilisant une seconde source pour fournir la composante en excès. Des couches amorphes enrichies en Se ne pouvaient être obtenues que pour des échantillons avec au moins 59 at.% de Se. Pour les couches enrichies en Cd, l'excès de Cd s'agglomère et la grosseur des cristallites de CdSe est inférieure à celle qu'on observe dans les couches stoéchiométriques. Les propriétés électriques et optiques s'échelonnent en fonction du contenu en Cd, et les couches deviennent de type métallique lorsque le contenu en Cd croît au-delà de 60 at%. Les propriétés de transport électrique sont très différentes pour les couches polycristallines et ne sont pas les mêmes pour le CdSe déposé sur une surface chaude et pour celui déposé sur une surface froide et recuit à la même haute température. On montre que des couches de CdSe amorphe impur peuvent être déposées si la pression résiduelle dans le système est élevée.

[Traduit par la rédaction]

Can. J. Phys. 69, 124 (1991)

1. Introduction

In the last 20 years, the polycrystalline phase of CdSe deposited on substrates at or above room temperature has been studied extensively (1–5). These studies have been motivated by the potential application of CdSe in thin-film transistors. In particular, thin-film transistors of CdSe deposited in a matrix pattern are used to switch pixels on and off as part of a liquid crystal display in a flat screen configuration (6). Prototype displays have already been reported (7).

Although the polycrystalline phase of CdSe has been studied, little is known of the amorphous phase. Only one attempt to study pure amorphous CdSe (a-CdSe) is known (8) and this work reports an attempt to fabricate and study the properties of a-CdSe thin films. However, stoichiometric, stable, high-purity a-CdSe was not obtained.

Rieckhoff (8) flash evaporated CdSe onto glass substrates held near 100 K. The films were deposited in a vacuum system with a base pressure of 1×10^{-7} Torr (1 Torr = 133 Pa) and the pressure during deposition rose to 1×10^{-6} Torr. The dc conductivity of the films was measured *in situ* as the films warmed from low temperature to room temperature and this changed irreversibly from an "amorphouslike" curve (strongly temperature dependant conductivity) to a "polycrystallinelike" curve (almost temperature independent conductivity), characteristic of other a-II–VI compounds that have been crystallized from the amorphous state (9, 10). The CdSe films were observed to be polycrystalline at the time the structural analysis was performed at room temperature. From the change of the electrical properties, it was suggested that the films probably crystallize below room temperature.

The fabrication of low-purity a-CdSe has been reported (2). These films were vacuum-deposited with low deposition rates in a relatively poor vacuum. The amorphous structure of these films was believed to have been assisted by the incorporation of residual gases into the growing film (2).

In a number of previous studies of some amorphous II–VI compounds prepared in this laboratory, the amorphous films were made with very low vacuum pressures present during evaporation of the materials (9, 10), leading to the formation of high-purity films. From the results given in ref. 2, one notes that low-purity amorphous CdSe films can be fabricated but that it is more difficult to fabricate and study high-purity amorphous CdSe films (8, 2).

In this work, we studied some of the properties of high-purity CdSe thin films vacuum-deposited onto liquid-nitrogen (LN_2) cooled substrates and annealed at room temperature. The objective was to prepare and study pure amorphous films. Both stoichiometric films and films with a varying Cd/Se ratio were prepared, but only some of these latter materials could be deposited and studied in the amorphous phase. The films were

[1]Present address: Department of Physics, McGill University, Montreal, Que., Canada H3A 2T8.

TABLE 1. Deposition conditions

Deposition pressures (Torr)	$10^{-8} - 3 \times 10^{-5}$
Substrate temperatures (K)	98–137 and 474
Deposition rates (nm s^{-1})	0.03–6
Thicknesses (nm)	180–1550
Se-source temperature (K)	490–504
Cd-source temperature (K)	506–564

characterized by observing some of their electrical, optical, and structural properties. The effects of annealing and (or) crystallizing the films at higher temperatures are reported.

2. Experimental method

CdSe films were deposited onto LN_2-cooled substrates (Corning 7059 glass) using an RD Mathis doubly baffled source (SO-10). The glass substrates had electrical leads pre-attached so that a planar contact configuration could be deposited and the electrical measurements completed *in situ*. The distance between the source and substrate was 25 cm. To shift stoichiometry, a second source was added to increase the vapour pressure of one component. An RD Mathis CH-10 source equipped with a copper–constantan thermocouple was used to evaporate the excess component that was contained in an Al_2O_3 crucible. A controlled leak valve was used to introduce air into the deposition system when low-purity films were made. The source materials used were CERAC 99.999% pure CdSe 325 mesh powder; A. P. Mackay Inc. 99.999% pure Cd shot; and Apache Chemicals 99.9999% pure Se shot.

Before a deposition, the system was baked overnight under vacuum at ≈120°C. The base pressure of this system is normally between 8×10^{-9} and 2×10^{-8} Torr after the bake out cycle. During the deposition, the pressure can be kept between 1×10^{-8} and 3×10^{-8} Torr. The principal residual gases present before a deposition are H_2O, N_2, CH_4, O_2, and CO_2. During the deposition, the peaks for N_2, O_2, and CO_2 increase. This increase in residual gas pressure is minimized by outgassing the sources, i.e., heating the sources to near the evaporation temperature prior to deposition. Outgassing the sources was found to be an important procedure for obtaining a cleaner vapour flow. Table 1 summarizes the deposition conditions.

The dc conductivity was measured by applying a constant voltage to the gold contacts and recording the resulting current. A four probe measurement was used to study high-conductivity samples, i.e., above 100 S cm^{-1}. All samples were annealed overnight at room temperature, and in each case linear current–voltage characteristics were assumed to indicate ohmic contacts. All contacts were ohmic in the range of electric fields used (i.e., up to fields of 100 V cm^{-1}). Structural information was obtained using a Siemens D500 diffractometer and a copper target with a Ni filter (λ = 0.154 06 nm). For some samples, the film was later scraped from the substrate to compare the diffractometer results with Debye–Scherrer powder patterns. A quantitative X-ray microanalysis technique (Kevex Analyst 8000 microanalyser) was used to determine the composition of the films. The X rays were excited by 10 KeV electrons provided in a scanning electron microscope. The uncertainty in sample composition is ≈2% for ideal conditions using this method. The optical gap was determined with a double beam spectrophotometer (Varian DMS 200), but for some Cd-rich samples, a Cary-14 double beam spectrophotometer was required to extend the spectral range into the infrared. The data

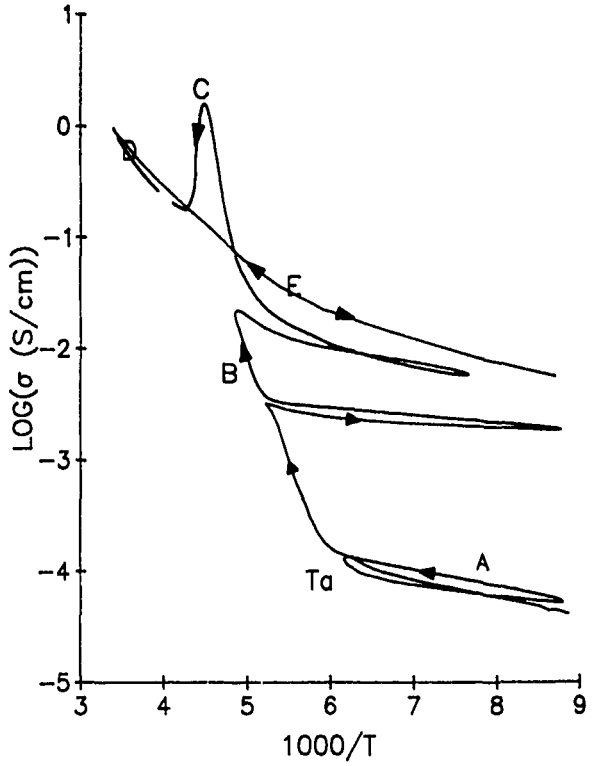

FIG. 1. The general behaviour of the dc conductivity of a stoichiometric CdSe film is illustrated as the temperature is cycled from the as-made stoichiometric sample to the annealed polycrystalline sample.

obtained from the polycrystalline films enable one to determine the optical gap from a plot of α^2 vs. $h\nu$. This assumes that crystalline CdSe has a direct allowed transition at the band edge (11). The data for all the amorphous samples and all samples with very small crystallites embedded in an amorphous matrix could be fit to a plot of $(\alpha h\nu)^{1/2}$ vs. $h\nu$ (a Tauc plot) (12) and this was used to obtain the optical gap for these films.

3. Results and discussion

3.1. Pure stoichiometric CdSe films

Figure 1 represents the Arrhenius plot of a typical sample as it is thermally cycled after deposition. This curve can be separated into four parts. Part A corresponds to a stable conductivity regime. If the sample is thermally cycled below a critical temperature *Ta* (≈167 K), the conductivity is reproducible. As the temperature is increased above *Ta*, part B is obtained and corresponds to an irreversible change in the conductivity, i.e., if the sample is cooled again in this regime, the conductivity is always higher than in part A. If one continues to warm the sample above the highest temperature the sample had attained before cooling, the conductivity continues to increase irreversibly. The sample appears to go through a series of metastable states that correspond to changes in bonding configurations or a partial crystallization. Extensive changes in the dc conductivities occur during this annealing transition, e.g., between four and nine orders of magnitude depending on the deposition rate for the sample. The conductivities of samples deposited using the lowest deposition rate change the most. Part C corresponds to a regime in which the conductivity goes through a local maximum in a process that resembles the

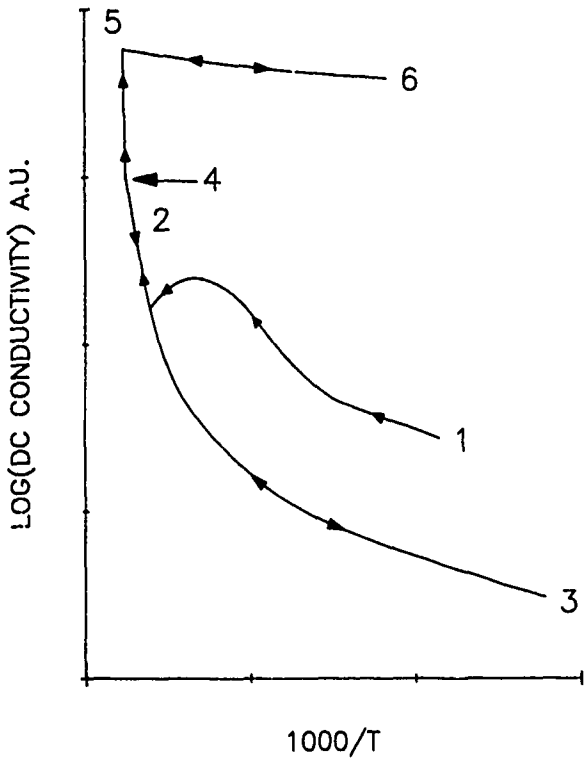

FIG. 2. The general behaviour of the dc conductivity vs. 1000/T for some amorphous II–VI semiconductors as they are annealed, then crystallized.

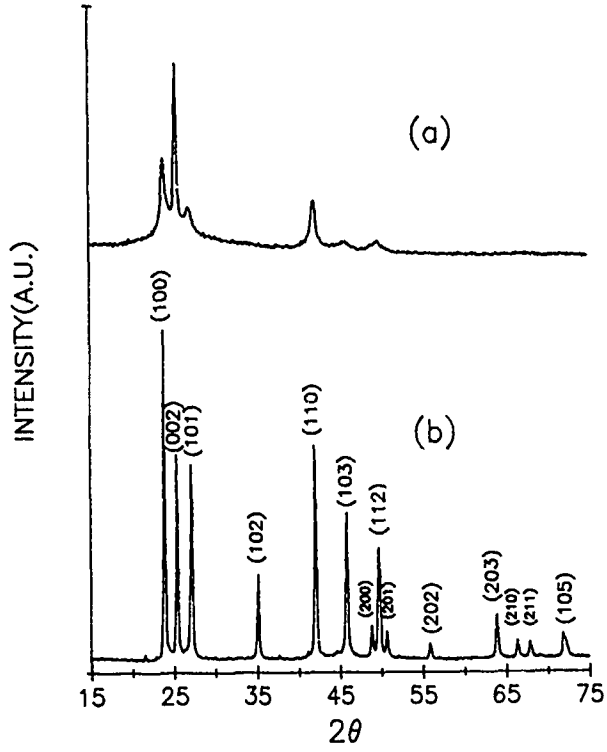

FIG. 3. Diffraction pattern of a typical film (*a*) compared with the diffraction pattern of the CdSe source powder (*b*). The numbers in brackets are Miller indices for the wurtzite lattice.

annealing phase of other a-II–VI compounds. After attaining state D, the conductivity is reproducible again as represented by curve E as long as the sample temperature does not exceed the highest annealing temperature used.

Figure 2 shows a schematic Arrhenius plot of a typical a-II–VI semiconductor as it is thermally cycled from the initially amorphous film to the polycrystalline film. The curve between 1 and 2 exhibits the annealing of the sample as it is warmed up from a low temperature to the annealing temperature for the first time. If the temperature is then kept below 2, the conductivity of the amorphous sample is reproducible between 2 and 3. If one warms the sample from 2 to 5, crystallization occurs. After this irreversible transition, one now obtains the curve 5 to 6, and this behaviour is characteristic of those materials that have been crystallized from the amorphous phase.

Figures 1 and 2 exhibit similar irreversible changes in the conductivity during the annealing process. However, all stoichiometric pure CdSe films investigated in this study were polycrystalline by the time the structure was observed at room temperature. It is not known whether the CdSe films contain crystallites that grow when they are deposited initially, or whether crystallites form during the annealing process. However, no obvious crystallization temperature is evident in any of the annealing curves represented by Fig. 1.

It is not understood at the moment why stoichiometric CdSe is so different from some of the other II–VI compounds that can be prepared as pure amorphous films (9, 10, 13). It may be that the strong ionicity of the bond enhances the formation of crystallites. Some high-purity amorphous CdTe films have been produced (13) (the CdTe bond is less ionic than that for CdSe), but CdS (a more ionic bond than the CdSe bond) was difficult to prepare even at background vacuum pressures of 10^{-6} Torr (14), although it has been prepared in a poorer vacuum (15).

Figure 3*a* shows the intensity of the diffracted X rays as a function of the scattering angle 2θ for a typical vacuum-deposited film and Fig. 3*b* shows a reference powder pattern obtained using the source material. The patterns of Figs. 3*a* and 3*b* represent the hexagonal phase of CdSe and the crystallites in the film grown with a preferred orientation. As one can see from Fig. 3*a*, the (002) planes scatter more X rays than the (100) planes and this is reversed in the reference pattern. From the diffraction pattern, one can evaluate the crystallite size d, using the relation (16):

$$d = \frac{0.9\,\lambda}{\alpha \cos(\theta_B)}$$

where λ is the X-ray wavelength (0.154 06 nm), θ_B is the Bragg angle of the line, and α is the FWHM in radians. The (002) diffraction lines have been used to determine the crystallite sizes and the values obtained range between 43 and 50 nm for the stoichiometric films. The uncertainty in these values is estimated to be 10%, due largely to the difficulty of locating the baseline and noise in the signal.

It was noted that pure a-ZnSe and a-ZnTe were obtained under similar conditions to those used here for CdSe (10), but only if the deposition rate exceeded 2.5 nm s^{-1}. The deposition rate used for CdSe in this study, was varied from 0.03 to 6 nm s^{-1}, but only polycrystalline films were observed after annealing to room temperature. However, this variation in deposition rate results in very large differences in the electrical conductivities observed initially for the different films, e.g.,

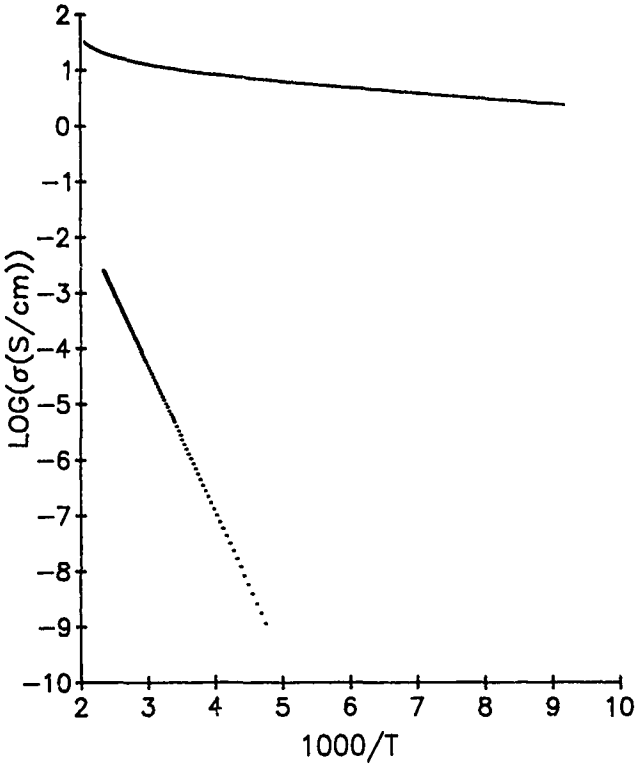

FIG. 4. Effect of the substrate temperature during deposition on the dc conductivities of two types of films. One sample (solid line) was deposited onto a substrate held at 110 K and annealed at 487 K while the other (the dotted line) was deposited on a substrate held at 474 K.

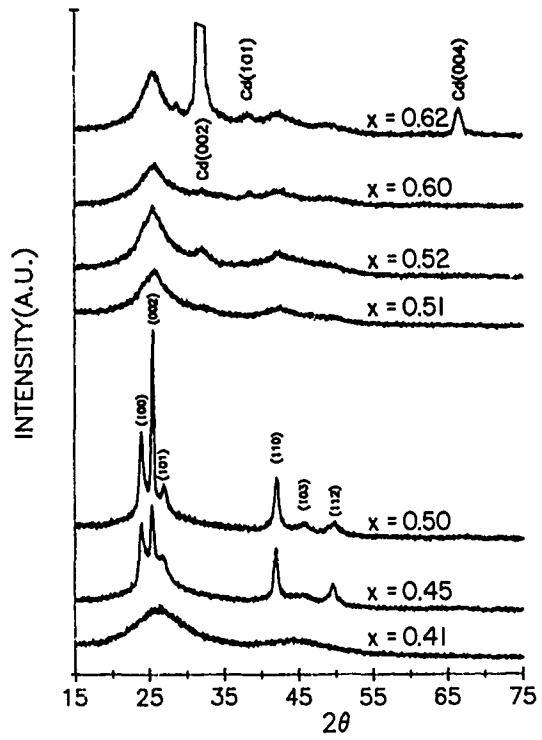

FIG. 5. X-ray diffraction patterns for Cd_xSe_{1-x} for $0.41 \leq x \leq 0.62$. x has an uncertainty of 2%.

the initial dc conductivity below *Ta* (Fig. 1) varied systematically from 10^{-9} to 10^{-2} S cm^{-1} with increasing deposition rate. Even so, the room temperature conductivities for all of the annealed films are comparable with values around 1 S cm^{-1}.

The annealed conductivity in each case could be fit to a sum of two exponentials and this gives a low-and high-temperature activation energy for each sample. The low-temperature activation energy for annealed samples decreases from 0.04 to 0.003 eV with increasing deposition rate. On the other hand, all of the higher temperature activation energies observed were 0.15 ± 0.03 eV.

Sample reproducibility was determined by making three samples using the same deposition conditions. The annealing process as well as the final electrical properties were reproduced satisfactorily although some variations were measurable. One might expect even small variations in the deposition conditions and (or) the thermal history of the source or sample (5, 9) to yield measurable differences in the properties.

The optical gaps evaluated for these CdSe films lie between 1.7 and 2.0 eV. The optical gap for single crystal CdSe ranges from 1.7 (17) to 1.8 eV (18). The differences between measured optical gaps in polycrystalline samples and the optical gap of single crystal CdSe are, for many samples, larger than the error due to the uncertainties. Some differences may be observed due to scattering effects at the grain boundaries and nonsmooth surfaces that may be obtained in polycrystalline films (19).

Figure 4 shows the electrical conductivities for two CdSe films; one was deposited onto a substrate held at 474 K, while the other was deposited onto a substrate held at 110 K and annealed to 487 K. Two very different stable materials were obtained. The conductivity for the reference film (i.e., Ts = 474 K) can be modelled with only one exponentially activated conductivity regime (activation energy of 0.51 eV and a conductivity pre-exponential factor of 2.5×10^3 S cm^{-1}). This result agrees well with previous work (1).

The diffraction patterns of both of these films are consistent with polycrystalline hexagonal CdSe. The film deposited on a hot substrate shows a trace of the CdSe (102) line, which is not present in the annealed film. Crystallite sizes obtained from X-ray line widths indicate that the two materials have the same average crystallite size (i.e., 50 nm) within experimental error. Also the atom ratios in these two films are the same to within the limits of the experiments. In addition, the film made with Ts = 474 K is a reasonable photoconductor while the film made with Ts = 110 K has a barely detectable photoconductivity when viewed under the same conditions. The electrical properties of the film deposited on the hot substrate appears to be representative of a good-quality polycrystalline film in which the electrical characteristics are dominated by grain-boundary trapping (1). On the other hand, the electrical characteristics of the annealed film deposited on the cold substrate appears to have electrical characteristics representing transport via highly conducting grain boundaries or at least grain boundaries that do not introduce barriers between the grains. If there are small differences in the atom ratios for the two films, this would be amplified in the grain boundaries for an annealed film.

3.2. Nonstoichiometric pure films

Figure 5 shows the effect of varying the atom ratio on the films' structural properties. In Cd_xSe_{1-x}, an excess of 5 at.% Se (x = 0.45), decreases the crystallite size. Furthermore, 59 at.% and higher concentrations of excess Se ($x \leq 0.41$) yield the only completely high-purity amorphous materials obtained

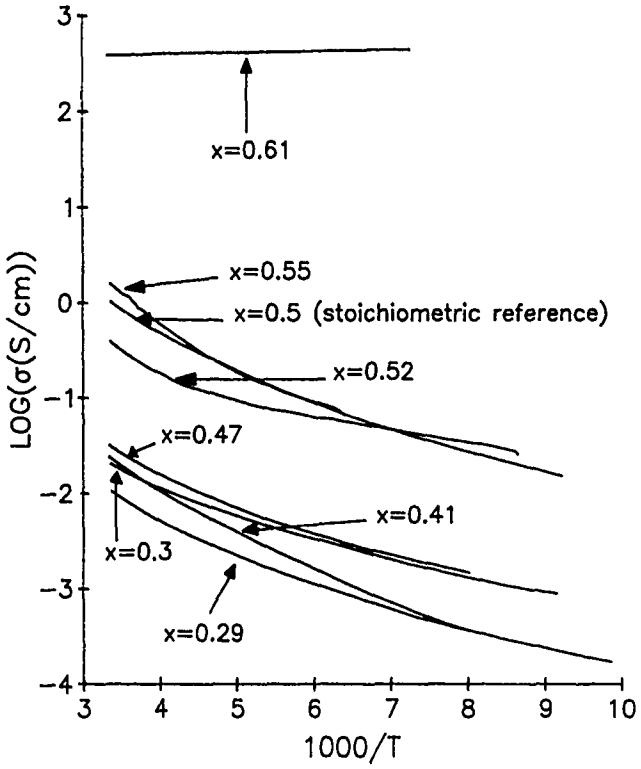

FIG. 6. dc conductivities vs. 1000/T for Cd_xSe_{1-x} samples for $0.29 \leq x \leq 0.61$. x has an uncertainty of 2%.

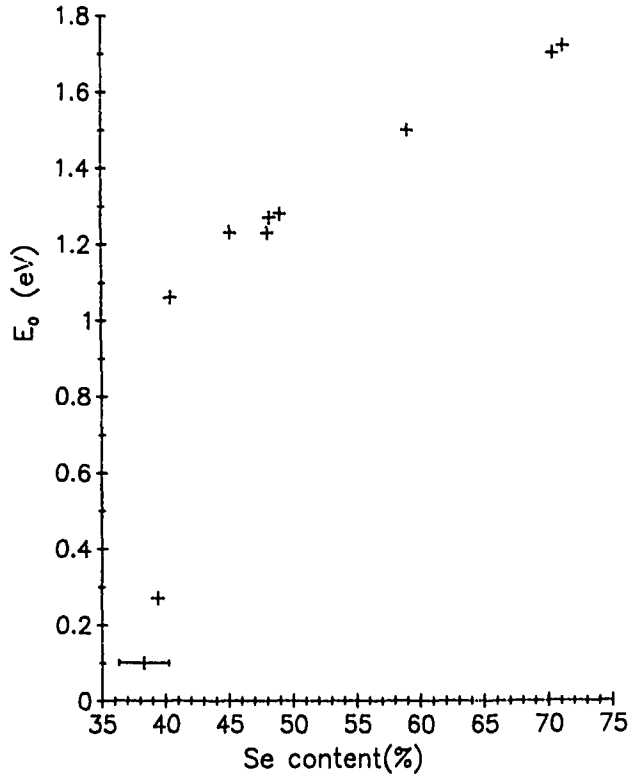

FIG. 7. Optical gaps vs. sample composition for high-purity films. E_0's are obtained from Tauc plots. All of these samples yielded diffuse diffraction rings in the X-ray patterns and many of the patterns also contained lines indicating the presence of small crystallites.

in this study. Since Se is amorphous when deposited on a room-temperature substrate, it is expected that increasing the concentration of Se will ultimately result in an amorphous material.

Excess Cd has a more immediate effect on the structural properties of the films, i.e., less Cd is needed to initiate significant changes in the structure. 1 at.% excess Cd decreases the crystallite size evaluated with the (002) line to less than those evaluated for stoichiometric films and a weak hexagonal Cd line (002) appears in the spectrum. One can still see broad CdSe lines in the diffraction pattern, e.g., the (110) and (112) lines, and can almost resolve the (100) and the (002) lines. The presence of these Cd and CdSe crystallites as well as the diffuse rings are also seen in the Debye–Scherrer patterns.

With increasing Cd content, more Cd lines appear, i.e., the hexagonal Cd (101) and (004) lines. Films made with $x = 0.52$ and $x = 0.62$ were made from the same batch of CdSe source material and those for $x = 0.51$ and $x = 0.60$ were made using material from a different batch, although both were supplied by the same company with the same purity. The trend is indicated consistently by these two pairs of samples, i.e., the increasing Cd agglomeration and the decrease in CdSe crystallite size.

The increasing amplitudes of Cd lines, the presence of the remanent of CdSe lines and the diffuse rings suggest that the films are heterogeneous, with small Cd crystallites as well as small CdSe crystallites embedded in an amorphous matrix.

Figure 6 shows the effect of changing the atom ratio on the electrical conductivity for fully annealed films. Excess Se ($x < 0.5$) decreases the dc conductivity from that observed for a stoichiometric reference sample. The three samples with the largest Se content are completely amorphous, i.e., the presence of crystallites could not be detected, while the fourth film containing 53 at.% Se, contains crystallites up to 37 nm in size. The electrical transport in the polycrystalline film is similar to that for the three amorphous films, suggesting that the transport properties are dominated by the properties of the amorphous matrix in which the crystallites are embedded.

Generally, the higher temperature conductivities increase with increasing x (see Fig. 6) and in the vicinity of $x = 0.6$, films become metallic. As the Cd content increases to $\cong$60 at.%, it is assumed that the Cd islands coalesce and provide electrically continuous paths through the film.

The low-temperature transport appears to be dominated by the defect structure associated with the amorphous matrix of the nonstoichiometric films. It is significantly more difficult to reproduce the defect density, since this requires a more exact duplication of the deposition conditions and the thermal anneal history as well as the purity (9, 10). Even so, the general trend of increasing conductivity with increasing Cd content is apparent.

Figure 7 shows the optical gap obtained from Tauc plots versus the Se content for nonstoichiometric samples. The optical gap varies linearly between $x = 0.41$ and 0.71 with increasing Se content. This linear variation in the optical gap with the Cd/Se ratio is reminiscent of Vegards' law, but the agreement is not perfect. The data in Fig. 7 were obtained only for samples for which a diffuse pattern was present in the X-ray spectrum and the optical data could be fit rather well by a Tauc plot. This would suggest that a-CdSe should have an optical gap near 1.3 eV. However, all of our pure stoichiometric CdSe samples are polycrystalline and give optical gaps between 1.7 and 2.0 eV and as well the optical absorption data are not described by a Tauc plot.

For samples with values of x above 0.6, near the transition to metallike conduction, the optical gap decreases rapidly, probably strongly influenced by the agglomerating excess Cd. Due to the mixture of crystallites and amorphous material present in most of these nonstoichiometric samples, it is probably not meaningful to try to relate these data to the work of O'Reilly and Robertson (20).

A Se-rich amorphous film was crystallized in order to follow the crystallization process. Figure 8 shows the Arrhenius plots for two samples, i.e., one was initially amorphous (x = 0.30) and crystallized at the higher temperature, while the other was initially polycrystalline (x = 0.47) and just annealed at the higher temperature. For the initially amorphous film (solid line), the conductivity increases until it reaches a maximum value at T = 400 K and then decreases as the temperature approaches the final annealing value of 487 K. After annealing for 10 min at 487 K, the sample was cooled again and the dc conductivity followed that of a relatively good-quality polycrystalline sample. This conductivity can be modeled with a single activation energy yielding a value of 0.21 eV. Analysis verified that the sample had crystallized. Another amorphous Se-rich sample (x = 0.41) crystallized in the same manner yielding the same activation energy. This behavior is qualitatively opposite to that illustrated in Fig. 2, which is characteristic of a number of other a-II–VI compounds.

The dotted curve in Fig. 8 is the Arrhenius plot of a polycrystalline, Se-rich (x = 0.47) film. The conductivity is recorded as the sample is annealed to 487 K. One can conclude that this very different behaviour in the conductivity due to the annealing process is related to the fact that one sample was completely amorphous initially since both of these are Se-rich.

The final conductivities of the initially amorphous Se-rich samples and the initially polycrystalline Se-rich samples are not the same. It is tempting to speculate that the final electrical properties observed in both Figs. 4 and 8, are determined by the crystallite nucleation process, which is dependent on whether the crystal growth is initiated on a cold substrate or on a warmer substrate. The sample shown in Fig. 8, which was initially amorphous, appears to represent a polycrystalline film with electrical properties that are more characteristic of a film whose crystallites had nucleated on a hot substrate (see Fig. 4).

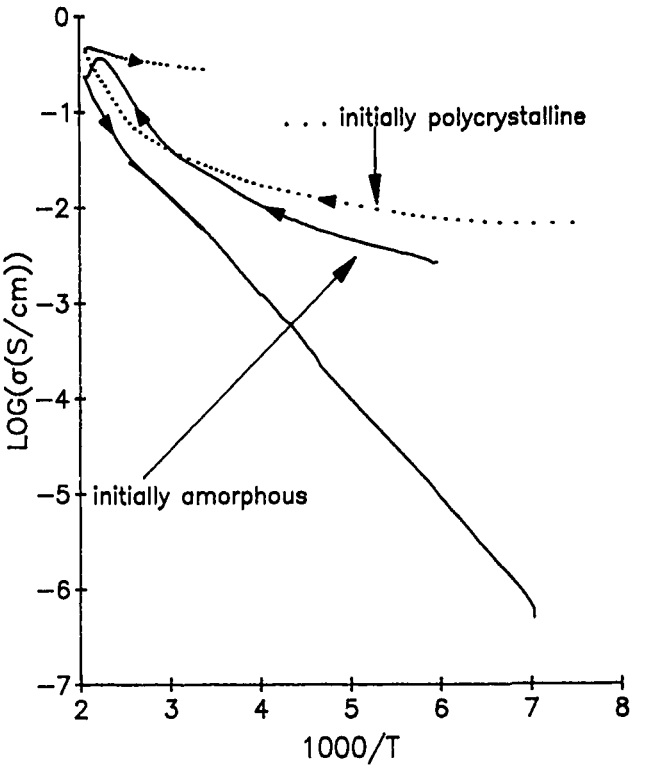

FIG. 8. Changes in dc conductivity with annealing for two Se-rich samples. The solid curve represents the crystallization of a Se-rich (x = 0.3) initially amorphous sample. The dotted curve represents the annealing of a Se-rich sample (x = 0.47) that initially contained crystallites.

3.3. Low-purity CdSe films

To confirm the role of residual gases in the formation of a-CdSe films, the deposition pressure was varied by introducing air through a controlled leak valve with a deposition rate near 0.3 nm s^{-1}.

Diffraction patterns indicate that amorphous samples can be fabricated with ambient air pressures near 3×10^{-5} Torr, but some crystallites are still present when this pressure is as large as 5×10^{-6} Torr. The crystallite size measured by the width of the (002) line decreases with increasing residual gas pressure, decreasing from 52 nm at 1×10^{-8} Torr to 40 nm at 5×10^{-6} Torr. The incorporation of impurities from the air appears to inhibit the crystallite formation.

4. Conclusion

High-purity CdSe thin films were deposited onto substrates held near 100 K using a doubly baffled source. Pure stoichiometric films were always polycrystalline wurtzite CdSe when their structure was observed at room temperature. Some amorphous films were fabricated, but all of those contained excess Se, or were impure having been deposited in a high ambient pressure.

An extensive irreversible annealing process (observed via the dc conductivity) occurs in pure stoichiometric CdSe films deposited onto LN2-cooled substrates, as the film is warmed to room temperature.

As a stoichiometric film made on a LN2-cooled substrate is annealed to 487 K, the conductivity increases and the activation energy decreases continually and the resulting annealed film has very different electrical properties compared with those for a film deposited onto a substrate held at 474 K.

High-purity amorphous nonstoichiometric films are obtained when the Se content is higher then or equal to ≈59 at.%. A small excess of Cd appears to inhibit the growth of larger CdSe crystallites and the film morphology is a mixture of small Cd and CdSe crystallites embedded in an amorphous matrix. The electrical and optical properties of these films scale as a function of the Cd content and the films become metallike near 60 at.% Cd.

Initially polycrystalline Se-rich films, anneal similarly to high-purity stoichiometric films and in both cases, the conductivity increases. Initially amorphous Se-rich films, anneal in a different way, and the conductivity decreases when they crystallize. It is suggested that the temperature at which the crystallites nucleate is an important parameter affecting the way the structure evolves and hence the final conductivities of the films.

Finally, lower purity amorphous CdSe can be prepared when the system background pressure is high enough (i.e., equal to or greater than $\approx 3 \times 10^{-5}$ Torr in the present case).

Acknowledgements

The authors would like to thank Dr. Robert Audas for providing the data acquisition and analysis programs, and also for helpful discussions. Special thanks is due to Dr. Linda Nazar for the use of the Siemens diffractometer. The financial support of the Natural Sciences and Engineering Research Council of Canada is also acknowledged.

1. D. E. BRODIE and J. LACOMBE. Can. J. Phys. **45**, 1195 (1967).
2. A. KUBOVY, J. HAMERSKY, and B. SYMERSKY. Thin Solid Films, **4**, 35 (1969).
3. R. M. MOORE, J. T. FISCHER, and F. KOZIELEC, JR. Thin Solid Films, **26**, 363 (1975).
4. D. S. H. CHAN and A. E. HILL. Thin Solid Films, **35**, 337 (1976).
5. N. G. DHERE, N. R. PARIKH, and A. FERREIRA. Thin Solid Films, **44**, 83 (1977).
6. A. VAN CALSTER. Thin Solid Films, **126**, 219 (1985).
7. F.-C. LUO. *In* Applications of cadmium selenide thin film transistors in flat panel displays. Mater. Res. Soc., Pittsburgh, PA. 1984. **33**, 239 (1984).
8. B. A. RIECKHOFF. M.Sc. Thesis. University of Waterloo, Waterloo, 1977.
9. C. J. L. MOORE and D. E. BRODIE. Can. J. Phys. **60**, 340 (1982).
10. C. J. L. MOORE, B. S. BHARAJ, and D. E. BRODIE. Can. J. Phys. **59**, 924 (1981).
11. S. M. SZE. *In* Physics of semiconductor devices. Wiley-Interscience, New York, London, Sydney, Toronto. 1969. p. 52.
12. J. TAUC. *In* Amorphous and liquid semiconductors. *Edited by* J. Tauc. Plenum Press. New York and London. 1974. p. 178.
13. J. MENDOLIA and D. LEMOINE. Phys. Status Solidi A, **97**, 601 (1986).
14. S. M. BARLOW and D. E. BRODIE. Can. J. Phys. **55**, 61 (1977).
15. L. MAGAFAS, A. N. ANAGNOTOPOULOS, and J. G. ANTONOPOULOS. Phys. Status Solidi A, **111**, K175 (1989).
16. B. D. CULLITY. *In* Elements of X-ray diffraction. 2nd. ed. Addison-Wesley Publishing Company Inc., Reading, MA. 1978. p. 102.
17. B. JENSEN and A. TORABI. J. Opt. Soc. Am. B, **3**, 857 (1986).
18. N. KH. ABRIKOSOV, V. F. BANKINA, L. V. PORETSKAYA, L. E. SHELIMOVA, and E. V. SKUDNOVA. *In* Semiconducting II–VI, IV–VI and V–VI compounds. Plenum Press, New York. 1969. p. 26.
19. J. H. WOLGEMUTH, D. E. BRODIE, and P. C. EASTMAN. Can. J. Phys. **54**, 785 (1976).
20. E. P. O'REILLY and J. ROBERTSON. Phys. Rev. B, Condens. Matter, **34**, 8684 (1986).

Reactive evaporation of BaF_2 in water vapour for *in situ* growth of $YBa_2Cu_3O_x$ thin films

YUAN GAO AND R. W. CLINE
Department of Physics, University of British Columbia, Vancouver, B.C., Canada V6T 2A6
AND
T. TIEDJE
Departments of Physics and Electrical Engineering, University of British Columbia, Vancouver, B.C., Canada V6T 2A6

Received April 6, 1990

The conversion of BaF_2 thin films to BaO during deposition in an oxidizing ambient was investigated as a first step towards the *in situ* growth of superconducting thin films of $YBa_2Cu_3O_x$ from Y, Cu, and BaF_2 source materials. This conversion was found to occur at a temperature of 800°C when BaF_2 was evaporated in a partial pressure of H_2O. The observed conversion temperature agrees well with an equilibrium thermodynamic model. Methods to reduce the growth temperature to the 600–700°C range are proposed.

La conversion de couches minces de BaF_2 en BaO, au cours de la déposition d'un oxydant ambiant, a été étudiée, comme première étape pour réaliser la croissance *in situ* de couches minces supraconductrices de $YBa_2Cu_3O_x$, à partir des ingrédients Y, Cu et BaF_2. On trouve que cette conversion se produit à une température de 800°C lorsque BaF_2 est évaporé sous une pression partielle de H_2O. La température de conversion observée s'accorde bien avec un modèle d'équilibre thermodynamique. On propose des méthodes pour ramener la température de croissance dans l'intervalle 600–700°C.

[Traduit par la rédaction]

Can. J. Phys. **69**, 131 (1991)

1. Introduction

Following the discovery of high-temperature superconductivity by Bednorz and Müller (1) and the subsequent discovery by Chu *et al.* (2) of the superconductivity of $YBa_2Cu_3O_x$ with a transition temperature greater than 90 K, there has been great interest in making superconducting thin films for use in studying the nature of superconductivity and for making superconducting devices. A number of techniques have been widely used to make films, including sputtering (3), electron-beam evaporation (4), and laser ablation (5).

Good control over the stoichiometry is essential for growth of high-quality films. In films codeposited from multiple source to achieve the correct stoichiometry, it is important to have stable and controllable evaporation rates. Elemental Ba and BaO that react readily with O_2 and H_2O, respectively, in the ambient, are inconsistent in their evaporation behavior. In contrast BaF_2, which is inert in air, is very easy to evaporate and provides a relatively stable evaporation rate. Mankiewich *et al.* (6) showed that the use of BaF_2 as the Ba source provided a much improved reproducible method for $YBa_2Cu_3O_x$ thin-film fabrication. They also found that more robust samples could be made by coevaporation starting with Y, Cu, and BaF_2. Vasquez *et al.* (7) reported that the sensitivity of the $YBa_2Cu_3O_x$ films in the air was reduced by the formation of an oxyfluoride on the film surface. In addition, films made using this technique were found to have higher critical current densities.

As-deposited coevaporated films are normally amorphous and insulating, and require post-deposition annealing. For films made by evaporation with BaF_2 as the source of Ba, a two-step annealing process is typically needed: a high-temperature anneal at about 850°C in the presence of oxygen and water vapour converts the fluoride to oxide, followed by a low-temperature anneal at about 400°C in pure oxygen, which forms the superconducting phase.

In electronic applications where multilayered structures are required, the high-temperature anneal can cause problems with interdiffusion between the superconductor film and the underlying material, and cracking of the films due to differential thermal expansion. Also, superconducting junction devices require abrupt interfaces. For these reasons, it is desirable to eliminate the high-temperature anneal, or as a minimum, reduce the annealing temperature. The film-processing temperature should be as low as possible while still allowing the $YBa_2Cu_3O_x$ film to crystallize and oxidize (8). It has been shown by Berkley *et al.* (9) using the electron-beam coevaporation technique that one can form $YBa_2Cu_3O_x$ superconducting films *in situ* at a temperature of 600°C by introducing atomic oxygen into the deposition chamber during the growth process.

We investigated the possibility of combining the advantages of the BaF_2 source material with that of *in situ* growth of the superconductor. To do this, we studied the conditions for the *in situ* conversion of BaF_2 to BaO. This work is discussed in the remainder of this paper, which is divided as follows: Sect. 2 describes how the films were made and the results of these measurements, Sect. 3 presents a model that accounts for the results, and Sect. 4 is a discussion of the results.

2. Film-growth procedure

The thin-film samples were made in a commercial Varian/NRC 3117 evaporator system equipped with two Airco-Temescal electron-beam guns, one resistively heated boat, a resistively heated substrate block, a flow-type rf discharge gas source, and three quartz-crystal deposition-rate monitors (see Fig. 1). Cu and Y were evaporated by means of the electron-beam guns, and BaF_2 by means of the resistively heated boat.

Single crystal MgO ⟨100⟩ substrates were mounted on a heated copper block 34 cm above the centre of the three evaporation sources. The substrates were tightly pressed against the block by means of a stainless steel holder. The copper block could be heated to above 850°C using four 150 W cartridge heaters that were imbedded within it. The temperature of the block was measured with an iron–constantan thermocouple.

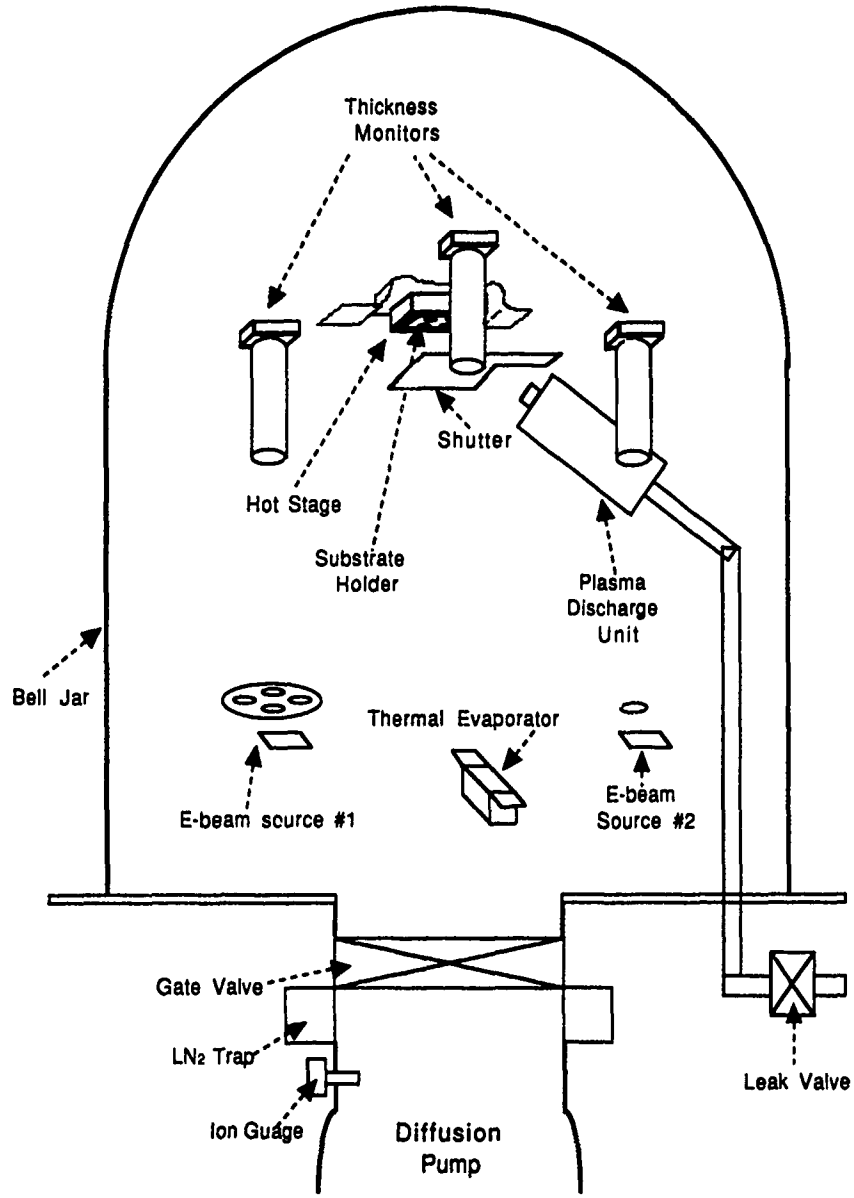

FIG. 1. The vacuum evaporation system.

The flow-type rf discharge gas source made it possible to introduce gases or a plasma into the vicinity of the substrates during the evaporation. The flow rate of gas into the chamber was controlled with a Granville–Phillips leak valve. When desired, a helical resonantor inside the vacuum chamber driven at 50 MHz by a 50 W power amplifier produced a plasma discharge in the inlet gas, just before it entered the chamber.

The evaporation rate of each source material was monitored separately by means of three quartz-crystal thickness monitors, each mounted directly above one of the sources. Crosstalk betwen the three sources was almost entirely eliminated through the use of 7.5 cm long by 2.5 cm diameter stainless steel shield tubes, as shown in Fig. 1. The evaporation rate of each material was controlled with feedback from the monitors to the evaporation sources.

The stoichiometry of coevaporated films was measured by comparing the composition of the evaporated film with that of a ceramic sample of known composition using energy dispersive X-ray analysis. The desired 1:2:3 ratio was produced by appropriately adjusting the evaporation rates with an accuracy of 4% for each of the components.

For the studies of the *in situ* conversion of BaF_2 to BaO, BaF_2 was evaporated from a tantalum boat onto a MgO ⟨100⟩ substrate. H_2O vapour was introduced during the deposition to give a background pressure of 1.5×10^{-5} Torr (1 Torr = 133.3 Pa) (the base pressure in the system was 10^{-6} Torr). The partial pressure of H_2O in front of the substrate was estimated to be 1×10^{-4} Torr from the size of the gas inlet orfice, its distance from the substrate, the pressure rise and volume of the vacuum system, and its pumping speed (10). Films 0.5 μm

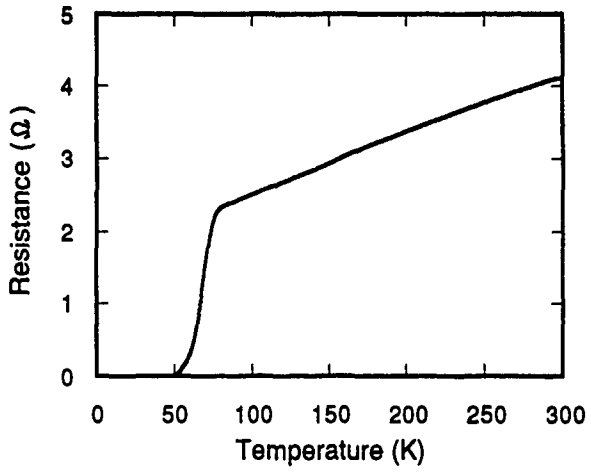

FIG. 2. The temperature dependence of the resistance of the best codeposited $YBa_2Cu_3O_x$ film.

thick were deposited at a rate of 1.0 Å s^{-1} (1 Å = 10^{-10} m). The substrate was heated to determine the effect of temperature on the conversion. Once the conditions for the *in situ* conversion of BaF_2 to BaO were established, coevaporated films of $YBa_2Cu_3O_x$ 1 μm thick were deposited.

As a check on our ability to make superconducting films, $YBa_2Cu_3O_x$ was deposited by sequential evaporation and also by coevaporation of Y, Cu, and BaF_2. The 1 μm thick films were annealed in a furnace after deposition in wet O_2 at 850°C followed by dry O_2 at 400°C. As shown in Fig. 2, the best film had an onset temperature of 87 K and zero resistance at 53 K. The broad transition is believed to be due to deviations in the stoichiometry from the ideal ratio.

A number of BaF_2 films were produced by evaporation in a background pressure of water vapour with the substrate heated to between 600 and 850°C. The BaF_2 and BaO content of the deposited films was measured using powder X-ray diffraction.

The powder diffraction patterns of the as-deposited BaF_2 films over the temperature range 775–850°C are shown in Fig. 3. Also shown in Fig. 3, are the powder diffraction patterns of BaF_2 and BaO for reference. BaO has a relatively complex diffraction pattern due to the existance of many hydrated forms of BaO. The conversion of BaF_2 to BaO, as the temperature increases, can be clearly seen. Although the peak intensities in the powder diffraction patterns are not useful for a quantitative determination of the relative concentration of BaF_2 and BaO owing to the strong orientation dependence of the intensities, they can provide a qualitative picture of the extent of conversion. We define the approximate BaO concentration as,

$$x_{BaO} = \frac{I_{BaO_{max}}}{I_{BaO_{max}} + I_{BaF_{2_{max}}}}$$

where $I_{BaO_{max}}$ and $I_{BaF_{2_{max}}}$ are the highest peak intensities corresponding to BaO and BaF_2, respectively, in the film powder diffraction patterns.

Figure 4 is a plot of the measured BaO concentration, as defined above, versus the temperature at which the films were deposited. The composition of the as-deposited films changes from BaF_2 to BaO at around 800°C. The actual surface temperature of the substrate is expected to be lower than the measured temperature of the heated block owing to radiative cooling of the substrate and imperfect thermal contact between the substrate and block. The fact that similar data were obtained at 805 and 820°C suggests that the reproducibility of the substrate temperature was approximately 15°C.

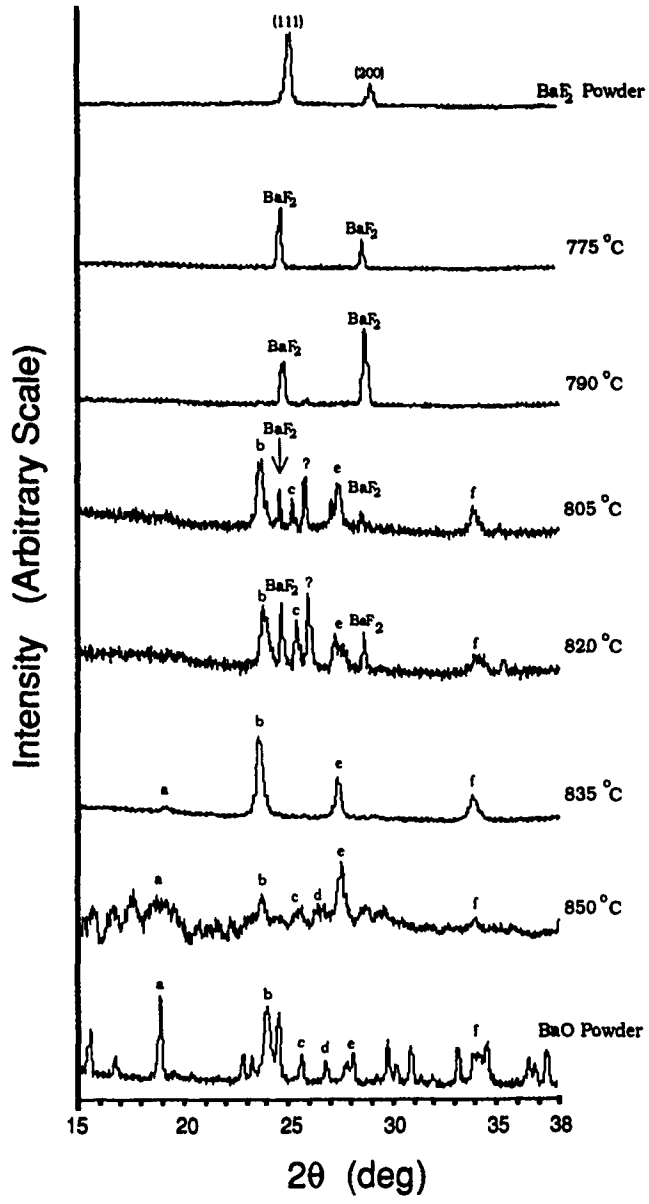

FIG. 3. X-ray diffraction patterns for a series of films made by evaporation of BaF_2 in H_2O vapour, on substrates heated to the indicated temperatures. The X-ray diffraction patterns of BaF_2 and BaO powders are shown for reference.

To study the effect on the oxidation of BaF_2 of different oxygen-containing gases and of dissociating the gas with a plasma discharge, we deposited BaF_2 films under the same conditions as above, but with H_2O vapour replaced by (*i*) H_2O vapour + O_2, (*ii*) O_2 plasma, and (*iii*) H_2O plasma. No reduction in the temperature of the BaO conversion was found with the plasma discharge; O_2 was found to be less effective than H_2O.

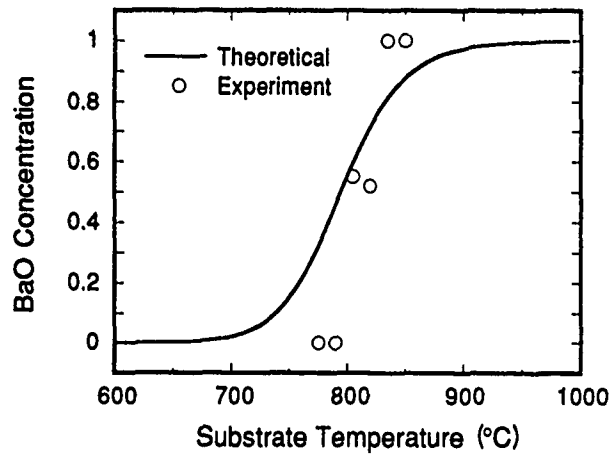

FIG. 4. BaO concentration as a function of substrate temperature showing both the experimental results as well as the predictions of an equilibrium thermodynamic model.

3. Thermodynamic model of the conversion of BaF_2 to BaO

The BaO concentration in the film as a function of the substrate temperature can be calculated in an equilibrium thermodynamic model as follows. The overall reaction taking place during the film deposition process is

$$[1] \quad BaF_{2(s)} + H_2O_{(g)} = BaO_{(s)} + 2HF_{(g)}$$

The direction of the reaction is determined by the concentrations of reactants and products, the temperature, and the pressures of the gases. Entropy favors the forward reaction, enthalpy the reverse reaction. The equilibrium concentrations can be obtained by minimizing the total free energy as a function of temperature. The equilibrium approximation is valid when the deposition rate of BaF_2 is much slower than the reaction rates in both directions. The total Gibbs free energy of the system can be written as

$$[2] \quad G_{\text{total}} = \sum_i h_i - T \sum_j s_j$$

where $\sum_i h_i$ is the total enthalpy and $\sum_j s_j$ is the total entropy of the system summed over all the reactants and products.

We assume for simplicity that there are N sites on the surface of the film and that each site is occupied either by two fluorines or by one oxygen. Therefore,

$$[3] \quad \sum_i h_i = Nx_{BaO} h_{BaO} + N(1 - x_{BaO}) h_{BaF_2} + 2Nx_{BaO} h_{HF} + [N' - Nx_{BaO}] h_{H_2O}$$

where x_{BaO} is the BaO concentration and h_i denotes the enthalpy of the ith material. Because H_2O vapour was constantly supplied during the deposition process, N' is an independant constant.

The total entropy can similarly be written as,

$$[4] \quad \sum_j s_j = Nx_{BaO} s_{BaO} + N(1 - x_{BaO}) s_{BaF_2} + 2Nx_{BaO} s_{HF} + [N' - Nx_{BaO}] s_{H_2O} + S_{site}$$

where s_{BaO}, s_{BaF_2}, s_{HF}, and s_{H_2O} stand for entropies of BaO, BaF_2, HF, and H_2O molecules. S_{site} is the entropy due to the occupation of the surface sites by F_2 or O. Therefore,

$$[5] \quad S_{site} = k \ln \left(\frac{N!}{n_O! n_{F_2}!} \right)$$

where $n_O = x_{BaO}N$ and $n_{F_2} = (1 - x_{BaO})N$ are the numbers of surface sites occupied by oxygen and fluorine, respectively; k is the Boltzmann constant.

Minimizing the total free energy with respect to x_{BaO}, one has

$$[6] \quad \frac{dG_{\text{total}}}{dx_{BaO}} = 0$$

Note that h_{HF} and h_{H_2O} are dependent on the partial pressures P_{HF} and P_{H_2O}, respectively,

$$[7] \quad h_{HF} = h^0_{HF} + kT \ln \left(\frac{P_{HF}}{P_{atm}} \right) = h^0_{HF} + kT \ln \mathcal{P}_{HF}$$

and

$$[8] \quad h_{H_2O} = h^0_{H_2O} + kT \ln \left(\frac{P_{H_2O}}{P_{atm}} \right) = h^0_{H_2O} + kT \ln \mathcal{P}_{H_2O}$$

where h^0_{HF} and $h^0_{H_2O}$ are standard enthalpies at 1 atm. $\mathcal{P} = \frac{P}{P_{atm}}$ denotes the dimensionless pressure normalized by P_{atm}.

Since the HF pressure in steady state is proportional to the rate at which BaF_2 is converted to BaO,

$$[9] \quad P_{HF} \propto 2Nx_{BaO}$$

and

$$[10] \quad P_{H_2O} \propto (N' - Nx_{BaO})$$

Then we have,

$$[11] \quad \frac{dh_{HF}}{dx_{BaO}} = \frac{kT}{x_{BaO}}$$

and

$$[12] \quad \frac{dh_{H_2O}}{dx_{BaO}} = -\frac{NkT}{N' - Nx_{BaO}}$$

Putting [2]–[6] together and using the approximation $\ln N! \approx N \ln N - N$, we obtain,

$$[13] \quad kT + \Delta h - T\Delta s + kT \ln \left(\frac{x_{BaO}}{1 - x_{BaO}} \right) = 0$$

where

[14] $\Delta h = h_{BaO} + 2h_{HF} - h_{BaF_2} - h_{H_2O}$

and

[15] $\Delta s = s_{BaO} + 2s_{HF} - s_{BaF_2} - s_{H_2O}$

Immediately from [13], we have

$$[16]\quad x_{BaO} = \frac{\exp\left(\frac{\Delta s}{k} - 1\right)\exp -\left(\frac{\Delta h}{kT}\right)}{1 + \exp\left(\frac{\Delta s}{k} - 1\right)\exp\left(-\frac{\Delta h}{kT}\right)} = \frac{\exp\left(\frac{\Delta S^0}{R} - 1\right)\exp\left(-\frac{\Delta H}{RT}\right)}{1 + \exp\left(\frac{\Delta S^0}{R} - 1\right)\exp\left(-\frac{\Delta H}{RT}\right)}$$

where $\Delta H = N_A \Delta h$, $\Delta S^0 = N_A \Delta s$ and N_A is Avogadro's constant. ΔH can be expressed as (11),

$$[17]\quad \Delta H = \Delta H^0 + RT \ln\left(\frac{\mathcal{P}^2_{HF}}{\mathcal{P}_{H_2O}}\right)$$

where $\mathcal{P}_{HF}$ and $\mathcal{P}_{H_2O}$ are partial pressures of HF and H_2O normalized by P_{atm} and

[18] $\Delta H^0 = \Delta_f H^0_{BaO} + 2\,\Delta_f H^0_{HF} - \Delta_f H^0_{BaF_2} - \Delta_f H^0_{H_2O}$

[19] $\Delta S^0 = S^0_{BaO} + 2\,S^0_{HF} - S^0_{BaF_2} - S^0_{H_2O}$

The $\Delta_f H^0$'s and S^0's appearing on the right-hand side of [18] and [19] are the enthalpies of formation and the entropies of the individual compounds. Values of these quantities at 1 atm and a range of temperatures are available from standard references; see, for example, ref. 12. Because of the weak temperature dependence of ΔH^0 and ΔS^0 and also because the experiments took place at a 1000 K temperature range the values of $\Delta_f H^0$ and S^0 at 1000 K were used in the calculations. Thus, we have,

$$[20]\quad x_{BaO} = \frac{\frac{\mathcal{P}_{H_2O}}{\mathcal{P}^2_{HF}}\exp\left(\frac{\Delta S^0}{R} - 1\right)\exp\left(-\frac{\Delta H^0}{RT}\right)}{1 + \frac{\mathcal{P}_{H_2O}}{\mathcal{P}^2_{HF}}\exp\left(\frac{\Delta S^0}{R} - 1\right)\exp\left(-\frac{\Delta H^0}{RT}\right)}$$

From the above information, the equilibrium curves for different values of the $\mathcal{P}_{H_2O}/\mathcal{P}^2_{HF}$ ratio in $x_{BaO} - T$ space were obtained and are plotted in Fig. 5. The partial pressure of the reaction product HF just in front of the film, which depends on the heated area exposed to the BaF_2, on the substrate-holding block, and on the BaF_2 deposition rate was estimated to be 1×10^{-6} Torr from the residence time of a HF molecule in the system, which is known from the volume and pumping speed of the vacuum system (10). It follows that the ratio $\mathcal{P}_{H_2O}/\mathcal{P}^2_{HF}$ is about 1×10^{11}. The heated area exposed to the BaF_2 was about 2×10^{-3} m^2. The solid line in Fig. 5 shows the equilibrium $x_{BaO} - T$ curve with $\mathcal{P}_{H_2O}/\mathcal{P}^2_{HF} = 1 \times 10^{11}$, which represents the experimental conditions in the film preparation.

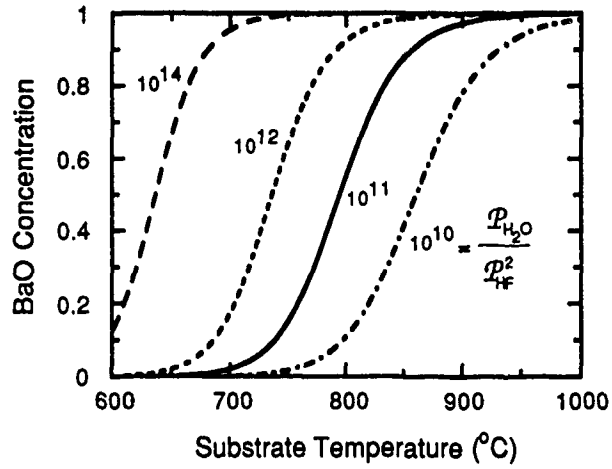

FIG. 5. BaO concentration as a function of temperature, as predicted by the equilibrium thermodynamic model for conversion of BaF_2 to BaO in the presence of H_2O. The solid line corresponds to the ratio $\mathcal{P}_{H_2O}/\mathcal{P}^2_{HF} = 1 \times 10^{11}$ that represents the experimental conditions in the film deposition. A ratio of 1×10^{14} moves the transition down to the 600°C range.

4. Discussion of results

Conversion of BaF_2 to BaO is essential for the *in situ* growth of $YBa_2Cu_3O_x$ films with BaF_2 as the Ba source. For this work to be applicable to the growth of high-T_c superconductors, we assume that the presence of the Y and Cu atoms does not effect the oxidation of the fluoride, such as might result from a catalytic effect. Experimentally we find that the substrate must be heated to about 800°C for the conversion of BaF_2 to BaO to occur in the presence of H_2O during the deposition process. As shown in Fig. 4, the observed conversion temperature agrees well with our equilibrium thermodynamic model. This suggests that equilibrium has been achieved with the H_2O vapour. Therefore, a plasma is not likely to improve the conversion of BaF_2 to BaO because the primary effect of the plasma is expected to be to facilitate the achievement of equilibrium by breaking down activation barriers. As shown above, equilibrium is already achieved in the absence of the plasma. This is consistent with the fact that the observed conversion temperature was not affected by the presence of the H_2O plasma.

The experiments were also conducted with a film deposition rate of 5.0 Å s^{-1}. No significant conversion of BaF_2 was found at substrate temperatures of up to 850°C. This result is consistent with the theory in that higher deposition rates increase the HF partial pressure, which in turn increases the conversion temperature. The experiments were not conducted with deposition rates lower than about 1.0 Å s^{-1}.

As mentioned previously, neither the H_2O vapour + O_2 nor the O_2 plasma had any beneficial effect on the conversion. This result can be explained with a similar equilibrium thermodynamic analysis except with the reaction

$$BaF_2 + \frac{1}{2}O_2 = BaO + F_2$$

It has been reported by Garzon *et al.* (13) that there was negligible oxidation of the BaF_2 in $YBa_2Cu_3O_x$ films made with BaF_2 as the Ba source after a post-deposition anneal carried out at 850°C in dry oxygen.

An attempt was made to grow a codeposited $YBa_2Cu_3O_x$ film at 800°C in water vapour. The resulting film was transparent even though according to the thickness monitors the final thickness of the film was 1 μm. It appears that this temperature is too high for the growth of $YBa_2Cu_3O_x$ films, presumeably because the copper re-evaporates (Cu has a vapour pressure of 10^{-6} Torr at 850°C and CuO has a vapour pressure of 10^{-4} Torr at 600°C). According to the model discussed earlier, the growth temperature (which is determined by the need for BaF_2 to BaO conversion) could be decreased by increasing the ratio of $\mathcal{P}_{H_2O}/\mathcal{P}^2_{HF}$. As shown in Fig. 5, a ratio of 10^{14} would reduce the growth temperature to the 600°C range. The maximum allowable pressure of the H_2O vapour is limited to about 10^{-4} Torr by the requirement that the evaporated molecules and the electrons in the electron-beam gun have a long mean free path, however, the partial pressure of HF could be reduced by adding an HF getter (such as quartz wool) to the film-growth environment, or by reducing the heated area exposed to BaF_2 that generates the HF.

If the process studied is to be used in the *in situ* growth of $YBa_2Cu_3O_x$ superconductor thin films, the question arises as to whether water vapour would oxidize the copper as well as the BaF_2 at 600°C. Applying the same model as was used to explain the oxidation of BaF_2, we surmise that water vapour should also oxidize the copper.

In conclusion, we have investigated the conditions for the *in situ* oxidation of BaF_2 in a reactive evaporation in H_2O vapour, both experimentally and theoretically. This *in situ* conversion temperature of BaF_2 was found to be in agreement with an equilibrium thermodynamic model. The model suggests that the conversion temperature could be reduced by reducing the partial pressure of HF, which provides a possibility for low temperature *in situ* growth of $YBa_2Cu_3O_x$ superconductor thin films with BaF_2 as the Ba source.

Acknowledgements

We thank Norman Osborne for his help with the X-ray diffraction measurements. This work was supported by the Natural Sciences and Engineering Research Council of Canada.

1. J. G. Bednorz and K. A. Müller. Z. Phys. B: Condens. Matter, **64**, 189 (1986).
2. C. W. Chu, P. H. Hor, R. L. Meng, L. Gao, Z. H. Huang, and Y. Q. Wang. Phys. Rev. Lett. **58**, 405 (1987).
3. M. Hong, S. H. Liou, J. Kwo, and B. A. Davidson. Appl. Phys. Lett. **51**, 694 (1987).
4. R. B. Laibowitz, R. H. Koch, P. Chaudhari, and R. J. Gambino. Phys. Rev. B: Condens. Matter, **35**, 8821 (1987).
5. D. Dijkkamp, T. Venkatesan, X. D. Wu, S. A. Shaheen, N. Jisrawi, Y. H. Min-Lee, W. L. McLean, and M. Croft. Appl. Phys. Lett. **51**, 619 (1987).
6. P. M. Mankiewich, J. H. Scofield, W. J. Skocpol, R. E. Howard, A. H. Dayem, and E. Good. Appl. Phys. Lett. **51**, 1753 (1987).
7. R. P. Vasquez, B. D. Hunt, and M. C. Foote. Appl. Phys. Lett. **54**, 2373 (1989).
8. H. Adachi, K. Hirochi, K. Setsune, M. Kitabatake, and K. Wasa. Appl. Phys. Lett. **51**, 2263 (1987).
9. D. D. Berkley, B. R. Johnson, N. Anaud *et al.* Appl. Phys. Lett. **53**, 1973 (1988).
10. Y. Gao. M.Sc. Thesis. University of British Columbia, Vancouver. 1990.
11. M. K. Kemp. Physical chemistry. Marcel Dekker Inc., New York. 1979. pp. 202 and 600.
12. M. W. Chase, C. A. Davies, J. R. Downey, D. J. Frurip, R. A. Mcdonald, and A. N. Syverud. J. Phys. Chem. Ref. Data, **14** (Suppl. 1), 332 (1985); **14** (Suppl. 1), 1015 (1985); **14** (Suppl. 1), 1066 (1985); **14** (Suppl. 1), 1274 (1985).
13. F. H. Garzon, J. G. Beery, D. R. Brown, R. J. Sherman, and I. D. Raistrick. Appl. Phys. Lett. **54**, 1365 (1989).

Neutron diffraction study of the structure of the antifluorite crystal $(NH_4)_2TeCl_6$

ROBIN L. ARMSTRONG[1] AND PAUL DUFORT
Department of Physics, University of Toronto, Toronto, Ont. Canada M5S 1A7
AND
BRIAN M. POWELL
Atomic Energy of Canada Limited Research, Chalk River Laboratories, Chalk River, Ont., Canada K0J 1J0

Received August 16, 1990

A neutron diffraction study of the crystal structure of $(NH_4)_2TeCl_6$ is presented. The data support a previous contention that this crystal undergoes a ferrorotative structural phase transition at 85 K, from a cubic structure with space group O_h^5 to a trigonal structure with space group C_{3i}^2. The primary-order parameter is the rotation angle, Φ, of the $TeCl_6$ octahedra about a [111] axis of the cubic phase. The data indicate that the temperature dependence of Φ is non-mean-field like over an extended reduced temperature range.

On a présenté une étude par diffraction des neutrons de la structure cristalline de $(NH_4)_2TeCl_6$. Les données confirment l'affirmation antérieure que ce cristal subit une transition de phase structurale à 85 K, passant d'une structure cubique avec groupe spatial O_h^5 à une structure trigonale avec groupe spatial C_{3i}^2. Le paramétre d'ordre primaire est l'angle de rotation, Φ, de l'octaèdre $TeCl_6$ autour d'un axe [111] de la phase cubique. Les données indiquent que la dépendance de la température, pour l'angle Φ, n'est pas selon la théorie du champ moyen pour un intervalle étendu de température réduite.
[Traduit par la rédaction]

Can. J. Phys. 69, 137 (1991)

1. Introduction

Structural phase transitions driven by the softening of the longitudinal rotary lattice mode in cubic A_2MX_6 compounds are known to occur in a number of cases. The structural alteration involves the static rotation of the $(MX_6)^{2-}$ octahedral ions; the rotation angle Φ of these ions relative to their equilibrium orientation in the cubic phase is the primary-order parameter. Transitions associated with the T_{1g} (Γ) mode involve in-plane ferrorotations of the $(MX_6)^{2-}$ octahedral ions so that the unit-cell size remains unchanged. Examples of this type of rotational displacive transition have been reported in which the static rotation occurs about the four-fold axis (1, 2) and about the three-fold axis (3) of the $(MX_6)^{2-}$ ions. In the former case, as occurs in K_2OsCl_6, the single-line chlorine nuclear quadrupole resonance (NQR) spectrum of the cubic, O_h^5, phase splits into two components with intensity ratio 2:1 in the tetragonal, C_{4h}^5, phase below T_c. The associated structural changes were identified by neutron diffraction methods (1). In the latter case, as occurs in $(NH_4)_2PbCl_6$, the chlorine NQR spectrum consists of a single line both in the cubic, O_h^5, phase and in the trigonal, C_{3i}^2, phase below T_c; the temperature dependence of the line exhibits a cusp in the vicinity of T_c (4, 5). Again, the associated structural changes were measured by neutron diffraction (3).

The chlorine NQR spectrum of the compound $(NH_4)_2TeCl_6$ behaves in a similar fashion (4, 5) to that in $(NH_4)_2PbCl_6$ and the behaviour cannot be explained by a change in the nature of the rotational motion of the $(NH_4)^+$ ions. In this paper we report neutron diffraction measurements made on a sample of $(NH_4)_2TeCl_6$. These measurements were undertaken to determine whether or not a structural phase transition occurs in the vicinity of 85 K and if so to obtain the space group of the low-temperature phase and the temperature dependence of the primary-order parameter for the transition.

[1]Present address: Department of Physics, University of New Brunswick, Fredericton, N.B., Canada E3B 5A3.

2. Experimental

The sample of $(NH_4)_2TeCl_6$ was provided by Professor J. Pelzl of Ruhr Universitat, Bochum, Federal Republic of Germany. The neutron powder diffraction patterns were measured with the E3 spectrometer using a 30 element detector at the NRU reactor, Chalk River. the sample, enclosed in a thin-walled vanadium can 0.5 cm in diameter, was mounted in a variable temperature cryostat. The monochromator was Si(115) and the neutron wavelength was 1.4814 Å (1 Å = 10^{-10} m). The collimation before the sample was 0.3°. The effective collimation following the sample is determined by the sample and detector diameters and their separation. In our experiment it has the value 0.2°. To minimize possible effects due to finite crystalline grain size the cryostat was rotated continuously throughout the experiment. The intensity of the scattered neutrons was measured as a function of scattering angle, 2θ, at intervals of 0.05° over the range $5° \leq 2\theta \leq 120°$. Measurements were made at 10 temperatures between 12 and 100 K. The experimental results obtained at 100 and at 20 K are shown by the dots in Fig. 1.

The diffraction profiles were analyzed by the profile-refinement technique developed by Rietveld (6), as modified by Pawley (7) to allow additional constraints to be imposed; in this case, for example, that bond lengths within a $(TeCl_6)^{2-}$ octahedron must be equal. A set of programs (8), previously written to facilitate the specification of crystal structures relative to the cubic structure, was used. The three width parameters U, V, and W, and the asymmetry parameter P were used to describe the angle-dependent width and asymmetry of the Debye–Scherrer peaks. These parameters were determined by fitting to the 100 K profile and the values obtained were used for all other profiles. The background was represented by a cubic spline function fitted to the observed background counts at more or less regular intervals across the spectra. The fitted structural parameters were derived by minimizing the quantity

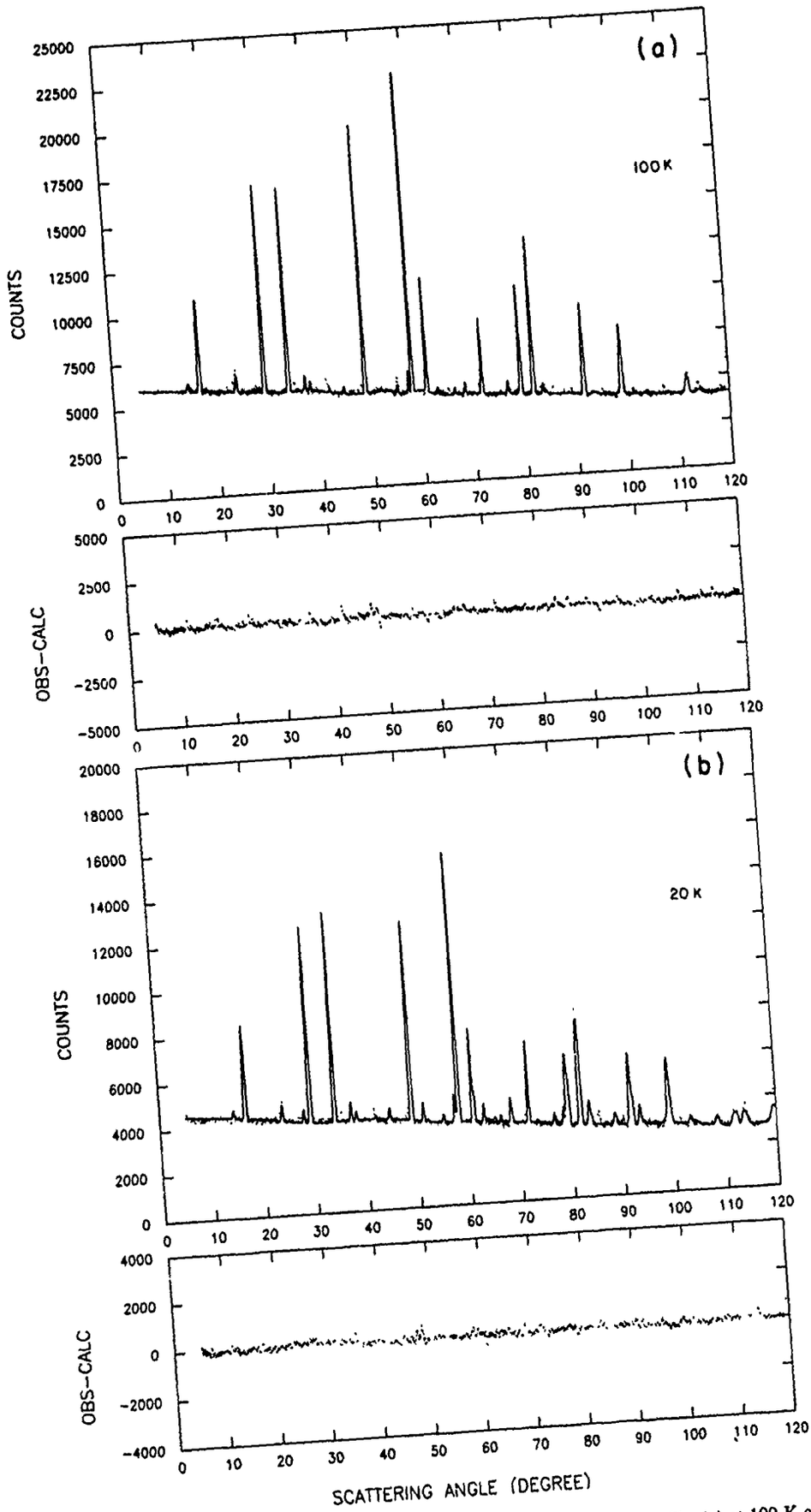

FIG. 1. The comparison of observed and fitted powder diffraction profiles for $(NH_4)_2TeCl_6$: (*a*) at 100 K and (*b*) at 20 K.

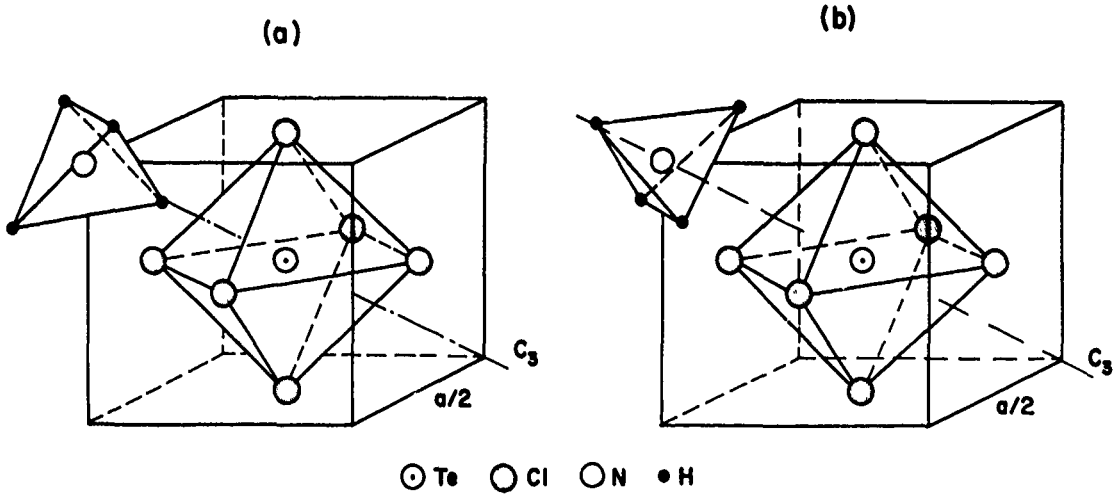

FIG. 2. Two static models for the orientation of the $(NH_4)^+$ ions relative to the $(TeCl_6)^{2-}$ ions: orientation parameter (*a*), $Q = 0$; (*b*), $Q = 1$.

$$\chi^2 = \frac{\sum_i \frac{(y_i^{obs} - y_i^{calc})^2}{y_i^{obs}}}{N-n}$$

where y_i^{obs} (y_i^{calc}) are the observed (calculated) counts at scattering angle $2\theta_i$, N is the total number of data points, and n is the number of adjustable parameters in the model. The coherent neutron scattering lengths, in units of 10^{-12} cm, are (9) −0.374 for *H*, 0.936 for N, 0.543 for Te, and 0.958 for Cl.

The cubic high-temperature phase of $(NH_4)_2TeCl_6$ has space group O_h^5. The diffraction data taken at 100 and 88 K were fitted to a model having this symmetry. The structural parameters are the lattice constant, *a*, the bond length Te—Cl = *r*, and four Debye–Waller factors $< u(NH_4)^2 >$, $< u(TeCl_6)^2 >$, $< \theta(NH_4)^2 >$, and $< \theta(TeCl_6)^2 >$. The Debye–Waller factors describe the mean-square amplitudes of the translational and rotational thermal molecular motions. The N—H bond length was fixed at the value 0.95 Å since the strong correlation between this bond length and the mean-square angular displacement of the $(NH_4)^+$ ion precluded their separate determination.

Various possibilities were considered for the orientation of the $(NH_4)^+$ ions. The eight protons occupy Wyckoff *f* sites of the space group O_h^5. Two static models, **A** and **B**, correspond to the protons pointing towards, or away from, the nearest-neighbour chlorines, respectively. Figure 2 is a sketch of the relative orientation of the $(NH_4)^+$ tetrahedra and $(TeCl_6)^{2-}$ octahedra for these two static models. Nine other intermediate orientations were also selected. An orientation parameter Q was introduced such that, in the limit of $Q = 0$, model **A** applies, and in the limit of $Q = 1$, model **B** applies. Intermediate values of Q correspond to linear combinations of models **A** and **B**; $Q = 0.5$ represents a dynamic model in which the $(NH_4)^+$ ions are hopping between the two static orientations and spending equal amounts of time in each. The resulting χ^2 values for the best fits for each of 11 values of Q for the data at both 88 and 100 K are shown in Fig. 3. It is seen that three minima occur for the Q values 0, 0.5, and 1 and that the overall best fit corresponds to $Q = 1$; i.e., the static model with the protons pointing away from the nearest-neighbour chlorines. This preferred orientation agrees with previous determinations for $(NH_4)_2PtBr_6$ (8), $(NH_4)_2PbCl_6$ (3).

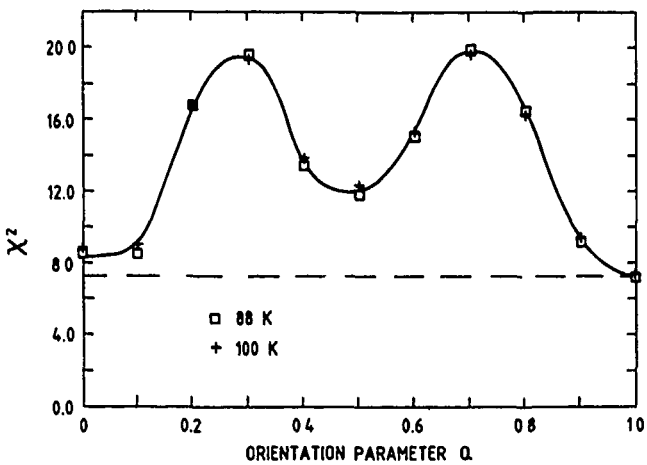

FIG. 3. Plot of χ^2 as a function of the orientation parameter Q.

Figure 1 shows a comparison of the observed (dots) and fitted (solid line) profiles together with the difference $(y_i^{calc} - y_i^{obs})$ for the 100 and 20 K data. At 100 K the value of χ^2 is 7.5. A measure of fit more familiar to crystallographers is the *R* value defined as

$$R_p = \frac{100 \times \sum_i |y_i^{obs} - y_i^{calc}|}{\sum_i y_i^{obs}}$$

This value should be compared with R_{exp}, the value expected from statistical errors alone

$$R_{exp} = \frac{(N-n)^{1/2}}{\sum_i y_i^{obs}}$$

For the fit to the 100 K profile $R_p = 2.5$ while $R_{exp} = 1.4$. The apparent fit as seen "by eye" is quite satisfactory. The structural parameters for the fits at 100 and 88 K are listed in Table 1. In all cases the parameters decrease with temperature as expected, although with the exception of the lattice constant

TABLE 1. Structural parameters for the O_h^5 model used above T_c

	100 K	88 K
χ^2	7.5	7.3
R_p	2.5	2.5
R_{exp}	1.4	1.4
a (Å)	10.0866 ± 0.0003	10.0816 ± 0.0003
r (Å)	2.524 ± 0.003	2.524 ± 0.003
$< u(NH_4)^2 >$ (Å^2)	0.0178 ± 0.0017	0.0173 ± 0.0016
$< \theta(NH_4)^2 >$ (deg^2)	304 ± 20	300 ± 19
$< u(TeCl_6)^2 >$ (Å^2)	0.0022 ± 0.0015	0.0018 ± 0.0015
$< \theta(TeCl_6)^2 >$ (deg^2)	12.4 ± 1.2	11.7 ± 1.2

TABLE 2. χ^2 vs. temperature for various space groups

T (K)	χ^2		
	O_h^5	C_{4h}^5	C_{3i}^2
100	7.5		
88	7.3		
80	6.3	6.3	6.2
70	8.8	6.9	6.6
60	13.4	9.3	6.8
50	16.6	12.0	7.8
40	16.7	12.1	6.2
30	19.9	13.2	7.0
20	20.3	13.3	5.6
12	27.0	19.6	8.5

the changes are within the experimental uncertainties. The parameters are comparable with those obtained for $(NH_4)_2PbCl_6$.

The diffraction data for the eight temperatures below T_c were fitted to three models with symmetry O_h^5, C_{4h}^5, and C_{3i}^2, respectively. Since no superlattice reflections were observed below T_c it was assumed that the structural phase transition involves a ferrorotation of the $TeCl_6$ octahedra. This is certainly the most probable case. The C_{4h}^5 model structure is obtained by a rotation of the octahedra about the four-fold [001] symmetry axis; the C_{3i}^2 model structure is obtained by a rotation of the octahedra about the three-fold [111] symmetry axis. The χ^2 values for the best fits to each model at each temperature are listed in Table 2. It is seen that only the C_{3i}^2 model is able to account for the data equally well over the entire temperature range.

A description in terms of rhombohedral axes is the more natural one to describe a trigonal distortion along the cubic [111] direction, but for greater convenience hexagonal axes were used to describe the model. Figure 4 shows how the cubic, hexagonal, and rhombohedral axes are related. Three extra parameters were necessitated by the lower symmetry of space group C_{3i}^2; the rotation angle, Φ, of the $TeCl_6$ octahedra about the three-fold axis of the cubic lattice, an $(NH_4)^+$ ion displacement, Δ, along the same three-fold axis and a second lattice parameter, b. The $(TeCl_6)^{2-}$ ions themselves are assumed to be rigid and not to distort as a result of the phase transition. Tetrahedral $(NH_4)^+$ ions cannot be located in a structure having trigonal symmetry without the possibility of a distortion. In the crystal structure refined, the eight protons in the formula unit are located in the Wyckoff f and c sites (six sites and two sites, respectively). However, the atomic coordinates found for the protons show that no significant distortion of the $(NH_4)^+$ ion

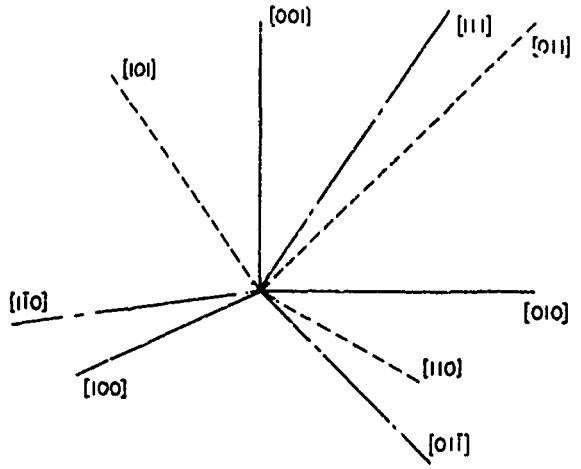

FIG. 4. Cubic axes [100], [010], [001]; hexagonal axes [111], [110], [011]; rhombohedral axes [101], [011], [110].

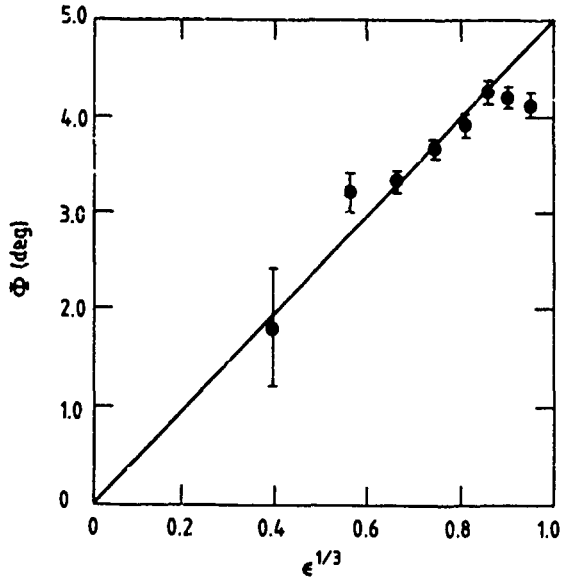

FIG. 5. Plot of the rotation angle Φ as a function of $\epsilon^{1/3} = [(T_c - T)/T_c]^{1/3}$.

has occurred. The two nitrogen atoms are also in c sites, while the six chlorine atoms are in e sites, and the tellurium atom in an a site.

Figure 1 shows the fitted (solid line) profile and the difference spectrum for the 20 K data. The value of χ^2 is 5.6; the R_p value is 2.8. The structural parameters for all temperatures are listed in Table 3. The changes in the lattice parameters are consistent with thermal expansion. The bond length, Te—Cl, was fixed for the final fits; for when allowed to vary, it remained unchanged within experimental uncertainty. The thermal parameters are qualitatively reasonable. The parameter Δ is small but statistically significant; it shows no measurable temperature dependence. The most interesting parameter is the rotation angle, Φ, of the $(TeCl_6)^{2-}$ octahedral ion; it is the primary-order parameter for the transition.

In Fig. 5, Φ is plotted as a function of

$$\epsilon^{1/3} = -\left(\frac{[T - T_c]}{T_c}\right)^{1/3}$$

TABLE 3. Structural parameters for the C_{3i}^2 model for temperatures $T < T_c$

	T (K)							
	80	70	60	50	40	30	20	12
χ^2	6.2	6.6	6.8	7.8	6.2	7.0	5.6	8.5
R_p	2.6	2.5	3.1	2.9	2.9	3.0	2.8	3.1
R_{exp}	1.4	1.4	1.6	1.4	1.6	1.6	1.6	1.4
a (Å)	10.0722 ±0.0012	10.0614 ±0.0007	10.0533 ±0.0006	10.0419 ±0.0006	10.0404 ±0.0005	10.0370 ±0.0006	10.0324 ±0.0005	10.0234 ±0.0005
b (Å)	5.0410 ±0.0003	5.0416 ±0.0002	5.0468 ±0.0002	5.0415 ±0.0002	5.0454 ±0.0002	5.0455 ±0.0002	5.0444 ±0.0002	5.0399 ±0.0002
r (Å)	2.524	fixed for final fits						
Φ (deg)	1.79 ±0.25	3.21 ±0.11	3.34 ±0.08	3.65 ±0.07	3.90 ±0.06	4.26 ±0.07	4.19 ±0.06	4.11 ±0.07
Δ (Å)	0.07±0.02	0.08±0.02	0.05±0.02	0.05±0.02	0.05±0.02	0.05±0.02	0.05±0.02	0.03±0.02
D_1	0.012 ±0.002	0.009 ±0.002	0.009 ±0.002	0.008 ±0.002	0.009 ±0.002	0.012 ±0.002	0.010 ±0.002	0.007 ±0.002
D_2	337±19	349±20	328±18	320±20	322±16	283±21	297±19	295±20
D_3	0±0.002	0±0.002	0±0.002	0±0.002	0±0.002	0±0.002	0±0.002	0±0.002
D_4	4.2±1.5	5.3±1.3	6.8±1.3	2.3±1.5	3.0±1.4	5.3±1.4	4.2±1.2	3.3±1.5

NOTE: $D_1 = < u(NH_4)^2 >$ in Å^2, $D_2 = < \theta(NH_4)^2 >$ in (deg)^2, $D_3 = < u(TeCl_6)^2 >$ in Å^2, and $D_4 = < \theta(TeCl_6)^2 >$ in (deg)^2. The hexagonal lattice parameters of the C_{3i}^2 phase are given by $c_h = 3^{1/2} a$ and $a_h = 2^{1/2} b$.

The data are well represented by a straight line except for the largest values of ϵ. This analysis indicates that the primary-order parameter is non-mean-field like over an extended range of reduced temperatures. Although this result is somewhat surprising, it is in agreement with the result obtained for K_2OsCl_6 from measurements of the temperature dependences of Bragg peaks in the vicinity of T_c for a single crystal sample (1).

3. Conclusion

The neutron diffraction data support the postulate that $(NH_4)_2TeCl_6$ undergoes a structural phase transition at 85 K from a cubic structure with space group O_h^5 to a trigonal structure with space group C_{3i}^2. The transition is ferrorotative with primary-order parameter Φ, the rotation angle of the $(TeCl_6)^{2-}$ octahedra about the [111] axis of the cubic phase. The temperature dependence of Φ is non-mean-field like over an extended reduced temperature range. A small lattice distortion and a $(NH_4)^+$ ion displacement along [111] also occur and constitute secondary-order parameters for the transition.

Acknowledgements

The authors thank Professor J. Pelzl for supplying the sample and H. F. Nieman and P. A. Moss for expert technical assistance. The authors acknowledge the support of the Natural Sciences and Engineering Research Council of Canada.

1. R. L. ARMSTRONG, D. MINTZ, B. M. POWELL, and W. J. L. BUYERS. Phys. Rev. B, Condens. Matter, **17**, 1260 (1978).
2. R. L. ARMSTRONG, R. M. MORRA, and B. M. POWELL. Can. J. Phys. **63**, 998 (1985).
3. R. L. ARMSTRONG, B. LO, and B. M. POWELL. Can. J. Phys. **67**, 1040 (1989).
4. C. DIMITROPOULOS and J. PELZL. Z. Naturforsch. A, Phys. Phys. Chem. Kosmophys. **44**, 109 (1989).
5. U. KAWALD, S. MULLER, and J. PELZL. Solid State Commun. **67**, 239 (1988).
6. H. M. RIETVELD. J. Appl. Crystallogr. **2**, 65 (1969).
7. G. S. PAWLEY. Adv. Struct. Res. Diffr. Methods, **4**, 32 (1972).
8. M. SUTTON, R. L. ARMSTRONG, B. M. POWELL, and W. J. L. BUYERS. Can. J. Phys. **59**, 449 (1981).
9. V. F. SEARS. *In* Methods in experimental physics. Vol. 23A. Neutron Scattering. *Edited by* K. Skold and D. L. Price. Academic Press, New York. 1986. p. 521.
10. R. L. ARMSTRONG, R. M. MORRA, B. M. POWELL, and W. J. L. BUYERS. Can. J. Phys. **61**, 997 (1983).

A new scaling length for semiconductor-device modeling

S. S. De and A. K. Ghosh
Centre of Advanced Study in Radio Physics and Electronics, University of Calcutta, 1, Girish Vidyaratna Lane, Calcutta 700 009, India

Received April 6, 1990

Through the use of an approximate solution of Poisson's equation, a new scaling length has been introduced that is appropriate to semiconductor-device modeling of surface problems or step-junction problems in regions where the fixed charges are dominant.

En utilisant une solution approximative de l'équation de Poisson, on a introduit une nouvelle longueur d'échelle qui est appropriée à la modélisation par dispositifs semiconducteurs des problèmes de surface ou des problèmes de jonctions abruptes dans des régions où les charges fixes sont dominantes.

[Traduit par la rédaction]

Can. J. Phys. **69**, 142 (1991)

1. Introduction

Scaling length is used in device modeling. Its purpose is to reduce redundancy in a function of position and other independent variables. Kingston and Neustadter (1) treated the semiconductor surface problem numerically, and chose the intrinsic Debye length L_{D_i} for distance normalization in plotting curves of potential versus position. Their plots had families of curves with enormous redundancy. Jindal and Warner (2) used the extrinsic Debye length for normalization, and this removed the redundancy completely from the potential solution all the way from the threshold plane to the region of neutrality. The scaling length L_{JW}, chosen for position normalization, is a function of the extrinsic Debye length and bulk potential. It is used to reduce redundancy, specially for normalized bulk potential at higher values. The extrinsic Debye length is not appropriate for scaling depleted regions in the vicinity of the pn junctions and semiconductor surfaces. Therefore, earlier workers choose a scaling length (L_{JW}) as a complement to the extrinsic Debye length for investigating depleted regions. An analytical solution of the Poisson–Boltzmann equation, appropriate to semiconductor modeling, cannot be derived exactly. Previous workers obtained either approximate analytical solutions or made exact numerical computations, although all of these are helpful or appropriate to certain fields of application (3). They obtained approximate expressions for the potential as a function of position in various ranges of potential. Subsequently, others have used different methods of modeling the C–V profiles of high–low junctions and heterojunctions, involving the integration of Poisson's equation (4).

In this presentation, an alternative expression for scaling length has been derived by the use of an approximate analytical solution of Poisson's equation (5). It replaces the extrinsic Debye length that is appropriate to the semiconductor-device modeling of surface problems or step-junction problems in regions where the fixed charges are dominant. The new scaling length, thus obtained, may be useful for modeling pn junctions, and step-junction and MOS (metal oxide semiconductor) structures. Although the new scaling length is approximate, it is useful in different ranges of potential profiles under a solitary boundary condition beyond the inversion regime.

2. Derivation of scaling length

The expression for the normalized position from the integral of Poisson's equation is given by

$$[1]\quad \frac{x}{L_D} = 2^{-1/2}\int_W^{W_J}\left\{\frac{\exp(U_{20})+\exp(-U_{20})}{\exp(U_{20})\,[\exp(-W')+W'-1]+\exp(-U_{20})\,\{\exp W'-W'-1\}}\right\}^{1/2} dW'$$

where U_{20} = normalized bulk potential and x = distance normal to the plane of the junction.

The transformation relations among different potentials are given by $U_{20} - U_J \equiv W_J \equiv$ total potential difference, and $U_{20} - U \equiv W \equiv$ potential difference between the remote-end region and that at an arbitrary point.

The integration of [1] cannot be performed analytically for all ranges of value of W. From the transformation relations and the situation where the term $\exp(-W)$ may be ignored, one can integrate [1] analytically by a series expansion technique except at $W = 1$ and $W_J = 1$, where the situation would introduce error (5). Thus for $W_J > W$, also as U_{20} is large, [1] may be written as

$$[2]\quad \frac{x}{L_D} = 2^{-1/2}\int_W^{W_J}\frac{dW'}{[(W'-1)+\exp(-2U_{20})(\exp W'-W'-1)]^{1/2}}$$

On simplification, [2] yields

$$[3]\quad \frac{x}{L_D} = 2^{-1/2}\int_W^{W_J}\frac{dW'}{(W'-1)^{1/2}} - 2^{-3/2}\int_W^{W_J}\frac{\exp(-2U_{20})(\exp W'-W'-1)}{(W'-1)^{3/2}}dW'$$

and [3] can be written as

$$[4] \quad \frac{x}{L_D} = 2^{1/2}\left[(W_J - 1)^{1/2} - (W - 1)^{1/2}\right] - 2^{-3/2} I$$

where

$$I = \int_W^{W_J} \frac{\exp(-2U_{20})(\exp W' - W' - 1)}{(W' - 1)^{3/2}} dW'$$

From previous work (5), the solution of [4] can be written as

$$[5] \quad \frac{x}{L_D} = 2^{1/2}\left[(W_J - 1)^{1/2} - (W - 1)^{1/2}\right] + 2^{-1/2}\exp\left[\frac{}{}(2U + 1)\right]\left\{\left[(W_J - 1)^{-1/2}\left(W_J - \frac{(W_J - 1)^2}{6} + \frac{(W_J - 1)^3}{30} - \frac{(W_J - 1)^4}{168} + \ldots\right) - (W - 1)^{-1/2}\left(W - \frac{(W - 1)^2}{6} + \frac{(W - 1)^3}{30} - \frac{(W - 1)^4}{168} + \ldots\right)\right]\left[1 - 2^{3/2}\exp(-1)\right] + 2^{-1/2}\exp(-1)\left[(W_J - 1)^{1/2}\left(1 - \frac{(W_J - 1)}{3} + \frac{(W_J - 1)^2}{10} - \frac{(W_J - 1)^3}{42} + \frac{(W_J - 1)^4}{216} - \ldots\right) - (W - 1)^{1/2}\left(1 - \frac{(W - 1)}{3} + \frac{(W - 1)^2}{10} - \frac{(W - 1)^3}{42} + \frac{(W - 1)^4}{216} - \ldots\right)\right]\right\}$$

Equation [5] represents an alternative analytical solution of the Poisson–Boltzmann equation.

For $W = 1$, i.e., when the potential difference between the remote-end region and that at the arbitrary point becomes unity, then

$$[6] \quad \frac{\Delta x}{L_D} = 2^{1/2}(W_J - 1)^{1/2} + 2^{-1/2}\exp(-2U_{20} + 1)\left\{\left[(W_J - 1)^{-1/2}\left(W_J - \frac{(W_J - 1)^2}{6} + \frac{(W_J - 1)^3}{30} - \frac{(W_J - 1)^4}{168} + \ldots\right)\right]\left[1 - 2^{3/2}\exp(-1)\right] + 2^{-1/2}\exp(-1)\left[(W_J - 1)^{1/2}\left(1 - \frac{(W_J - 1)}{3} + \frac{(W_J - 1)^2}{10} - \frac{(W_J - 1)^3}{42} + \frac{(W_J - 1)^4}{216} - \ldots\right)\right]\right\}$$

Δx is the separation between two points depicted by $W = 1$ and $W = W_J$. The situation yields $W < W_J < 2|U_{20}|$.

The sharp spatial boundary corresponds to the position where $W_J = 2|U_{20}|$, which may be conveniently considered as the threshold point for strong inversion. Hence, the maximum depletion-layer thickness, or depletion distance that can be sustained in a sample having a bulk potential of magnitude $|U_{20}|$ under equilibrium conditions, will be given by

$$[7] \quad \left.\frac{\Delta x}{L_D}\right|_{\max} = 2^{1/2}(2|U_{20}| - 1)^{1/2} + 2^{-1/2}\exp(-2|U_{20}| + 1)\left\{\left[(2|U_{20}| - 1)^{-1/2}\left(2|U_{20}| - \frac{(2|U_{20}| - 1)^2}{6} + \frac{(2|U_{20}| - 1)^3}{30} - \frac{(2|U_{20}| - 1)^4}{168} + \ldots\right)\right]\left[1 - 2^{3/2}\exp(-1)\right] + 2^{-1/2}\exp(-1) \times \left[(2|U_{20}| - 1)^{1/2}\left(1 - \frac{(2|U_{20}| - 1)}{3} + \frac{(2|U_{20}| - 1)^2}{10} - \frac{(2|U_{20}| - 1)^3}{42} + \frac{(2|U_{20}| - 1)^4}{216} - \ldots\right)\right]\right\}$$

Restricting the series to an appropriate range from the physical standpoint, a modified scaling length may be chosen as

$$[8]\quad L_{mod} = 2^{1/2} L_D (2|U_{20}| - 1)^{1/2} + 2^{-1/2} L_D \exp(-2|U_{20}| + 1) \left\{ \left[(2|U_{20}| - 1)^{-1/2} \left(2|U_{20}| - \frac{(2|U_{20}| - 1)^2}{6} + \frac{(2|U_{20}| - 1)^3}{30} - \frac{(2|U_{20}| - 1)^4}{168} + \ldots \right) \right] \left(1 - 2^{3/2} \exp(-1) \right) + 2^{-1/2} \exp(-1) \left[(2|U_{20}| - 1)^{1/2} \times \left(1 - \frac{(2|U_{20}| - 1)}{3} + \frac{(2|U_{20}| - 1)^2}{10} - \frac{(2|U_{20}| - 1)^3}{42} + \frac{(2|U_{20}| - 1)^4}{216} - \ldots \right) \right] \right\}$$

The modified scaling length, L_{mod}, thus gives the maximum depletion-layer thickness for a uniformly doped semiconductor at equilibrium. For higher values of $|U_{20}|$, [8] yields the previous result; see ref. 2. But for moderate values, the terms other than the first on the right-hand side of [8] will contribute to L_{mod}.

The expression for the position, normalized with respect to this new scaling length, can be written as

$$[9]\quad \frac{x}{L_{mod}} = 2^{-1/2} \int_w^{W_J} \left[\frac{\exp(U_{20}) + \exp(-U_{20})}{\exp(U_{20}) \{\exp(-W') + W' - 1\} + \exp(-U_{20}) \{\exp W' - W' - 1\}} \right]^{1/2} \left(\frac{1}{\left. \frac{\Delta x}{L_D} \right|_{max}} \right) dW'$$

In the depletion region, where $2|U_{20}| > W > 1$, the expression for normalized distance becomes

$$[10]\quad \frac{x}{L_{mod}} = 2^{-1/2} \int_w^{2|U_{20}|} \left\{ \frac{\exp(U_{20}) + \exp(-U_{20})}{\exp(U_{20}) \{\exp(-W') + W' - 1\} + \exp(-U_{20}) \{\exp W' - W' - 1\}} \right\}^{1/2} \left(\frac{1}{\left. \frac{\Delta x}{L_D} \right|_{max}} \right) dW'$$

Integration of [10] yields

$$[11]\quad \frac{x}{L_{mod}} = \frac{2^{1/2}}{A} \left[(2|U_{20}| - 1)^{1/2} - (W - 1)^{1/2} \right] + \frac{2^{-1/2}}{A} \exp\left[-(2U + 1) \right] \left\{ \left[(2|U_{20}| - 1)^{-1/2} \left(2|U_{20}| - \frac{(2|U_{20}| - 1)^2}{6} + \frac{(2|U_{20}| - 1)^3}{30} - \frac{(2|U_{20}| - 1)^4}{168} + \ldots \right) - (W - 1)^{-1/2} \left(W - \frac{(W - 1)^2}{6} + \frac{(W - 1)^3}{30} - \frac{(W - 1)^4}{168} + \ldots \right) \right] \times \left[1 - 2^{3/2} \exp(-1) \right] + 2^{-1/2} \exp(-1) \left[(2|U_{20}| - 1)^{1/2} \left(1 - \frac{(2|U_{20}| - 1)}{3} + \frac{(2|U_{20}| - 1)^2}{10} - \frac{(2|U_{20}| - 1)^3}{42} + \frac{(2|U_{20}| - 1)^4}{216} - \ldots \right) - (W - 1)^{1/2} \left(1 - \frac{(W - 1)}{3} + \frac{(W - 1)^2}{10} - \frac{(W - 1)^3}{42} + \frac{(W - 1)^4}{216} - \ldots \right) \right] \right\}$$

where

$$A = \left(\left. \frac{\Delta x}{L_D} \right|_{max} \right)$$

3. Results and discussion

Equation [11] gives the relation of normalized distance as a function of potential derived through this new scaling length. The variation of normalized distance with normalized potential is studied through the present derivation. For various values of W_J and $|U_{20}|$, plots of $W/|U_{20}|$ versus x/L_{mod} are shown in Fig. 1. The curves indicate the doping dependence of the depletion sets, which is in agreement with previous results (2). For relatively lower values of $|U_{20}|$, the curves so obtained are in partial agreement with the works of Jindal and Warner (2). To account for the influence of $|U_{20}|$, the normalized potential ($W/|U_{20}|$) has been considered in the plot; see ref. 2.

The present expression of the new scaling length, as obtained by an alternative approach, can be used to model the depletion-layer thickness to replace the extrinsic Debye length in device modeling.

An example is considered to illustrate the use of the analysis. The case of a MOSFET (metal oxide semiconductor field effect transistor) is taken for this purpose as having bulk doping $N_D = 3.9 \times 10^{16}$ cm^{-3}. The corresponding value of the normalized bulk potential is $U_{20} = \ln(N_D/n_i) = 15$. If a voltage is applied to the sample such that the surface potential $U_S = -10$, then using the conversion relation, one gets

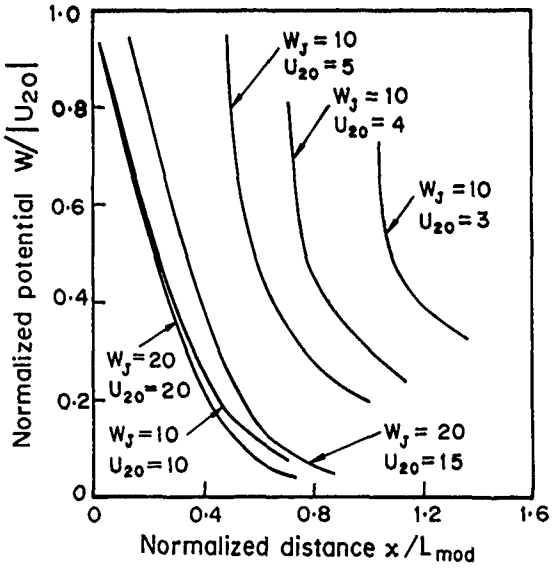

FIG. 1. Plots of the normalized potential $W/|U_{20}|$ versus the normalized distance x/L_{mod} for the depletion set for different values of W_J and $|U_{20}|$.

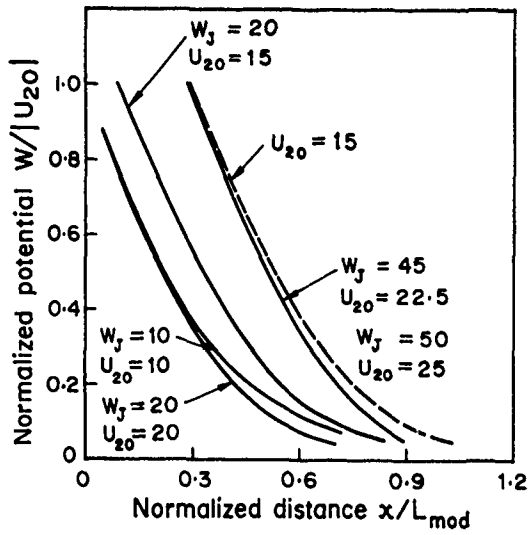

FIG. 3. Plots of $W/|U_{20}|$ versus x/L_{mod} for different values of $|U_{20}|$ and W_J based on the present analysis. The broken line depicts the work of Jindal and Warner (2) for $|U_{20}| = 15$.

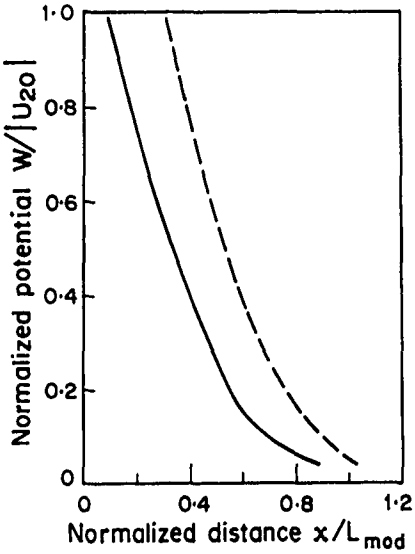

FIG. 2. Curves showing the variation of $W/|U_{20}|$ with x/L_{mod} for $|U_{20}| = 15$ where the solid curve and the broken-line curve are the results of the present analysis and the analysis given in ref. 2, respectively.

$$W_S = U_{20} - U_S = 15 - (-10) = 25$$

When $U_{20} = 15$, the threshold value of inversion would be $W_T = 2|U_{20}| = 30$. Since $W_S < W_T$, there is no inversion layer. Because the value of W lies far below the value of $2|U_{20}|$, Fig. 1 simply represents the depletion sets only. For lower values of $|U_{20}|$, the curves approach the accumulation region. Here graphs are drawn with different values for the parameters W_J and $|U_{20}|$ to show the trends and character of the normalized potential as a function of normalized position. In Fig. 2, the solid curve is the result of present analysis for $|U_{20}| = 15$; it is superimposed on the results of Jindal and Warner (2) for $|U_{20}| = 15$; which are shown by the broken line. The present result approaches the previous work (2) for lower values of normalized potential and diverges slowly with higher values. Numerical analysis from this alternate approximate solution is nearly in agreement with the previous results.

The graphs in Fig. 3 are drawn in the depletion region choosing different values of W_J and $|U_{20}|$ along with the results of Jindal and Warner (2) for $|U_{20}| = 15$, which are shown by the broken line. Graphs resulting from the present work seem to approach a common origin. Thus by making a suitable choice of the values of $|U_{20}|$ and W_J, graphs may be drawn that will be coincident. In Fig. 3, it occurs at $|U_{20}| = 22.5$, and $W_J = 45$ as well as $|U_{20}| = 25$ and $W_J = 50$. Thus, the present analysis is also effective in reducing redundancy from the potential solution through scaling length.

1. R. H. KINGSTON and S. F. NEUSTADTER. J. Appl. Phys. **26**, 718 (1955).
2. R. P. JINDAL and R. M. WARNER, JR. IEEE Trans. Electron Devices, **ED-29**, 1944 (1982).
3. R. M. WARNER, JR. and R. P. JINDAL. Solid-State. Electron. **26**, 335 (1983).
4. M. MISSOUS and E. H. RHODERICK. Solid-State. Electron. **28**, 233 (1985).
5. S. S. DE and A. K. GHOSH. Solid-State Electron. **32**, 517 (1989).

Generalized characters of the level-one Wess–Zumino–Witten model for simply laced groups on Riemann surfaces

JAE HOON CHOI AND JAE K .N KIM
Department of Physics, Korea Advanced Institute of Science and Technology, P.O. Box 150, Chongryang, Seoul, Korea

Received October 2, 1990

The generalized characters of the level-one A_l, D_l, and E_l Wess–Zumino–Witten models on the higher genus Riemann surfaces are obtained from their behaviors under the pinching limit of the zero-homology cycles. It is important in the construction of the higher genus characters that these models have fusion rules of the same type as the rational Gaussian model. The two-point correlators are also obtained by pinching the nonzero-homology cycle.

Les caractères généralisés des modèles Weiss–Zumino–Witten A_l, D_l et E_l de niveau un sur les surfaces de Riemann de genre élevé sont obtenus à partir de leurs comportements à la limite de constriction des cycles d'homologie zéro. Le fait que ces modèles ont des règles de fusion du même type que le modèle gaussien rationnel joue un rôle important dans la construction des caractères de genre élevé. Les corrélateurs à deux points sont aussi obtenus par constriction du cycle d'homologie non nulle.

[Traduit par la rédaction]

Can. J. Phys. **69**, 146 (1991)

1. Introduction

The two-dimensional conformal field theories (CFT's) (1) have been very attractive in the study of two-dimensional critical statistical models and the string theory. The two-dimensional statistical model with a particular boundary condition is equivalent to the same model on the corresponding Riemann surface. The string theory also treats Riemann surfaces. Therefore one needs the higher genus characters and correlators to give a complete description of CFT's.

We constructed the higher genus characters of the critical Ising model, and the level-one and -two SU(2) Wess–Zumino–Witten (WZW) models by using the sewing bootstrap program (2) and the Goddard–Kent–Olive coset construction (3). The characters of the level-one SU(3) WZW model on the Riemann surface were studied by Kaul *et al.* (4).

The WZW models can be used as the internal spaces for the string compactification, and are related to the (2 + 1)-dimensional Cherin–Simons–Witten theory (5), which exhibits a one-to-one correspondence between the generalized characters and the vectors in the Hilbert space on the Riemann surface. The partition functions of the level-one WZW models on the simply laced groups, A_l, D_l, and E_l, were calculated and the Bose–Fermi equivalence was shown on compact Riemann surfaces. Recently their correlation functions were also calculated by a constructive method (6). But the explicit construction of the higher genus characters and the conformal blocks of correlators is not clear. In this paper, we obtain the generalized characters of these models on the higher genus Riemann surfaces. They have the fusion rules of a special type such that the operator product expansion (OPE) of a primary field and its conjugate contains only the identity field and no other primaries. Then all the intermediate propagators between blobs are fixed to be the identity fields. It means that the pinching limit of a zero-homology cycle leads to the factorization to the lower genus characters at the leading order in the pinching parameter t, which is nothing but the intermediate propagator. The bootstrap program with these special fusion rules simply sews the genus-one characters to obtain the higher genus ones. In this procedure the modular transformation property plays an important role.

2. Special fusion rules and sewing program

We consider here only the simply laced affine algebras (7, 8). Since the Cartan matrices are symmetric, so the dual lattice M is equal to the root lattice

$$\bar{Q} = \sum_{i=1}^{l} Z\,\bar{\alpha}_i$$

The highest weights of level one that correspond to the primary fields are given by the fundamental weights and some automorphisms σ of the Dynkin diagram; $\{\Lambda_i | i = \sigma(0)\}$. The fundamental weights,

$$\{\Lambda_i = (\bar{\Lambda}_i, a_i, 0) | i = 0, 1, \ldots, l\}$$

satisfy the following orthonormality condition with respect to the simple roots,

$$[1] \quad \delta_{ij} = (\Lambda_i, \alpha_j) = (\bar{\Lambda}_i, \bar{\alpha}_j) + a_i\delta_{j0}$$

where the constants a_i are defined via

$$\frac{\theta}{\theta^2} = \sum_{i=1}^{l} \frac{a_i\alpha_i}{\alpha_i^2}$$

for the highest root θ. $\bar{\Lambda}$ is the restriction of Λ to the weight space of the finite algebra. In these cases, the central charge c is equal to the rank l, and the characters are expressed in terms of the Dedekind η function and the Kac -Moody theta functions of level one defined on the root space.

$$[2] \quad \chi_\lambda(\tau) = \mathrm{tr}_{[\phi_\lambda]}\left(\exp\left[i2\pi\tau\left(L_0 - \frac{c}{24}\right)\right]\right)$$

$$= \frac{1}{\eta(\tau)^l}\Theta_{\lambda,1}(0, \tau)$$

where

$$[3] \quad \Theta_{\lambda,k}(z, \tau) = \sum_{\gamma \in M + \frac{\bar{\lambda}}{k}} \exp\left[i\pi k\tau|\gamma|^2 - i2\pi(\gamma, z)\right]$$

with the notation $|\gamma|^2 = (\gamma, \gamma)$.

The modular transformation $S: \tau \to -1/\tau$ gives us the information about the fusion rules of the corresponding WZW models.

$$[4] \quad S: \chi_\lambda \to \sum_\mu S_\lambda{}^\mu \chi_\mu$$

where

$$[5] \quad S_\lambda{}^\mu = e^{-i2\pi(\lambda, \mu)}$$

The fusion rules are determined by Verlinde's formula: (9)

$$[6] \quad N_{\lambda\mu}{}^\nu = \sum_\gamma \frac{S_\lambda{}^\gamma S_\mu{}^\gamma S_\gamma^{\dagger\nu}}{S_0{}^\gamma} = \sum_\gamma \exp\left[-i2\pi(\lambda + \mu - \nu, \gamma)\right]$$

For the level-one simply laced affine Lie algebras, the above fusion rules are of a special type such that there is only one unique representation $[\phi_\nu]$ for the OPE of two given primary fields ϕ_λ and ϕ_μ. This type is reexpressed, i.e., the OPE of a primary field and its conjugate produces only the (descendants of) identity field and nothing else. Such a fusion rule is of the same type as that of the well-known $c = 1$ rational Gaussian model (10) and is also the special case where all the primary fields are simple currents (11).

Consider the higher genus characters of these systems in the "multiperipheral" basis (12). Look at a vertex in the first blob that contains one in-coming and one out-going primary field ϕ_{λ_1}. The out-going field ϕ_{λ_1} is equal to the in-coming conjugate field $\phi_{\lambda_1^\vee}$. The Gaussian-type fusion rule determines the third internal line to be the identity. Repeat this argument at each vertex, then all the intermediate propagators between blobs are fixed as the identity fields, by the fusion rules. Then the number of characters on the genus-g Riemann surface is N^g, where N is the number of primary fields.

The higher genus characters are easily obtained by the bootstrap program, which simply sews the genus-one characters together. When the fusion rule is not of the Gaussian type, we need more information apart from the genus-one characters, e.g., one- and two-point correlators, to apply the sewing program (2). The modular invariance of the partition function is a powerful guidance in this step. This procedure is verified by the factorization that the pinching limit of a zero-homology cycle (13) produces here two one-point correlators of the identity field (14), which are just the lower genus characters. The two-point correlators are constructed by pinching the nonzero-homology cycle (14), and it is straightforward to obtain the n-point correlators by repeating the pinching procedure of appropriate homology cycles.

3. Level-one A_l WZW models

The level-one A_l WZW models have $l + 1$ primary fields. The highest weights corresponding to the primary fields are Λ_0, ..., Λ_l;

$$[7] \quad \Lambda_i = (\bar{\Lambda}_i, 1, 0), \qquad i = 1, \ldots, l$$

where

$$\bar{\Lambda}_i = \sum_{k=1}^{l} \left(\min(k, i) - \frac{ki}{l+1}\right) \bar{\alpha}_k$$

The conformal dimension h_i of the primary field ϕ_i is given by

$$[8] \quad h_i = \frac{|\Lambda_i|^2}{2} = \frac{i(l+1-i)}{2(l+1)}$$

The genus-one character of the primary field ϕ_i is (7)

$$[9] \quad \chi_i(\tau) \equiv \chi_{\Lambda_i}(\tau) = \frac{1}{\eta(\tau)^l} \Theta_{\Lambda_i:1}(0, \tau)$$

The fusion rule is readily calculated by the modular transformation S.

$$[10] \quad S_j^k = \frac{1}{\sqrt{l+1}} \exp\frac{i2\pi jk}{(l+1)}$$

$$[11] \quad N_{jk}{}^m = \frac{1}{l+1} \sum_{n=0}^{l} \exp\frac{i2\pi(j+k-m)n}{(l+1)} = \delta_{j+k,\, m \,(\mathrm{mod}\, l+1)}$$

like the momentum conservation. It is certainly of Guassian type, and the primary fields ϕ_i and ϕ_{l+1-i} are conjugate to each other, so $\chi_i(\tau)$ and $\chi_{l+1-i}(\tau)$ are identical because

$$\Theta_{\Lambda_i 1}(0, \tau) = \Theta_{\Lambda_{l+1-i}:1}(0, \tau)$$

Therefore, the independent characters are χ_0, χ_1, ..., $\chi_{[(l+1)/2]}$.

We rewrite the Kac–Moody theta function in terms of the classical theta functions defined on the group manifold of SU(2).

$$[12] \quad \Theta_{\Lambda i:1}(0, \tau) = \sum_{\{a_k \in Z/kZ\}} \prod_{k=1}^{l} \theta_{(k+1)a_k(i) - ka_{k+1}(i),\, \frac{k(k+1)}{2}}(0, \tau)$$

where

$$[13] \quad \theta_{a:k}(z, \tau) = \sum_{n \in Z} \exp\left[i2\pi k\tau\left(n + \frac{a}{2k}\right)^2 - i2\pi kz\left(n + \frac{a}{2k}\right)\right]$$

$$[14] \quad a_k(i) = a_k + \min(k, i)$$

and $a_1 = a_{l+1} = 0$.

The higher genus characters are obtained by the sewing bootstrap program generalizing the Kac–Moody theta function and the Dedekind η function on the Riemann surface.

$$[15]\quad \chi_{\lambda}(\Omega) = \frac{1}{Z_1^{l/2}}\,\Theta_{\lambda:1}(0, \Omega)$$

where $Z_1^{-1/2}$ is the partition function of a chiral scalar field on the Riemann surface of genus g and the higher genus Kac–Moody theta function is defined by

$$[16]\quad \Theta_{\lambda:1}(z, \Omega) = \sum_{\{\gamma i \in M + \bar{\lambda}i\}} \exp\left[i\pi(\gamma, \Omega\cdot\gamma) - i2\pi(\gamma, z)\right]$$

where $\boldsymbol{\lambda} = (\lambda_1,\ldots, \lambda_g)$, $\boldsymbol{\gamma} = (\gamma_1,\ldots, \gamma_g)$, and $z = (z_1,\ldots, z_g)$ with the extended bilinear form

$$(\boldsymbol{\gamma}, z) = (\gamma_1, z_1) + \ldots + (\gamma_g, z_g)$$

Here λ_i represents the primary field ϕ_i circulating around the ith blob. We rewrite the Kac–Moody theta function in terms of the higher genus classical SU(2) theta functions, and we have

$$[17]\quad \chi_{\lambda}(\Omega) = \frac{1}{Z_1^{l/2}} \sum_{\{a_k \in Z^g/kZ^g\}} \prod_{k=1}^{l} \theta_{(k+1)a_k(\lambda) - ka_{k+1}(\lambda):\frac{k(k+1)}{2}}(0, \Omega)$$

where

$$[18]\quad \theta_{a:k}(z, \Omega) = \sum_{n \in Z_g} \exp\left[i2\pi k\tau\left(n + \frac{a}{2k}\right)\cdot\Omega\cdot\left(n + \frac{a}{2k}\right) - i2\pi kz\cdot\left(n + \frac{a}{2k}\right)\right]$$

and $\boldsymbol{a}_k(\boldsymbol{\lambda})$ is defined as, for $\boldsymbol{\lambda} = (\Lambda_{i_1},\ldots, \Lambda_{i_g})$,

$$[19]\quad \boldsymbol{a}_k(\boldsymbol{\lambda}) = (a_k^1 + \min(k, i_1),\ldots, a_k^g + \min(k, i_g))$$

with $a_1^i = a_{l+1}^i = 0$. The $l = 2$ case was studied by Kaul *et al.* (4).

The pinching limit of a zero-homology cycle exhibits the factorization to the lower genus characters:

$$[20]\quad \chi_{\lambda 1\,\lambda 2}(\Omega) \to \frac{1}{(Z_1^{l/2})_1}\Theta_{\lambda 1:1}(0, \Omega_1)\cdot\frac{1}{(Z_1^{l/2})_2}\Theta_{\lambda 2:1}(0, \Omega_2) + \sum_{n=1}^{\infty} t^n <\phi_{0,n}>_{\lambda 1} <\phi_{0,n}>_{\lambda 2}$$

$$= \chi_{\lambda 1}(\Omega_1)\,\chi_{\lambda 2}(\Omega_2) + O(t)$$

where $<\phi_{0,n}>_{\lambda}$ are the one-point correlators of the descendants of the identity field, which are dictated by the integral powers of the pinching parameter t. On the other hand, pinching a nonzero-homology cycle brings us the two-point correlator:

$$[21]\quad \chi_{\lambda\Lambda_i}(\Omega') \to \frac{1}{Z_1^{l/2}} \sum_{\gamma \in M + \bar{\Lambda}i} \left(\frac{t}{E(z, w)^2}\right)^{|\gamma|^2/2} \Theta_{\lambda:1}((z - w)\gamma, \Omega) = t^{h_i} <\phi_i(z)\,\phi_{l+1-i}(w)>_{\lambda}$$

$$+ \sum_{n=1}^{\infty} t^{h_i + n} <\phi_{i,n}\phi_{l+1-i,n}>_{\lambda}$$

where

$$h_i = \frac{i(l + 1 - i)}{2(l + 1)}$$

and $<\phi_{i,n}\phi_{l+1-i,n}>_{\lambda}$ are the two-point correlators of the descendants of ϕ_i and its conjugate ϕ_{l+1-i}. $E(z, w)$ is the prime form defined as

$$E(z, w) = \frac{\theta[\boldsymbol{\alpha}](z - w|\Omega)}{\sqrt{\sum_i v_i(z)\,\partial_i\theta\,[\boldsymbol{\alpha}](0|\Omega)}\,\sqrt{\sum_i v_i(w)\,\partial_i\theta\,[\boldsymbol{\alpha}](0|\Omega)}}$$

where the characteristic $\boldsymbol{\alpha}$ is odd and $v_i(z)$ are g holomorphic differentials. Therefore, the two-point correlator of the primary fields ϕ_i and ϕ_{l+1-i} is

$$[22]\quad <\phi_i(z)\phi_{l+1-i}(w)>_\lambda = \frac{1}{Z_1^{l/2}}\frac{l}{E(z,w)^{2h_i}} \sum_{\gamma \in M+\bar{\Lambda}_i,\ |\gamma|^2 = 2h_i} \Theta_{\lambda:1}((z-w)\gamma, \Omega)$$

The partition function is the sum over the characters:

$$[23]\quad Z_{k=1A_l} = \sum_\lambda |\chi_\lambda(\Omega)|^2$$

$$= \frac{1}{|Z_1|^l} \sum_\lambda |\Theta_{\lambda:1}(0,\Omega)|^2$$

The normalized two-point correlators are obtained by summing the conformal blocks over the internal fields passing around blobs and dividing by the partition function:

$$[24]\quad <\phi_i(z,\bar{z})\,\phi_{l+1-i}(w,\bar{w})> = \frac{1}{|E(z,w)|^{4h_i}} \frac{\sum_\lambda |\sum_{\gamma \in M+\bar{\Lambda}_i,\ |\gamma|^2 = 2h_i} \Theta_{\lambda:1}((z-w)\gamma,\Omega)|^2}{\sum_\lambda |\Theta_{\lambda:1}(0,\Omega)|^2}$$

4. Level-one D_l WZW models

The level-one D_l WZW models have four primary fields ϕ_0, ϕ_1, ϕ_{l-1}, and ϕ_l with conformal dimensions 0, 1/2, $l/8$, and $l/8$, respectively, which correspond to the adjoint, vector, and two spin representations. The number of primary fields is independent of the rank l unlike the case of A_l. From the Dynkin diagram one can pick up the highest weights of level one corresponding to the primary fields as Λ_0, Λ_1, Λ_{l-1}, and Λ_l. As explained in the preceding section, the fundamental weights are expressed in terms of the simple roots:

$$[25]\quad \bar{\Lambda}_1 = \sum_{k=1}^{l-2} \bar{\alpha}_k + \frac{1}{2}\bar{\alpha}_{l-1} + \frac{1}{2}\bar{\alpha}_l$$

$$[26]\quad \bar{\Lambda}_{l-1} = \sum_{k=1}^{l-2} \frac{k}{2}\bar{\alpha}_k + \frac{l}{4}\bar{\alpha}_{l-1} + \frac{l-2}{4}\bar{\alpha}_l$$

$$[27]\quad \bar{\Lambda}_l = \sum_{k=1}^{l-2} \frac{k}{2}\bar{\alpha}_k + \frac{l-2}{4}\bar{\alpha}_{l-1} + \frac{l}{4}\bar{\alpha}_l$$

Then the modular transformation matrix S_i^j of the genus-one characters

$$[28]\quad \chi_\lambda(\tau) = \frac{1}{\eta(\tau)^l}\Theta_{\lambda:1}(0,\Omega)$$

is readily calculated as

$$[29]\quad S = \frac{1}{2}\begin{bmatrix} 1 & 1 & 1 & 1 \\ 1 & 1 & -1 & -1 \\ 1 & -1 & e^{-i\pi l/2} & -e^{-i\pi l/2} \\ 1 & -1 & -e^{-i\pi l/2} & e^{-i\pi l/2} \end{bmatrix}$$

We define the matrices N_i such that $(N_i)_j^k = N_{ij}^k$, then they are given by

$$[30]\quad N_1 = \begin{bmatrix} 0 & 1 & 0 & 0 \\ 1 & 0 & 0 & 0 \\ 0 & 0 & 0 & 1 \\ 0 & 0 & 1 & 0 \end{bmatrix}$$

$$[31]\quad N_{l-1} = \begin{bmatrix} 0 & 0 & 1 & 0 \\ 0 & 0 & 0 & 1 \\ (1+(-1)^l)/2 & (1-(-1)^l/2 & 0 & 1 \\ (1-(-1)^l)/2 & (1+(-1)^l)/2 & 0 & 0 \end{bmatrix}$$

$$[32]\quad N_l = \begin{bmatrix} 0 & 0 & 0 & 1 \\ 0 & 0 & 1 & 0 \\ (1-(-1)^l)/2 & (1+(-1)^l/2 & 0 & 1 \\ (1+(-1)^l)/2 & (1-(-1)^l)/2 & 0 & 0 \end{bmatrix}$$

and $N_0 = I$. The fusion rules of these models have the dependence of the rank l modulo 2. For l even, every ϕ_i is self-conjugate, while for l odd, ϕ_1 is self-conjugate but ϕ_{l-1} and ϕ_l are conjugate to each other. Both of the two classes of the fusion rules are of Gaussian type, so one can apply the sewing bootstrap program simply.

The Kac–Moody theta functions can be rewritten in terms of the classical SU(2) theta functions as

$$[33]\quad \Theta_{\lambda:1}(0,\tau) = \sum_{\{a_k \in Z/2Z\}} \prod_{k=1}^{l-2} \theta_{2a_k + 2a_{k-1} + a + a':2}(0,\tau)\, \theta_{a_{l-2} + a + b:1}(0,\tau)\, \theta_{a_{l-2} + a' + b:1}(0,\tau)$$

where $a_0 = 0$, $a = \delta_{\lambda, \Lambda_{l-1}}$, $a' = \delta_{\lambda, \Lambda_l}$, and $b = \delta_{\lambda, \Lambda_1}$. The bootstrap program with this special fusion rule leads us to the higher genus characters

$$[34]\quad \chi_\lambda(\Omega) = \frac{1}{Z_1^{l/2}} \Theta_{\lambda:1}(0,\Omega)$$

$$= \frac{1}{Z_1^{l/2}} \sum_{\{a_k \in Z^8/kZ^8\}} \prod_{k=1}^{l-2} \theta_{2a_k + 2a_{k-1} + a + a':2}(0,\Omega)\, \theta_{a_{l-2} + a + b:1}(0,\Omega)\, \theta_{a_{l-2} + a' + b:1}(0,\Omega)$$

where $a_i = \delta_{\lambda_i, \Lambda_{l-1}}$, $a_i' = \delta_{\lambda_i, \Lambda_l}$, and $b_i = \delta_{\lambda_i, \Lambda_1}$. The two-point correlators are also given by

$$[35]\quad <\phi_1(z)\,\phi_1(w)>_\lambda = \frac{1}{Z_1^{l/2}} \frac{1}{E(z,w)} \sum_{\gamma \in M + \bar{\Lambda}_1,\ |\gamma|^2 = 1} \Theta_{\lambda:1}((z-w)\gamma, \Omega)$$

for l even,

$$[36]\quad <\phi_{l-1}(z)\,\phi_{l-1}(w)>_\lambda = \frac{1}{Z_1^{l/2}} \frac{1}{E(z,w)^{l/4}} \sum_{\gamma \in M + \bar{\Lambda}_{l-1},\ |\gamma|^2 = l/4} \Theta_{\lambda:1}((z-w)\gamma, \Omega)$$

$$[37]\quad <\phi_l(z)\,\phi_l(w)>_\lambda = \frac{1}{Z_1^{l/2}} \frac{1}{E(z,w)^{l/4}} \sum_{\gamma \in M + \bar{\Lambda}_l,\ |\gamma|^2 = l/4} \Theta_{\lambda:1}((z-w)\gamma, \Omega)$$

for l odd,

$$[38]\quad <\phi_{l-1}(z)\,\phi_l(w)>_\lambda = \frac{1}{Z_1^{l/2}} \frac{1}{E(z,w)^{l/4}} \sum_{\gamma \in M + \bar{\Lambda}_{l-1},\ |\gamma|^2 = l/4} \Theta_{\lambda:1}((z-w)\gamma, \Omega)$$

Since there are two classes in the level-one D_l WZW models depending on the rank l modulo 2, the numbers of their two-point correlators are different.

5. Level-one E_l WZW models

5.1. Level-one E_8 WZW model

This model is trivial because it has just one primary field, i.e., the identity. The character is itself the chiral partition function given by

$$[39]\quad \chi(\tau) = \frac{1}{\eta(\tau)^8} \Theta_{\Lambda_0:1}(0,\tau)$$

$$= \frac{1}{2\eta(\tau)^8} \sum_{\text{even}} \theta^8[\alpha](0|\tau)$$

It is modular invariant and the above Kac–Moody theta function is a cusp form of weight 4. Extending to higher genus, the modular invariant character is

[40] $$\chi(\Omega) = \frac{1}{2^8 Z_1^4} \sum_{\text{even}} \vartheta^8 [\alpha] (0|\Omega)$$

where the sum is over all the even-spin structures.

5.2. Level-one E_7 WZW model

There are two primary fields, 1 and ϕ of conformal dimensions 0 and 3/4, respectively. The fusion rule is $\phi \times \phi = 1$, which is similar to that of the level-one SU(2) WZW model. The highest weights of level one are found to be the fundamental weights, Λ_0 and Λ_7.

The genus-one characters are expressed as

[41] $$\chi_\lambda(\tau) = \frac{1}{\eta(\tau)^7} \Theta_{\lambda:1} (0, \tau)$$

with

$$= \frac{1}{Z_1^{1/2}} \sum_{\{a_k \in Z^8/kZ^8\}} \prod_{k=1}^{l-2} \theta_{2a_k + 2a_{k-1} + a + a':2} (0, \Omega) \theta_{a_{l-2} + a + b:1} (0, \Omega) \theta_{a_{l-2} + a' + b:1} (0, \Omega)$$

[42] $$\Theta_{\lambda:1} (0, \tau) = \sum_{d1 \in Z/4Z} \sum_{\{di \in Z/2Z\},\ i = 2,\ldots,5} \theta_{d_2:2} (0, \tau) \theta_{d_1 + d_2:1} (0, \tau) \theta_{2d_2 + 2d_3 - d_1:2} (0, \tau) \theta_{2d_3 + 2d_4 - d_1:2} (0, \tau)$$

$$\times \theta_{2d_4 + 2d_5 - d_1 + 2a:2} (0, \tau) \theta_{2d_5 - d_1:2} (0, \tau) \theta_{2d_1 + 2a:4} (0, \tau)$$

$$= \theta_{a:1}^3 (0, \tau) [\theta_{a:1}^4 (0, \tau) + 7\theta_{a+1:2}^4 (0, \tau)]$$

where $a = \delta_{\lambda, \Lambda_7}$, and we used in the second equality some theta identities (15).

Sewing the genus-one characters by the bootstrap program, we gain the following higher genus characters:

[43] $$\chi_\lambda(\Omega) = \frac{1}{Z_1^{1/2}} \Theta_{\lambda:1} (0, \Omega)$$

$$= \frac{1}{Z_1^{1/2}} \theta_{a:1}^3 (0, \Omega) \sum_{b \in Z^8/2Z^8} 7^{\sum_i b_i} \theta_{a+b:1}^4 (0, \Omega)$$

where $a_i = \delta_{\lambda_i, \Lambda_7}$. The nonzero-homology pinching limit of the characters contains the two-point correlators:

[44] $$< \phi(z) \phi(w) >_\lambda = \frac{56}{E(z, w)^{3/2}} \frac{1}{Z_1^{1/2}} \theta_{a:1}^3 (z - w, \Omega) \sum_{b \in Z^8/2Z^8} 7^{\sum_i b_i} \theta_{a+b:1}^4 (0, \Omega)$$

where the factor 56 means the number of group charges of the primary field ϕ.

5.3. Level-one E_6 WZW model

It consists of three primary fields 1, ϕ_1, and ϕ_6 of conformal dimensions 0, 2/3, and 2/3, respectively, which correspond to the fundamental weights Λ_0, Λ_1, and Λ_6, respectively.

[45] $$\bar{\Lambda}_1 = \frac{4}{3}\bar{\alpha}_1 + \bar{\alpha}_2 + \frac{5}{3}\bar{\alpha}_3 + 2\bar{\alpha}_4 + \frac{4}{3}\bar{\alpha}_5 + \frac{2}{3}\bar{\alpha}_6$$

[46] $$\bar{\Lambda}_6 = \frac{2}{3}\bar{\alpha}_1 + \bar{\alpha}_2 + \frac{4}{3}\bar{\alpha}_3 + 2\bar{\alpha}_4 + \frac{5}{3}\bar{\alpha}_5 + \frac{4}{3}\bar{\alpha}_6$$

The fusion rule is

[47] $$\phi_1 \times \phi_6 = 1, \qquad \phi_1 \times \phi_1 = \phi_6, \qquad \phi_6 \times \phi_6 = \phi_1$$

which is similar to the level-one SU(3) WZW model and is of Gaussian type. The genus-one characters are rewritten in terms of the classical SU(2) theta functions using the theta function identities:

$$[48]\quad \chi_\lambda(\tau) = \frac{1}{\eta(\tau)^6}\,\Theta_{\lambda:1}(0,\tau)$$

$$= \frac{1}{\eta(\tau)^6} \sum_{d_1 \in Z/4Z} \sum_{\{d_i \in Z/2Z\},\ i=2,3,4} \theta_{d_2:1}(0,\tau)\,\theta_{d_1+d_2:1}(0,\tau)$$

$$\times\, \theta_{2d_2+2d_3-d_1:2}(0,\tau)\,\theta_{2d_3+2d_4-d_1:2}(0,\tau)\,\theta_{2d_4-d_1+2a':2}(0,\tau)\,\theta_{3d_1+2a'+4b':6}(0,\tau)$$

$$= \frac{1}{2\eta(\tau)^6} \sum_{a,\,b \in \frac{1}{2}Z/Z,\ 4ab = 0 \bmod 2} \theta[{}^{c+a}_{3b}](0|3\tau)\,\theta^5[{}^{a}_{b}](0|\tau),$$

where $a' = \delta_{\lambda,\Lambda_6}$, $b' = \delta_{\lambda,\Lambda_1}$, and $c = \frac{a'}{3} + \frac{2}{3}b'$. Therefore, $\chi_{\Lambda_1}(\tau) = \chi_{\Lambda_5}(\tau)$ and we check again that ϕ_1 is conjugate to ϕ_6.

We obtain the higher genus characters

$$[49]\quad \chi_\lambda(\Omega) = \frac{1}{Z_1^3}\,\Theta_{\lambda:1}(0,\Omega)$$

$$= \frac{1}{2^8 Z_1^3} \sum_{a,\,b \in \frac{1}{2}Z^8/Z^8,\ 4a\cdot b = 0 \bmod 2} \theta[{}^{c+a}_{3b}](0|3\Omega)\,\theta^5[{}^{a}_{b}](0|\Omega),$$

where

$$c_i = \frac{2}{3}\delta_{\lambda_i,\Lambda_1} + \frac{1}{3}\delta_{\lambda_i,\Lambda_6}$$

One can pick up the two-point correlatois from the pinching limits of the nonzero-homology cycles:

$$[50]\quad \langle \phi_1(z)\,\phi_6(w)\rangle_\lambda = \frac{1}{E(z,w)^{4/3}}\frac{1}{2^8 Z_1^3}\left[\sum_{\text{even}} \theta[{}^{c+a}_{3a}](2(z-w)|3\Omega)\,\theta^5[{}^{a}_{b}]0|\Omega) + 2^4 \sum_{a,b} e^{i4\pi a\cdot b}\,\theta[{}^{a+a}_{3b}]\left(\frac{(z-w)}{2}|3\Omega\right)\theta^5[{}^{a}_{b}]\left(\frac{(z-w)}{2}|\Omega\right)\right]$$

$$= \frac{1}{E(z,w)^{4/3}}\frac{1}{Z_1^3} \sum_{\gamma \in M+\bar{\Lambda}_1,\ |\gamma|^2 = \frac{4}{3}} \Theta_{\lambda:1}((z-w)\gamma,\Omega)$$

6. Discussion and conclusion

The level-one WZW models for the simply laced groups have fusion rules of the Gaussian type, which fix all the intermediate propagators between blobs of the Riemann surface to be the identity fields. Then the zero-homology pinching limit merely shows the factorization of the characters into lower genus ones at the leading order in the pinching parameter. So the sewing bootstrap program leads us to the higher genus characters in simple ways and the two-point correlators are obtained by pinching the nonzero-homology cycle.

Summarizing the results, the higher genus characters of the level-one WZW models for the simply laced groups, A_l, D_l, and E_l, are

$$[51]\quad \chi_\lambda(\Omega) = \frac{1}{Z_1^{l/2}}\,\Theta_{\lambda:1}(0,\Omega)$$

and the conformal blocks of the two-point correlators are

$$[52]\quad \langle \phi_\Lambda(z)\,\phi_{\Lambda^\vee}(w)\rangle_\lambda = \frac{1}{E(z,w)^{2h_\Lambda}} \sum_{\gamma \in M+\bar{\Lambda},\ |\gamma|^2 = 2h_\Lambda} \Theta_{\lambda:1}((z-w)\gamma,\Omega)_\Lambda$$

where λ_i represents the primary field circulating around the ith blob, $\Lambda^\vee$ is the conjugate of Λ, and h_Λ the conformal dimension of ϕ_Λ. The one-point correlators of the nontrivial primary fields vanish on any Riemann surface owing to the fusion rules.

The Gaussian-type fusion rules permit us to extend the theories easily onto the higher genus Riemann surfaces, because they could be considered as free theories actually and also realized by the vertex operator formalism. The models considered

in this paper are solved by the genus-one characters alone. Further investigation of such theories may bring a new clue to the study of the rational CFT's on the general Riemann surfaces.

Acknowledgment

This work was supported in part by Korea Science and Engineering Foundation.

1. A. A. BELAVIN, A. M. POLYAKOV and A. B. ZAMOLODCHIKOV. Nucl. Phys. **B241**, 333 (1984).
2. J. H. CHOI and J. K. KIM. Phys. Rev. D, Part. Fields, **41**, 484, (1990); **41**, 1908 (1990).
3. P. GODDARD, A. KENT, and D. OLIVE. Commun. Math. Phys. **103**, 105 (1986).
4. R. K. KAUL, R. P. MALIK, and N. BEHERA. Phys. Rev. D, Part. Fields, **41**, 478 (1990).
5. E. WITTEN. Commun. Math. Phys. **121**, 351 (1989); Nucl. Phys. **B322**, 629 (1989).
6. A. REDLICH, H. J. SCHNITZER, and K. TSOKOS. Nucl. Phys. **B288**, 397 (1987); H. J. SCHNITZER and K. TSOKOS. Nucl. Phys. **B291**, 429 (1987); S. G. NACULICH and H. J. SCHNITZER. Nucl. Phys. **B332**, 583 (1990).
7. V. G. KAC. Infinite dimensional lie algebras. Birkhauser Boston Inc. Cambridge, MA. 1983; V. G. KAC and D. H. PETERSON. Adv. Math. **53**, 125 (1984).
8. D. GEPNER and E. WITTEN. Nucl. Phys. **B278**, 493 (1986).
9. E. VERLINDE. Nucl. Phys. **B300**, 360 (1988).
10. R. DIJKRAAF, E. VERLINDE, and H. VERLINDE. Commun. Math. Phys. **115**, 649 (1988).
11. A. N. SCHELLEKENS and S. YANKIELOWICZ. Int. J. Mod. Phys. A, **5**, 2903 (1990).
12. G. MOORE and N. SEIBERG. Commun. Math. Phys. **123**, 177 (1989). Appendix B.
13. J. D. FAY. Lect. Notes Math. **352**, (1973).
14. D. FRIEDAN and S. SHENKER. Nucl. Phys. **B281**, 509 (1987).
15. D. MUMFORD. Tata lectures on theta. Birkhauser Boston Inc. Cambridge, MA. 1983.

Microscopic description in the Gaussian approximation of the nematic-isotropic phase transition

P. A. PASHKOV AND S. I. VASILIEV
Faculty of Physics, Leningrad State University, Leningrad, 198904, U.S.S.R.

Received October 26, 1990

The nematic-isotropic phase transition of a system of nonpolar rodlike molecules is considered. The mean-field theory is extended to take into account the local field fluctuations in the Gaussian approximation. The calculations are performed in the five-dimensional space of the order-parameter components. The numerical results are obtained for the lattice system of molecules and compared with the calculations in the mean-field theory, cluster approximation, and Monte-Carlo simulation data.

On considère la transition de phase nématique-isotrope d'un système de molécules non polaires de type bâtonnets. La théorie du champ moyen est généralisée pour tenir compte des fluctuations du champ local dans l'approximation gaussienne. Les calculs sont effectués dans l'espace à cinq dimensions des composantes du paramètre d'ordre. Des résultats numériques sont obtenus pour le système de molécules en réseau et comparés avec les calculs effectués dans le cadre de la théorie du champ moyen, avec l'approximation d'amas et par simulation Monte Carlo.

[Traduit par la rédaction]

Can. J. Phys. 69, 154 (1991)

1. Introduction

Fluctuations play an essential role in the critical behavior of nematic liquid crystals (1). Most theoretical considerations of the nematic-isotropic phase transition including fluctuations are based upon the phenomenological Landau–de Gennes theory (see ref. 2 for a review). The microscopic approaches, on the other hand, are not sufficiently developed and either do not take into account the fluctuations as in the hard-rod model (3) or the Maier–Saupe theory (4), or consider fluctuations in an indirect way as in the Krieger–James approximation (5) and other theories (6, 7). Cluster approximations (8, 9) include short-range orientational correlations of a few nearest molecules. The purpose of this work is to extend the mean-field theory to take into account the fluctuations of the local field, which acts on a given molecule and is due to all the others.

The interaction between the molecules in liquid crystals has a tensor character. Therefore the usual field-theory methods are difficult to apply. We formulate a $5N$-dimensional model of a nematic liquid crystal with a vector interaction equivalent to the classical tensor model. Calculations are performed in the Gaussian approximation for the local field fluctuations. Within the framework of this method, shortcomings of the mean-field description such as unrealistic values of the critical temperature T_c and the temperature T^* of a disappearance of the disordered phase cannot be removed. However, this approximation allows us to investigate in a simple way the influence of the local-field fluctuations on the thermodynamic quantities of the system. It is known that the quadratic approximation is not applicable in the neighborhood of the critical point of a second-order phase transition (see ref. 10 for example). The nematic-isotropic transition is a weak first-order one. As it will be shown, simple analytical expressions for the thermodynamic functions can be obtained in the Gaussian approximation for the lattice system of rodlike molecules for all temperatures. These expressions establish the connection between thermodynamic quantities of the system and its translational symmetry plus the radial dependence of the pair interaction potential. The results of our calculations are compared with those of the mean-field treatment (4), the cluster model (8, 9), and Monte-Carlo simulations (11, 12).

2. Vector model for nematic

We are concerned with the system of N molecules, which are assumed to be nonpolar and to have cylindrical symmetry. The symmetric traceless matrix Q_i corresponding to each molecule is:

$$[1] \quad Q_i^{\alpha\beta} = n_i^\alpha n_i^\beta - \frac{1}{3}\delta^{\alpha\beta}$$

where n_i^α are the Cartesian components of a unit vector $\boldsymbol{n}_i$ along the symmetry axis of the molecule i.

Assume that interaction between the molecules i and j has the form:

$$[2] \quad V_{ij} = -C_{ij} P_2(\cos\theta_{ij}) = -\frac{3}{2} C_{ij} \operatorname{tr} Q_i Q_j$$

where C_{ij} defines a dependence of the interaction energy on the intermolecular distance r_{ij}, θ_{ij} is the angle between the unit vectors $\boldsymbol{n}_i$ and $\boldsymbol{n}_j$. Then in the absence of external fields the Hamiltonian of the system is:

$$[3] \quad \boldsymbol{H} = -\frac{3}{4} \sum_{ij} C_{ij} \operatorname{tr} Q_i Q_j$$

Consider a linear vector space $\boldsymbol{L}$ of all symmetric traceless matrices 3×3. A scalar product of two elements $A, B \in \boldsymbol{L}$ is defined by the relation $(AB) \equiv \operatorname{tr} AB$. The matrix Q_i is expandable in terms of the basis elements $\{X_\alpha\}_{\alpha = 1,\ldots,5}$ of the space $\boldsymbol{L}$:

$$X_1 = \frac{1}{\sqrt{2}}\begin{pmatrix} 0 & 1 & 0 \\ 1 & 0 & 0 \\ 0 & 0 & 0 \end{pmatrix}, \qquad X_2 = \frac{1}{\sqrt{2}}\begin{pmatrix} 0 & 0 & 1 \\ 0 & 0 & 0 \\ 1 & 0 & 0 \end{pmatrix}$$

$$[4] \quad X_3 = \frac{1}{\sqrt{2}}\begin{pmatrix} 0 & 0 & 0 \\ 0 & 0 & 1 \\ 0 & 1 & 0 \end{pmatrix}, \qquad X_4 = \frac{1}{\sqrt{2}}\begin{pmatrix} 1 & 0 & 0 \\ 0 & -1 & 0 \\ 0 & 0 & 0 \end{pmatrix}$$

$$X_5 = \sqrt{\frac{2}{3}}\begin{pmatrix} -1/2 & 0 & 0 \\ 0 & -1/2 & 0 \\ 0 & 0 & 1 \end{pmatrix}$$

$$Q_i = a_i^\alpha(\theta_i, \varphi_i) X_\alpha$$

$$a_i^1 = \frac{1}{\sqrt{2}}\sin^2\theta_i \sin 2\varphi_i, \qquad a_i^2 = \frac{1}{\sqrt{2}}\sin^2\theta_i \cos\varphi_i$$

[5]

$$a_i^3 = \frac{1}{\sqrt{2}}\sin 2\theta_i \sin\varphi_i, \qquad a_i^4 = \frac{1}{\sqrt{2}}\sin^2\theta_i \cos 2\varphi_i$$

$$a_i^5 = \sqrt{\frac{2}{3}} P_2(\cos\theta_i)$$

where θ_i and φ_i are the polar angles of the unit vector n_i. Summation over repeated indices is assumed in [5] and further; Greek indices vary from 1 to 5. The Hamiltonian [3] can be rewritten in the form:

[6] $$H = -\frac{3}{4} C_{ij}\delta^{\alpha\beta} a_i^\alpha a_j^\beta = -\frac{3}{4} QIQ$$

where

$$Q = (a_1^1, \ldots, a_1^5, \quad a_2^1, \ldots, a_2^5, \ldots, a_N^1, \ldots, a_N^5)$$

is a $5N$-dimensional vector defining a configuration of the system, $I = C \otimes I$ is the interaction matrix. The elements of the matrix C are the coefficients C_{ij}, I is the unit matrix 5×5.

In the presence of the external field, which has a value H_i at molecule i, the Hamiltonian is written as

[7] $$H = -\frac{3}{4} QIQ - \frac{1}{2} GQ$$

where G is a $5N$-dimensional vector with the components defined by coefficients of the expansion of N matrices:

$$G_i^{\alpha\beta} = \Delta\chi\,(H_i^\alpha H_i^\beta - \frac{1}{3}\delta^{\alpha\beta} H_i^2)$$

in terms of the basis elements [4], $\Delta\chi = \chi_\perp - \chi_\parallel$ is the anisotropy of the molecular polarizability.

Then the partition function of the system is

[8] $$Z(\beta, G) = \int_M dQ \exp\left(\frac{3}{4}\beta QIQ + \frac{1}{2}\beta GQ\right)$$

where $\beta = 1/k_B T$ is an inverse temperature in energy units. In [8] the integration is performed over $2N$-dimensional surface M given in L the relations [5], and

$$dQ = 2^N \prod_{i=1}^{N} \sin\theta_i\, d\theta_i\, d\varphi_i$$

is an element of M.

To calculate partition function [8], we replace the interaction between the molecules by the interaction of the molecules with an effective fluctuating vector field b. For this purpose one can use the identity:

$$\exp\left[\frac{3}{4}\beta QIQ\right] = \left[\left(\frac{4\pi}{3\beta}\right)^{-5N} \det I\right]^{1/2} \times \int_{R^{5N}} db \exp\left[-\frac{3}{4}\beta bIb + \frac{3}{2}\beta bIQ\right]$$

and rewrite [8] in the form:

[9] $$Z(\beta, G) = \left[\left(\frac{4\pi}{3\beta}\right)^{-5N} \det I\right]^{1/2} \times \int_{R^{5N}} db \exp\left[-\frac{3}{4}\beta bIb\right] Z_0(G, b)$$

where b is a $5N$-dimensional vector with components that vary from $-\infty$ to $+\infty$, and

[10] $$Z_0(\beta, G, b) = \int_M dQ \exp\left(\frac{3}{2}\beta QIQ + \frac{1}{2}\beta GQ\right)$$

is the partition function of the system of noninteracting molecules. The function of the effective field distribution can be written as:

[11] $$\exp[-\beta\phi(b)] = \exp\left[-\beta\left(\frac{3}{4} bIb - \frac{1}{\beta}\log Z_0(\beta, G, b)\right)\right]$$

3. Gaussian approximation for fluctuating fields

To calculate [9], we use the Gaussian approximation. Then

[12] $$\exp[-\beta\phi(b)] \approx \exp\left\{-\beta\left[\phi(B) + \frac{1}{2}(b - B) J (b - B)\right]\right\}$$

where the stationary point B is the solution of the equation:

[13] $$B = \frac{\int_M dQ \exp\left[\frac{3}{2}\beta BIQ + \frac{1}{2}\beta GQ\right] Q}{\int_M dQ \exp\left[\frac{3}{2}\beta BIQ + \frac{1}{2}\beta GQ\right]}$$

One can conclude from [13] that B has a sense of Q vector in the mean-field approximation, i.e.,

$$B = \langle Q\rangle \equiv (\langle Q_1\rangle, \ldots, \langle Q_N\rangle)$$

The dispersion of the effective field $\boldsymbol{b}$ is given by the matrix J^{-1}:

$$[14] \quad J = \frac{\partial^2}{\partial \boldsymbol{b} \partial \boldsymbol{b}} \phi(\boldsymbol{b}) \Big|_{\boldsymbol{b} = \boldsymbol{B}}$$

Using the relations [11] and [14] we obtain:

$$[15] \quad J = \frac{3}{2} IR$$

where

$$[16] \quad R = \boldsymbol{1} - \frac{3}{2} \beta I [\langle \boldsymbol{Q} \otimes \boldsymbol{Q} \rangle - \langle \boldsymbol{Q} \rangle \otimes \langle \boldsymbol{Q} \rangle]|_{\boldsymbol{b} = \boldsymbol{B}}$$

In [16] the averages are calculated with the mean-field distribution function:

$$\exp \left[\frac{3}{2} \beta \boldsymbol{b} I \boldsymbol{Q} + \frac{1}{2} \beta \boldsymbol{G} \boldsymbol{Q} \right]$$

Taking into account [9]–[11] and [15] and [16] we find:

$$[17] \quad Z(\beta, \boldsymbol{G}, \boldsymbol{B}) \approx Z_0(\beta, \boldsymbol{G}, \boldsymbol{B}) [\det R]^{-1/2} \exp \left[-\frac{3}{4} \beta \boldsymbol{B} I \boldsymbol{B} \right]$$

Assume that the external fields $\boldsymbol{H}_i$ applied to the molecules have the same direction along the z axis of the laboratory frame. In this case:

$$\boldsymbol{G}_i = \Delta\chi H_i^2 \begin{pmatrix} -1/2 & 0 & 0 \\ 0 & -1/2 & 0 \\ 0 & 0 & 1 \end{pmatrix}$$

$$[18] \quad \langle Q_i \rangle = s_i \begin{pmatrix} -1/3 & 0 & 0 \\ 0 & -1/3 & 0 \\ 0 & 0 & 2/3 \end{pmatrix}$$

where $s_i = \langle P_2 (\cos (\theta_i)) \rangle$ is the order parameter of the molecule i. Then [13] for the stationary point can be written in the scalar form:

$$[19] \quad s_i = -\frac{1}{2} + \frac{3}{2} \frac{\int_0^1 t^2 \exp (m_i t^2) \, dt}{\int_0^1 \exp (m_i t^2) \, dt}$$

where

$$m_i = \frac{3}{2} \beta \left[C_{ik} s_k + \frac{1}{3} \Delta\chi H_i^2 \right]$$

For the partition function [17] we have:

$$[20] \quad Z(\beta, \boldsymbol{G}, \boldsymbol{B}) \approx Z_0(\beta, \boldsymbol{G}, \boldsymbol{B}) [\det R]^{-1/2} \times \exp \left[-\frac{1}{2} \beta C_{ij} S_i S_j \right]$$

where

$$Z_0(\beta, \boldsymbol{G}, \boldsymbol{B}) = (8\pi)^N \prod_{j=1}^{N} \exp \left[-\frac{1}{3} m_j (\beta, s) \right] \times \int_0^1 \exp [m_j (\beta, s) t^2] \, dt$$

Assume now that the external fields $\boldsymbol{H}_i$ have the same values and the order parameters of all molecules are equal, i.e.,

$$[21] \quad s_i = s_0, \qquad m_i = m, \qquad H_i = H$$

Under such conditions the system of equations [19] coincides with the Maier–Saupe equations (4) and has the form:

$$[22] \quad s_0 = -\frac{1}{2} + \frac{3}{2} \frac{\int_0^1 t^2 \exp (mt^2) \, dt}{\int_0^1 \exp (mt^2) \, dt}$$

$$m = \frac{3}{2} (\beta U) (s_0 + \gamma)$$

where the quantity

$$U = \sum_{i=1}^{N} C_{ij}$$

has the same value for all molecules, $\gamma = \Delta\chi H^2 / 3U$. With a help of [22] we obtain the following expressions for the partition functions:

$$Z(\beta, \boldsymbol{G}, \boldsymbol{B}) = Z_0(\beta, \boldsymbol{G}, \boldsymbol{B}) [\det R]^{-1/2} \times \exp \left[-\frac{1}{2} N \beta U s_0^2 \right]$$

$$[23] \quad Z_0(\beta, \boldsymbol{G}, \boldsymbol{B}) = (8\pi)^N \exp \left[-\frac{N}{3} m (\beta, s_0) \right] \times \left[\int_0^1 \exp (mt^2) \, dt \right]^N$$

To calculate det R under conditions [21] the matrix R can be written as follows:

$$R = \boldsymbol{1} - \beta C \otimes A$$

where A is the diagonal matrix with the elements:

$$A^{\alpha\beta} = \frac{3}{2} [\langle a^\alpha a^\beta \rangle - \langle a^\alpha \rangle \langle a^\beta \rangle]$$

$\boldsymbol{1}$ is the unit matrix $5N \times 5N$. Then we find:

$$[24] \quad \det R = \exp [\operatorname{tr} \log (\boldsymbol{1} - \beta C \otimes A)] = \prod_{\alpha=1}^{5} \prod_{i=1}^{N} (1 - \beta U \omega_i \mu^\alpha)$$

where ω_i and μ^α are the proper values of the matrices C/U and A, respectively. Since

$$\sum_{i=1}^{N} \frac{C_{ij}}{U} = 1$$

matrix C/U is a stochastic one. Hence, $\omega_i \leqslant 1$. Assuming that $\beta U \mu^\alpha < 1$, we get:

[25] $$\det R \approx \exp\left[-\frac{1}{2}(\beta U)^2\, \omega_i \omega_i \mu^\alpha \mu^\alpha\right]$$

$$= \exp\left[-\frac{1}{2} N (\beta U)^2\, \Theta\, \mu^\alpha \mu^\alpha\right]$$

where Θ is a dimensionless parameter:

[26] $$\Theta = \frac{1}{N}\omega_i \omega_i = \sum_{i=1}^{N} \frac{C_{ij}^2}{U^2}$$

Thus, one can easily see from [25] and [15] that under the conditions [21] the dispersion matrix $D = J^{-1}$ is diagonal. The dispersions $D_{ii}^{\alpha\alpha}$ are independent of i and can, to the accuracy of a constant factor, be written as:

$$D^{\alpha\alpha} \sim \exp\left[\frac{1}{2}(\beta U)^2\, \Theta\, (\mu^\alpha)^2\right]$$

Using [23] and [24], we now write the expressions for the average energy E, order parameter $\langle s \rangle$, entropy S, and log Z in the Gaussian approximation:

[27] $$\frac{\log Z}{N} = \frac{\log Z_0}{N} - \frac{1}{2}\beta U s_0^2 - \frac{1}{2}\sum_{\alpha=1}^{5} \frac{1}{N} \times \sum_{i=1}^{N} \log\left[1 - \beta U\, \omega_i \mu^\alpha\right]$$

$$\approx \frac{\log Z_0}{N} - \frac{1}{2}\beta U s_0^2 - \frac{1}{2}\,(\beta U)^2\, \Theta\, \mu^\alpha \mu^\alpha$$

[28] $$\frac{E}{NU} = -\frac{\partial_\beta \log Z}{NU}$$

$$\approx \frac{E_0}{NU} - \frac{1}{2}\Theta\, \beta U\, [\mu^\alpha \mu^\alpha + \mu^\alpha\, m \partial_m \mu^\alpha]$$

[29] $$\langle s \rangle = \frac{\partial_\gamma \log Z}{N\beta U} \approx s_0 + \frac{3}{4}\Theta\, (\beta U)^2\, \mu^\alpha \partial_m \mu^\alpha$$

[30] $$\frac{S}{Nk_B} = \frac{\log Z + \beta E}{N}$$

$$\approx \frac{S_0}{Nk_b} - \frac{1}{2}\Theta\, (\beta U)^2 \left[\frac{1}{2}\mu^\alpha \mu^\alpha + \mu^\alpha m \partial_m \mu^\alpha\right]$$

where E_0, s_0, and S_0 are the Maier–Saupe theory value:

$$\frac{E_0}{NU} = -\frac{1}{2}s_0^2 - \gamma s_0$$

[31]

$$\frac{S_0}{Nk_B} = \log(8\pi) - \frac{1}{2}\beta U\, (s_0 + \gamma)\, (2s_0 + 1) + \log \int_0^1 \exp(mt^2)\, dt$$

The proper values μ^α of the matrix A are calculated with the help of the following relations:

$$\mu^1 = \mu^4 = \frac{3}{8}(1 - 2T_2 + T_4)$$

[32]

$$\mu^2 = \mu^3 = \frac{3}{2}(T_2 - T_4), \qquad \mu^5 = \frac{9}{4}(T_4 - T_2^2)$$

obtained from [22], where

$$T_2 = \frac{\int_0^1 t^2 \exp(mt^2)\, dt}{\int_0^1 \exp(mt^2)}$$

$$T_4 = \frac{\int_0^1 t^4 \exp(mt^2)\, dt}{\int_0^1 \exp(mt^2)\, dt}$$

Uniform states of a nematic are degenerate in the five-dimensional space of the order parameter components (1). This corresponds to the identities $\mu^1 = \mu^4$ and $\mu^2 = \mu^3$. In fact, the matrices X_1 and X_2 are equivalent to X_4 and X_3, respectively, because they can be transformed each to other by rotations around the z axis in the laboratory frame. The choice of $\langle Q \rangle$ in the form [18] fixes and the z axis and leads to $\mu^{1,4} \neq \mu^{2,3}$, since the transformation $\mu^{1,4} \Rightarrow \mu^{2,3}$ involves the rotation of the z axis. As one can show from [32], above the critical point T_c in a zero external field $\mu^\alpha = 1/5$, $\alpha = 1,\ldots, 5$ and the symmetry is reconstructed. It should be noted that the fluctuations of the effective field $\boldsymbol{b}$ are biaxial. The reason is that the field $\boldsymbol{b}$ represents in three-dimensional space the sum of matrices [4] with coefficients varying independently.

Using [22] and [32] below the critical temperature T_c $\mu^{2,3}$ can be expressed as follows:

[33] $$\mu^{2,3} = \frac{1}{\beta U}\frac{s_0}{s_0 + \gamma}$$

Therefore, at $\gamma = 0$ the expression [27] for log Z contains a logarithmic singularity, which is integrated in the thermodynamic limit $N \to \infty$. According to the expressions [32] we can write for $m \to \infty$:

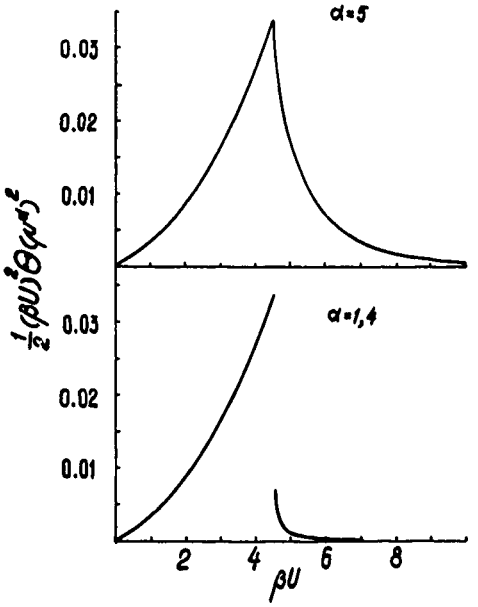

FIG. 1. The variation of the quantities (see [25] and [36]) defining the values of the fluctuating field dispersions as a function of the dimensionless inverse temperature βU for $\Theta = 0.0879$.

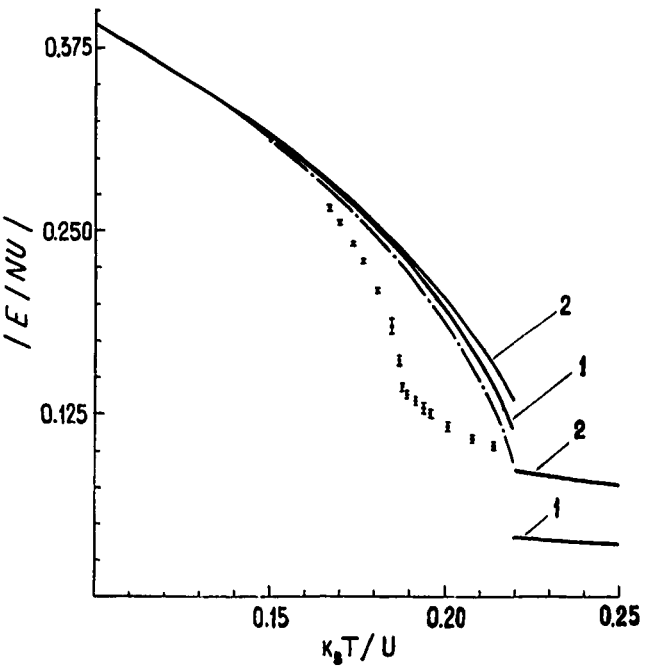

FIG. 2. The temperature dependence of the energy of the system per particle. The ● represent the Monte-Carlo simulation data (11), the · – · – · curve the mean-field calculations, the — lines, 1 and 2, the results of the calculations in the Gaussian approximation for Θ = 0.0879 and 1/6, respectively.

[34] $$\mu^{1,4} \sim \frac{3}{4} m^{-2}, \qquad \mu^{2,3} \sim \frac{3}{2} m^{-1}, \qquad \mu^{5} \sim \frac{9}{4} m^{-2}$$

Hence, for $\beta \to \infty$ the terms in [28] and [29] containing μ^α can be neglected and [28] and [29] become the usual mean-field formulas for E and $\langle s \rangle$. However, the Gaussian correction to the mean-field entropy S_0 has a finite value $\Theta/[2(1 + \gamma)^2]$ in the low-temperature limit as follows from [33].

4. Numerical results

The numerical calculations with the formulas [27]–[30] have been performed for the system of molecules placed in the sites of a simple cubic lattice. The external field was assumed to be zero. Equation [22] was used to obtain the stationary point B. The radial dependence of the intermolecular potential was taken in the form:

[35] $$C_{ij} = \frac{1}{r_{ij}^6}$$

where r_{ij} is the distance between the molecules i and j. In this case the parameter Θ has the value 0.0879 and is independent of the lattice spacing and interaction constant. The computations have been also carried out at Θ = 1/6 since the approximation of the z nearest-neighbors interaction, which was used in the Monte-Carlo simulations (11, 12) and the cluster model calculations (8, 9) leads to $\Theta = 1/z$.

Figure 1 shows the dependence of the quantities (1/2) $(\beta U)^2 \Theta(\mu^\alpha)^2$ defining the dispersions of the vector-fluctuating fields on the dimensionless inverse temperature βU for Θ = 0.0879 and α = 1, 4, 5. As one can see, the condition for the applicability of the Gaussian approximation:

[36] $$\frac{1}{2} (\beta U)^2 \Theta (\mu^\alpha)^2 \ll 1$$

is satisfied for all temperatures. In the case α = 2, 3 below the critical point one has:

$$\frac{1}{2} (\beta U)^2 \Theta (\mu^\alpha)^2 = \frac{1}{2} \Theta$$

and we conclude that the Gaussian approximation is valid for all types of three-dimensional lattices $\Theta \leq 0.25$.

The temperature dependence of the energy is shown in Fig. 2. The results of the computations of the order parameter $\langle s \rangle$ as a function of the reduced temperature T/T_c for Θ = 1/6 and 0.0879 are presented in Fig. 3. The quantitative agreement of our calculations with the Monte-Carlo simulation data is achieved for $T/T_c < 0.97$ in the case Θ = 1/6. At Θ = 0.0879 a satisfactory agreement is obtained only for $T/T_c < 0.93$. The calculations in the Gaussian approximation reproduce unsatisfactorily the behavior of the Monte-Carlo curve in the vicinity of the critical point where the fluctuations are strong. On the other hand, the cluster model more accurately describes the shape of the order-parameter dependence on the reduced temperature.

The values of energy, order-parameter, and entropy discontinuities at the critical temperature are presented in Table 1. The comparison shows that the account of the local field fluctuations in the Guassian approximation decreases the magnitudes of the discontinuities by at least 40 and 30% for the energy and entropy with respect to the mean-field-theory predictions. Our estimates are very close to those calculated in the two-particle cluster model. The difference between our results obtained in the approximation of the interaction with the nearest neighbors and in the case of the radial dependence [35] reach

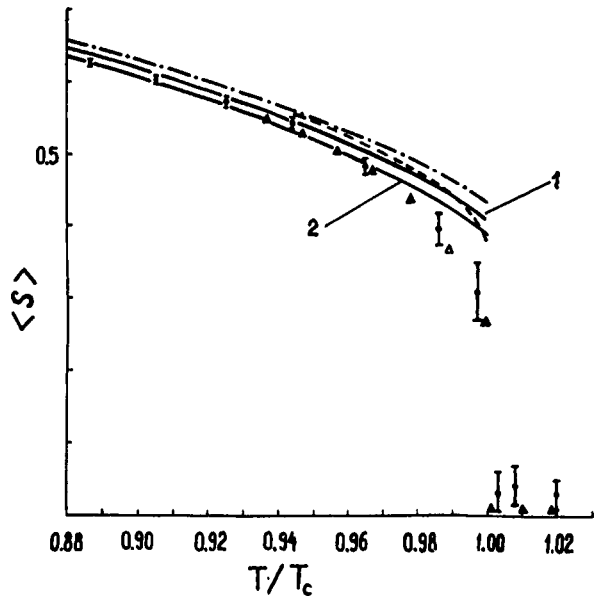

FIG. 3. The dependence of the order parameter $\langle s \rangle$ on the reduced temperature. The ● represent the Monte-Carlo simulation data (11), the △ the Monte-Carlo data (12), the - - - and · – · – · lines the results of the two-particle cluster approximation (8) and mean-field theory, the — lines, 1 and 2, the calculations in the Gaussian approximation for $\Theta = 1/6$ and 0.0879, respectively.

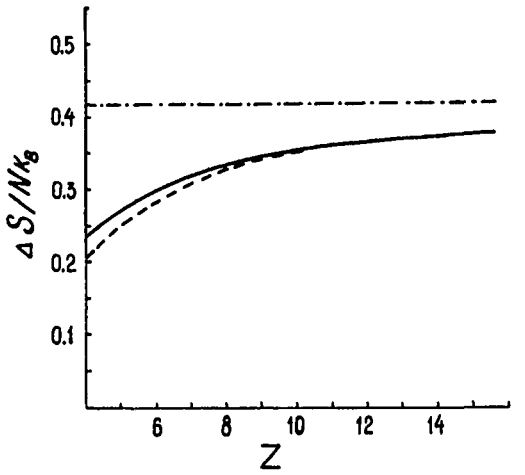

FIG. 4. The variation of the entropy discontinuity as a function of the effective number $z = 1/\Theta$ of the nearest neighbors. The - - - and — lines are the results of the two-particle cluster model (8) and present work, the · – · – · line shows the mean-field value.

TABLE 1. The values of the discontinuities of the thermodynamic quantities in the critical point calculated using the Monte-Carlo method (MC), mean-field theory (MF), Gaussian approximation (GA), and two- and four-particle cluster approximation (2-CA, 4-CA)

	MC (ref. 11)	MF (ref. 4)	GA $\Theta = \frac{1}{6}$	GA $\Theta = 0.0879$	2-CA (ref. 8)	4-CA (ref. 9)
$\frac{k_B T_c}{U}$	1.127±0.003	1.321	1.321	1.321	1.160	1.142
$\langle s_c \rangle$	0.27±0.02	0.429	0.390	0.407	0.382	0.347
$\Delta E/NU$	0.07±0.01	0.551	0.337	0.437	0.327	—
$\Delta s/Nk_B$	—	0.418	0.298	0.354	0.282	—

5, 20, and 15% for the order parameter, energy, and entropy, respectively.

Figure 4 shows the similarity of variations of the entropy discontinuity $\Delta S/Nk_B$ as a function of the effective coordination number $z = 1/\Theta$ in the present approach and cluster approximation.

5. Conclusions

In this work we have developed a microscopic method of calculating the thermodynamic characteristics of nematics in a five-dimensional space. The equations of the mean-field theory are obtained as a special case. The method gives reasonable results within the limitations of the Gaussian approximation. The predicted dependence of the order parameter on T/T_c agrees with the Monte-Carlo simulation data excluding the neighborhood of the critical point T_c. The calculations based on the proposed approach are not restricted to the nearest-neighbor-interaction approximation. In the case of the realistic radial dependence of the intermolecular potential $1/r^6$, taking into account the interaction with molecules outside the first coordination sphere leads us to variations of the thermodynamic quantities comparable with the Gaussian corrections and to increase the values of the discontinuities at the critical point.

A comparison of our results with those of the cluster approximation allows us to conclude that the description of the Monte-Carlo-simulation data may be improved by a combination of the two approaches. In the framework of our formalism the short-range correlations can be included at the level of [19].

The tendency toward weakening of the transition with a decreasing of the number z of nearest neighbors shows that certain liquid properties of nematics are important. We remark that [19] has been obtained without any assumptions about the spacial structure of the system. They are general enough to admit fluctuations of the C_{ij} in space.

Acknowledgments

The authors thank T. A. Rotinian, I. A. Merkulov, and V. V. Ponomarenko for fruitful discussions. The Department of Phys-

ics of ÅBO Akademi, Finland is gratefully acknowledged for the use of their facilities in the final preparation of this article.

1. A. Z. POTASHINSKII and V. L. POKROVSKII. Fluktuatzionnaia teoria fazovych perechodov. Nauka. Moskva. 1982.
2. M. A. ANISIMOV. Mol. Cryst. Liq. Cryst. **162A**, 1 (1988); Kriticheskie javlenia v gidkostiach i gidkich kristallach. Nauka, Moskva. 1987.
3. L. ONSAGER. Ann. N. Y. Acad. Sci. **51**, 627 (1949).
4. W. MAIER and A. SAUPE. Z. Naturforsch. A **13**, 564 (1958).
5. T. J. KRIEGER and H. M. JAMES. J. Chem. Phys. **22**, 796 (1954).
6. J. G. I. YPMA and G. VERTOGEN. Solid State Commun. **18**, 475 (1976).
7. G. VERTOGEN and B. W. VAN DER MEER. Phys. Rev. A, Gen. Phys. **19**, 370 (1979).
8. P. SHENG and P. J. WOJTOWICZ. Phys. Rev. A, Gen. Phys. **14**, 1883 (1976).
9. R. VAN DER HAEGER, J. DEBRUYNE, R. LUYCKX, and H. N. W. LEKKERKERKER. J. Chem. Phys. **73**, 2469 (1980).
10. I. A. MERKULOV, YU. A. PAPAVA, V. V. PONOMARENKO, and S. I. VASILIEV. Can. J. Phys. **66**, 135 (1988).
11. G. R. LUCKHURST and P. SIMPSON. Mol. Phys. **47**, 251 (1982).
12. H. MEIROVITCH. Chem. Phys. **21**, 251 (1977).

RESEARCH NOTE / NOTE DE RECHERCHE

Nuclear-mass dependent spin-orbit interaction

T. L. SORDO AND J. A. SORDO
Departamento de Quimica Fisica, Universidad de Oviedo, 33007 Oviedo, Spain
AND
S. FRAGA
Department of Chemistry, University of Alberta, Edmonton, Alta., Canada T6G 2G2

Received November 2, 1990

The nuclear-mass dependent spin-orbit interaction is discussed. The corresponding interaction operator is given in tensor form and the expression for its matrix elements in a basis of *SL* functions is presented. Monoconfigurational calculations have been performed for the ground states of carbon and oxygen. The results for the *J*-level splittings show that the contribution from this interaction is comparable with, or even greater than, the contribution from the hyperfine-structure interactions.

On discute l'interaction spin-orbite dependante de la masse nucléaire. On donne l'opérateur d'interaction correspondant sous forme tensorielle et on présente l'expression pour ses éléments de matrice dans une base de fonctions SL. Des calculs monoconfigurationnels ont été effectués pour les états fondamentaux du carbone et de l'oxygéne. Les résultats obtenus pour les séparations des niveaux *J* montrent que la contribution de cette interaction est du même ordre et même plus grande que celle des interactions de structure hyperfine.

[Traduit par la rédaction]

Can. J. Phys. **69**, 161 (1991)

Introduction

Research in atomic structure centered in the past in overcoming the main difficulties, such as those encountered in the determination of satisfactory functions and the consideration of the energy contributions from the most important relativistic corrections. Nowadays these difficulties have been overcome: Hartree–Fock functions (whether monoconfigurational- or multiconfigurational) may be obtained in a routine fashion using, for example, the program of Fischer (1); and formulations and programs exist as well for the evaluation of the *SL* nonsplitting corrections and the fine- and hyperfine-structure interactions. (See, e.g., the work of Eissner *et al.* (2), Glass and Hibbert (3), Glass (4), and Fraga *et al.* (5, 6)).

As experimental measurements become more acurate, however, the need exists to refine the theoretical results by consideration of interactions, which although numerically not so important, must be included to obtain agreement between the theoretical and the experimental values.

Such is the case, in particular, for some of the nuclear-mass dependent interactions. The normal and specific (7) as well as the relativistic (8) mass corrections, which offered no difficulty, have been included for a long time in atomic calculations but other mass-dependent corrections, namely the mass-dependent orbit-orbit and spin-orbit interactions have received scant attention.

These interactions, first derived by Stone (9, 10), may also be obtained from the Hegstrom Hamiltonian (11) as well as directly (12) from the formulation of Bethe–Salpeter (7). At the numerical level, the mass dependence of the fine structure of helium and helium-like ions has been studied by Douglas and Kroll (13), Lewis and Serafino (14), and Drake and Makowski (15, 16).

The purpose of this work is to present the formulation for the matrix elements of the mass-dependent spin-orbit interaction in a basis of *SL* functions and to report the values obtained for the ground states of carbon and oxygen. Those results show that the order of magnitude of this interaction is comparable with that of the hyperfine-structure effects, thus confirming the need for its consideration in accurate calculations.

Theoretical formulation

The nuclear-mass dependent electron-spin–nucleus-orbit interaction operator may be written, when working within the centre of mass system (assumed at rest), as

$$H_{so} = \alpha^2\left(\frac{Z}{mm_a}\right) \sum_{\rho} \sum_{\sigma} r_\rho^{-3} (s_\rho \cdot [r_\rho \times p_\sigma])$$

where m and m_a are the electron and nuclear mass; Z is the nuclear charge; the summations over ρ and σ extend to all the electrons characterized by the position, linear momentum, and spin angular momentum vectors r, p, and s, respectively; and α is the fine-structure constant.

In tensor form, this operator becomes

$$H_{so} = \alpha^2\left(\frac{Z}{mm_a}\right) \sum_{\rho} \sum_{\sigma} \{-2r_\rho^{-2} r_\sigma^{-1} (s_\rho^{(1)} [C_\rho^{(1)} \times R_\sigma^{(1,1)}]^{(1)})^{(0)} + \sqrt{2} r_\rho^{-2} (s_\rho^{(1)} \cdot [C_\rho^{(1)} \times C_\sigma^{(1)}]^{(1)})^{(0)} \partial_\sigma\}$$

CAN. J. PHYS VOL 69, 1991

where the usual tensor notation has been used and

$$R^{(k,k')} = [C^{(k)} \times l^{(1)}]^{(k')}$$

where $C^{(k)}$ represents a modified spherical harmonic tensor and $l^{(1)}$ is the orbit angular momentum tensor. The symbol ∂_σ stands for $\partial/\partial r_\sigma$.

The corresponding matrix elements are given by

$$(C\beta SLJM_J|H_{so}|C'\,\beta'\,S'\,L'\,J'\,M_J') = \alpha^2\left(\frac{Z}{mm_a}\right)\delta(M_S\,M_L\,JM_J,\,M_S'\,M_L'\,J'M_J')\,(-1)^{S'+L+J}\,[(2S+1)(2L+1)]^{1/2}$$

$$[(L'\,M_L'\,10|LM_L)\,(S'\,M_S'\,10|SM_S)]^{-1}\begin{Bmatrix} S' & L' & J \\ L & S & 1 \end{Bmatrix}\sum_u\sum_v\Big\{(\{l\}\,\{m\mu\}_u\,M_S\,M_L\,|\beta SL)\,(\{l'\}\,\{m'\,\mu'\}_v\,M_S\,M_L\,|\beta'\,S'\,L')$$

$$\sum_i\sum_j\omega_{ij}\,P_{ij}'\,(-1)^{m_i-m_i'}\,\delta(m_i+m_j,\,m_i'+m_i')\,\delta(\mu_i,\mu_j,\mu_i',\mu_j')\,\mu_i\left[\frac{(2l_i'+1)(2l_j'+1)}{(2l_i+1)(2l_j+1)}\right]^{1/2}$$

$$\{l_i'\,m_i'\,1m_i-m_i'\,|l_i\,m_i\}\,\{l_j'\,m_j'\,1m_j-m_j'\,|l_jm_j\}\left\{-\frac{1}{2}[l_j(l_j+1)-l_j'(l_j'+1)-2]\,R(i,j;i',j')+R'(i,j;i',j')\right\}\Big\}$$

where $(\{l\}\,(m\mu)_u\,M_s\,M_L\,|\beta SL)$ denotes an SL-coupling coefficient, $\{l\}$ and $\{m\mu\}$ stand for the sets of quantum numbers l_1, l_2,... l_n and $m_1\mu_1$, $m_2\mu_2$,.... $m_n\mu_n$, N being the number of electrons, and m_i and μ_i the orbital and spin angular-momentum z-component quantum numbers. The summations over i and j extend to the spin orbitals and the summations over u and v extend over the sets of quantum numbers $\{m\mu\}$. The coefficient ω_{ij} takes the values 1 (for any i, j if the two configurations are identical), δ_{jq} (if the two configurations differ in the spin orbitals at the q position), $\delta_{ip}\,\delta_{jq}$ (if the two configurations differ in the spin orbitals at the p and q positions), and 0 (if the two configurations differ in more than two spin orbitals). P_{ij}' stands for $1-T_{ij}'$, where T_{ij}' denotes the transposition of the spin orbitals $n_i'\,l_i'\,m_i'\,\mu_i'$ and $n_j'\,l_j'\,m_j'\,\mu_j'$. The symbol δ represents the usual Kronecker delta, C denotes the configuration, and β includes all the additional details needed in order to completely label the sate, while S, M_S, L, M_L, J, and M_J, are the usual quantum numbers. The usual notation has been used for the $6j$-symbols and $(L'\,M_L'\,10|LM)$, $(S'\,M_S'\,10|SM_S)$, etc., represent vector-coupling coefficients (related to $3j$-symbols); in addition the notation

$$\{l_i'\,m_i'\,1\,m_i-m_i'\,|\,l_i\,m_i\} = (l_i'\,m_i'\,1\,m_i-m_i\,|\,l_i\,m_i)\times(l_i'\,010|l_i0)$$

has been used.

The radial integrals are given by:

$$R(i,j;i',j') = \int dr_1\,R_i(r_1)\,R_i'(r_1)\int r_2\,dr_2\,R_j(r_2)\,R_j'(r_2)$$

$$R'(i,j;i',j') = \int dr_1\,R_i(r_1)\,R_i'(r_1)\int r_2^2\,dr_2\,R_j(r_2)\times\left[\frac{\partial R_j'(r_2)}{\partial r_2}\right]$$

where R_i denotes the radial function of the orbital n_il_i (n_i being the principal quantum number).

Numerical results

Calculations have been performed for the ground states of carbon ($^3P_{0,1,2}$, $A = 11$, $M = 11.011\,4333$ au) and oxygen ($^3P_{2,1,0}$, $A = 17$, $M = 16.999\,1333$ au).

Numerical monoconfigurational Hartree–Fock functions, obtained with the program of Fischer (1), were used and the SL-coupling coefficients were determined using the program of Nussbaumer (17).

The splittings obtained

Carbon: $^3P_1 - {}^2P_0 = 244.9$ MHz,

$$^3P_2 - {}^3P_0 = 489.8\text{ MHz}$$

Oxygen: $^3P_1 - {}^3P_2 = 809.6$ MHz,

$$^3P_0 - {}^3P_1 = 1619.2\text{ MHz}$$

although small (for which reason they have been given in MHz), are certainly comparable with, or even greater than, the contributions of the hyperfine-structure interactions.

Therefore, it is evident that this interaction should be included in accurate calculations whenever isotopic effects are to be studied.

1. C. F. Fischer. Comput. Phys. Commun. **14**, 145 (1978).
2. W. Eissner, M. Jones, and H. Nussbaumer. Comput. Phys. Commun. **8**, 270 (1974).
3. R. Glass and A. Hibbert. Comput. Phys. Commun. **16**, 19 (1978).
4. R. Glass. J. Phys. B: At. Mol. Phys. **11**, 3459 (1978).
5. S. Fraga, M. Klobukowski, J. Muszynska, K. M. S. Saxena, and J. A. Sordo. Phys. Rev. A: Gen. Phys. **34**, 23 (1986).
6. S. Fraga, M. Klobukowski, J. Muszynska, K. M. S. Saxena, J. A. Sordo, J. D. Climenhaga, and P. Clark. Comput. Phys. Commun. **47**, 159 (1987).
7. H. A. Bethe and E. E. Salpeter. Quantum mechanics of one- and two-electron atoms. Academic Press Inc., New York. 1957.

8. J. KARWOWSKI and S. FRAGA. Can. J. Phys. **52**, 536 (1974).
9. A. P. STONE. Proc. Phys. Soc. **77**, 786 (1961).
10. A. P. STONE. Proc. Phys. Soc. **81**, 868 (1963).
11. R. A. HEGSTROM. Phys. Rev. A: Gen. Phys. **7**, 451 (1973).
12. S. FRAGA and J. KARWOWSKI. Can. J. Phys. **52**, 1045 (1974).
13. M. DOUGLAS and N. M. KROLL. Ann. Phys. (N.Y.), **82**, 89 (1974).
14. M. L. LEWIS and P. H. SERAFINO. Phys. Rev. A: Gen. Phys. **18**, 867 (1978).
15. G. W. F. DRAKE and A. J. MAKOWSKI. J. Phys. B: At. Mol. Phys. **18**, L103 (1985).
16. G. W. F. DRAKE and A. J. MAKOWSKI. J. Opt. Soc. Am. B, **5**, 2207 (1988).
17. H. NUSSBAUMER. Comput. Phys. Commun. **1**, 191 (1969).

INSTRUCTIONS TO AUTHORS

CANADIAN JOURNAL OF PHYSICS

The *Canadian Journal of Physics* publishes reports representing significant contributions to any area of Physics. Reports may be submitted in English or in French for pubication as an article, research note, or a communication. A Research note is a short paper less than 14 manuscript pages. A communication is a report on research sufficiently important to merit prompt preliminary publication in condensed form. Including any tables and figures, the communication should not exceed six double-spaced typewritten pages in length. To expedite publication, proofs of communications are not sent to authors.

Publication is facilitated if authors check very carefully the symbols, abbreviations, and technical terms for accuracy, consistency, and readability and ensure that manuscripts and illustrations meet the journal requirements outlined below. It is helpful to examine the journal itself for details of layout, especially for tables and reference lists.

Delays in publication can be avoided by adherence to the instructions below.

THE MANUSCRIPT

All parts of the manuscript, including footnotes, tables, reference list, and captions for illustrations, should be typewritten or word processed, **double-spaced**, on quality paper 21.5 × 28 cm with margins of 3–4 cm. The manuscript will include, in the following order, the title page, the abstract, a brief introduction, main text, concluding section, any acknowledgements, reference list, any appendices, tables (each starting on a separate page and including a title), and figure captions. The figure captions should be typed on one or more separate sheets in numerical order. Each page of the manuscript should be numbered at the top of the page, beginning with the title page. Lines need not be justified. Nothing should be underlined unless it is to be set in italics; if a word processor is used, underlining is preferred over an italic font. Capital letters are used only when the letters or words should appear in capitals in the printed paper. The first line of all paragraphs in the text and of all captions and footnotes should be indented. **The original copy and three duplicates are required.** Only material typed on one side of the paper is acceptable. Manuscripts that do not conform to this preferred format may be returned to the author for correction before review. Authors who plan to submit a series of more than two articles at the same time are advised to consult the Editor in advance to ensure that adequate arrangements can be made for reviewing. Sometimes editors and referees are assisted if subsidiary data not intended for publication (and so marked) are submitted for inspection.

The **title page** of the manuscript should contain **only** the title, the authors' names, institution of origin, address (with postal code), corresponding author's address, phone number and, if appropriate, electronic-mail address, any necessary footnotes, and the **index classification of the paper according to the current indexing scheme of Physics Abstracts**. This subject index appears in the December issue of the *Canadian Journal of Physics*.

An **abstract** (p. 2) of not more than 200 words is required for articles. A shorter abstract should be used for communications and research notes. This abstract should be the **only** item on the second page of the manuscript. Authors who can submit abstracts in both fluent English and fluent French are encouraged to do so. Both titles and abstracts provide information for contemporary **alerting and information retrieval services**, and should therefore be informative but brief.

Articles should have an **Introduction** explaining in precise terms the problem with which the article is concerned, the motivation for the work, and its relation to existing knowledge. Articles should also have a **Concluding Section** outlining the contribution made to knowledge and evaluating its significance.

Acknowledgements should follow the body of the paper in a separate section.

References should be verified by checking the original publications. In the bibliography, listed at the end of the main text, they should be numbered and listed in the order in which they are first cited in the text. Each reference should be cited in the text and designated therein by its key number typed on the line and in parentheses. In a reference to the periodical literature, initials should precede the surnames of the authors and these should be followed by the name of the periodical (abbreviated in the form used in CASSI (*Chemical Abstracts Service Source Index*, Chemical Abstracts Service, P.O. Box 3012, Columbus, OH 43210), the volume number, the initial page number, and the year. In case of doubt, authors should write out the full name of the periodical. The style for listing references to books, conference proceedings, theses, etc., depends on the nature of the publication cited. In general, the information required includes the name(s) and initials of the author(s), the title of the publication along with the name(s) of its editor(s) (if any), the name of the publisher, the city and year of publication, and the page or chapter cited. Recent issues of the journal may be examined for examples of the appropriate format:

Journal: J. KING, L. BOSK, AND U. MANN. Can. J. Phys. **65**, 29 (1987).

Book: A. R. SINGH. *In* Physico-chemical processes. Vol. 2. *Edited by* G. Ball. Academic Press, New York. 1982. pp. 18–22.

Conference: L. ROBIN. *In* Proceedings of the 4th International Conference on kinetics, London, June 4–5, 1980. *Edited by* J. Jones. Plenum Press, London. 1981. pp. 98–103.

A manuscript in press, with the name of the journal, may be used as a reference, but **private communications and reports not yet accepted for publication are not acceptable references**. The latter should be included in the text in parentheses, e.g. (A.B. Jones, manuscript in preparation), or given as a footnote.

Spelling should follow that of Webster's Third New International Dictionary or the Oxford English Dictionary. Authors are responsible for consistency in spelling.

Symbols, units, and nomenclature should conform to current practice in each area of research or to international recommendations such as those of the International Union of Pure and Applied Physics (see Document U.I.P. 11 S.U.N. 65-3, 1965) and the International Union of Pure and Applied Chemistry (see the new Manual of Symbols and Terminology for Physiochemical Quantities and Units, 1975). Normally metric units should be used and the use of SI (système international d'unités) is encouraged. Superscripts and subscripts should be legible and appropriately placed, and unusual and Greek characters must be identified clearly.

Footnotes should be cited in the manuscript by superscript Arabic numbers (except in the tables) and should be numbered serially beginning with any that appear on the title page. Each footnote should be typed on the manuscript page on which the reference to it is made; **footnotes should not be included in the reference list.**

Equations must be typed. **All letters of the Latin alphabet must be typed.** If a typewriter with Greek and special mathematical symbols is not available, these may be handwritten but an identifying list must be supplied. **Manuscripts with illegible equations will be returned to the author for typing.** Numbers identifying equations should be in square brackets and placed flush with the left margin of the text. In numbering, no distinction is made between mathematical and chemical equations.

Tables should be numbered in Arabic numerals in the order cited in the text and each should have a brief title. All information in the tables should be typewritten, double-spaced, except for mathematical or chemical equations, chemical structures, or a large number of complicated entries, which should be triple-spaced. Each table should be typed on a separate sheet. Tables that run to more than one page must be clearly labelled on each page to indicate this. When tables are larger than 23 × 30 cm, the original is not required. Four photocopies of good quality, reduced to the size of two columns, are acceptable. Tables should not be more than three times the size of the final reproduction. Abbreviations may be used in the brief column headings with explanatory footnotes where necessary. The tables should not contain vertical rules or superfluous horizontal rules, authors should refer to recent issues of the journal for examples. Footnotes are indicated either by symbols (*, †, ‡, §, ‖, ¶, #) or lowercase italic superscript letters. Other descriptive notes may be placed below the table, designated by NOTE.

Supplementary material — The National Research Council of Canada maintains a **depository for supplementary material**, such as extensive tables or detailed calculations. Authors wishing to use this service should submit their complete work for examination and mark the parts to be deposited. Each copy of the manuscript should be accompanied by one copy of the material for depository. For some papaers, the editor may require a certain part of an article to be deposited. The existence of material in the depository is indicated in the printed paper by an appropriate footnote. Copies of material on deposit may be purchased from the Depository of Unpublished Data, CISTI, National Research Council of Canada, Ottawa, Ont., Canada K1A 0S2.

Copyright material — If a manuscript contains material (figures, tables, etc.) that is protected by copyright, the author must submit to the editor, before publication, **written permission from the copyright holder** for its reproduction.

ILLUSTRATIONS

General — Figures, individually or in groups, should be planned to fit into one or two columns of text after reduction. The final maximum dimensions for a one-column illustration are 8.9 × 24 cm and for two columns, 18.4 × 24 cm. Figures should be numbered in Arabic numerals in the order of their mention in the text, and should be referred to in the text even though they may be self-explanatory. Terms, abbreviations, and symbols used in the figures should be the same as those appearing in the text. Only essential details should be identified; more detailed information may be given in the legend. Each illustration should be identified, preferably in the lower left-hand corner, by the figure number and authors' names. Do not fold illustrations for mailing. Oversize illustrations are difficult to handle and are often received in damaged condition.

Line drawings — The original drawings, or unmounted well-focussed photographs, and three sets of clear copies are required. For original drawings larger than 23 × 30 cm., four sets of **clear** photographic copies, reduced to the dimensions of two columns or less, are acceptable; the original drawings need not be submitted. Drawings should not be more than three times the size of the final reproduction. Drawings should be made with India ink on plain or blue-lined white paper or other suitable material. Any coordinate lines to appear should be ruled in. All lines must be sufficiently thick to reproduce well, and all symbols, superscripts, subscripts, decimal points, and periods must be large enough to allow for any necessary reduction.

Letters and numerals should be made neatly with a printing device (scriber) or come from sheets of printed characters (transfer type) and be of such size that the smallest character will not be less than 1.5 mm high when reduced. **Typewritten or freehand lettering is not acceptable** The same size and font of lettering should be used for all figures of similar size in any one paper. Care should be taken to have the drawing and lettering in good proportion so that both can take the same reduction. Use a clear sans serif font and avoid heavy or thick lettering, which tends to close up on reduction, and unusual symbols, which the printer may not be able to reproduce in the figure caption (use open and filled circles, squares, and triangles). Computer-generated graphics **may be acceptable** provided they are in **black**, on high-quality paper, and the lines, lettering, and symbols are very smooth and large enough to permit the required reduction without any loss of detail. It is strongly recommended that letters and numbers on such graphs be made with dry transfer lettering or standard ink lettering templates because lettering made with older dot matrix printers is not acceptable. Authors should send original computer graphics (not photocpies) with their initial manuscript submission so that the Editor can determine suitability and quality.

Photographs — Four sets of all photographs are required: one set mounted on light cardboard, ready for reproduction, and three other sets that can be photographic reproductions of the mounted set and are suitable for review purposes. Prints must be of high quality, made on glossy paper, with strong contrasts. The copies for reproduction should be **trimmed to show only essential features** and mounted on white cardboard, with **no space** between those arranged in groups. The best results will be obtained if authors match the contrast and density of all figures arranged as a single plate. A photograph, or group of them, should be planned to fit into the area of either one or two columns of text **with no further reduction**. Magnification should be indicated wherever size is important. A scale bar included in the picture is recommended.

Color illustrations — Illustrations may be accepted for reproduction in color subject to the Editor's decision that the use of color is essential. **Authors will be responsible for all costs** and must accept other conditions, which may be obtained from the Publishing Department.

A recommended reference that defines guidelines for the publication of illustrations in scientific journals and books is *Illustrating Science: Standards for Publication* (published in 1988 by the Council of Biology Editors, Inc., Bethesda, MD 20814). The preparation of artwork, graphs, maps, computer graphics, halftones, and camera-ready copy, as well as color printing, are all clearly explained and illustrated.

STEPS IN THE PUBLICATION PROCESS

Submission — A manuscript should be submitted to the appropriate Associate Editor, as indicated on page *i* of each issue. Once a paper has been accepted, all correspondence should be with the Publishing Department in Ottawa, whose address is given on the inside front cover.

Galley Proofs — A galley proof, illustration proofs, the copy-edited manuscript, and a reprint order from are sent to the author. Galley proofs must be checked very carefully, as they will not be proofread by the Publishing Department, and must be returned within 48 hours of receipt. The proof stage is not the time to make extensive corrections, additions, or deletions. The cost of changes introduced by the author and deemed to be excessive will be charged to the author.

Reprints — If reprints are desired, the reprint order form must be filled out completely and returned with payment (cheque, credit card number, purchase order number, or journal voucher) together with the corrected proofs and manuscript. or, in the case of a communication, as soon as possible. Orders submitted after the Journal has been printed are subject to considerably higher prices. The Journal does not provide free reprints, and reprints are not mailed until payment is received.

Revised January 1991.

RECOMMANDATIONS AUX AUTEURS

La *Revue canadienne de physique* (Can. J. Phys.) publie, en français ou en anglais, les résultats de travaux originaux sous forme d'articles, de notes de recherche ou de communications dans l'un ou l'autre des domaines de la physique. Un **article** doit présenter une étude complète sur un sujet d'importance et d'un intérêt fondamental dans le domaine en question. Une **note de recherche** est un bref article. Elle ne doit pas comporter plus de 14 pages dactylographiées. Une **communication** cherche à diffuser rapidement un travail particulièrement important et opportun. Elle ne doit pas comporter plus de six pages dactylographiées, y compris les figures et les tableaux, tout en fournissant suffisamment de détails pour que les experts dans le domaine puissent reproduire l'expérience. Aucune épreuve n'est envoyée aux auteurs de communications afin de hâter la publication. Tous les manuscrits doivent suivre les étapes normales de l'évaluation.

Pour faciliter la publication, les auteurs devraient vérifier l'exactitude et l'homogénéité des symboles, des abréviations et des termes techniques. Il est bon de consulter un numéro de la revue afin d'en connaître la présentation.

Il est possible d'éviter les délais de publication en se conformant aux directives décrites ci-dessous.

MANUSCRIT

Généralités — Toutes les parties du manuscrit, y compris les notes infrapaginales, les tableaux, les légendes des illustrations et la bibliographie, doivent être dactylographiées à double interligne, d'un seul côté de feuilles de papier de 21,5 sur 28 cm et avec marges de 3 à 4 cm. Le traitement de texte par ordinateur est admis en autant que tous les caractères, en particulier les accents, sont clairement distincts. L'auteur ne doit souligner que pour demander des italiques et ne se servir de majuscules que pour demander des majuscules dans le texte imprimé; le soulignement est préféré aux caractères en italique dans le cas des traitements de texte par ordinateur. La première ligne d'un paragraphe dans le texte, d'une légende ou d'une note infrapaginale est toujours en retrait. La première page ne doit comporter que le titre de l'article, les noms des auteurs ainsi que leurs adresses respectives (y compris l'adresse pour le courrier électronique, si possible), leurs numéros de téléphone, de télex et de télécopieur (si disponible), et toute note infrapaginale qui s'impose L'adresse de l'auteur doit être celle de l'établissement où les recherches ont été effectuées. L'adresse actuelle de l'auteur correspondant, si différente, doit apparaître dans une note infrapaginale. Le numéro approprié de l'**index de classification thématique** adopté par les *Physics Abstracts* (voir le numéro de décembre du Can. J. Phys.) doit également paraître sur la première page. Le manuscrit comprend, dans l'ordre, les résumés (sur une page distincte), la section **Introduction,** le texte principal, les sections **Conclusion** et **Remerciements,** puis la bibliographie, les tableaux, les légendes des figures et les annexes. Les légendes des figures doivent être regroupées sur une ou plusieurs feuilles et présentées par ordre numérique. Chaque page du manuscrit doit être numérotée, en commençant par celle du titre, au haut de la page. **Le texte original dactylographié et trois copies bien lisibles du manuscrit sont nécessaires.** Les photocopies recto–verso ne sont pas acceptées.

Le **résumé** doit être précédé de la référence bibliographique complète (une copie, en page détachée, est destinée au traducteur). Il ne doit pas excéder une page et doit être beaucoup moins long s'il s'agit d'une note ou d'une communication. **Il ne doit comporter aucune abréviation.** Les références y sont admises seulement si elles sont absolument essentielles et doivent être citées avec l'information bibliographique complète. Tout manuscrit doit être accompagné d'un résumé. Les auteurs qui peuvent soumettre des résumés dans les deux langues officielles du Canada, c'est-à-dire en anglais et en français courants, sont encouragés à le faire. Les **services de repérage de l'information** utilisent les titres ainsi que les résumés dans l'élaboration de leurs bases de données; ceux-ci doivent par conséquent être brefs et informatifs.

L'**introduction** doit expliquer en termes précis le problème auquel se rapporte l'article considéré et exposer les raisons qui ont déterminé l'exécution de l'étude en cause, ainsi que sa relation avec les connaissances existantes.

La **conclusion** doit indiquer l'importance que revêt l'étude en question et mettre en lumière la contribution à l'ensemble des connaissances.

Les **références bibliographiques** doivent être vérifiées auprès des publications originales. **Dans la bibliographie,** elles doivent être classées par ordre numérique de mention dans le texte. La présentation doit suivre les numéros récents de la revue. Exemples :

1. C. LAFORÊT et D. LAPLANTE. Ann. Soc. Sci. Bruxelles, Ser. 1, **74**, 50 (1979).
2. A. R. SINGH. Nuclear data tables. *Dans* Review of nuclear science. Vol. 2, *Éditeurs* : S. Hall et C. Stern. Academic Press, New York. 1979. p. 25–40.
3. L. CAGNIARD, P. LAVOIE et N. GIROUX (éditeurs). Réflection et réfraction des ondes séismiques progressives. Gauthier-Villard, Paris, 1979.
4. L. ROBIN. *Dans* Compte rendu de la 10e Conférence internationale sur les métaux et alliages liquides. Paris, 8 au 16 juin 1977. *Éditeur* : G. Lott. Masson et Cie, Paris. p. 12.

À noter que seulement la page initiale du domaine de pagination est indiquée dans le cas des articles. Le titre d'une revue doit être abrégé conformément à *CASSI (Chemical Abstracts Service Source Index,* édition 1984 et suppléments, Chemical Abstracts Service, P.O. Box 3012, Columbus, OH 43210). En cas de doute, les auteurs doivent écrire le nom de la revue au complet. Les rapports qui ne sont pas encore approuvés pour publication et les communications personnelles ne font pas partie de la bibliographie et ne doivent être mentionnés qu'en notes infrapaginales ou entre parenthèses dans le texte, en spécifiant les noms de tous les auteurs et leurs initiales. L'auteur doit s'assurer que toute référence est complète et exacte; il lui incombe de vérifier que les articles « sous presse » ont été acceptés pour fins de publication dans la revue citée et de donner le numéro de volume, la page initiale et l'année de publication, lorsque disponibles, lors du renvoi des épreuves en placards. **Dans le texte,** les références doivent être signalées à l'aide des numéros clés inscrits sur la ligne, entre parenthèses.

L'**orthographe** doit suivre *Le Robert*. Les auteurs sont responsables de l'uniformité de l'orthographe dans l'ensemble du texte. Les accents doivent être insérés sur les majuscules.

La nomenclature, les abréviations et les symboles de grandeurs et d'unités de mesure doivent être conformes aux recommandations internationales, entre autres celles de l'Union internationale de physique pure et appliquée et de l'Union internationale de chimie pure et appliquée. Il faut se servir du **Système international d'unités** ou au moins en indiquer les équivalents. Ce système est décrit dans le *Guide de familiarisation au système métrique* publié en 1980 par l'Association canadienne de normalisation (178, boulevard Rexdale, Rexdale (Ontario), Canada M9W 1R3) et dans le *Guide des unités SI* publié en 1982 par le Service des communications, Centre de recherche industrielle du Québec (333, rue Franquet, C.P. 9038, Sainte-Foy (Québec), Canada G1V 4C7). **Les abréviations et les sigles des noms de substances, de procédés, d'organisations, etc., doivent être définis la première fois qu'ils sont utilisés.** Les abréviations à significations multiples sont à éviter. Les **symboles** et les **caractères grecs ou d'usage peu répandu** doivent être identifiés clairement; les **indices supérieurs et inférieurs** doivent être lisibles et correctement placés ou indiqués.

Les **notes infrapaginales** sont numérotées de façon continue tout au long du texte. Les appels de notes sont désignés par des chiffres arabes supérieurs (sauf dans les tableaux) alors que les notes en bas de pages sont précédées d'un chiffre inscrit sur la ligne et suivi d'un point. Chaque note doit figurer au bas de la page où elle est signalée. **Aucune note infrapaginale ne doit apparaître dans la bibliographie.**

Les **équations** doivent être dactylographiées clairement, à triple interligne, et identifiées par des numéros placés entre crochets alignés sur la marge de gauche. **Tous les caractères de l'alphabet latin doivent être dactylographiés.** Si une machine à écrire avec les caractères grecs et les symboles mathématiques spéciaux n'est pas disponible, ceux-ci peuvent être écrits à main levée mais une liste d'identification doit être fournie. **Les manuscrits dont les équations sont illisibles seront retournés aux auteurs pour être redactylographiés.**

Les **tableaux** doivent être numérotés de façon continue en chiffres arabes, comporter un titre bref et être mentionnés dans le texte bien que tous leurs éléments doivent être intelligibles en eux-mêmes. Toute information contenue dans les tableaux doit être dactylographiée à double interligne, sauf les équations mathématiques ou chimiques, les structures chimiques ou les entrées complexes, qui doivent être dactylographiées à triple interligne. Chaque tableau doit être dactylographié sur une page distincte. Les tableaux comprenant plus d'une page doivent être identifiés clairement sur chacune des pages. Les descripteurs et les notes descriptives infrapaginales doivent être brefs. Les tableaux ne doivent pas contenir de lignes verticales, ni de lignes horizontales superflues. Les auteurs sont priés de consulter un numéro récent de la revue pour la présentation et le lignage. Les notes infrapaginales doivent être signalées par des symboles (*,†,‡,§,‖,¶,) ou des lettres minuscules supérieures en italique. Une note descriptive qui n'est pas introduite par un appel de note peut être inscrite au bas du tableau à titre de NOTA.

La documentation complémentaire, telle que les grands tableaux, les calculs détaillés et les illustrations en couleur, est versée au Dépôt des données non publiées du Conseil national de recherches du Canada. Le travail des examinateurs et de la rédaction se trouverait parfois facilité par la présentation de telles données. Les auteurs qui désirent utiliser ce service doivent soumettre leur document au complet et indiquer les parties dont ils demandent le dépôt. Le directeur scientifique peut exiger que certaines parties d'un article soient déposées. Toute donnée déposée fait l'objet d'une note infrapaginale à la section appropriée du document. Des copies des données déposées peuvent être obtenues contre paiement en s'adressant au Dépôt des données non publiées, ICIST, Conseil national de recherches du Canada, Ottawa (Ontario), Canada K1A 0S2.

Droits de reproduction — L'auteur d'un article qui utilise de la documentation (tableaux, figures, etc.) protégée par les droits d'auteur **doit obtenir une permission écrite du titulaire de ces droits d'auteur** et la présenter au directeur scientifique avant la publication.

ILLUSTRATIONS

Généralités — Chaque figure ou groupe de figures doit être préparé de manière à occuper une ou deux colonnes du texte. Les dimensions finales et maximales d'une illustration sur une colonne sont de 8,9 × 24 cm, et 18,4 × 24 cm pour une illustration sur deux colonnes. Les figures sont numérotées en chiffres arabes selon leur ordre de mention et doivent être annoncées dans le texte bien que tous leurs éléments doivent être intelligibles en eux-mêmes. Les termes, les abréviations et les symboles utilisés dans les figures doivent être les mêmes que ceux apparaissant dans le texte. Seuls les détails essentiels doivent être identifiés; l'information plus détaillée doit être donnée dans la légende. Chaque illustration doit être identifiée, de préférence au bas, à gauche, par le numéro de la figure et les noms des auteurs. Les illustrations ne doivent pas être pliées lors de leur envoi. Les auteurs doivent se rappeler que les illustrations de grande dimension sont difficiles à manipuler et qu'elles sont souvent endommagées en cours de route.

Les **dessins au trait** originaux et trois séries de copies de bonne qualité sont exigés. Lorsque les dessins excèdent 23 × 30 cm, l'original n'est pas requis; il suffit de présenter quatre séries de photographies **de bonne qualité**, réduites aux dimensions d'une illustration sur deux colonnes. Les dimensions des originaux ne doivent pas excéder le triple de celles des reproductions définitives. Des photocopies ne peuvent être substituées aux originaux. Les dessins doivent être exécutés à l'encre de Chine noire sur papier blanc uni ou ligné bleu de première qualité, de préférence du papier vélin. Toutes les lignes de coordonnées apparentes doivent être tracées à la règle. L'épaisseur des lignes doit être suffisante pour que la reproduction soit nette; les signes décimaux, points de ponctuation, pointillés, etc., doivent être suffisamment marqués pour permettre la réduction nécessaire. Les lettres, les chiffres et les symboles doivent être composés soigneusement à l'aide d'un normographe, de gabarits de traçage ou de feuilles de lettrage à transfert direct (**pas à la machine à écrire, ni à l'aide d'une imprimante par points produisant des caractères irréguliers, ni à main levée**); leurs dimensions doivent être telles, qu'après réduction, la hauteur du plus petit caractère ne soit pas inférieure à 1,5 mm. **Le même type de lettrage (fonte et dimension) doit être utilisé pour toutes les figures de même dimension d'un article.** On doit veiller à proportionner les dessins et le lettrage de façon à pouvoir leur appliquer le même pourcentage de réduction Ne pas utiliser de caractères gras ou épais qui ont tendance à se refermer lors de la réduction, ni de symboles peu courants que l'imprimeur pourrait avoir de la difficulté à reproduire dans la légende (utiliser plutôt des cercles, des carrés et des triangles vides et pleins ainsi que des caractères sans empattement, avec zéros sans barre oblique). Les symboles et les caractères plus complexes doivent être incorporés dans une légende concise à même l'illustration. Les graphiques produits par ordinateur sont acceptés à la condition qu'ils répondent aux critères de précision mentionnés précédemment. Les originaux (non pas des photocopies) doivent être soumis en même temps que le manuscrit afin de permettre au directeur scientifique de juger de leur qualité.

Les **photographies** doivent être fournies en quatre exemplaires : l'un d'entre eux sera monté sur carton **léger**, prêt pour la reproduction; les trois autres peuvent être des reproductions photographiques de l'exemplaire monté sur carton et servent à l'évaluation. Les épreuves doivent être de première qualité, avec contrastes bien marqués, et tirées sur du papier glacé. Les copies destinées à la reproduction doivent être **rognées de façon à ne laisser paraître que les éléments essentiels** et doivent être montées sur carbon blanc en ne laissant **aucun espace** entre les photographies constituant une même illustration. Une photographie ou un groupe de photographies doit être préparé de manière à occuper, **sans réduction supplémentaire**, une ou deux colonnes du texte. On évitera les pertes de détail et de contraste inhérentes au procédé d'imprimerie en agençant le contraste et la densité de toutes les photographies montées sur une même planche. Si une figure est formée d'une demi-teinte et d'un dessin au trait, la photographie originale doit être montée avec l'original du dessin; on ne doit pas envoyer de photographie de l'ensemble. Dans le cas des micrographies électroniques et des photomicrographies, le grandissement doit être indiqué et nous recommandons l'ajout d'une échelle graphique sur les photographies.

Les **illustrations en couleur** doivent être soumises à l'approbation du directeur scientifique qui jugera de la nécessité d'utiliser la couleur. **Les auteurs devront défrayer les coûts que cela entraine** et se conformer à d'autres dispositions que l'on peut connaître en s'adressant au Service de publication.

La publication *Illustrating Science* : Standards for Publication (1988) du Council of Biology Editors, Inc. (Bethesda, MD 20814) fournit des directives quant à la publication des illustrations dans les revues et les livres scientifiques. **Nous la recommandons pour la préparation des dessins,** des graphiques, des cartes, des graphiques sur ordinateur et des demi-teintes, qui y est clairement expliquée et illustrée, de même que le procédé de quadrichromie.

PROCESSUS DE PUBLICATION

Soumission — Les auteurs doivent présenter leur manuscrit au directeur scientifique associé approprié (voir page i de chaque numéro). Une fois le manuscrit accepté, toute correspondance se fera entre l'auteur correspondant et le Service de publication à Ottawa, dont l'adresse se trouve au verso du plat supérieur de chaque numéro.

Épreuves en placard — Une épreuve en placard, des épreuves des illustrations, une copie du manuscrit corrigé et un bon de commande de tirés à part sont envoyés à l'auteur. **Les épreuves en placard doivent être relues attentivement, car elles ne sont pas corrigées par le Service de publication;** elles doivent en outre être retournées dans les 48 heures suivant leur réception. Au stade des épreuves, il n'est plus temps d'apporter des modifications importantes ni de faire des ajouts ou des suppressions. Les frais occasionnés par des modifications excessives devront être assumés par l'auteur.

Tirés à part — Pour obtenir des tirés à part, il est nécessaire de remplir le bon de commande et de le retourner avec le paiement (chèque, numéro de carte de crédit, numéro du bon d'achat ou pièce de journal interne) en même temps que les épreuves corrigées et le manuscrit ou, dans le cas des communications, dès que possible. Le tarif des tirés à part qui sont commandés après la parution du numéro de la revue est fortement majoré. Les tirés à part ne sont pas fournis gratuitement; ils ne seront envoyés qu'après réception du paiement.

Révisé en janvier 1991

In the March–April Issue...

FIFTH CANADIAN SEMICONDUCTOR TECHNOLOGY CONFERENCE

The Westin Hotel
Ottawa, ON, Canada
August 14–16, 1990

President, program committee	*Chairman*	*Guest Editor*
A.P. Roth	J.B. Webb	E. Fortin

◆◆◆◆◆◆◆◆◆◆◆◆◆◆◆◆◆◆◆◆◆◆◆◆

Dans le numéro de mars–avril...

CINQUIÉME CONFÉRENCE CANADIENNE SUR LA TECHNOLOGIE DES SEMICONDUCTEURS

L'Hôtel Westin
Ottawa, ON, Canada
14–16 août, 1990

Président, comité du programme	*Président*	*Directeur de publication invité*
A.P. Roth	J.B. Webb	E. Fortin

National Research Council Canada | Conseil national de recherches Canada

ISSN 0008-4204

Canadian Journal of Physics

Editor: R.W. Nicholls

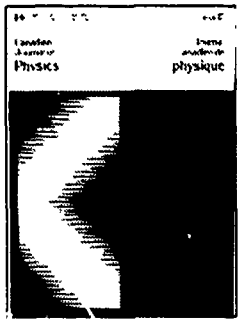

The *Canadian Journal of Physics* publishes research papers in all areas of physics, as well as in cross-disciplinary areas. The Journal from time to time publishes topical review articles and encourages the publication of special issues in which there is a strong concentration of articles in a given field. Recent special issues include "Proceedings of the International Conference on the Kinetics of Nonhomogeneous processes and nonlinear dynamics" (September 1990), "Proceedings of the Fifth Canadian Semiconductor Technology Conference" (April 1990), and the "Space Research" (Summer 1991). An internationally recognized general physics journal, it has published articles submitted by authors in more than 25 countries and attracts subscriptions from more than 65 countries

Subscription Information:

Canadian Journal of Physics is published monthly. Subscription rates for 1991 **Canada** $84.00 personal and $255.00 institutional. **U.S.A. and Foreign** $84.00 (US) personal and $255.00 (US) institutional. Canadian customers please include 7% GST. Payment must accompany order.

Order Form

Please check the appropriate box and return to **Subscription Office, Research Journals, National Research Council of Canada, Ottawa, Ontario, Canada K1A 0R6**

☐ I would like to subscribe to the *Canadian Journal of Physics*

☐ I wish to pay by cheque (cheques made payable to the Receiver General for Canada, credit NRC)

☐ I wish to pay by ☐ MasterCard ☐ Visa

Card No. ☐☐☐☐☐☐ ☐☐☐☐☐☐☐☐

Expiry Date _____ Signature _____

Please send a free sample of the *Canadian Journal of Physics*

Name _____

Address _____

City _____ Country _____ Postal Code _____

Canada

Code No.

GRANTS FOR MONOGRAPHS

The **Natural Sciences and Engineering Research Council of Canada (NSERC)** has introduced a second competition for grants in aid of the publication of monographs and books through its Scientific Publication Grants Program.

NSERC helps with publication of high-quality monographs and charts of relevance to Canada, or of books that present original scientific material in the natural sciences and engineering. The applications must be submitted by a publisher, or by a sponsoring scientific society or group. Grants are not made to authors. There is no limit on the number of applications that may be submitted by a sponsoring organization. The research communication must be published in Canada and the publishing rights reserved by a Canadian publisher.

Applications are considered twice each year, in **May** and in **October**. The deadline dates for receipt of applications are **April 15** and **October 1.**

For more information on the Scientific Publication Grants Program, contact:

Ginette Drouin
Natural Sciences and Engineering Research Council of Canada
200 Kent St.
Ottawa,Ontario, Canada
K1A 1H5

SUBVENTIONS POUR MONOGRAPHIES

Le **Conseil de recherches en sciences naturelles et en génie du Canada (CRSNG)** a récemment introduit un deuxième concours de subventions pour publication de monographies ou livres dans le cadre de son Programme de subventions pour publications scientifiques.

Le **CRSNG** appuie la publication de monographies de haute qualité, de cartes spécialement intéressantes pour le Canada ou de livres présentant des résultats scientifiques originaux en sciences naturelles et en génie. Les demandes de subventions doivent être soumises par un éditeur, une société ou un groupe scientifique canadien. On n'accorde pas de subventions aux auteurs. Le nombre de demandes que peut soumettre un organisme donné n'est pas limité. Les ouvrages doivent être publiés au Canada et les droits doivent être réservés par un éditeur canadien.

Les concours ont lieu deux fois par année, en **mai** et en **octobre**. Les dates limites de réception des demandes sont le **15 avril** et le **1er octobre**.

Pour de plus amples renseignements sur le Programme de subventions pour publications scientifiques, veuillez communiquer avec :

Ginette Drouin
Conseil de recherches en sciences naturelles et en génie du Canada
200, rue Kent
Ottawa (Ontario), Canada
K1A 1H5

Annual Subscription Rates / Abonnements annuels*†‡

Publication	Volume	Code	Canada ($CAN) Institutional/ Collectif (CI)	Canada ($CAN) Personal/ Personnel (CP)	Foreign / Étranger ($US) Institutional/ Collectif (FI)	Foreign / Étranger ($US) Personal/ Personnel (FP)	Foreign / Étranger ($US) Air mail / Par avion Add / ajouter
Monthly / Mensuelle							
Biochemistry and Cell Biology / Biochimie et biologie cellulaire	69	44	202	75	202	75	75
Canadian Journal of Botany / Journal canadien de botanique	69	45	290	115	290	128	150
Canadian Journal of Chemistry / Journal canadien de chimie	69	46	380	120	380	130	150
Canadian Journal of Earth Sciences / Journal canadien des sciences de la Terre	28	47	285	91	285	100	150
Canadian Journal of Forest Research / Journal canadien de recherche forestière	21	54	250	82	250	82	75
Canadian Journal of Microbiology / Journal canadien de microbiologie	37	48	205	81	205	81	75
Canadian Journal of Physics / Revue canadienne de physique	69	49	255	84	255	84	75
Canadian Journal of Physiology and Pharmacology / Journal canadien de physiologie et pharmacologie	69	50	275	90	275	90	75
Canadian Journal of Zoology / Journal canadien de zoologie	69	51	310	120	310	135	150
Bimonthly / Bimestrielle							
Canadian Journal of Civil Engineering / Revue canadienne de génie civil	18	52	200	65	200	65	75
Genome / Génome	34	70	185	76	185	76	75
Canadian Geotechnical Journal / Revue canadienne de géotechnique	28	53	160	60	160	66	50
Quarterly / Trimestrielle							
Computational Intelligence / Intelligence informatique	7	79	125	50	125	50	25

*Price of single issues of current volumes of all journals: institutional, $36.00; personal, $17.50. / Prix des volumes courants de toutes les revues, par numéro collectif, 36,00$; personnel, 17,50$.

†Rates include second-class postage. Canadian customers please include additional 7% GST. / Affranchissement de deuxième classe compris. Clients canadiens veuillez ajouter 7% pour la TPS.

‡Special rates apply for members of Canadian scientific and engineering societies if they subscribe through their respective societies. / Les tarifs spéciaux sont offerts aux membres des sociétés scientifiques et des sociétés de génie au Canada, s'ils s'abonnent par l'intermédiaire de leur société respective.

Subscriptions, renewals, requests for single or back numbers, and all remittances should be sent to Subscription Office, Research Journals, National Research Council of Canada, Ottawa, Ontario, Canada K1A 0R6. Remittances should be made payable to the Receiver General for Canada, credit National Research Council of Canada. Telephone enquiries: Helen Goulet 613-993-9084.

Subscriptions are entered for the calendar year. There are no refunds on cancelled subscriptions once delivery has begun.

Change of address - Send change of address information (complete old address, customer code, and new address) to Subscription Office, Research Journals, National Research Council of Canada, Ottawa, Ontario, Canada K1A 0R6.

Claims for missing numbers should be made within four months (North America) or six months (outside North America) following the date of publication. The publisher expects to supply missing numbers only when losses have been sustained in transit and when the reserve stock will permit.

Abonnements - Pour toutes les questions d'abonnements, paiements, demandes de vieux numéros de la revue, etc., on doit s'adresser au Bureau d'abonnements, Revues scientifiques, Conseil national de recherches du Canada, Ottawa (Ontario), Canada K1A 0R6. Les chèques et mandats seront formulés à l'ordre du Receveur général du Canada, au crédit du Conseil national de recherches du Canada. Renseignements : Helen Goulet 613-993-9084.

La durée des abonnements correspond à l'année civile. Les abonnements annulés ne pourront être remboursés une fois que le premier numéro sera envoyé.

Changement d'adresse - Faire parvenir tous renseignements (ancienne adresse, code du client et nouvelle adresse) au Bureau d'abonnements, Revues scientifiques, Conseil national de recherches du Canada, Ottawa (Ontario), Canada K1A 0R6.

Les réclamations de numéros manquants doivent être adressées dans les quatre mois (en Amérique du Nord) ou les six mois (à l'étranger) suivant la date de publication. L'éditeur s'engage à remplacer les numéros manquants seulement lorsque les pertes ont été subies en transit et lorsque ses réserves le permettent.

National Research Council Canada
Ottawa, Canada
K1A 0R6

Conseil national de recherches Canada
Ottawa, Ontario
K1A 0R6

Postage paid at Ottawa
Second class mail
Registration No 5435

Port payé à Ottawa
Courrier de deuxième classe
Enregistrement nº 5435

Canadian Journal of Physics

Volume 69 Number 2 February 1991

Revue canadienne de physique

Volume 69 numéro 2 février 1991

ELEMENTARY PARTICLES AND NUCLEAR PHYSICS/ PARTICULES ÉLÉMENTAIRES ET PHYSIQUE NUCLÉAIRE

ATOMIC AND MOLECULAR PHYSICS/PHYSIQUE ATOMIQUE ET MOLÉCULAIRE

GASES, FLUID DYNAMICS, AND PLASMAS/GAZ, DYNAMIQUE DES FLUIDES ET PLASMAS

CONDENSED MATTER/ÉTAT CONDENSÉ

Canada

Typeset and printed in Canada by / Composé et imprimé au The Runge Press Limited